

The American Monsoon System: variability and teleconnections



Jorge Luis García Franco

Wadham College

University of Oxford

A thesis submitted for the degree of

Doctor of Philosophy

Michaelmas 2021

Acknowledgements

This thesis would not exist without the support of my family, my supervisors and my friends. Lesley Gray and Scott Osprey offered me their help, guidance and kindness even before I applied to the DPhil. I am forever grateful for their help and support and that I was able to be part of their group and that I was able to learn from them. To Robin Chadwick, for always being willing to help me and provide very helpful advice and engage in discussions.

Thanks so much as well to Antje Weishemer, Philip Stier and Tim Woollings for reading my Confirmation and Transfer of Status reports and their helpful feedback which as certainly improved this thesis. Many thanks as well for Zane Martin for useful discussions and support throughout this project. To Andrea and Lucy, for helping me navigate all the administrative processes.

My deepest gratitude goes to the Richard's family, which supported my studies at Oxford through the Oxford-Richards scholarship at Wadham College. Acknowledgements to Wadham College and Dr. Hanna Christensen for all their support and advice. To Andrew Bushell, Robin Chadwick and the UK Met Office for the PhD CASE Studentship I was awarded through the Met Office Partnership program which was key to support the science found in this thesis.

To my parents, Virginia and Jorge, that have always encouraged and supported me all along the way, all together. Thank you. Things would be very different without me crossing paths with all the Ambiguos: Karen, Pablo, Diego, Adán, Alinne, Montse, Carolina, Marcos and Dieguito. Thank you for always welcoming me back home. Special thanks to Karen Solorzano, Karen Ines and Pablo Bonilla for supporting me at a long distance throughout the difficult times. And to Verónica, for without your support this thesis would not exist. To everyone in Mexico and Leeds that helped me get here: Michel, Angel, Juliane, Paloma, Marcos and Melissa. I also wish to thank all the great friends I made in Oxford: Kate, Aaron, RJ, Oscar, Hank, Filippo, Matt and Emily.

Abstract

This thesis investigates the representation of the variability and teleconnections of the American Monsoon System in the state-of-the-art general circulation models. The models exhibit several biases including an overestimation of the strength of the East Pacific Intertropical Convergence Zone (ITCZ) and the position of the Atlantic ITCZ. The representation of the seasonality and magnitude of monsoon precipitation in the North American and Central American monsoons has improved compared to previous generations of the models, however, the spatial distribution of precipitation in the South American Monsoon is still poorly represented due to biases in the equatorial Atlantic sea-surface temperatures (SSTs)s. These simulations reasonably represent the seasonal cycle of precipitation in southern Mexico and Central America, where a bimodal signal known as the Mid-summer drought (MSD) has been important for agriculture in the region for centuries. A wavelet transform method is developed to diagnose the timings of the bimodal seasonal cycle and results illustrate that the method can diagnose monsoon timings in any monsoon region for any precipitation time series, including climate model output. Using this method, several theories that explain the existence and timing of the MSD signal in southern Mexico and Central America are evaluated using reanalysis and climate models. These results suggest that the MSD can be most consistently explained through the effect of seasonally varying moisture transport driven by the low-level flow in the Caribbean Sea. The influence of the quasi-biennial oscillation (QBO) teleconnections is explored in several climate model simulations, and the results suggest that the QBO could affect ocean-atmosphere phenomena. More frequent positive phases of El Niño-Southern Oscillation and the Indian Ocean Dipole, and a weaker Walker circulation are found during QBOW compared to QBOE in the models. Atmosphere-only and coupled ocean-atmosphere experiments are performed where the zonal winds in the equatorial stratosphere are specified, by relaxing them towards reanalysis data. The representation of the QBO is improved in these experiments, particularly in the lower stratosphere. However, the surface impacts of the QBO in the experiments with the relaxation result in a weaker tropical response to the QBO phase compared to the free-running models. These results imply that the relaxation has disrupted processes and/or feedbacks that are important for the surface impact of the QBO. The results of these experiments highlight the importance of SST feedbacks and the interaction of tropical waves with the zonal flow in the stratosphere for the interaction of the QBO on tropical convection.

Contents

List of Abbreviations	vii
1 Introduction	1
1.1 Motivation	1
1.2 Thesis aims and outline	4
2 Background	8
2.1 The tropical circulation and the global monsoon	8
2.2 The American Monsoon System	15
2.3 A review of the physical mechanisms for the Midsummer drought	19
2.4 El Niño Southern Oscillation: impacts on the American monsoon system . .	24
2.5 The QBO and tropical convection	28
2.5.1 The Quasi-biennial oscillation (QBO)	28
2.5.2 Tropical teleconnections of the QBO	29
3 Data and methods	35
3.1 Observations and reanalysis data	35
3.1.1 Gridded precipitation datasets	35
3.1.2 ERA-5	38
3.2 The Unified Model of the Met Office Hadley Centre	39
3.2.1 The Global Coupled Configurations of HadGEM3	39
3.2.2 The CMIP6 experiments	42
3.3 The Moist Static Energy Budget	43
4 The American monsoon system in UKESM1 and HadGEM3	46
4.1 Introduction	46
4.2 Methods and data	48
4.3 Surface temperature and low-level wind	50
4.4 The Atlantic and Pacific ITCZs and the SACZ	55
4.5 Precipitation and convection in the AMS	59
4.5.1 Mean seasonal precipitation	59
4.5.2 The annual cycle of rainfall	62

4.5.3	Characteristics of convective activity	64
4.6	ENSO Impacts	67
4.6.1	Canonical impacts to the AMS	67
4.6.2	The role of ENSO flavours	73
4.6.3	A possible influence of the QBO on tropical ENSO teleconnections .	74
4.7	Summary and discussion	78
5	A wavelet transform method to determine monsoon onset and retreat	83
5.1	Introduction	83
5.2	Data	86
5.2.1	Precipitation datasets and reanalysis data	86
5.2.2	Model data	87
5.3	The wavelet transform method	87
5.3.1	Identification of Monsoon Onset and Retreat	89
5.3.2	Extension for Application to the MSD signal	93
5.3.3	Comparative Methodologies	95
5.4	Results	96
5.4.1	The North American Monsoon	97
5.4.2	The Indian Monsoon	100
5.4.3	The midsummer drought	103
5.5	Summary and discussion	112
6	The Midsummer drought in the MOHC CMIP6 experiments	116
6.1	Introduction	116
6.2	Data and methods	120
6.2.1	Observations and reanalysis data	120
6.2.2	CMIP6 data	121
6.2.3	Determination of the timings of the MSD	121
6.3	Climatological features	123
6.4	The role of East Pacific SSTs	130
6.5	The role of cloud-radiative effects	137
6.6	The role of the Caribbean Low-Level Jet	145
6.7	A short look at the MSD through the lense of the moist static energy budget	150
6.8	Summary and discussion	159

7 The tropical route of QBO teleconnections in UKESM1 and HadGEM3	164
7.1 Introduction	164
7.2 Methods and data	168
7.2.1 CMIP6 data	168
7.2.2 Indices	169
7.2.3 Analysis techniques	170
7.2.4 Nudging experimental setup	171
7.3 Teleconnections in the pre-industrial control experiments	173
7.3.1 Precipitation and SST response	174
7.3.2 ITCZ and monsoons	177
7.3.3 ENSO and the IOD	180
7.3.4 The Walker circulation	184
7.3.5 ENSO influence on the QBO	187
7.4 The nudging experiments	189
7.4.1 Atmosphere-only experiments	189
7.4.2 Coupled experiments	192
7.5 Summary and discussion	197
8 Conclusions	201
8.1 Summary and contributions	201
8.2 Limitations and future work	206
Bibliography	209

List of Abbreviations

AMS	American Monsoon System.
CLLJ	Caribbean Low-Level Jet.
CMIP	Coupled Model Intercomparison Project.
CRE	Cloud-radiative Effect.
ENSO	El Niño-Southern Oscillation.
GCM	General Circulation Model.
IOD	Indian Ocean Dipole.
ITCZ	Inter-tropical Convergence Zone.
MOHC	Met Office Hadley Centre.
MSD	Mid-summer Drought.
MSE	Moist Static Energy.
OLR	Outgoing Longwave Radiation.
QBO	Quasi-biennial Oscillation.
SACZ	South Atlantic Convergence Zone.
SAMS	South American Monsoon System.
SST	Sea-surface Temperature.
TWC	Total water content.
WT	Wavelet Transform.

1

Introduction

The American Monsoon System (AMS) is the main source of rainfall for most of Latin America and the southwestern United States, regions where agricultural activity is an important economic activity and a vast wealth of ecosystems and biodiversity are supported by monsoon rainfall in this region. Changes to the amount, timing and location of rainfall over different temporal scales have direct consequences for society and ecosystems. For that reason, improving our physical understanding of the mechanisms that cause temporal changes to the AMS rainfall is crucial to improve our medium-range forecasts and our climate predictions which could ultimately render key information for risk assessments, climate adaptation and agricultural strategies. In this context, this thesis aims to tackle outstanding questions in the American Monsoons using a global climate model with a particular interest in better understanding the physical mechanisms associated with variability and teleconnections of this monsoon.

1.1 Motivation

Temporal and spatial variability of rainfall is important for society throughout the planet, but the short and long-term changes to precipitation are increasingly relevant in agriculturally active and biodiverse hotspot tropical regions (Sultan et al., 2005; Jain et al., 2015). In the AMS, changes to rainfall, i.e., variability on inter-annual scales can produce long-lived

droughts that are associated with crop loss and forest fire intensification (Chen et al., 2009; Harvey et al., 2018). A large body of monsoon research is consequently focused in understanding the physical mechanisms responsible for precipitation variability across temporal and spatial scales (Wang et al., 2017; Gadgil, 2018).

The AMS was recognized as a monsoon only after the 1990s (Adams and Comrie, 1997; Zhou and Lau, 1998), which is relatively recent, as the definition for a monsoon has evolved from an initial dynamical definition based on a reversal of the prevailing winds to an agronomical definition that recognizes the seasonality of precipitation as the dominant feature of a monsoon (Wang et al., 2017; Gadgil, 2018). This means, however, that our understanding of the AMS is more limited compared to other monsoons given the lower number of studies on the AMS from a monsoon perspective compared to other monsoons such as the Indian monsoons, where monsoon forecasts exist since the 19th century (Blanford, 1886).

Recently, theories for monsoon dynamics (Bordoni and Schneider, 2008; Biasutti et al., 2018; Hill, 2019; Geen et al., 2020) have arisen to coherently explain the monsoons through a general physical mechanism. Most of these theories aim to explain a global inter-hemispheric band of convection that is driven by the seasonal cycle of solar insolation. Several characteristics of the North and South American monsoons, however, challenge the basic physical inferences or predictions of these theories, which means that these frameworks cannot readily be applied to the AMS. For this reason, several primary questions about the AMS remain open such as mechanisms and sources for interannual variability and teleconnections (Cai et al., 2020), the effect of greenhouse forcing on the monsoon dynamics (Liebmann and Mechoso, 2011; Pascale et al., 2019) and the role of soil-atmosphere interactions (Dominguez et al., 2008; Malhi et al., 2009; Adams et al., 2013).

The lack of understanding of the basic physical mechanisms that drive the seasonal cycle of rainfall in southern Mexico and Central America is one example of the gaps in the literature of the AMS. The so-called Midsummer drought is a robust bimodal feature of the seasonal cycle of precipitation during the wet season that has had implications for agricultural practices in the region since the Mayan Empire (AD 800-900) (Jobbová et al., 2018). Despite the importance of region-wide agricultural practices, the physical mechanisms that can explain this seasonal variation of rainfall remain disputed over recent

years (Karnauskas et al., 2013; Herrera et al., 2015; Zermeño-Díaz, 2019). The topic of drought in southern Mexico and Central America will be a central aspect of this thesis.

El Niño-Southern Oscillation (ENSO) is a coupled-ocean atmosphere phenomena in the Pacific Ocean that produces long-distance impacts throughout the planet (McPhaden et al., 2006), and is known to be a prominent influence of interannual variability in the AMS regions (Magaña et al., 2003; Vera et al., 2006; Marengo et al., 2014). Progress has been made in understanding the impacts and pathways of ENSO to South America (Marengo et al., 2012; Cai et al., 2020), and current research has found that ENSO variability promotes different impacts to South America (Hill et al., 2009; Tedeschi et al., 2015). However, the interaction of ENSO teleconnections with other aspects of climate variability is still an active topic of research (Cai et al., 2020; Jimenez et al., 2021).

For instance, a growing number of studies have suggested a link between the stratosphere and the tropical troposphere, called stratospheric-tropospheric coupling (Haynes et al., 2021). This coupling is suggested to include tropospheric features such as ENSO and other modes of tropical intraseasonal variability (Hitchman et al., 2021; Martin et al., 2021b). There is no full description of the causes for these observed relationships yet, but if the stratosphere is found to be a relevant factor to modulate aspects of tropical convection, such as ENSO impacts, there would be an opportunity to better predict tropospheric variability because the equatorial stratosphere is generally predictable at longer time-scales than the troposphere. Therefore, stratospheric-tropospheric will be another central topic of this thesis.

One key tool to understand the causes for regional changes to monsoon rainfall are general circulation models (GCMs). These models are useful to evaluate the roles of climate features such as orography, vegetation-atmosphere and ocean-atmosphere feedbacks, ENSO and their impacts over many aspects of Earth's climate including monsoons (Zhou et al., 2016). However, the use of GCMs to address key questions of the AMS has been scarce and detailed accounts of the biases –differences between the simulated climate of a model and the real world – are rarely done with explicit emphasis on the AMS. In other words, GCMs are rarely evaluated in the AMS, so our understanding is deficient in the knowledge of the relevant biases in current GCMs and, therefore, GCMs are less frequently used to address scientific questions related to the AMS.

This thesis focuses on the AMS and several outstanding questions regarding aspects of climate variability and teleconnections affecting this monsoon. The first results of this thesis begin with Chapter 4 by evaluating a state-of-the-art climate model in the AMS region and comparing the model with several observational datasets. This assessment highlights that the UM model is fit to investigate two outstanding research questions in the AMS and monsoon literature: the physical mechanisms that control the seasonal cycle of rainfall in southern Mexico and Central America, and the role of the tropical stratosphere for tropical convection and monsoons.

For the first research question, Chapter 5 describes a new method to determine monsoon timings, including the timings of bimodal regimes of precipitation in observations and climate model output. This method is then used in Chapter 6 to investigate the physical mechanisms of the seasonal cycle of precipitation in southern Mexico and Central America.

1.2 Thesis aims and outline

The main aim of this thesis is to investigate the physical causes of variability and the mechanisms associated with teleconnections to the AMS. The specific key aims of this thesis are:

1. To characterize the large-scale biases in a state-of-the-art GCM that are relevant for the representation of rainfall in the AMS.
 - (a) To characterize the main biases in the thermodynamical and dynamical features over the large scale tropical domain and the regional AMS sub-domains.
 - (b) To evaluate the roles of large-scale biases, horizontal resolution and the use of Earth system processes for regional monsoon representation.
 - (c) To assess the representation of the teleconnection associated with the main driver of interannual variability, i.e., ENSO in a GCM with specific emphasis on the causes for non-linearity and non-asymmetry in the teleconnections.
2. Evaluate the seasonal variability of the monsoon onset, withdrawal and intra-seasonal changes in the GCM and compare to observational datasets.

3. Describe and investigate the physical mechanisms associated with the seasonal cycle of rainfall in Central America and southern Mexico by testing previous hypothesis of physical mechanisms within the model.
4. To investigate the role of stratospheric-tropospheric coupling in the tropics and the role of the tropopause for convection in the AMS and for ENSO teleconnections.

The remainder of this thesis is structured as follows:

- Chapter 2 provides a review of the literature on key aspects of the American monsoons. The chapter begins by introducing the concepts of monsoons, their different physical interpretations as a global phenomena and the place of regional monsoons in the global scale. Then, the North and South American monsoons are introduced and detail is given on the applicability of large-scale monsoon theories to these regional monsoons. This section is followed by a literature review of the proposed physical mechanisms that drive the seasonal cycle of rainfall in Central America, southern Mexico and the Caribbean. El Niño-Southern Oscillation impacts over North and South America and, finally, the chapter summarises the literature on stratospheric-tropospheric coupling in the tropics, discussing possible mechanisms by which the stratospheric quasi-biennial oscillation may be influential for tropical convection.
- Chapter 3 describes the observational datasets used in this thesis, composed of four gridded precipitation datasets and one reanalysis dataset: ERA5. The chapter also described the UK Met Office Hadley Centre Unified Model (UM) and the configurations of the UM used in this thesis and the Coupled Model Intercomparison Project phase 6 (CMIP6).
- Chapter 4 evaluates the representation of the AMS in three configurations of the UM model submitted to CMIP6. The chapter describes large-scale biases over the tropics and regional scale biases in the precipitation amount and seasonality in key regions of the AMS. ENSO teleconnections are also evaluated over the AMS examining the non-linearity of simulated and observed teleconnections and the role of ENSO flavours.

This chapter highlights relevant questions that are of interest to the wider AMS community that are tackled in the remaining chapters: first, the skill of the models in reproducing a bimodal signal in the seasonal cycle of rainfall in Central America and southern Mexico and second, a possible modulation of ENSO teleconnections by the stratospheric quasi-biennial oscillation. The majority of the work in this chapter has been published in *Weather and Climate Dynamics* as García-Franco et al. (2020).

- Chapter 5 details a wavelet covariant transform method used to diagnose the start and end of the rainy season in a monsoon using precipitation time-series. The method is extended to determine the timing of bimodal regimes, and even whether or not a bimodal regime exists or not in a given region. The method is illustrated in the North American and Indian monsoons, and for the Mid-summer Drought signals of the Caribbean and southern Mexico. This chapter has been published in the *The International Journal of Climatology* as García-Franco et al. (2021).
- Chapter 6 uses the wavelet method to investigate the physical mechanisms that cause the bimodal regime of precipitation in southern Mexico in the UM CMIP6 models. The chapter tests elements of three leading hypothesis for the Mid-summer drought, specifically the chapter examines the roles of the East Pacific sea-surface temperatures, the cloud-radiative effects and shortwave radiation and the Caribbean Low-Level Jet. Furthermore, the chapter uses a moist static energy budget, which provides useful insight into the physical mechanisms that dominate intra-seasonal changes to precipitation.
- Chapter 7 investigates the tropical route of QBO teleconnections in the pre-industrial control experiments of HadGEM3 and UKESM1 and in targeted nudging experiments. The observational evidence that links the QBO with the ITCZ, ENSO and the Walker circulation is examined within these simulations to evaluate whether similar relationships to the observations are found within a state-of-the-art GCM. The results from these CMIP6 simulations are very similar to observations suggesting robust relationships between the QBO phase, the ITCZs and the Walker circulation. The

experiments with a nudged stratosphere improve the biases in the representation of the QBO, so their results can be used to test the causal pathway through which the tropical troposphere and stratosphere interact with each other. The results of this chapter show that when the relaxation was applied most of the teleconnections observed in the control experiments disappear, indicating either that the mechanisms that modulate stratospheric-tropospheric coupling were obscured by the experimental design or that the QBO variability is not driving these teleconnections.

2

Background

This chapter provides the necessary background for the topics of the thesis; first by summarising the main aspects of the tropical circulation and of the global monsoon and discussing the existing theories to explain the monsoon phenomena. Then, the American Monsoon System is introduced and detail is given on the Midsummer drought of southern Mexico and Central America and El Niño Southern Oscillation teleconnections to this monsoon. Finally, a summary of the literature on tropical stratospheric-tropospheric coupling is given by describing the stratospheric quasi-biennial oscillation (QBO) and existing evidence linking the QBO to the tropical troposphere and monsoons.

2.1 The tropical circulation and the global monsoon

Tropical climate is a result of the strong solar insolation that year-round provides a stronger surface heating compared to extra-tropical latitudes. These latitudinal differences in insolation generate a meridional heat transport by the coupled atmosphere-ocean system. This means that the tropics have a positive annual net energy and the extra-tropics show an annual negative net energy balance. Tropical dynamics is also distinct from extra-tropical latitudes due to other physical features such as the relative extent and location of the continents, the Coriolis effect, and the spectrum and speed characteristics of wave-propagation through the atmosphere. Generally, tropical dynamics is considered to be less well understood

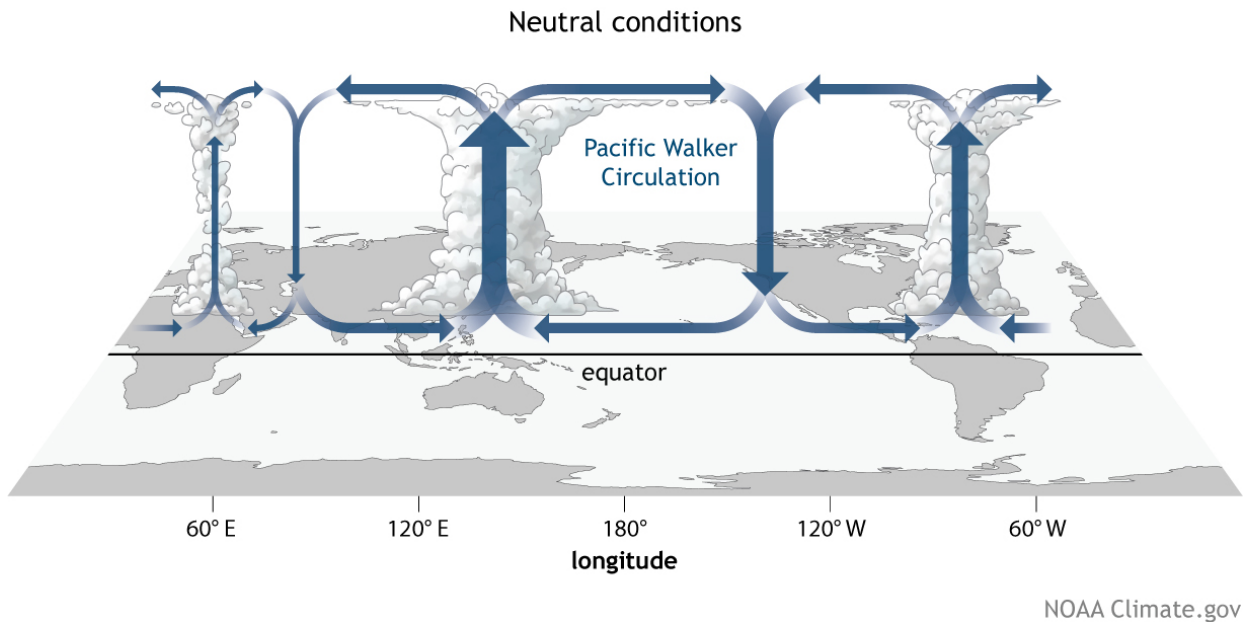


Figure 2.1: A schematic of the Walker circulation, depicting the mean zonal and vertical circulations, under neutral conditions of El Niño-Southern Oscillation. Schematic originally from: www.climate.gov/.

than mid-latitude dynamics, because most of the assumptions of mid-latitude dynamical frameworks break down in the tropics, but also because reliable data in the tropics was scarce until satellite observations of the tropics began in the 1980s (Emanuel, 2007; Webster, 2020).

Moist convection is one of the characteristic traits of a tropical climate as the dynamic and thermodynamic effects of deep moist convection provide important feedbacks to the regional and large-scale circulation (Emanuel et al., 1994; Webster, 2020). Convective activity can generate large-scale propagating waves and modify the regional or large-scale scale circulation, causing long-distance impacts (Hartmann, 2015; Li and Hsu, 2018). Moist convective systems span different spatial and temporal scales, from short-lived cumulonimbus showers to tropical cyclones. Deep convection is intertwined with the large-scale tropical circulation, which is typically divided into meridional and zonal overturning circulations, the Hadley and Walker circulations.

The Hadley cell is the meridional overturning circulation that arises from the differential heating between the tropics and the midlatitudes. This overturning cell is characterized by ascending motions in the tropics and descending motions in the subtropics and acts to transport heat poleward from the equator (Lorenz, 1967). The ascending section of the

Hadley circulation migrates meridionally with the seasonal cycle, the winter and summer cells interact with each other but also with the midlatitudes through eddy momentum fluxes (Bordoni and Schneider, 2008). The Hadley cell is not zonally symmetric; the boreal summer Hadley cell, for instance, is primarily a result of ascent in the Indian Ocean and the West Pacific regions with a minor contribution from ascending motions in Central and North America (Hoskins et al., 2020).

In turn, zonal circulations also exist in the tropical atmosphere and the most prominent example is the Walker circulation. The Walker circulation is the zonal overturning circulation that is found in the equatorial Pacific Ocean, illustrated in Figure 2.1 and characterized by ascending motion over the West Pacific and descending motions over the East Pacific (Walker, 1924; Bjerknes, 1969; Gill, 1980). The dynamic and thermodynamic effects of the location and strength of convection associated with the Walker circulation have strong impacts across the tropical and extra-tropical atmosphere, known as teleconnections (Cai et al., 2019).

Another relevant aspect of the tropical circulation is the Intertropical Convergence Zone (ITCZ), which is a tropical band of convective clouds and precipitation that migrates meridionally with the seasons, characterized by a strong convergent flow at low levels and a strong divergent flow at upper levels (Schneider et al., 2014). The ITCZ is intertwined with the Hadley cell as the position of the ITCZ is collocated with the ascending branch of the Hadley cell (Donohoe et al., 2013; Hartmann, 2015), and is arguably one of the most relevant features of tropical climate due to the strong influence of convective activity in the ITCZ over the low- and upper-level circulation, tropospheric latent heating due to deep moist convection, as well as the fact that the largest precipitation rates in the tropics are found in the ITCZ.

The position and strength of the ITCZ results from the inter-hemispheric energy and momentum balances so that the ITCZ is predominantly north of the equator because of the inter-hemispheric temperature contrast (Donohoe et al., 2013; Bischoff and Schneider, 2016). Over regional scales, the seasonal migration of the ITCZ follows closely the seasonal cycle of SSTs, which depends on the solar insolation and the coupling between SST gradients, cloud radiative heating and the low-level easterly flow (Richter et al., 2014; Siongco et al., 2015; Oueslati and Bellon, 2015; Harrop and Hartmann, 2016). Variability in the characteristics of the ITCZ can affect relatively remote regions through impacts in the tropical convective

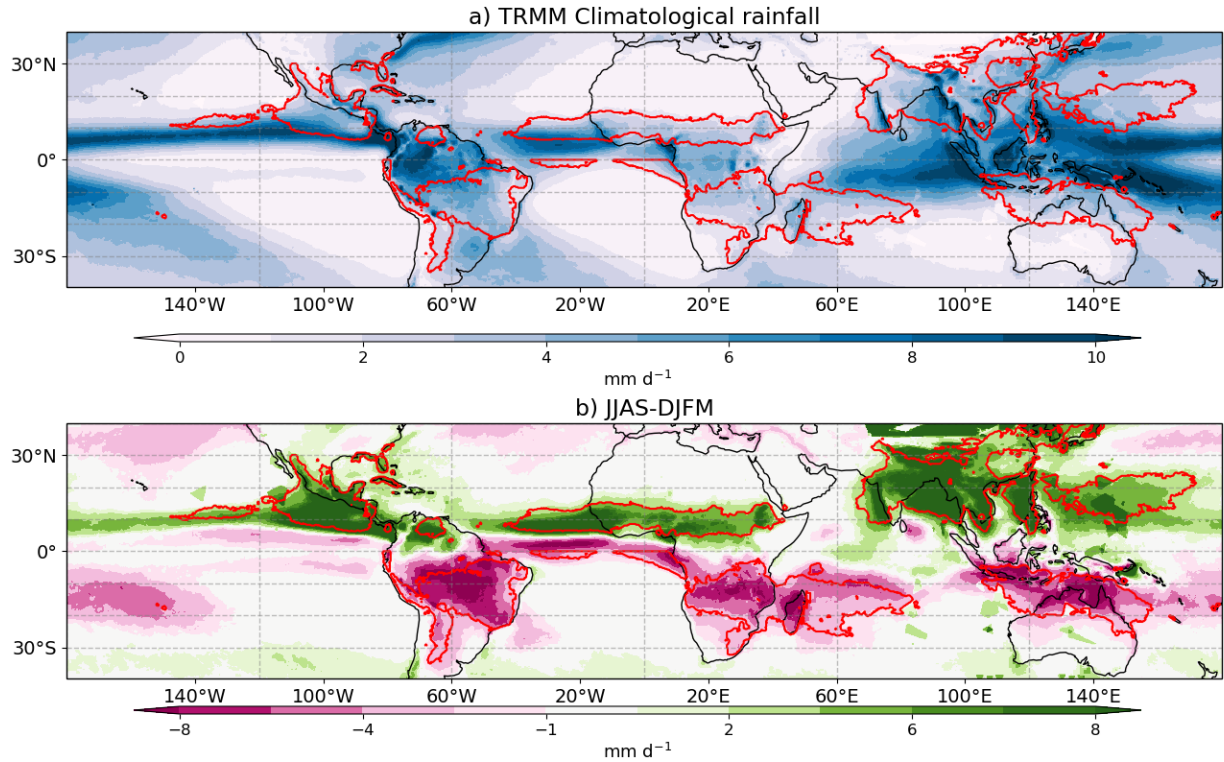


Figure 2.2: a) Climatological mean annual rainfall rates in the tropics using data from the Tropical Rainfall Measurement Mission (TRMM) dataset (1999-2018). b) The mean rainfall rate difference between boreal summer (JJAS) and austral summer (DJFM). The red contours highlight the regions where the mean summer rainfall amount accounts for more than 55% of the mean total annual rainfall accumulation.

heating, a modulation of the wave-train propagation and of the strength and location of mass-flux descent (Neelin and Su, 2005; Neelin, 2007; Cai et al., 2019).

In spite of the global impact of the ITCZ and tropical circulations, one of the phenomena of tropical climate that first generated research interest is the monsoon (Halley, 1687). The word *monsoon* stems from the Arabic word for *season* and this definition illustrates the very first conceptions of a monsoon. The first widely accepted view of a monsoon suggested that it was the result of a large-scale land-sea breeze associated with the differential warming of the land and the ocean that force a seasonal reversal of the low-level winds bringing seasonal rainfall to a region (Halley, 1687).

The traditional definition of the monsoon as a land-sea breeze has several shortcomings. Firstly, several mid-latitude regions would fit a monsoon definition based solely on a seasonal reversal of the wind (Gadgil, 2018), and secondly, regions that are now recognized as a

region with a monsoon climate, e.g. in South America, do not show a seasonal reversal of the winds, and the wind flow may just exhibit seasonal changes in direction and strength (Vera et al., 2006). For these reasons, the land-sea breeze view of monsoons has recently been replaced by three alternative conceptions, an ITCZ-monsoon framework, a convective quasi-equilibrium interpretation and a moist static energy (MSE) zonal-mean energetic interpretation (Biasutti et al., 2018; Hill, 2019; Geen et al., 2020).

The first framework explains monsoons as a poleward extension of the ITCZ into land generalizing all monsoons as an expression of global tropical convergence resulting from the energy balance (Chao and Chen, 2001; Gadgil, 2018). This interpretation has led to the concept of *the global monsoon*, a term that encompasses all the regions in the tropics that exhibit a strong seasonality in precipitation (Zhou et al., 2016; Gadgil, 2018). In practice, the global monsoon refers to those regions of the planet where more than 70% of the total annual rainfall is observed during the local summer season, therefore, the concept of a global monsoon recognises the seasonality of precipitation as the key feature to diagnose a monsoon (Zhou et al., 2016; Wang et al., 2017).

Figure 2.2 shows the global monsoon as depicted by the TRMM dataset. By this definition, the majority of the regions over land between 5 and 10 degrees away from the equator are part of the global monsoon. A regional monsoon, such as the Indian Monsoon, is then a subset of the global monsoon with unique regional characteristics that shape this monsoon differently to other regional monsoons in terms of the seasonality, the strength and the dynamics. The American Monsoon System is then the regional monsoon that is located in the subtropics of North and South America.

Bordoni and Schneider (2008) provide an alternative conceptual view of monsoons, describing the characteristic rapid onset of a monsoon as a regime transition of the Hadley cell from an eddy momentum -driven circulation, which resembles a canonical ITCZ regime, to a thermally direct circulation which resembles a monsoon-like circulation. The zonal mean MSE meridional gradient drives the ITCZ location and determines the strength of the overturning circulation by modulating the ventilation from the midlatitudes that bring cooler and drier air in a feedback mechanism (Geen et al., 2020). Even though Bordoni

and Schneider (2008) propose an axisymmetric framework, their predictions were broadly consistent with the Asian monsoon circulation.

Convective quasi-equilibrium (CQE) is a theory for moist convection where convection sets the vertical temperature and moisture profiles to a convectively neutral state, thereby setting the free tropospheric temperature (Neelin, 2007). For a monsoonal circulation, this theory emphasizes the coupling of convection and dynamics predicting that the sub-cloud layer equivalent potential temperature maxima must be collocated with the free tropospheric saturation equivalent potential temperature (Nie et al., 2010; Geen et al., 2020). The rapid onset of the Asian monsoon is associated with the boundary layer moist entropy distribution, in agreement with predictions of CQE (Nie et al., 2010; Boos, 2015; Ma et al., 2019).

Several studies examine the monsoon as a large-scale phenomenon through an axisymmetric framework that assumes zonal symmetry investigated through global energetic diagnostics (e.g. Faulk et al., 2017; Geen et al., 2019; Byrne and Zanna, 2020). The zonal-mean framework is common to the Hadley cell interpretation of monsoons (Bordoni and Schneider, 2008), as well as the ITCZ-monsoon theory. However, regional monsoons are shaped by the asymmetries imposed by the orography, the characteristics of the surrounding ocean basins, land-sea contrasts and also the role of vegetation-hydrology coupling (Wang et al., 2017; Pascale et al., 2019). The importance of zonal asymmetries has raised multiple issues with large-scale so-called monsoon dynamics theories, as several predictions of these theories are not consistent with observations of regional monsoons (e.g. Nie et al., 2010; Smyth et al., 2018; Biasutti et al., 2018; Pascale et al., 2019).

The MSE budget framework suffers both from theoretical and practical shortcomings. One practical shortcoming is that the calculation of the budget terms post hoc in reanalysis or models results in very large residuals (Hill, 2019), so these frameworks work best when the calculations of the budget terms are integrated online at each time-step (e.g. Ma et al., 2019). Another shortcoming is that the surface fluxes over land, e.g., in the Sonoran and Saharan deserts and the deep Amazon make the estimations of the roles of hydrology-vegetation feedbacks and their potential contributions to the MSE budget in observations very difficult to assess (Boos and Korty, 2016; Pascale et al., 2019). The use of simpler moisture budgets has proven useful in a regional context to investigate the sources of

moisture for monsoons in current (Ordoñez et al., 2019; Martinez et al., 2019) and future climates (Smyth and Ming, 2020), but this budget is mostly a tool and not a coherent theory for the dynamics of monsoons.

Recent reviews acknowledge that all these frameworks have significant shortcomings when applied to regional monsoons (Biasutti et al., 2018; Hill, 2019; Geen et al., 2020). These reviews conclude that a framework that reconciles the global energetic perspective with the characteristics of regional monsoons would be crucially important and very useful, but as several authors point out (e.g. Biasutti et al., 2018; Hill, 2019), also very hard to formulate. **There is no detailed physical description of the global monsoon system with a single theoretical formulation that can explain the observed features of all the regional monsoons.**

The Hadley cell interpretation of monsoons has significant shortcomings to depict some regional monsoons, particularly those that are not the Asian monsoon as the overturning circulation in the South Asian monsoon is strong enough to be represented by a clear thermally direct regime. However, this energetic framework assumes no zonal transport of energy, which minimizes the role of orography and land-sea interaction (Biasutti et al., 2018), which may explain why the North American monsoon does not exhibit the circulation described by Bordoni and Schneider (2008). One might reasonably infer from these results that the timing of the transition in the zonal mean overturning cells would be similar for monsoons at different longitudes but similar latitudes, which is not the case (Wang et al., 2017).

Furthermore, a monsoon restricted to a small area, such as the North American and African monsoons may not show a clear zonally averaged overturning regime and may be significantly affected by local shallow and deep circulations (Zhai and Boos, 2015). For instance, Smyth et al. (2018) show that the simulated West African monsoon when forced with different solar forcings exhibits a decoupling between the zonal-mean ITCZ location, the strength of the local Hadley cell and the monsoon rainfall, in opposition to the predictions of this framework (Bordoni and Schneider, 2008).

In short, despite significant progress in our understanding of the monsoon phenomena at the planetary scale through zonal mean energetic frameworks, there is an important gap between large-scale theories of monsoon dynamics and the observed regional monsoons. The next section presents a summary of the North and South American monsoon literature,

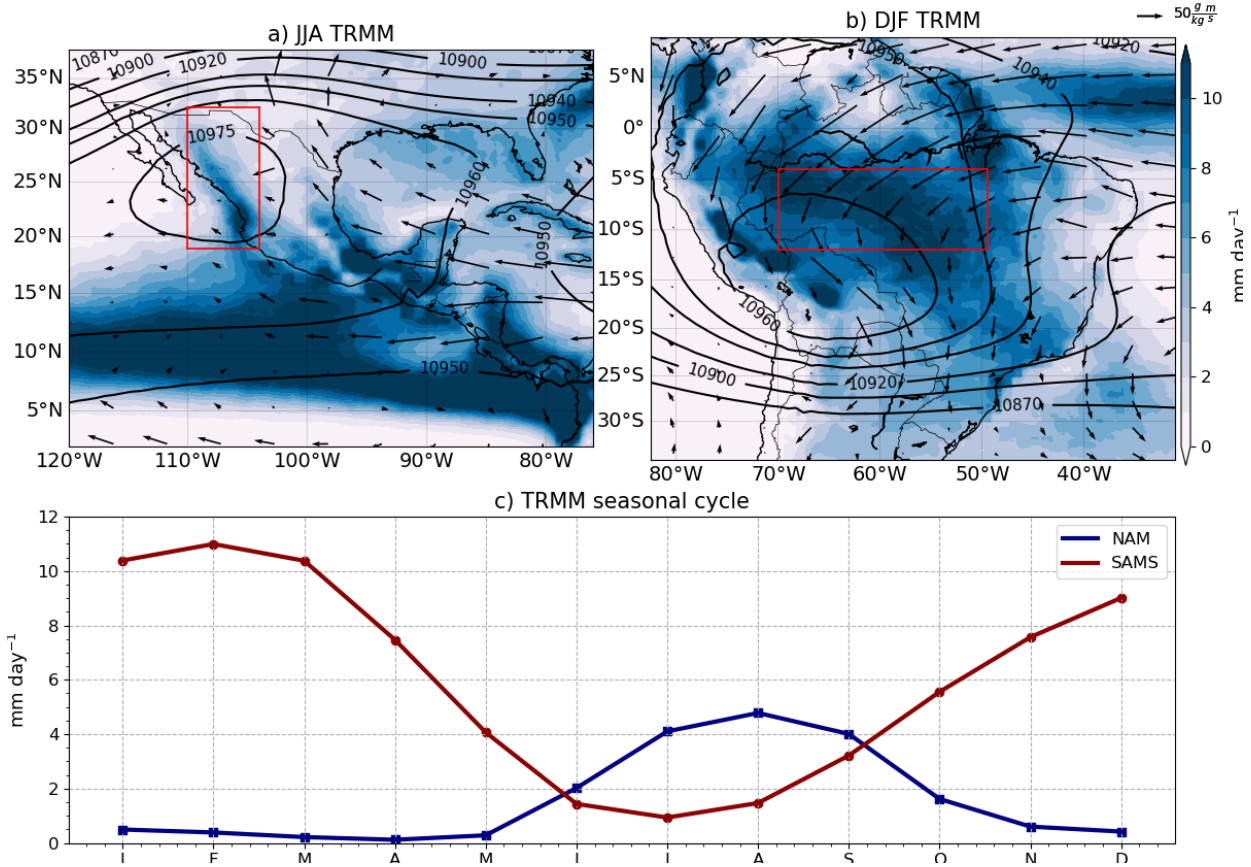


Figure 2.3: Climatological mean a) boreal and b) austral summer rainfall (shading), 850 hPa moisture flux (vectors) and geopotential height at 250 hPa (contours) in a) southern North America and b) South America. c) Monthly-mean seasonal march of precipitation in the TRMM dataset for two area-averaged time-series, the North American Monsoon (NAM) and the South American Monsoon System (SAMS) shown in the red rectangles in a-b).

which explains the characteristics of these monsoons through the effect of regional features and dynamics, seemingly detached from the literature in this section.

2.2 The American Monsoon System

The American Monsoon System (AMS) is the main source of rainfall for tropical Latin America and is typically subdivided into the North and South American monsoon systems (Vera et al., 2006). Although the spatial definition of the AMS is quite varied amongst studies, a general consensus is that the North American Monsoon is found in south-western North America (Figure 2.3a) extending north from central-west Mexico into the southwestern United States and the South American Monsoon is centred in the deep Amazon south

to the river mouth (Figure 2.3b) but southeastern Brazil (Adams and Comrie, 1997; Stensrud et al., 1997; Vera et al., 2006).

The seasonal cycle of rainfall in the North American Monsoon is characterised by a wet July-August-September season and significantly drier conditions during the rest of the year (Adams and Comrie, 1997) (Figure 2.3c). Three temporal stages describe the evolution of the North American Monsoon (Adams and Comrie, 1997; Geil et al., 2013). First, the onset stage (May-June) starts with a strong surface warming that leads to very high temperatures in the desert region. Simultaneously, the subtropical jet weakens and migrates north decreasing the frequency of mid-latitude disturbances in the monsoon region (Douglas et al., 1993; Turrent and Cavazos, 2009). These factors combine to develop a low-level thermal surface low pressure linked with an upper-level anticyclone and moisture influx from the nearby Gulf of California and easternmost Pacific Ocean (Douglas et al., 1993; Geil et al., 2013).

Maturity (July-August) is the peak period of monsoon rainfall characterised by sustained deep convection (Barlow et al., 1998) and significant increases in low and mid-level moisture flux convergence and mid-level latent heating (Adams and Comrie, 1997; Cook and Seager, 2013). The latent heating caused by deep convection can be diagnosed in the upper-level geopotential height (Figure 2.3a) in the form of an anticyclone centred on the monsoon region. The moisture flux convergence decreases in August, after which precipitation recycling (Dominguez et al., 2008) plays an important role in keeping deep convection active until September. Decay (September-October) is the last stage of the monsoon, in many ways opposite to the onset stage, as is characterised by the equatorward migration of the subtropical jet (Higgins et al., 1997; Geil et al., 2013), evaporation in the nearby basins decreases and deep convection in the monsoon region disappears (Douglas et al., 1993).

The origin of moisture at low and mid-levels in the monsoon region has been a matter of debate (Adams and Comrie, 1997; Barlow et al., 1998; Vera et al., 2006; Ordoñez et al., 2019), with several studies suggesting that the main source of moisture for the North American Monsoon is the East Pacific Ocean and, to second order, mid-level moisture advected from the Gulf of California (e.g. Adams and Comrie, 1997; Stensrud et al., 1997; Vera et al., 2006; Turrent and Cavazos, 2009; Ordoñez et al., 2019). However, a more puzzling aspect is how moisture is exactly advected and organized specifically on the western coast of northern

Mexico. Orography seems to be the dominant fact as the Sierra Madre Occidental (SMO) found in the core NAMS region is a key feature of this monsoon.

Early studies suggest that the role of the SMO is to channel moisture from the East Pacific and Gulf of California (Seastrand et al., 2015) or in a mountain-sea breeze mechanism operating with the diurnal cycle of the low-level winds (Nesbitt et al., 2008). However, Boos and Pascale (2021) provides an alternative hypothesis for the role of the SMO in the organization of the monsoon in southwestern North America. Their results suggest that the role of the SMO is to deflect the subtropical jet and produce an eastward upward flow that organizes convection in a confined region with relative high surface moist static energy.

The South American Monsoon System (SAMS) is a primary source of precipitation for South America, especially in the Amazon region (Gan et al., 2004; Vera et al., 2006; Jones and Carvalho, 2013). During austral summer (DJF), monsoon rainfall accounts for over 60% of the total annual precipitation in the Amazon (Gan et al., 2004; Marengo et al., 2012), whereas austral winter rainfall accounts for less than 5% of the total annual rainfall (Vera et al., 2006). In the central Amazon, convective precipitation is observed from early October but the main rainy season extends from December to April (Machado et al., 2004; Adams et al., 2013), whereas convection in southeastern Brazil and Paraguay starts in November and peaks in January and February (Marengo et al., 2001; Nieto-Ferreira and Rickenbach, 2011). A surface heat low appears in Bolivia in early austral summer, known as El Chaco Low, as a result of strong warming in austral spring (Marengo et al., 2012; Sulca et al., 2018). Simultaneously, an upper-level anti-cyclone (Fig. 2.3b), known as the Bolivian High, develops in the same region as a signature of strong deep convection and latent heating (Marengo et al., 2001; Vera et al., 2006).

The South American Low-Level Jet (SALLJ) and the South Atlantic Convergence Zone (SACZ) are two primary climatic features of the SAMS (Vera et al., 2006; Marengo et al., 2012; Jones, 2019). The SACZ is observed as a northwest-southeast oriented band of convection (Carvalho et al., 2004; Nobre et al., 2012; Jorgetti et al., 2014; Zilli et al., 2019) that is more frequently active during austral summer in association with the onset of the SAMS (Marengo et al., 2012; Perez et al., 2021).

The coherent band of organized convection in the SACZ forms from the convergence of moisture emanating from the South Atlantic Subtropical High and from the northerly flow from the Amazon (Marengo et al., 2012; Zilli et al., 2019). Moreover, mid-latitude disturbances or wave-trains are key for the establishment and variability of the SACZ (Carvalho et al., 2004; Nieto Ferreira and Chao, 2013; Van Der Wiel et al., 2015; Zilli and Hart, 2021). Variability of the SACZ diagnosed as shifts to the position and strength of the band of convection are intertwined with the continental-scale moisture transport and precipitation in south eastern Brazil and central South America (Mo and Paegle, 2001; Jorgetti et al., 2014; Perez et al., 2021).

The low-level wind circulation imports moisture from the Atlantic Ocean, once the flow has crossed through the Amazon, the low-level winds are steered by the Andes cordillera into the SALLJ (Geen et al., 2019; Jones, 2019). The variability of the SALLJ can modulate active and break phases of the monsoon as well as active days of the SACZ, through the modulation of the moisture transport across the continent (e.g. Liebmann and Mechoso, 2011; Grimm, 2011; Jones, 2019). In short, the SACZ and the SALLJ are prominent features of the mean SAMS but their variability also modulates the SAMS precipitation on multiple temporal timescales (e.g. Marengo et al., 2012; Junquas et al., 2012; Perez et al., 2021).

South American orography, which features the long Andes cordillera, has long been investigated for its role in the dynamics of the SAMS (e.g. Rodwell and Hoskins, 2001; Campetella and Vera, 2002; Insel et al., 2010; Saurral et al., 2015; Junquas et al., 2016). Evidence shows that the Andes cordillera deflects the low-level wind flow from the equatorial Atlantic southward mechanically forcing the SALLJ (Campetella and Vera, 2002; Insel et al., 2010) and thereby contributing to the tropical-to-subtropical moisture transport. The Andes cordillera also blocks the westerly winds from the Pacific Ocean which would ventilate low-level moisture in South America (Insel et al., 2010) and the existence of the cordillera is key to the formation and location of the SACZ (Junquas et al., 2016).

The global monsoon theories discussed in the previous section struggle to accurately depict several aspects of the NAMS and the SAMS. For example, the North and South American Monsoons depart from CQE, as precipitation does not follow the maxima in sub-cloud equivalent potential temperature (Nie et al., 2010; Geen et al., 2020). The role

of orography and soil-atmosphere interactions may be playing a big part in both the SMO and the Amazon to decouple the sub-cloud MSE and the free troposphere (see e.g. Boos and Pascale, 2021). One alternative hypothesis is that ventilation of low moist entropy air from the midlatitudes is responsible for this decoupling of the boundary layer and the free troposphere in the American monsoons (Boos, 2015). Similarly, the meridional circulations associated with these monsoons do not fit the framework of Bordoni and Schneider (2008), which suggests an alignment of the maximum ascent with the maximum surface MSE, which is not observed in either monsoon of the AMS. As such, existing monsoon theories either do not fit the observed AMS, or need to be tailored to explain only one of these monsoons.

2.3 A review of the physical mechanisms for the Midsummer drought

The characteristics of the seasonal cycle of precipitation in northwestern Central America, the Caribbean and southern Mexico fit the definition of a monsoon climate (Wang et al., 2017) with a clear separation of the wet and dry seasons. However, this region shows a unique climatological precipitation feature. After monsoon onset, rainfall decreases considerably around midsummer; this decrease is followed by a secondary increase in precipitation in the late summer (Mosíño and García, 1966), and for this reason this feature of the seasonal cycle is most commonly referred to in the literature as the Midsummer drought (MSD) (Magaña et al., 1999). Although the MSD regions sometimes features in AMS studies (see e.g. Pascale et al., 2019), and is technically part of North America by some definitions, this region is not considered to be part of the North American monsoon.

The intraseasonal variations of precipitation associated with the MSD have been known for centuries and have shaped agricultural practices in the region. For example, ancient Mayan texts suggest that agricultural rituals associated with the plea for rain-bearing clouds to the gods were significantly more frequent during the drier MSD period (Jobbová et al., 2018). In current days, the MSD is well known by local farmers who refer to the drier midsummer period as ‘El Veranillo’ in Central America and ‘canícula’ in southern Mexico because the drier period coincides with the Canis Major constellation appearing in the sky (Dilley, 1996).

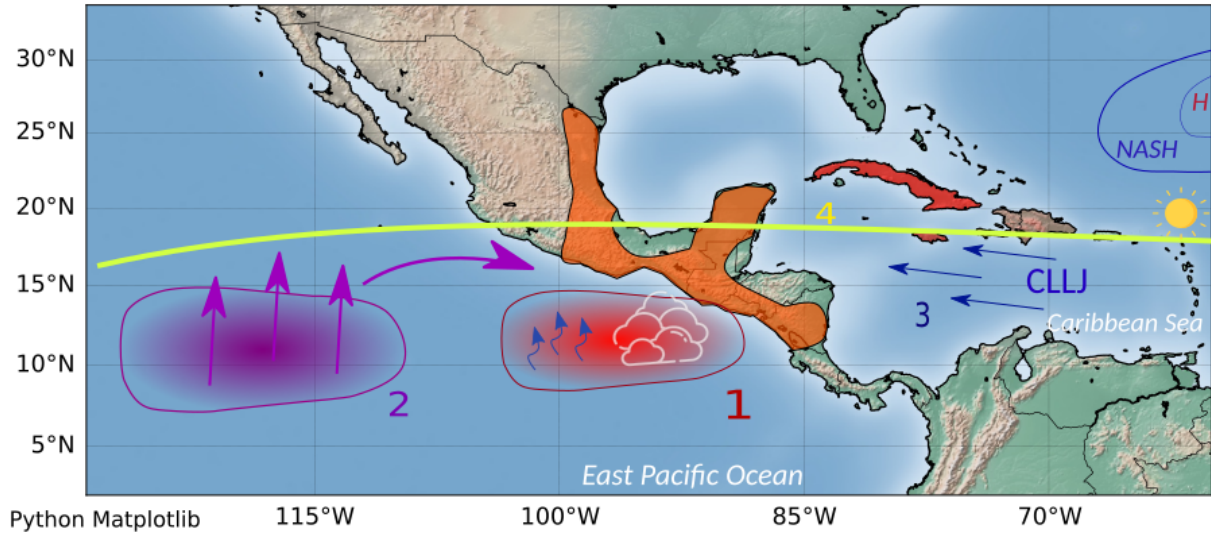


Figure 2.4: A schematic of the Intra Americas Seas region, depicting the four main mechanisms associated with the Midsummer drought in Mesoamerica (orange) and the Caribbean region (red). (1) The radiative-convective feedback mechanism associated with a double peak in East Pacific SSTs proposed by Magaña et al. (1999). (2) The ascending region west of the continent produces an anomalous descending motion over the continent through a direct circulation, argues Herrera et al. (2015). (3) The Caribbean Low-Level Jet (CLLJ) modulates the moisture transport for all the region, with several studies supporting the hypothesis that seasonal cycle in the CLLJ is the main mechanism for seasonal fluctuations in rainfall (Durán-Quesada et al., 2017; Martinez et al., 2019). (4) The double-crossing of the solar declination angle, proposed by Karnauskas et al. (2013), suggests that each peak of precipitation is associated with peaks in the total shortwave radiation reaching the surface. Note that the Mesoamerican MSD is not part of the North American monsoon (Adams and Comrie, 1997).

The two peak structure of the MSD has been diagnosed in the observed climatological precipitation of several regions of Mexico, El Salvador, Belize, Guatemala, Costa Rica and Cuba (e.g. Mosiño and García, 1966; Magaña et al., 1999; Durán-Quesada et al., 2017; Perdigón-Morales et al., 2018; Martinez et al., 2019). However, notable differences in the seasonal cycle of precipitation have been found between mainland Central America and the Caribbean islands. The so-called first peak of precipitation occurs in June and the second peak in September in northern Central America whereas the two peaks are observed in May and October in the Caribbean.

Despite extensive research to understand the physical mechanisms associated with the MSD (e.g. Magaña et al., 1999; Giannini et al., 2000; Gamble et al., 2008; Herrera et al., 2015; Maldonado et al., 2017; Straffon et al., 2019), debate remains over which is the leading-order

mechanism that causes rainfall to decrease at midsummer and increase again at the end of the summer. Fundamental questions remain unclear such as whether the MSD is caused by two precipitation enhancing mechanisms (Karnauskas et al., 2013) or a mechanism that inhibits rainfall at midsummer (Durán-Quesada et al., 2017). Furthermore, the association between the MSD in Central America and the Caribbean is still disputed (Gamble et al., 2008), as most studies suggest that the two regimes are unrelated and therefore two different explanations are required to account for the two MSDs in these regions. Figure 2.4 summarises the four main mechanisms that will be addressed in this section and this thesis.

One of the first hypotheses to account for the bi-modal distribution of rainfall was proposed by Hastenrath (1967) who argue that a double-crossing of the ITCZ can explain the MSD so that the first peak of precipitation is associated with early summer northward crossing of the ITCZ and the second peak the return or southward displacement of the ITCZ during late summer. However, this theory fails to explain the MSD signal seen at latitudes as high as 29°N (Perdigón-Morales et al., 2018; Zhao et al., 2020), which is further north than the northernmost extension of the ITCZ (Schneider et al., 2014), and the ITCZ does not cross twice so far from the equator.

Magaña et al. (1999) and Magaña and Caetano (2005) proposed a mechanism driven by radiative-convective feedbacks between the East Pacific (EP) sea-surface temperatures (SSTs) and deep tropical convective clouds (mechanism 1 in Figure 2.4). The coupling between the height and strength of convection, the incoming shortwave radiation and the SSTs are the key features of their framework. The EP SSTs peak in May triggering large evaporative fluxes and deep convection in the EP ITCZ and the western coast of Central America. The high convective clouds produce a radiative cooling effect at the surface due to a decreased incoming shortwave radiation associated with the reflectance of shortwave radiation by clouds. This cooling decreases SSTs and deep convective activity and thus accounts for the decrease of rainfall during midsummer. The second peak in September is driven by an opposite mechanism, i.e., the decreased frequency of deep convective clouds during the MSD period in July and August reduces the cooling effect of the anvil clouds and increase the incoming shortwave radiation at the surface, SSTs and surface fluxes, all of which leads to an increase in precipitation during late August and September (Magaña et al., 1999).

A large number of studies, in contrast, propose that the seasonal evolution of the North Atlantic Subtropical High (NASH) is the leading mechanism for the MSD (e.g. Mapes et al., 2005; Small et al., 2007; Gamble et al., 2008; Curtis and Gamble, 2008; Muñoz et al., 2008; Martinez et al., 2019; Corrales-Suastegui et al., 2020). The NASH is the subtropical anticyclone in the North Atlantic Ocean that migrates southwest during early boreal summer. The expansion and intensification of the NASH in boreal summer, according to these studies, strengthens the low-level trade winds, controlling the seasonal cycle of a low-level jet found in the core of the Caribbean Sea known as the Caribbean Low-Level Jet (CLLJ).

The CLLJ is a key regional feature of the climate of the Caribbean and the Intra-Americas Sea because the strength and direction of the flow in the Caribbean controls the underlying Caribbean SSTs and the regional moisture transport (Giannini et al., 2000; Mestas-Nuñez et al., 2007; Martinez et al., 2019; García-Martínez and Bollasina, 2020). However, studies disagree on the specific roles that the CLLJ and the NASH play to modulate seasonal cycle of precipitation over the Mesoamerican region. For example, some studies (e.g. Giannini et al., 2000; Mestas-Nuñez et al., 2007; Gamble et al., 2008) suggest that the expansion of the western flank of the NASH strengthens the CLLJ which cools the SSTs, through the effect of wind stress and mixed-layer mixing. The cooling of SSTs diminishes evaporation and therefore low-level moisture which ultimately leads to less precipitation. In contrast, other studies propose that the seasonal cycle of the CLLJ (mechanism 3 in Figure 2.4) modulates seasonal variations of precipitation by modulating the regional moisture transport (Small et al., 2007; Muñoz et al., 2008; Herrera et al., 2015; Durán-Quesada et al., 2017; Martinez et al., 2019). In this second hypothesis, the changes to the intensity of CLLJ influenced by the NASH modify the convergence and divergence patterns in the Intra-Americas Sea. In other words, the midsummer strengthening of the CLLJ increases moisture divergence, drying the atmospheric column over the Caribbean.

Herrera et al. (2015) show that during the drier months in Central America in the Midsummer, convective activity west of the central American continent gets stronger with heavier precipitation (mechanism 2 in Figure 2.4). Their evidence suggests that the gap flow that originated from the CLLJ in the Caribbean Sea controls the location of ascending and descending motions, and the MSD may be explained by the seasonal variations of the coupling

of the low-level wind flow with the underlying EP SSTs. Herrera et al. (2015) further argued that the exit region of the CLLJ is located to the east of the region of the strongest MSD signal, which suggests that the moisture divergence effect over the central American MSD is minimal.

A different mechanism, proposed by Karnauskas et al. (2013), argues that the biannual crossing of the solar declination angle can control precipitation and explains the bimodal characteristics of the seasonal cycle (mechanism 4 in Figure 2.4). In this mechanism, the MSD is driven by two precipitation enhancing periods that are separated by a relatively normal, and drier, period. This theory differs from those previously discussed which explained the MSD through mechanisms that inhibit convective activity in the midsummer whereas Karnauskas et al. (2013) argues that the solar declination angle that crosses twice through Central America, once during June and a second time during September, increases convective activity during each crossing.

The variations of incoming shortwave radiation associated with the declination angle modulate the SSTs, surface fluxes and therefore convective activity. In other words, the first crossing of the solar declination angle increases the incoming shortwave radiation which increases the SSTs, evaporation and leads to a peak of precipitation, i.e., the first peak. After the shortwave radiation is reduced the MSD period appears. The second crossing of the solar declination angle, similarly, explains the second peak as the second increase in incoming shortwave radiation drives an increase in deep convection.

Other mechanisms have been proposed arguing that the MSD is a result of vertical wind shear affecting convective instability or the Saharan dust controlling the microphysics of clouds (Angeles et al., 2010). For instance, Perdigón-Morales et al. (2019) also finds a link between the frequency and spatial distribution of the first peak rainfall rates and the Madden-Julian Oscillation (MJO). [In short, a plethora of hypotheses exist for the causes of the MSD, however, a key aspect of the climate of the AMS, is the effect of ENSO, which is the following section.](#)

2.4 El Niño Southern Oscillation: impacts on the American monsoon system

El Niño-Southern Oscillation (ENSO) coupled ocean-atmosphere phenomenon in the equatorial Pacific Ocean that is profoundly important for the global climate system, which is why ENSO is commonly known as the leading mode of interannual variability. The term '*El Niño*' was coined by Spanish colonizers when they learnt from Peruvian fishermen that the SSTs in the easternmost Pacific Ocean increased notably in some years around December time. Later on, sir Gilbert Walker (1924) coined the term *Southern Oscillation* to describe the synchronous changes to the sea-level pressure of the Indo-Pacific region and South America.

The changes in the pressure field associated with the Southern Oscillation are now part of what is known as the Walker circulation, which intertwines the dynamics of the zonal circulation in the East Pacific with the SSTs over the underlying ocean. ENSO is then characterized as a coupled phenomenon composed of an oceanic part, *El Niño*, and an atmospheric component associated with the zonal circulation but best characterized by changes to the surface pressure field, i.e., the Southern Oscillation.

ENSO has several unique features, such as no robust periodicity as events may occur every 2 to 7 years and a seasonal phase-locking that are associated with ENSO events peaking in boreal winter in observations (Wang and Picaut, 2004). Even though the underlying physics that cause ENSO and explain the variability in the periodicity of the phenomena is still debated (Wang and Picaut, 2004; Christensen et al., 2017), several aspects are now better understood. For example, the impact of ENSO events on the location and strength of deep convection in the equatorial Pacific have been thoroughly described and the teleconnections pathways of ENSO are well characterized (Trenberth, 1997; Neelin et al., 1998).

During a neutral state of ENSO, the Walker circulation is found in the climatological state, with ascent and wet conditions in the West Pacific and descent and drier conditions in the East Pacific. During El Niño the Walker circulation and low-level trade winds weaken which is associated with an eastward shift of deep convection along the equatorial Pacific (Figure 2.5), with convective rainfall becoming more frequent in the central and even eastern Pacific than normal (Neelin et al., 1998; Wang and Picaut, 2004). During La Niña the

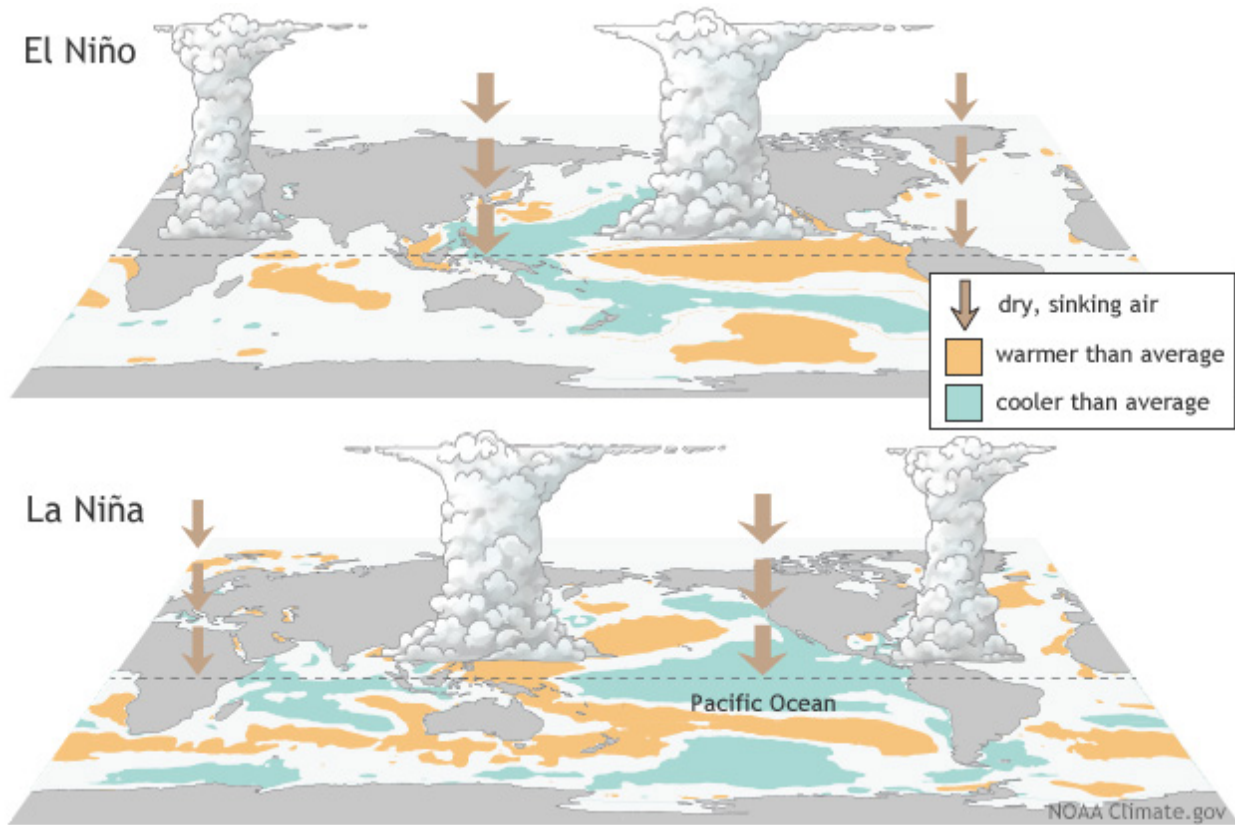


Figure 2.5: Schematic of the positive (upper) and negative (lower) phases of ENSO. Regions with tall clouds indicate more ascent and convection than normal whereas brown arrows indicate dry descending air. Obtained from the National Oceanic and Atmospheric Administration at <https://www.climate.gov/enso>.

opposite happens and the Walker circulation strengthens which leads to stronger convection in the West Pacific and stronger ascent on the East Pacific (Figure 2.5).

In other words, ENSO imposes a strong control on the location and strength of the Walker circulation (Figure 2.5). These changes to the strength and position of the convective regions in the Pacific Ocean can then propagate to other regions of the planet; these far-distant effects are commonly known as *teleconnections*. [ENSO teleconnections work through various pathways or mechanisms](#). For example, Figure 2.5 shows the impact of ENSO over other tropical regions outside of the Pacific through the Walker circulation, as upper-level wind anomalies induce anomalous vertical motions over West Africa (Ropelewski and Halpert, 1986, 1987) or South America (Sulca et al., 2018). Other mechanisms of ENSO teleconnections include extra-tropical routes which include changes to the position and strength of subtropical jets (Fereday et al., 2020), changes to the Pacific and North

American circulation patterns (Bayr et al., 2019) as well as impacts to the North Atlantic via the stratospheric polar vortex (Domeisen et al., 2019).

ENSO teleconnections impact the AMS both through the tropical and the extratropical pathways (Marengo et al., 2012; Sulca et al., 2018; Cai et al., 2020). The extratropical pathway refers to these anomalous Rossby wave-trains caused by tropical convective heating that propagate from the equatorial Pacific to the extratropical Pacific and Atlantic affecting both northern and southern hemispheres (Hoskins and Karoly, 1981; Jiménez-Esteve and Domeisen, 2018; Fereday et al., 2020). The influence of ENSO on the subtropical jets, or the storm track, can impact boreal winter climate in subtropical North and South America (Marengo et al., 2012; Bayr et al., 2019).

These wave-driven anomalies cause differences in the regional sea-level pressure systems and the location of the storm track. For example, ENSO induces changes to the Aleutian Low pressure system and similar SLP anomalies of opposite sign over the North American continent, in a teleconnection pattern that is more commonly referred to as the Pacific-North American (PNA) (Deser et al., 2010; Bayr et al., 2019; Jiménez-Esteve and Domeisen, 2020). A similar teleconnection is observed as wave trains travelling from the South Pacific to the South Atlantic, i.e., the Pacific-South American (PSA) pattern (Mo and Paegle, 2001; ?; Cai et al., 2020). Specifically, El Niño events induce a positive phase of the PNA pattern during boreal winter which leads to enhanced precipitation and colder conditions over northern Mexico due to the increased frequency of the intrusion of cold mid-latitude disturbances (Magaña et al., 2003).

The tropical pathway involves the changes to the location and strength of the Walker circulation explained above, in which anomalous descending and ascending anomalies are found in the Amazon region for El Niño and La Niña years, respectively. Another relevant pathway is the impact of ENSO associated with the PNA pattern, which induces changes to the easterly trade winds in the subtropical Atlantic and subsequent impacts to the ITCZ (Hastenrath, 2006; Fereday et al., 2020). For instance, El Niño teleconnections through the PNA pattern lead to a warming of the northern equatorial Atlantic SSTs and induce a delay in the seasonal migration southwards of the Atlantic ITCZ causing a drying of the northern South America (Hastenrath, 2006; Cai et al., 2020). The influence of the northern

tropical Atlantic and the delay in the southward shift of the Atlantic ITCZ has been shown to influence not only northeastern Brazil rainfall but also extreme events throughout the SAMS (Yoon and Zeng, 2010; Andreoli et al., 2012; Jimenez et al., 2021).

Current research on ENSO teleconnections to South America focuses on the observed non-linearity and non-symmetry of the impacts, which has mainly been attributed to ENSO diversity (Tedeschi et al., 2015; Cai et al., 2020; Jimenez et al., 2021). ENSO diversity refers to the observed feature that the maximum SST anomaly does not always appear in the same region of the Pacific Ocean (Ashok and Yamagata, 2009; Dommeneget et al., 2013). These differences in the SST patterns are referred to as ENSO *flavours* which can be broadly summarized as two flavours for each phase. The flavours are defined based on the location of the SST anomaly so the most common division is into Central and Eastern Pacific events. In observations, each type of event is usually also associated with the strength of the event (Dommeneget et al., 2013), with eastern Pacific events being usually stronger than Central Pacific events.

ENSO diversity has important implications for global teleconnections; specifically, precipitation impacts and the occurrence of droughts in the SAMS have been linked to non-linear effects associated with the location of the SST anomalies in the Pacific (Rodrigues et al., 2011; Sulca et al., 2018; Cai et al., 2020; Jimenez et al., 2021). Cai et al. (2020) provides a recent review on the differences in the impacts that Central and Eastern Pacific (CP and EP) events have on South American precipitation and climate features. The observed record shows that the teleconnections affecting the Amazon and northeastern Brazil are most pronounced during EP El Niño events and CP La Niña events than the CP El Niño events and EP La Niña events.

This recent review also highlights the need for further modelling work to test observation-driven hypothesis, as the observed record is too short to make confident statements about the mechanisms associated with non-linear ENSO teleconnections. Specifically, there are still open questions regarding the effect of other climate variability factors on the teleconnections, particularly for different ENSO flavours, and the role of other ocean basins such as the Indian and Atlantic Oceans in the modulation of ENSO effects (Cai et al., 2019).

2.5 The QBO and tropical convection

2.5.1 The Quasi-biennial oscillation (QBO)

The stratospheric quasi-biennial oscillation (QBO) was discovered 60 years ago through balloon observations that revealed that, in the tropical stratosphere (from 10-20 km up to 50 km in altitude (Andrews et al., 1987)), the zonal winds reverse direction in a semi-periodic way with accompanying temperature variations (Ebdon, 1960; Reed, 1964). Since the QBO was discovered, further observations have described it as alternating easterly and westerly wind regimes associated with a descending zonal wind shear with a mean oscillatory period of 28 months (Baldwin et al., 2001). The downward propagation of the easterly and westerly wind regimes, amplitude and the mean period have been explained by the interaction of a broad spectrum of gravity and Kelvin waves of tropospheric origin with the equatorial stratospheric zonal mean flow (Baldwin et al., 2001).

The wind variation in the middle stratosphere associated with the QBO are greater than the seasonal cycle (Andrews et al., 1987) and this vertical wind shear imposes a temperature signal through the thermal wind relationship, which can be expressed as:

$$\frac{\partial u}{\partial z} = \frac{-R}{H\beta} \frac{\partial^2 T}{\partial y^2}, \quad (2.1)$$

where $\partial u / \partial z$ is the vertical shear of the zonal wind, R is the ideal gas constant, y is the latitude, H is a scale height of the atmosphere (7-8 km) and β is the first derivative of the Coriolis term in the meridional coordinate y .

In order to maintain thermal wind a westerly (easterly) vertical shear requires a latitudinal temperature gradient with a warm (cold) temperature anomaly over the equator. These temperature anomalies are achieved through an induced mean meridional circulation, often referred to as the secondary circulation of the QBO (Plumb and Bell, 1982; Li et al., 1995; Baldwin et al., 2001; Ribera et al., 2004). This anomalous circulation is characterized by reduced upwelling during westerly shear phases and increased upwelling during the easterly phase. These meridional circulation perturbations adiabatically warm (anomalous descent at the equator) and cool (anomalous ascent) for westerly and easterly shears, respectively, at the equator.

These induced meridional circulations also give rise to an ozone anomaly, with positive (negative) ozone anomalies associated with a descending westerly (easterly) QBO phase, which further enhances the temperature anomalies. The combination of dynamic and thermodynamic effects of the QBO in the equatorial stratosphere are associated with long-distance impacts across the stratosphere (Holton and Tan, 1980; Lu et al., 2020) and down to the surface (Garfinkel and Hartmann, 2010; Gray et al., 2018). The most well-known teleconnection of the QBO is with the polar stratosphere, since the direction of the zonal mean flow in the equatorial stratosphere modulates the propagation of extratropical waves and therefore also influences the wintertime stratospheric polar vortex (Lu et al., 2020).

However, the temperature anomaly driven by the meridional circulations impact the height and temperature of the tropopause in the tropics (Baldwin et al., 2001; Tegtmeier et al., 2020a,b). The easterly phase of the QBO (QBOE) is associated with a higher and colder tropopause in the tropics whereas the westerly phase (QBOW) is observed with lower and warmer tropical tropopause (Tegtmeier et al., 2020a). These temperature variations near the tropopause, amongst other effects associated with the QBO, have been hypothesized to affect deep convective systems. The following section details the observational and modelling evidence that links the QBO to the tropical troposphere, as well as discusses the existing hypotheses that explain how the QBO could impact surface climate in the tropics.

2.5.2 Tropical teleconnections of the QBO

This sections introduces the topic of stratospheric-coupling in the tropics, and the literature on mechanisms through which the QBO could modulate aspects of tropical tropospheric climate.

The influence of the QBO on the dynamic and thermodynamic characteristics of the tropical upper-troposphere-lower stratosphere (UTLS) region has raised interest in possible indirect effects of the QBO over tropical deep convection and clouds, i.e., the tropical route of QBO teleconnections (Gray et al., 2018). Stratospheric-tropospheric coupling has gained attention as more evidence links the QBO with tropical convective phenomena such as monsoons (Giorgetta et al., 1999; Claud and Terray, 2007), the ITCZ (Gray et al., 2018), tropical SST and cloud variability (Garfinkel and Hartmann, 2011; Davis et al., 2013),

tropical cyclones (Ho et al., 2009; Jaramillo et al., 2021) and most recently, the MJO (Son et al., 2017; Lee and Klingaman, 2018; Wang et al., 2019; Martin et al., 2021b).

Gray (1984) was amongst the first to suggest an influence of the QBO over tropical systems, in particular, that Atlantic tropical cyclone activity was enhanced during QBOW compared to QBOE. Gray et al. (1992) proposed one of the first mechanisms to link the QBO to the tropical troposphere by arguing that the anomalous vertical wind shear in the UTLS associated with the QBO affects the strength of convection in monsoonal and convergence zones to the extent that the vertical wind shear can modify ENSO frequency. Their results suggest that El Niño events are favoured during QBOE and La Niña events are more frequent during QBOW.

The evidence by Gray et al. (1992) has motivated further observational and modelling research on QBO tropical teleconnections; some of this research has contested Gray's results (e.g. Chan, 1995; Camargo and Sobel, 2010; Hansen et al., 2016). For example, Giorgetta et al. (1999) was amongst the first to use a global climate model (ECHAM4) to investigate the effects of the QBO over tropical convection. Giorgetta et al. (1999) focused on the role that the QBO plays in modulating the strength of the East Asian and Indian monsoons. Their findings suggest that monsoon variability was partially modulated by the QBO, with strong effects over the properties of clouds at 100 hPa. Giorgetta et al. (1999) argue that these differences could be explained by the effect of the QBO on the UTLS static stability and a consequent effect over the vertical extent of deep tropical convection.

The suggestion that the variability in the UTLS static stability due to the QBO is arguably the leading hypothesis for the tropical route of QBO teleconnections (Giorgetta et al., 1999; Liess and Geller, 2012; Nie and Sobel, 2015). In short, this argument suggests that a upper-level static stability, decreased under QBOE and increased under QBOW, can impact the strength of convection. The response of convection to the UTLS temperature anomalies associated with the QBO was investigated in cloud-resolving model simulations by Nie and Sobel (2015). Their experimental design varied SST boundary conditions with increments over a baseline SST level of 301 K, using the weak-temperature gradient

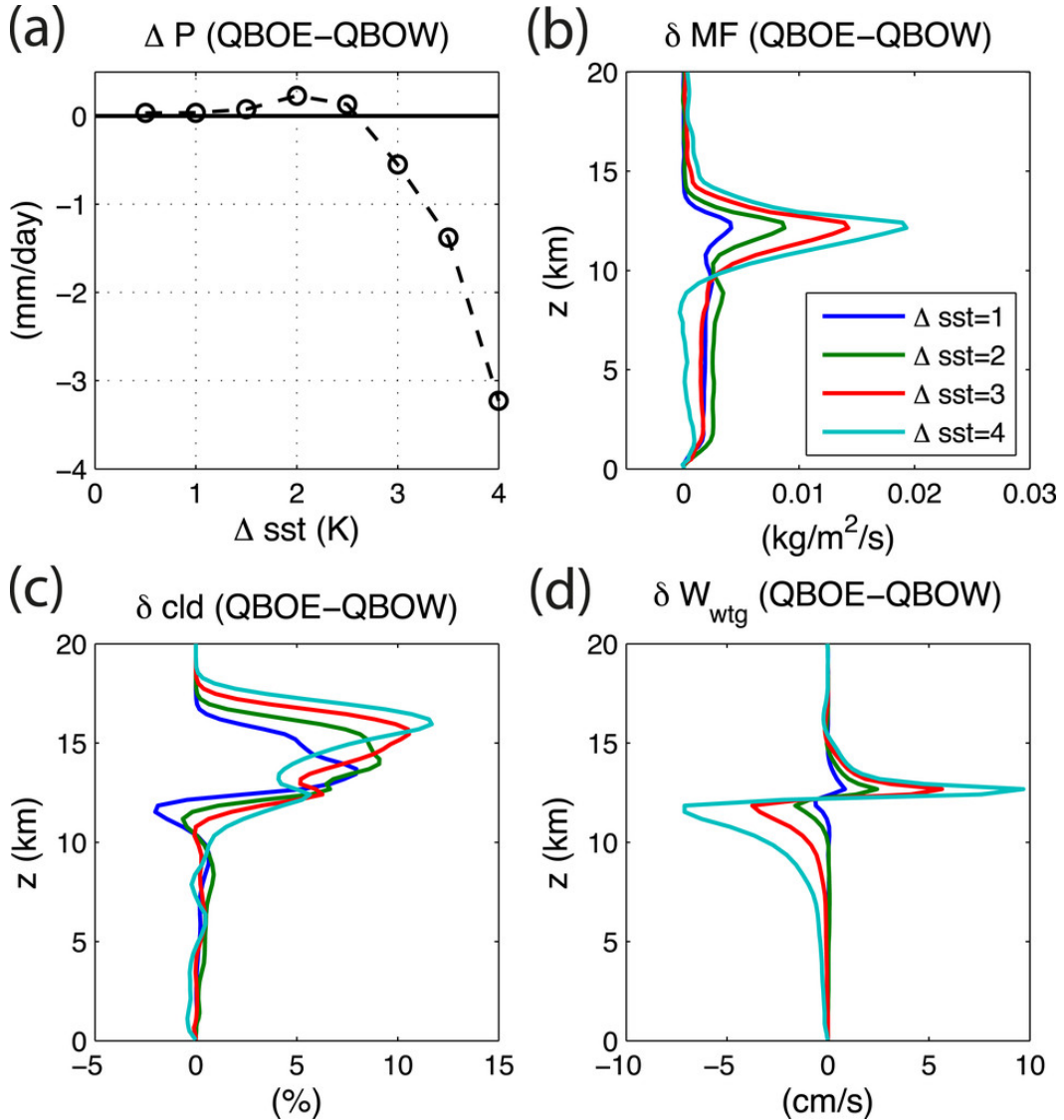


Figure 2.6: (a) QBO anomalous precipitation as a function of SST forcing. The δsst are increments over a baseline of 301 K throughout the whole model domain. (b)–(d) The differences of mass flux in cloud cores, cloud fraction, and the parametrized large-scale vertical velocity derived from the weak temperature gradient approximation, respectively, between experiments with the QBOE and QBOW temperature profiles. Figure 3 from Nie and Sobel (2015).

(WTG)¹ approximation and an idealized vertical temperature profile to simulate the effect of the QBO temperature signal.

Figure 2.6 shows that the precipitation differences between QBO phases depend on the SST forcing. The precipitation difference between QBO temperature anomalies is positive

¹The weak temperature gradient approximation makes use of the relatively small horizontal gradients of temperature and density in the tropics, which simplifies some of the primitive equations and has allowed several numerical analyses of tropical dynamics using simplified models (Sobel et al., 2001).

under relatively small SST anomalies but in experiments with large SST anomalies this difference becomes negative and overall larger than under small SSTs. The difference in mass flux and cloud fraction is also sensitive to the underlying SSTs, as increased mass flux during QBOE is increased for larger SSTs. In other words, the QBO influence on precipitation is non monotonic and largely depends on the underlying SST field.

The results of Nie and Sobel (2015) suggest that the QBO influences convection in two ways that are non-linear and that are the result of competing mechanisms. Their argument is that since the mass flux in the upper troposphere is increased during QBOE but there is also an increase in gross moist static stability (GMS) the result is an increase in the efficiency of large-scale vertical motions during QBOE for large SSTs, which acts to reduce precipitation. Secondly, the QBO modifies the fraction of high-level clouds resulting from deep convection which modifies the radiative heating to the column which increases precipitation during QBOE. Figure 2.6a then shows how these competing effects change for different SSTs with the gross moist stability mechanism dominating for large SSTs.

One influential study by Collimore et al. (2003) analysed satellite-derived out-going long-wave radiation (OLR) in the tropics composited by QBO phase. These composites suggest that OLR is significantly different between QBO phases in most monsoon regions, such as Central America and the West Pacific, with an overall indication that convective activity is reduced during QBOW compared to QBOE. This influence, however, was not found to be zonally symmetric and in fact the longitudinal variations of the QBO-related OLR differences were suggestive enough that Collimore et al. (2003) argue for a possible role for the QBO to modulate the Walker circulation, which would explain the lack of zonal symmetry in their results.

Further modelling work has been carried out, for instance by Garfinkel and Hartmann (2010) and Garfinkel and Hartmann (2011) that investigate the effect of the QBO over tropical precipitation, the subtropical jets and the wintertime polar vortex in a GCM. Garfinkel and Hartmann (2010) shows that the canonical ENSO teleconnections to the North Pacific are stronger during QBOW suggesting that the QBO modulates the wave propagation activity associated with ENSO events. Garfinkel and Hartmann (2011) uses perpetual winter conditions in the GCM to show that the QBO modifies the upper-tropospheric zonal

wind at the equator and the strength and location of subtropical jets, as the subtropical jet is weakened during QBOE conditions.

Another relevant study by Liess and Geller (2012) found that satellite-derived cloud thickness and frequency and upper-level velocity potential had a significant and longitudinally asymmetric response to the QBO. In particular, their results show increased convective activity during QBOE in the West Pacific but the opposite for the East Pacific. For this reason, Liess and Geller (2012) also argue that the strength of the tropical overturning circulation may be modulated by the QBO, indicating the possible role of both the vertical wind shear and the upper-level static stability to modulate deep convection. [Liess and Geller \(2012\)](#) suggests the possibility of an indirect of the QBO, in which the QBO modulates the zonal tropical overturning circulation causing impacts of opposite signs at equatorial latitudes.

The topic of QBO tropical teleconnections has regained attention due to recent findings suggesting a link between the QBO and the MJO (Son et al., 2017) which motivated extensive research (see e.g. Lee and Klingaman, 2018; Wang et al., 2019; Martin et al., 2020) due to the worldwide impact of the MJO. The MJO in observations shows a stronger amplitude and more predictability during QBOE, but further inspection in cloud-permitting and forecast models have not provided conclusive answers to this puzzle (Martin et al., 2019, 2020).

In short, multiple lines of evidence suggest relationships between the QBO and tropical convection. The leading hypothesis for these relationships suggests that the modulation of the UTLS temperature structure influences the upper-level static stability to the extent that the QBO can influence the strength of ascent. The effect of the QBO on vertical shear and feedbacks with the tropical overturning circulation have also been suggested as possible explanations for the observed responses to the QBO phase.

Questions still arise as to whether this tropical link is real or due to chance, for instance Wang et al. (2019) argued that the increased predictability of the MJO under the QBOE phase is included in the initial conditions, and thus not a result of a mechanistic effect of the QBO on the MJO. More generally, whether the QBO has a considerable effect on deep convection in general is debated as several plausible mechanisms exist in the literature (see e.g. Nie and Sobel, 2015) such as the effect of wind shear, the tropopause height,

the cold-point temperature, static stability and/or feedbacks with very high cirrus and cumulonimbus clouds or the tropical circulation.

3

Data and methods

3.1 Observations and reanalysis data

Continuous and reliable observations of Earth's atmosphere and ocean have only been possible in recent decades, due to the advent of satellites. In particular, precipitation analyses have benefited greatly from satellite-derived estimates of precipitation in regions where station-data is non-existent such as over oceans. This thesis uses several data sources for precipitation from various gridded precipitation datasets. Several dynamic diagnostics are also used in this thesis, which are taken from the latest reanalysis from the European Centre for Medium-Range Weather Forecasts (ECMWF), described below. Table 3.1 summarises relevant information of the observations and reanalysis datasets used in this study.

3.1.1 Gridded precipitation datasets

The Tropical Rainfall Measurement Mission (TRMM) dataset is a multi-satellite multi-sensor infra-red precipitation product. Several versions are available that use with different algorithms and calibrations with surface rain-gauge data (Huffman et al., 2007). This thesis uses the daily product TRMM version 7, product 3B4, provided by the Goddard Earth Sciences Data and Information Services Center (Mission, 2011) at https://disc.gsfc.nasa.gov/datasets/TRMM_3B42_7/.

Table 3.1: Summary of the datasets used in this study. For each dataset, the acronym used hereafter, the period of coverage, the field used and the horizontal resolution are shown. Some datasets extend further back in time, but only the satellite-era period is used in most of the datasets. The variables used are: precipitation, surface-air temperature ($2mT$), sea-level pressure (SLP), SSTs, the x and y components of the wind (u, v), the lagrangian tendency of air pressure (ω), outgoing longwave radiation (OLR), geopotential height (GPH) and specific humidity (q).

Dataset/ Version	Acronym	Variable	Period	Data type	Resolution	Reference
Global Precipitation Climatology Project v2.3	GPCP	Precipitation	(1979-2018)	Surface and satellite	$2.5^\circ \times 2.5^\circ$	(Adler et al., 2003)
Global Precipitation Climatology Centre	GPCC	Precipitation	(1940-2013)	Surface station	$0.5^\circ \times 0.5^\circ$	(Becker et al., 2011)
Climate Prediction Center Merged Analysis of Precipitation	CMAP	Precipitation	(1979-2016)	Satellite calibrated with surface rain-gauge	$2.5 \times 2.5^\circ$	(Xie and Arkin, 1997)
Climatic Research Unit TS v4.	CRU4	Surface temperature	(1979-2017)	Surface station	$0.5^\circ \times 0.5^\circ$	(Harris et al., 2014)
Climate Hazards Infrared Precipitation with Stations	CHIRPS	Precipitation	(1981-2018)	Surface rain-gauge and satellite	$0.05^\circ \times 0.05^\circ$	(Funk et al., 2015)
Tropical Rainfall Measurement Mission 3B42 V7	TRMM	Precipitation	(1999-2018)	Satellite calibrated with surface station	$0.25^\circ \times 0.25^\circ$	(Huffman et al., 2010)
Hadley Centre SST3	HadSST	SST	(1940-2018)	Buoy and satellite	$2.5^\circ \times 2.5^\circ$	(Kennedy et al., 2011)
European Centre for Medium-Range Forecasting ERA-5	ERA-5	$2mT$, SLP, u, v, ω , OLR, q , SST, GPH, precipitation	(1979-2018)	Reanalysis	$0.75 \times 0.75^\circ$	(C3S, 2017; Hersbach et al., 2020)

A set of microwave and infra-red sensors onboard low earth orbit (LEO) satellites, such as the Microwave Imager (TMI) and the Advanced Microwave Scanning Radiometer-Earth Observing System (AMSR-E), provide the main source of information about hydrometeors for TRMM. The microwave sensor data is used to calibrate the infrared data to produce the first estimate of precipitation. However, even using the products of several satellites there is a sparse sampling of time-space precipitation in passive microwave techniques. Therefore, this data is complemented by infrared measurements onboard geosynchronous earth orbit satellites. Other sources of information include a radar onboard TRMM and rain gauge analysis. Details of the research product can be found in Huffman et al. (2007) and Huffman et al. (2010).

The Climate Prediction Center Merged Analysis of Precipitation (CMAP) dataset is a global merged product of satellite and ground-based observations but also constrained by a numerical model (Xie et al., 2007). This dataset was first produced at monthly-mean resolution (Xie and Arkin, 1997) but is now available as a collection of products at several temporal scales. The pentad-scale version of CMAP is used in this study.

The Climate Hazards Infrared Precipitation with Stations (CHIRPS) is a relatively more recent merged product of precipitation (Funk et al., 2015). This dataset uses high-resolution rain-gauge station data that is complemented by satellite cloud cold duration estimates for regions where station data is sparse. The products are calibrated with TRMM data (Funk et al., 2015), so they cannot be considered a fully independent source of information from TRMM.

All these datasets have shortcomings, advantages and uncertainties in their representation of precipitation. The algorithm of merged products such as TRMM to combine different satellite sensors and calibration techniques as well as surface station rain-gauge data results in products that may have shortcomings to accurately depict extreme events (Trejo et al., 2016). As the source data of most of these datasets are shared, the datasets cannot be considered to be fully independent sources of information.

The TRMM dataset has a high horizontal and temporal resolution and was used in several CMIP assessments (Geil et al., 2013; Jones and Carvalho, 2013) as a reliable source of precipitation (Carvalho et al., 2012). Therefore, this thesis used TRMM as the best estimate

for the spatial and temporal characteristics of rainfall. However, the period covered by TRMM (1998-2018) is too short to analyse statistically robust teleconnections or variability, so GPCP, GPCC and CHIRPS are used to evaluate longer term variability. Although a thorough validation and comparison of these datasets across the AMS domain is missing, several studies have analysed one or more of these datasets in regions of the AMS (e.g. Franchito et al., 2009; Dinku et al., 2010; Trejo et al., 2016).

Gridded precipitation datasets will be used in all chapters throughout this thesis. In Chapter 4 these observational products are used to assess model performance, in Chapter 5 these datasets are key to illustrate the method to diagnose onset and retreat whereas in Chapters 6 and 7 they are used to evaluate observed interannual variability.

3.1.2 ERA-5

A reanalysis is a numerical description of the state of the atmosphere on a global or regional scale with a full set of gridded diagnostics available at multiple vertical levels, in other words, "maps without gaps" (Hersbach et al., 2020). A reanalysis assimilates a physically consistent blend of observations that are used to constrain a forecasting model by relaxing the model towards these observations (e.g. Fujiwara et al., 2021). Reanalyses are key tools for climate and weather research as they provide full pictures of the atmospheric state for long periods, a feature that could not be possible with our current purely observational tools. For this reason, reanalyses are typically used to validate GCM output.

The latest reanalysis from ECMWF, the fifth generation of their reanalysis, is called ERA5. ERA5 uses the Integrated Forecasting System (IFS) model and a 4D variational data assimilation system (4D-Var), a larger number of data sources for assimilation and also provides an output on higher horizontal resolution (Hersbach et al., 2020). The output is available on hourly to monthly-mean frequencies, from 1000 hPa to 0.1 hPa in the vertical and with horizontal resolutions as high as 0.25° . In this thesis, the horizontal resolution of all ERA5 data is 0.75° and all data was downloaded from the Climate Store at <https://climate.copernicus.eu/climate-reanalysis>.

ERA5 presents a notable improvement in the representation of the water cycle, by increasing the mean correlation to precipitation datasets such as GPCP. ERA5, as all

reanalysis, resolves precipitation rates in the driving physical model using the convective scheme and parametrisation. However, this reanalysis also assimilates radiances from several satellite instruments such as Global precipitation monitoring mission Microwave Imager, the TRM Microwave Imager (TMI) and Advanced Microwave Scanning Radiometer (AMSR-2) Hersbach et al. (2020). This assimilation of satellite data has improved the representation of the water cycle in ERA5 compared to older reanalysis such as ERA-interim (e.g. Hénin et al., 2018). These improvements are also due to changes to the parametrisations of the microphysics of clouds and rain (Forbes and Ahlgrimm, 2014) and the diurnal cycle of convection (Bechtold et al., 2014).

ERA5 will be used to investigate the dynamical biases in the models in Chapter 4, the skill of the reanalysis in reproducing the mean onset and retreat dates compared to observations in Chapter 5, the mechanisms of the MSD in Chapter 6 and of the QBO teleconnections in Chapter 7. Note that a reanalysis has large uncertainties where there is scarce data on the vertical profile of quantities such as humidity, which are crucial for most thermodynamic and dynamic processes in the tropics. However, ERA5 has sufficient vertical resolution to reasonably represent the QBO and the associated UTLS variability (Pahlavan et al., 2021).

3.2 The Unified Model of the Met Office Hadley Centre

The UK Met Office Hadley Centre (MOHC) released the first version of the Hadley Centre Global Environmental Model (HadGEM1) in 2006 (Johns et al., 2006), and has since continuously updated the HadGEM model and submitted experiments from the model to the various phases of the Coupled Model Intercomparison Project (CMIP), which is the backbone of the Intergovernmental Panel on Climate Change (IPCC) reports. This section first describes the third generation of the HadGEM model and subsequently describes the experiments from these versions of the model submitted for CMIP6.

3.2.1 The Global Coupled Configurations of HadGEM3

The MOHC Unified Model (UM) is a weather and climate global model that is based on a seamless modelling approach, which means that the UM consists of a dynamical core and

parameterization schemes that can be used across a wide range of temporal and spatial scales. The UM version that was used for CMIP6 experiments and is used throughout this thesis employs the Global Coupled (GC) configuration 3.1 (GC3.1) (Williams et al., 2018; Walters et al., 2019) which in turn is composed of the components: Global Atmosphere 7.0 (GA7.0), Global Land 7.0 (GL7.0), Global Ocean 6.0 (GO6.0), and Global Sea Ice 8.0 (GSI8.0).

The GC3.1 configuration runs with 85 atmospheric levels, 4 soil levels and 75 ocean levels and can be run with atmospheric horizontal resolutions ranging from 10 - 135 km (at the midlatitudes) with varying resolutions for the ocean component as well. The model top of GC3.1 is 85 km above sea level (Walters et al., 2019). [The vertical resolution of the UM in the GC3.1 configuration yields a sufficiently reasonable, and internally generated, QBO \(Richter et al., 2020\). For this reason, the MOHC UM is a particulary useful model to address the topic of the QBO teleconnections of Chapter 7.](#)

The GA7.0 configuration, described in Walters et al. (2019), built on previous configurations principally by updating several parameterization schemes including the rain and ice-cloud treatment as well as the convection scheme. Four critical errors were pinpointed and tackled by GA7.0 which include rainfall deficits in the Indian monsoon, temperature and humidity biases in the tropopause layer, deficiencies in numerical conservation and surface flux biases over the Southern Ocean. The GO6.0 configuration (Storkey et al., 2018) is in turn based on the NEMO ocean model code (version 3.6) and is responsible for determining the sea-ice extent, the ocean mixed-layer depth and deep water formation, amongst other key ocean processes.

In most GCMs, precipitation is a result of two simulated processes. First, precipitation due to grid-scale processes referred to as large-scale precipitation, is estimated by the microphysics, or cloud scheme, that evaluates the cloud fraction and saturation within the grid-box column where precipitation occurs by processes such as warm rain (Walters et al., 2019). The second process that simulates precipitation is associated with convection of varying depths and is considered a sub-grid process calculated by the convection scheme.

In GC3.1 the convective scheme follows three stages, according to Walters et al. (2019), first a diagnosis of the boundary layer to establish whether convection should occur at a given time-step and separately diagnoses shallow or deep convection, second, the shallow or

Table 3.2: Summary of the CMIP6 simulations in this study. The experiment, CMIP activity name, acronym model years, and number of ensemble members used in this study are presented for each simulation.

Model / Resolution	Experiment	Period	Activity	Acronym	Ens.	Reference
HadGEM3 N96	pre-industrial control	1850-2350	CMIP/DECK	GC3 N96-pi	1	(Ridley et al., 2018)
HadGEM3 N216	pre-industrial control	1850-2000	CMIP/Deck	GC3 N216- pi	1	(Ridley et al., 2019c)
HadGEM3 N96	historical	1979-2014	CMIP/DECK	GC3-hist	4	(Ridley et al., 2019b)
HadGEM3 N216	historical	1979-2014	CMIP/DECK	N216-hist	1	(Ridley et al., 2019c)
HadGEM3 N96	amip	1979-2014	CMIP/AMIP	GC3-amip	5	(Ridley et al., 2019a)
HadGEM3 N216	amip	1979-2014	CMIP/AMIP	N216-amip	1	(Ridley et al., 2019a)
UKESM1	pre-industrial control	2060-2600	CMIP	UKESM-pi	1	(Tang et al., 2019b)
UKESM1	historical	1979-2014	CMIP	UKESM- hist	5	(Tang et al., 2019a)

deep convection schemes are called and third, a call for mid-level convection. In other words, the convective scheme first decides whether the thermodynamic profile at each grid-point fits certain parameters that measure the buoyancy of the parcels and vertical velocity profile, which then separates areas of deep and shallow convection. After these routines, the model implements the mid-level convection scheme to remove instabilities from above the shallow convective regions or below the deep convective regions.

The closure of the deep convective scheme follows the convective available potential energy (CAPE) closure of Fritsch and Chappell (1980) which regulates the amount, strength and duration of convection based on the availability of buoyant energy. In addition, the scheme couples the detrainment rates of plumes to the column relative humidity and buoyancy as described in Derbyshire et al. (2011). Further details of the GC3 configuration including model description and biases can be found in Williams et al. (2018) and Kuhlbrodt et al. (2018).

3.2.2 The CMIP6 experiments

The MOHC submitted output from several experiments to various projects part of CMIP6 using different variations of the GC3.1 configuration, i.e., varying horizontal resolution and varying representation of processes. The main model, HadGEM3 GC3.1 (hereafter GC3) is the latest version of the HadGEM model, and was run at two horizontal resolutions for CMIP6: a low-resolution configuration, labelled as N96, with an atmospheric resolution of $1.875^\circ \times 1.25^\circ$ and a 1° resolution in the ocean model and a medium resolution configuration, labelled N216¹, with atmospheric resolutions of $0.83^\circ \times 0.56^\circ$ and a 0.25° oceanic resolution (Menary et al., 2018).

The dynamical core of the GC3.1 configuration used in the submissions of HadGEM3 to CMIP6 is used in a new Earth System model that aims to better represent ocean-biogeochemical, air-soil and air-chemistry interactions, the UK Earth System Model 1 (UKESM1). The UKESM1 was recently developed aiming to improve the UM climate model adding processes of the Earth System (Sellar et al., 2019). These additional components include ocean biogeochemistry with coupled chemical cycles and tropospheric-stratospheric interactive chemistry with the purpose of improving aspects of atmospheric chemistry, for example, aerosol-cloud and aerosol-radiation interactions (Mulcahy et al., 2018; Sellar et al., 2019). The physical atmosphere-land-ocean-sea-ice core of the HadGEM3 GC3.1 underpins the UKESM1, so that the UKESM1 and the HadGEM3 have the same dynamical core but the UKESM1 has the additional components mentioned above.

This study uses the output from several CMIP6 experiments, which are outlined in Table 3.2. First, the pre-industrial control (piControl) simulations, which are run with constant climate forcing that represents the best estimate for pre-industrial (1850) forcing of aerosols and greenhouse gas levels. Second, historical experiments are 164-yr integrations for 1850-2014 that include historical forcings of aerosol, greenhouse gas, volcanic and solar signals since 1850 (Eyring et al., 2016; Andrews et al., 2019a). The historical experiments of HadGEM3 and UKESM1 are composed of 4 and 9 ensemble members, respectively, but the results will be presented as the ensemble mean for the 1979-2014 period to provide a

¹Note also that the vertical resolution does not change with horizontal resolution.

direct comparison with the observed datasets in the same period. These experiments will be referred to as GC3-hist and UKESM1-hist hereafter. For further details, Andrews et al. (2020) extensively describes the historical simulations of HadGEM3-GC3.1.

In contrast to the pre-industrial control experiments, the historical experiments use time-varying aerosol and greenhouse gas emissions and land-use change (Eyring et al., 2016). In Latin-America, land-use change for agricultural purposes has dramatically decreased tree cover in Central America and south-eastern Brazil since the 1950s (Lawrence et al., 2012), thereby affecting the surface energy balance. The regional emissions of carbonaceous aerosols, nitrogen oxides and volatile organic compound in Latin America are also considered in the historical experiments. These emissions are noteworthy, e.g., due to the impact of black carbon emissions by increased biomass burning in the Amazon and northern Central America (Chuvieco et al., 2008).

The Atmosphere Model Intercomparison Project (AMIP) is a CMIP project that uses atmosphere-only (AO) simulations of the climate to understand the role of SST biases, variability and forcing climate signals. The standard AMIP experiment covers the period 1979-2014 and uses the observed SST fields in this period to drive the models with the same forcing as the historical simulations. Other AMIP experiments may use model-driven SSTs of other experiments to disentangle other processes. This thesis uses the five ensemble members of the AMIP experiment from GC3.

3.3 The Moist Static Energy Budget

The moist static energy (MSE) measures the gravitational, sensible heat and latent heat energy within a column and is therefore conserved following air parcels under moist adiabatic processes (Neelin and Su, 2005; Back and Bretherton, 2006; Ma et al., 2019). The use of the MSE budget has proven useful to understand tropical convective phenomena such as ENSO biases (Annamalai, 2020) and teleconnections (Neelin and Su, 2005), tropical cyclones (e.g. Wing et al., 2019), the MJO (Inoue and Back, 2015), axi-symmetric monsoons (e.g. Bordoni and Schneider, 2008) and regional monsoons (e.g. Smyth et al., 2018; Ma et al., 2019), to name a few examples.

The MSE arises from the first law of thermodynamics which decomposes the internal energy of a system into two components: one associated with heat in or out of the system and the second component associated with work done by the system. The MSE, also denoted as h is given by:

$$h = Lq + C_p T + gz = Lq + s \quad (3.1)$$

where C_p is the heat capacity at constant pressure, T is the air temperature, L is the latent heat of vaporization, q is the specific humidity and s is the dry static energy. Equation 3.1 separates the total moist energy of a parcel into a dry component also referred as dry-air enthalpy or heat content (Emanuel, 2007), and the last term is the potential energy associated with the gravitational acceleration. The MSE is conserved under pseudo-adiabatic processes and thus is considered to be a key variable of a moist system, a state variable that is not created or destroyed by convection but rather re-distributed by the coupling of convection with the large-scale circulation (Chou and Neelin, 2004; Emanuel, 2007).

The MSE budget equation can be derived from adding the thermodynamic and moisture equations that arise from the primitive equation (Neelin and Su, 2005), first by writing the material derivative as:

$$\frac{Dh}{dt} = \frac{\partial h}{\partial t} + \nabla \cdot \vec{u} h_p + \frac{\partial p}{\partial t} \frac{\partial h}{\partial p} \quad (3.2)$$

where \vec{u} is the horizontal wind vector, p is the air pressure used as a vertical coordinate so that $\partial p / \partial t = \omega$. The vertically integrated budget equation arises by rearranging and integrating equation 3.2 in the pressure coordinate (Back and Bretherton, 2006; Inoue and Back, 2015; Annamalai, 2020), leading to:

$$\left\langle \frac{dh}{dt} \right\rangle = - \left\langle \vec{u} \cdot \nabla_p h \right\rangle - \left\langle \omega \frac{\partial h}{\partial p} \right\rangle + F, \quad (3.3)$$

where the angle brackets $\langle \rangle$ denote vertical integrals from the surface pressure level up to the 100 hPa level, i.e.:

$$\left\langle \cdot \right\rangle = \int_{p_0}^{100} dp, \quad (3.4)$$

and the term F denotes the net forcing of MSE which is given by the surface fluxes and the radiative heating of the column:

$$F = LH + SH + \langle LW \rangle + \langle SW \rangle \quad (3.5)$$

where SH and LH are the surface turbulent sensible and latent heat fluxes, respectively, and LW and SW are the longwave and shortwave column-integrated heating rates, respectively.

The MSE budget is particularly useful because precipitation variations can be linked to variations in individual terms of the budget in equation 3.3 due to the moisture equation (Inoue and Back, 2015; Nie and Sobel, 2015; Inoue et al., 2021). Positive increases to the right hand side of 3.3 are proportional to increased precipitation rates (Inoue and Back, 2015). For example, increased horizontal import of h , measured by $\left\langle \vec{u} \cdot \nabla_p h \right\rangle$ will lead to increased precipitation, all else being equal. Similarly, vertical transport of h , column heating and surface fluxes can all be examined individually in their contribution to precipitation variations on multiple time-scales. For this reason, the MSE budget will be used to examine more closely the mechanisms that drive the variability of the MSD in Chapter 6.

4

The American monsoon system in UKESM1 and HadGEM3

This chapter evaluates the representation of the AMS in the CMIP6 models: UKESM1 and HadGEM3. The pre-industrial control, historical and AMIP experiments are evaluated highlighting the role of large and regional-scale biases, horizontal resolution and Earth System processes for the representation of the monsoon dynamics and teleconnections. This chapter is based on the publication: García-Franco et al. (2020) in which all the analysis was performed by the lead author.

4.1 Introduction

The response of regional monsoons to greenhouse forcing remains an open question (Zhou et al., 2016; Pascale et al., 2019) because the observational record is too short to exhibit significant trends but also because biases in GCMs increase uncertainty in future model projections. Although the thermodynamical response to greenhouse forcing in the tropics seems to be relatively well constrained, the dynamical response is less clear (Shepherd, 2014). The American Monsoon System (AMS) dynamics are shaped by regional features which means that in order to understand the precipitation response to greenhouse forcing in

a monsoon region, we need to better understand regional model biases and dynamical responses to a forcing.

The assessment of climate models in monsoon regions is key to understanding current and future changes to the water cycle in the tropics. However, and despite current recognition as a monsoon, model assessments of the AMS are scarcely done in each CMIP phase. These studies only provide a general view of the biases of each generation of models (see e.g. Geil et al., 2013; Ryu and Hayhoe, 2014). However, a deeper evaluation of individual models can be used to provide better insight into the processes associated with climatological biases in the large-scale circulation and ultimately better understand the causes for the model biases in the AMS regional features.

For example, in the South American Monsoon, CMIP5 models improved from the CMIP3 phase in their simulations of the distribution of precipitation during monsoon maturity and exhibited an improved seasonal cycle (Jones and Carvalho, 2013; Yin et al., 2013). However, some biases such as the underestimation of rainfall in the central Amazon have persisted from the first generation of GCMs up until CMIP5 (Li et al., 2006; Yin et al., 2013). The geographic distribution of rainfall during austral fall and several characteristics of the South Atlantic Convergence Zone (SACZ) and South American Low-Level Jet (SALLJ) are also poorly represented in CMIP5 in spite of their importance for the SAMS (Van Der Wiel et al., 2015; Zilli et al., 2019; Jones, 2019; Zilli and Hart, 2021). However, these studies provided little evidence as to the reasons for the improvements or the remaining biases in the models. A clear motivation to evaluate models in the South American Monsoon is that the accurate simulation of the geographic distribution and seasonality of rainfall in the Amazon rainforest is a relevant issue due to the impact of the rainforest on climate and society (e.g. Li et al., 2006; Malhi et al., 2009; Yin et al., 2013).

Climate research in recent decades has aimed to reduce uncertainty in climate projections by improving GCMs, but different approaches taken by modelling centres are seemingly disconnected (Jakob, 2014). One approach is to reduce horizontal grid spacing down to km-scale resolution to rely less on parameterizations and more on physical laws to represent clouds and convection (Palmer and Stevens, 2019). A second approach uses new explicit

representations of Earth System processes to better characterise complex land-atmosphere-ocean biogeochemical cycles that may provide a better constraint on aspects of the climate such as climate sensitivity, a parameter that depends on the carbon cycle (Marotzke et al., 2017; Sellar et al., 2019; Andrews et al., 2019a). Finally, recent modelling centres have chosen to include stochastic parametrisations of sub-grid processes since this approach has improved seasonal forecasts and may therefore improve climate projections (Palmer, 2019).

Model validation and assessment is important to analyse the effect of new parameterisations and to highlight missing processes but also evaluate which route provides the more substantial model improvement, stochastic parametrisations, increased resolution or Earth System processes. The focus of this chapter is to evaluate the CMIP6 experiments from HadGEM3 GC3.1 (GC3) and UKESM1 in the AMS. In this thesis, the AMS is considered to be composed of the North and South American monsoon systems, while also including the Midsummer drought region of southern Mexico and Central America as part of the AMS (as in e.g. Vera et al., 2006; Pascale et al., 2019).

The remainder of this chapter is organised as follows. The following section described the data and methods used in this chapter. Section 4.3 compares modelled and observed climatological temperature, sea-level pressure and low-level wind fields, whereas section 4.4 analyses the Pacific and Atlantic ITCZs. Section 4.5 analyses the spatial and temporal characteristics of rainfall and convection in the AMS while section 4.6 documents the simulated teleconnections of ENSO. A summary and discussion of the results is provided at the end of the chapter.

4.2 Methods and data

The model assessment of this chapter will use a range of experiments from the MOHC, described in section 3.2 using the HadGEM3 and the UKESM1 models. The experiments from HadGEM3 run at N96 (labelled GC3 N96) and N216 (labelled GC3 N216) resolutions are used to evaluate the role of horizontal resolution whereas Earth System Model UKESM1, which is run at N96 resolution in all the experiments, is used to evaluate the effect of representing atmospheric chemistry and other processes for the representation of the monsoon. In this

chapter, the term low resolution will refer to both UKESM1 and GC3 N96 experiments whereas medium resolution refers to GC3 N216 experiments.

The historical experiments are used to evaluate model skill in reproducing the observed period whereas the AMIP experiment from GC3 N96 is used to highlight the role of SST biases. The historical experiment data is used only in the 1979-2014 period to directly compare with the observed period. All the observational datasets used in this chapter are described in more detail in chapter 3 but in summary, the surface or near-surface air temperature data is taken from the CRU4 dataset, precipitation from TRMM, CHIRPS and GPCC and the rest of the diagnostics are from ERA5.

The climate indices of ENSO and the QBO used in this chapter were obtained by the following process. For ENSO, the deseasonalized and detrended time-series of the area-averaged SSTs (EN3.4 region [190-240°W, 5°S-5°N]) is used as an index to composite months into positive, negative and neutral phases. A month is determined to be in the positive phase (El Niño) when the index is higher than +0.65 K and a negative phase (La Niña) when the index is more negative than -0.65 K to select moderate to strong events. A neutral month is found where the magnitude of the index is smaller than 0.5 K and months with an index between 0.5 and 0.65 are discarded as they are borderline weak ENSO events or neutral cases. Other indices, including the use of a 5-month running mean (Trenberth et al., 1998), were tested without significantly changing the results. Previous studies (e.g. Menary et al., 2018; Kuhlbrodt et al., 2018) showed that the MOHC models reasonably simulate several characteristics of ENSO such as the period and SST patterns.

Principal component analysis (PCA) has shown that ENSO events may be separated into two categories: Central Pacific (CP) and East Pacific (EP) events (Cai et al., 2020), which highlight where the peak SST anomaly is found in the Pacific Ocean. PCA analysis was used on deseasonalized SST fields in the equatorial [12°S-12°N] Pacific Ocean [120°E-260°E]. The E-index is computed from $(PC1 - PC2)/\sqrt{2}$ and the C-index from $(PC1 + PC2)/\sqrt{2}$. EP (CP) events were defined where the E-index (C-index) was greater than 1.

The SACZ is evaluated in these models using the Empirical Orthogonal Function (EOF) methodology (Carvalho et al., 2004; Jorgetti et al., 2014). First, active days are constructed by computing the first EOF of the monthly-mean deseasonalized OLR and, then, the daily

OLR, previously filtered to remove periods higher than 99 days, is projected on the EOF pattern to produce a time series of pseudo-principal components. Active SACZ days are found when this time series of pseudo-PCs is greater than 1, and the persistence is measured as the number of continuous days where the time series is greater than 1.

Similarly, for the QBO, the deseasonalized and detrended time series of the equatorially averaged [10°S-10°N] zonal-mean zonal wind at the 70 hPa level is used as the QBO index for both reanalysis and model data. The westerly phase of the QBO (QBOw) is determined when the index is greater than 2 m s^{-1} and the easterly phase (QBOe) when the index is less than -2 m s^{-1} .

4.3 Surface temperature and low-level wind

This section evaluates how these simulations represent the near-surface air temperature and low-level wind fields in the vicinity of the AMS region (Figures 4.1 and 4.2). The biases of the historical experiments, computed as the differences between the model and observed fields, are shown in Figures 4.1c, d) for GC3 N96-hist and e, f) for UKESM1-hist. Only statistically significant differences are shown, according to a Welch t-test (Wilks, 2011). The significance for simulations with multiple ensemble members is estimated first for each ensemble member and then combined into a single probability or p-value using Fisher's method (Fisher, 1992). Pattern correlations and root-mean square error (RMSE) are shown in Figures 4.1c-f.

During DJF, the simulations show a colder-than-observed sub-tropical North America and a warm bias over the Amazon ($\approx +3.5 \text{ K}$). The west coast of South America also shows a significant warm bias ($> +4 \text{ K}$) in the historical simulations. The simulated circulation in austral summer in South America has a significant bias in the easterly flow coming from the equatorial and subtropical Atlantic. The low-level wind biases suggest a weaker easterly flow from the Atlantic into southeastern Brazil but also a strong southward flow from northern to southern South America. The South America Low-Level Jet, i.e., the low-level northwesterly flow in Bolivia, observed in Figure 1a, is stronger in the simulations. This stronger than observed jet is suggestive of a stronger moisture transport to the La Plata Basin, which

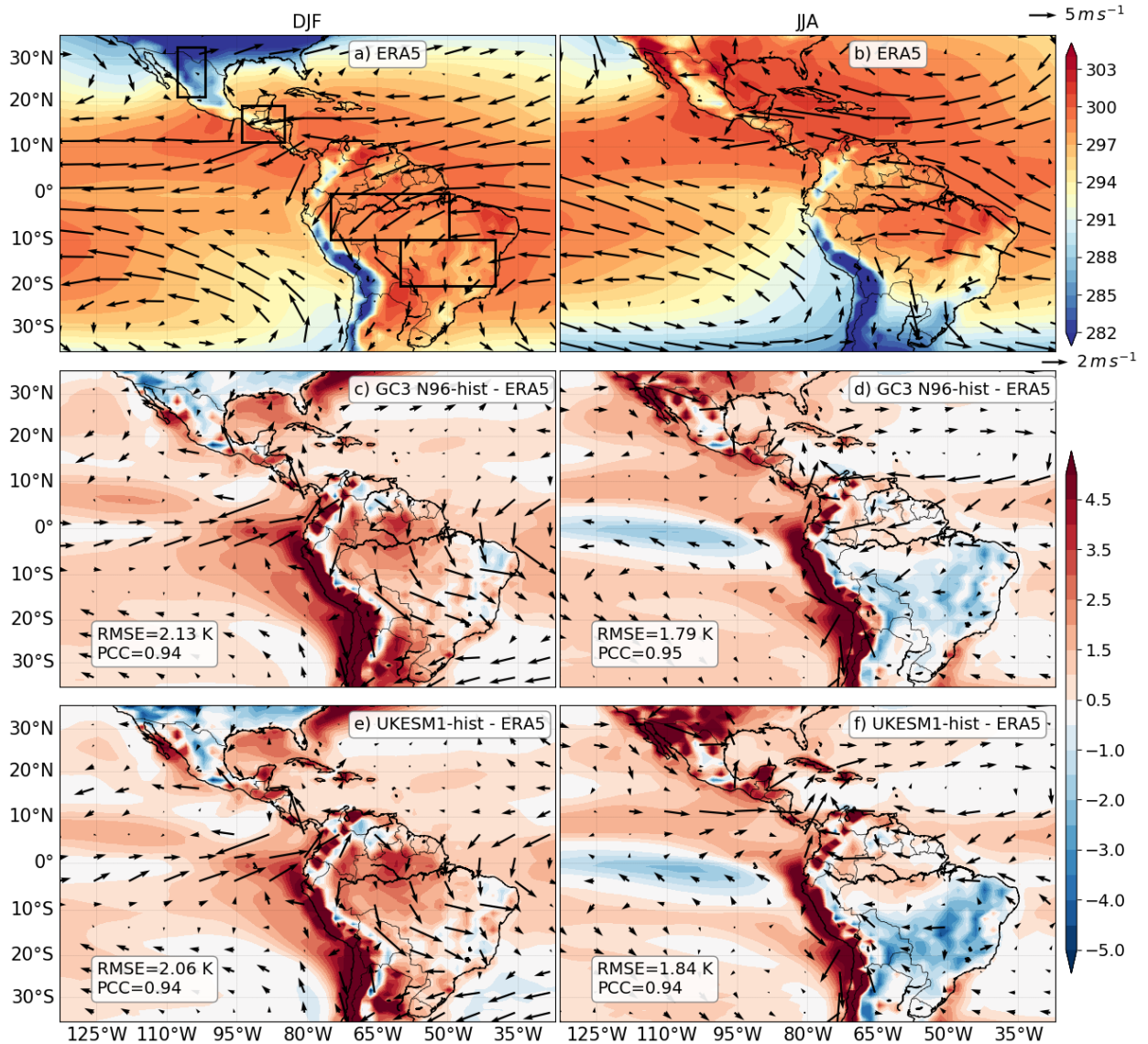


Figure 4.1: (a, b) Temperature (color-contours in K) and wind speed (vectors) at 850 hPa DJF and JJA climatogies in ERA5. The biases are shown as the differences between the ensemble mean from the historical experiment of (c, d) GC3 N96 and (e, f) UKESM1 and ERA5. The climatogies and biases are shown for (a, c, e) boreal winter (DJF) and (b, d, f) boreal summer (JJA). Only differences statistically significant to the 95% level are shown, according to a Welch t-test for each field. The key for the size of the wind vectors is shown in the top right corner of panels b) and d). The root-mean square error (RMSE) and pattern correlation coefficient (PCC) are shown on the bottom left of c-f.

has been associated with a drying of the Amazon and positive precipitation anomalies at the exit region of the jet (Marengo et al., 2012; Jones and Carvalho, 2018).

In turn, in boreal summer (Figures 4.1d, f), positive temperature biases are observed in southwestern North America ($> +3.5$ K), which are higher in UKESM1-hist than in

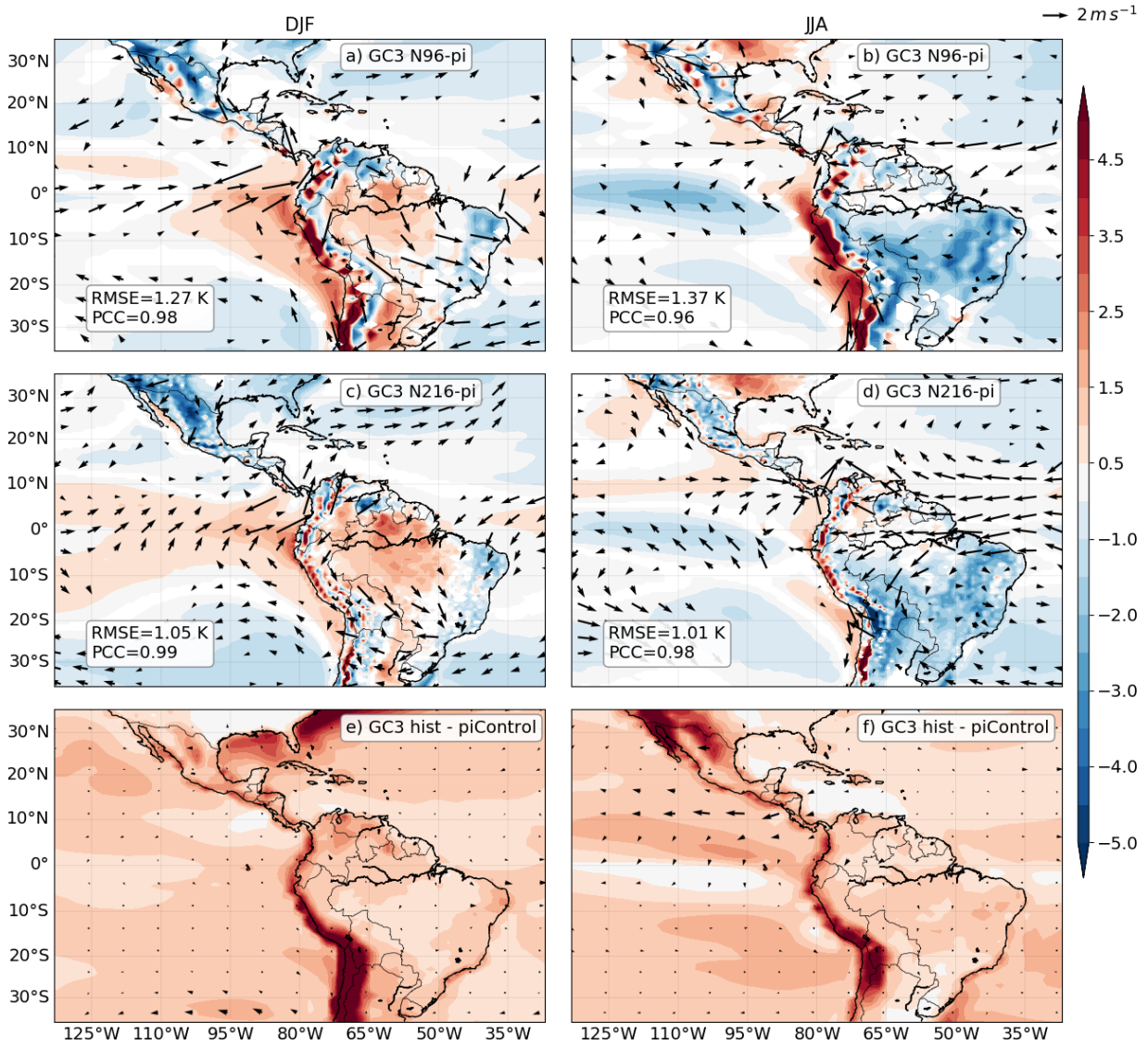


Figure 4.2: As in Figure 4.1, but showing the differences between the piControl simulations of (a, b) GC3 N96-pi and (c, d) GC3 N216-pi, and ERA5. (e, f) show the statistically significant differences between the historical (1979-2014) and piControl experiments of GC3. The RMSE and PCC are shown on the bottom left of a-d.

GC3 N96-hist. The easterly flow west of Central America has a negative bias in UKESM1 suggesting a weaker flow that crosses from the Caribbean Sea into the East Pacific Ocean. Also in JJA, the simulated East Pacific surface temperatures are colder than observed for both historical experiments. The inclusion of Earth System processes appears to make no improvement on the low-level circulation biases.

The temperature and low-level winds in the piControl simulations (Figures 4.2a-d) [are very](#)

similar to the historical simulations. In DJF, the piControl simulations show warmer than observed Amazon and differences in the circulation in South America which are essentially equal to the historical experiments. However, these differences with observations are smallest in GC3 N216-pi. In JJA, the piControl simulations do not show the warmer northwestern North America observed in the historical experiments. However, the weaker zonal wind over the easternmost Pacific is present in both piControl and historical simulations.

Figures 4.2e, f show the difference between the historical and piControl experiment of GC3 N96, illustrating the response to historical forcing in GC3 N96. The temperature response in austral summer in South America is observed as 1.5 K whereas in JJA in North America temperatures were 4 K higher in the historical experiment than in the piControl. The only significant difference in low-level winds, as a response to historical forcing, are the easterlies in the East Pacific Ocean during JJA, which are stronger in the historical simulation. A very similar temperature and wind flow pattern response to historical forcing was observed for UKESM1 (not shown) although of slightly different magnitude.

The seasonal cycle of temperature in key regions (depicted in Figure 4.1a) of the AMS is shown in Figure 4.3, comparing the simulations to ERA5 and the CRU4 dataset. The temperature in the North American Monsoon region ranges from the boreal winter mean temperature of 12°C to a maximum in June close to 27°C. Although the piControl simulated temperatures are colder than observed throughout the year, the models reasonably reproduce the seasonal cycle, which may be relevant for the simulated monsoon onset timing and strength (Turrent and Cavazos, 2009). The historical experiments notably show a colder than observed winter and a warmer than observed summer compared to piControl experiments.

The piControl simulations show a colder-than-observed winter in southern Mexico and northern Central America. The historical experiments show a warming signal, when compared to the piControl simulations, of about 1.5 K in winter and 2 K in the summer in this region. Despite these biases, all the experiments follow closely the seasonal cycle in North and Central America.

However, the seasonal cycle in South American regions (Figures 4.3 c, d) of southeastern Brazil and the central Amazon shows notable temperature biases. The simulations show a stronger than observed seasonal cycle, especially the historical experiments. For example,

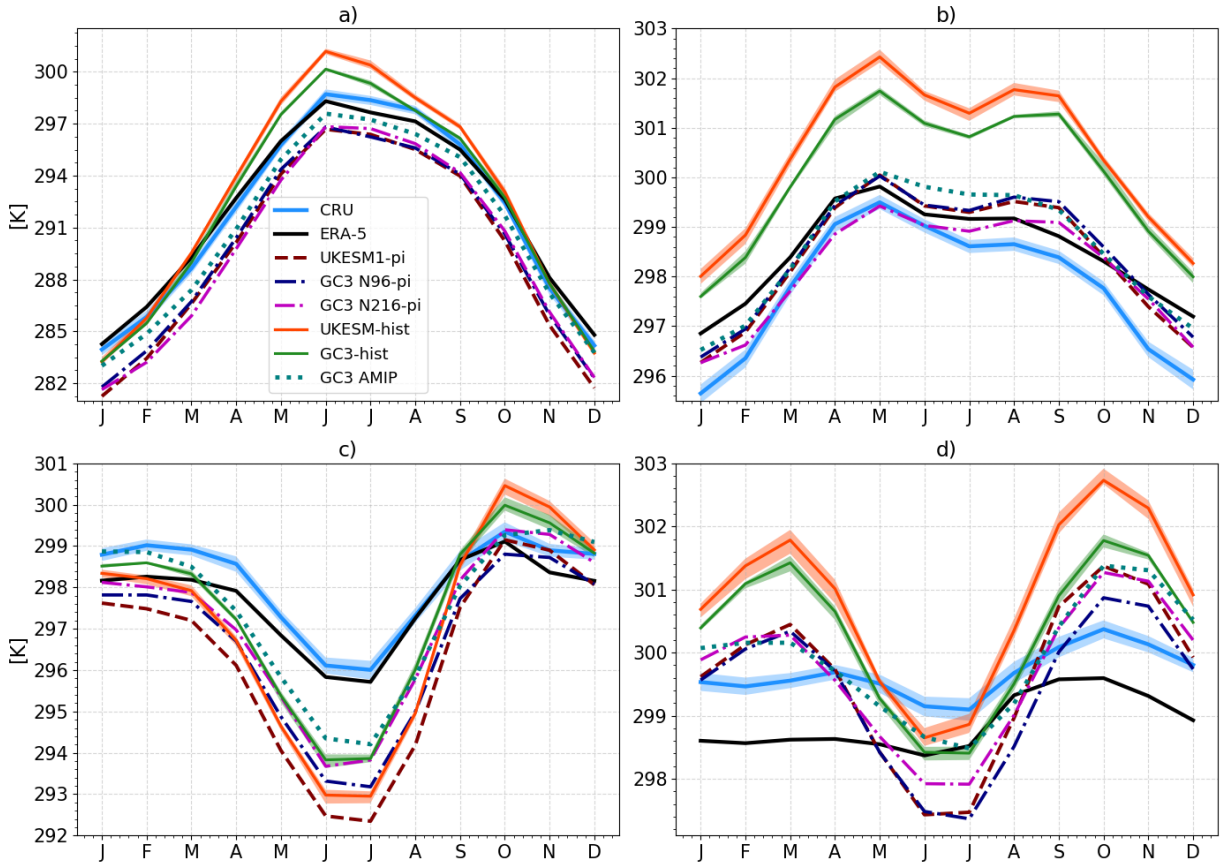


Figure 4.3: Monthly-mean temperature in the (a) North American Monsoon [$19\text{--}35^{\circ}\text{N}, 110\text{--}103^{\circ}\text{W}$], (b) the Midsummer drought [$11\text{--}19^{\circ}\text{N}, 95\text{--}85^{\circ}\text{W}$] (c) Eastern Brazil [$20\text{--}10^{\circ}\text{S}, 60\text{--}40^{\circ}\text{W}$] and (d) the Amazon basin [$-10\text{--}0^{\circ}\text{S}, 75\text{--}50^{\circ}\text{W}$] regions. The shadings for the CRU dataset represents the observational uncertainties and for the historical simulations the shading is the ensemble spread. The regions for this plot are shown in Figure 4.1a.

the modelled temperature difference between late austral winter and spring was ≈ 4 K whereas the observed temperature varies by less than 1 K in the same period. The models show a warm bias in the Amazon region (Fig. 4.3 d) which peaks in austral spring (SON), during the development of the monsoon (Marengo et al., 2012). In southeastern Brazil, the seasonal cycle is reasonably well reproduced but with a significant cold bias throughout the year which maximizes during austral winter (JJA), as models (e.g. UKESM1) simulate a temperature 4 K lower than observed. In all panels of Figure 4.3, the historical experiments show a significant warming signal as a response to historical forcing, which is generally stronger in UKESM1 than in GC3 N96.

The near-surface air temperature and the low-level wind structure during monsoon season

are intertwined with the processes that lead to monsoon rainfall which means that the biases presented in this section will likely be related to biases in precipitation, e.g., through cloud feedbacks. For example, a biased wind structure in eastern Brazil as well as the positive warm bias in the central Amazon during DJF may indicate biases in the moisture transport and cloud cover that lead to the dry Amazon bias (Jones and Carvalho, 2013).

4.4 The Atlantic and Pacific ITCZs and the SACZ

The AMS is intertwined with the seasonal migration of the East Pacific and Atlantic ITCZ as the ITCZ largely determines regions of ascending and descending motions, moisture transport and is modulated by the hemispheric energy balance (Oueslati and Bellon, 2013; Li and Xie, 2014; Zhou et al., 2016; Cai et al., 2019). The North American monsoon and MSD regions are influenced by the East Pacific ITCZ whereas the South American monsoon is affected by the Atlantic ITCZ (Yoon and Zeng, 2010; Marengo et al., 2012). Three simulations are evaluated in this section: two low-resolution (N96) runs, the ensemble-mean UKESM1-historical, the ensemble mean GC3 AMIP and a medium-resolution run, GC3 N216-pi. Other simulations are not shown as all the coupled low resolution (N96) simulations from UKESM1 and GC3 N96 showed very similar precipitation and ITCZ characteristics whereas the AMIP and medium-resolution experiments showed notable differences to the rest.

The climatological ITCZ in TRMM (Figure 4.4a) is found, on average, at 8°N in the East Pacific and at 6°N in the Atlantic. All the simulations reasonably represent the climatological position of the East Pacific (EP) ITCZ; however, the modelled Atlantic ITCZ near the coast of Brazil is found south of the equator at 3°S in the coupled model simulations. The location of the ITCZ in GC3 N216-pi and the spatial distribution of rainfall is more consistent with TRMM dataset than the rest of experiments. Rainfall near the Amazon river mouth is significantly larger in the low-resolution simulations than in the TRMM dataset. However, the GC3 AMIP shows the best agreement with TRMM in ITCZ position and rainfall distribution.

The seasonal cycle of the ITCZ location, precipitation rates and low-level winds in both basins are shown in Figure 4.5, for TRMM, UKESM1-hist, GC3 AMIP, GC3 N96-pi

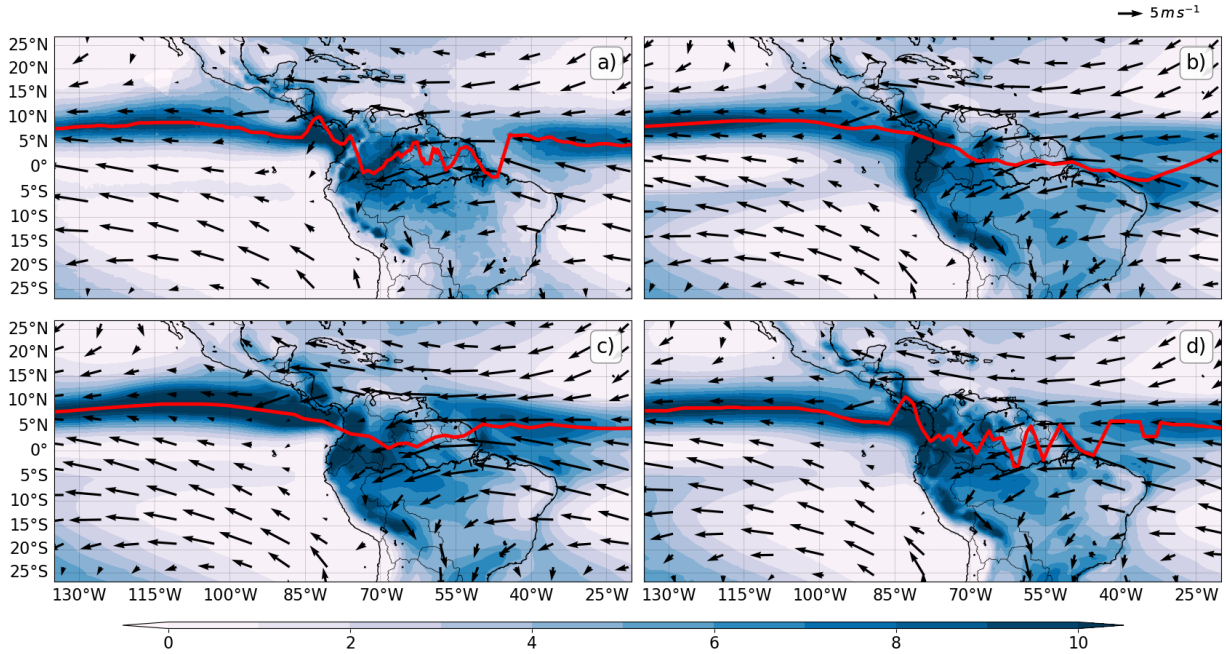


Figure 4.4: Climatological precipitation [mm day^{-1}] and low-level wind speed (850-hPa) in (a) TRMM and ERA-5, (b) the ensemble-mean UKESM-historical, (c) GC3-amip and (d) GC3 N216-pi. The red line highlights the maximum rainfall for each longitude as a proxy for the position of the ITCZ.

and GC3 N216-pi. The seasonal cycle of the ITCZ closely follows the seasonal march of the solar insolation and the SSTs (Doi et al., 2012; Donohoe et al., 2013), whereas both the variability and mean of this seasonal cycle are linked to the coupling of the low-level circulation and SST gradients (Hastenrath, 2006; Richter et al., 2014).

The EP ITCZ in observations (Fig. 4.5a) migrates southwards during the first days of the year and is weakest and at its southernmost position at 5°N around day 100 (mid-April). During boreal spring, the EP ITCZ migrates northward reaching a peak latitude and maximum rainfall at 10°N by day 250, or early September. The EP ITCZ during boreal winter is weaker than during the rest of the seasons. The low-level winds are predominantly easterly, which are stronger away from the ITCZ and weaker and convergent near the ITCZ position. The position and seasonal migration of the EP ITCZ is reasonably well represented in the four simulations (Fig. 4.5), but a noticeable bias in precipitation is observed in boreal winter south of the equator in the coupled simulations. The modelled low-level wind biases are characterized as stronger winds converging toward the ITCZ during boreal summer and spring and diverging away from the equator during boreal winter.

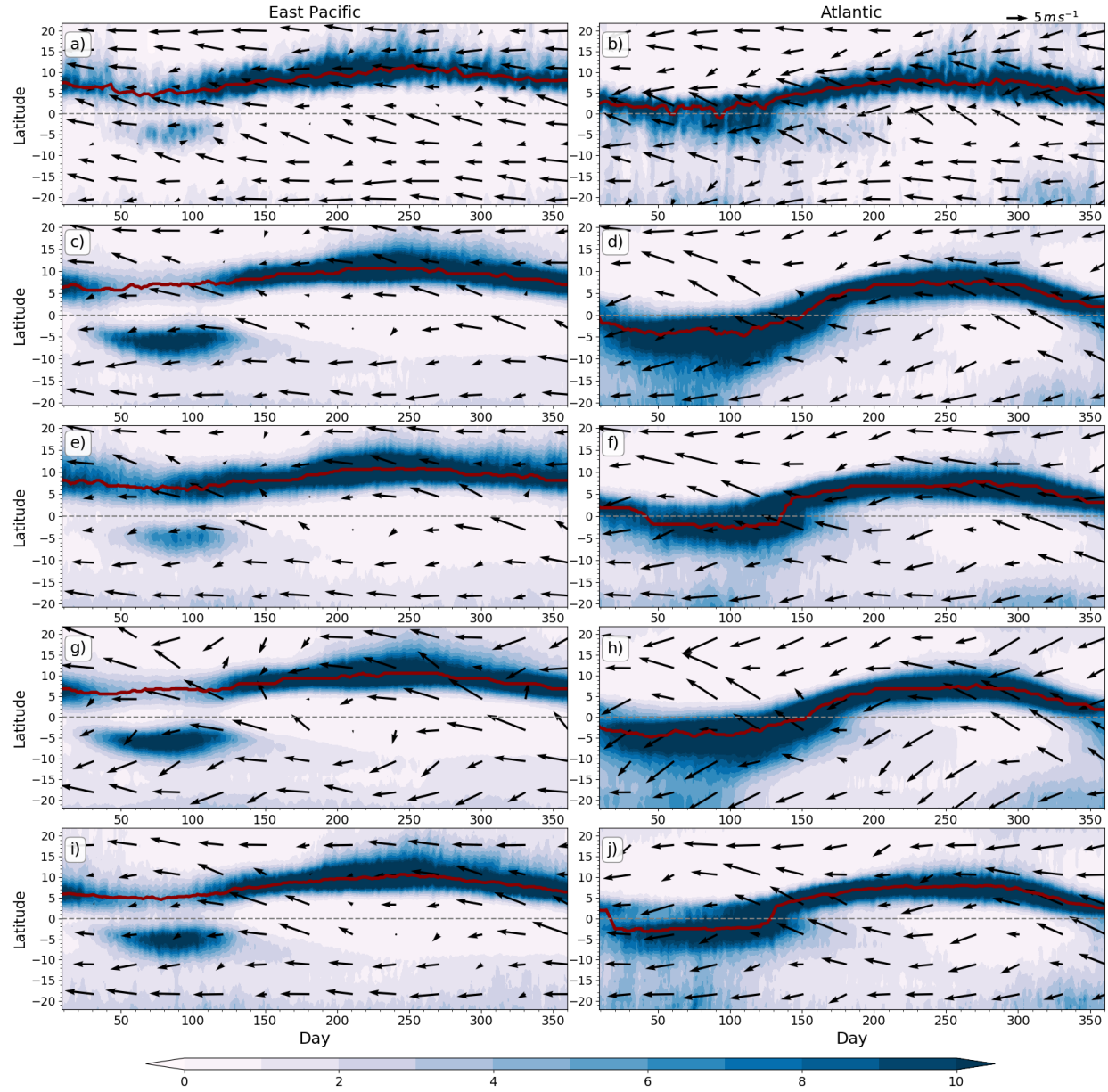


Figure 4.5: Time-Latitude plot of daily mean rainfall (colour contours) and low-level wind speed (850 hPa) longitudinally averaged over the (a, c, e, g) East Pacific [150°W - 100°W] and (b, d, f, h) Atlantic [40°W - 20°W] Oceans. (a, b) show rainfall from TRMM and winds from ERA-5, (c, d) the ensemble-mean UKESM-historical, (e, f) GC3 AMIP, (g, h) GC3 N96-pi and (i, j) GC3 N216-pi. The red solid line shows the ITCZ as the latitude of maximum precipitation.

The Atlantic ITCZ (Figure 4.5b) has a similar seasonal cycle to the EP ITCZ, located at 4°N at day 1 and migrates southwards at the start of the year reaching its southernmost position at 0° at the end of March. During boreal spring, the Atlantic ITCZ migrates north, reaching 8°N at the start of boreal summer. In contrast to the EP ITCZ, the maximum

rainfall in the Atlantic ITCZ does not weaken during any season. The position of the modelled ITCZ is generally biased south with respect to the observations. The simulated ITCZ crosses south of the equator during boreal winter, with maximum precipitation rates of 12 mm day^{-1} found in the $0\text{-}10^\circ\text{S}$ region. After boreal spring, the modelled ITCZ crosses back north of the equator and matches the observed ITCZ reasonably well for boreal summer and fall. Low-level wind vectors near the Atlantic ITCZ (Figures 4.5f and h) suggest a southerly bias north of the equator and a northerly bias south of 10°S .

The SACZ is a key element of the climate of the SAMS (Carvalho et al., 2004; Jorgetti et al., 2014; Van Der Wiel et al., 2015; Zilli et al., 2019) that is not frequently assessed in climate models. The mean representation of the SACZ features in [thesethis](#) simulations, defined by the outgoing long-wave radiation empirical orthogonal function analysis (Figure 4.6) closely resembles the pattern found in ERA5. The SACZ active days and the persistence of the SACZ are also compared and found to be in relatively good agreement between reanalysis and model datasets.

The simulations from UKESM1, and GC3 N96 and N216 appear to reasonably simulate

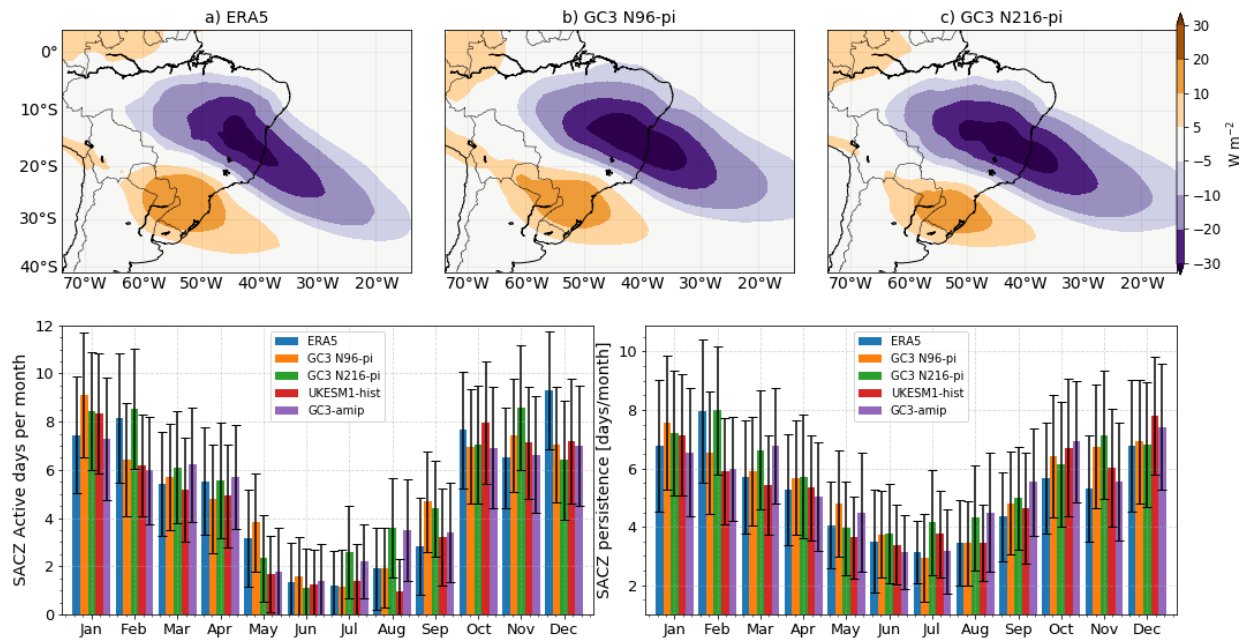


Figure 4.6: (a, b, c) OLR anomalies during active South Atlantic Convergence Zone (SACZ) events. (d, e) Frequency of active SACZ days and length of active SACZ events in reanalysis and model data, the standard deviation is shown as the error bar.

the spatial pattern of active SACZ days characterized by the low OLR in southeastern Brazil and higher OLR in the La Plata Basin. Similarly, the seasonal cycle of the frequency and persistence of SACZ active days is very well represented by the models with peak activity found from November through January and very little activity during austral winter. The impact that an accurate representation of the SACZ activity in GCMs has for representing short-scale variability of the South American Monsoon System is an open question, as the SACZ is rarely assessed in CMIP analyses.

GCMs have showed little improvement in their representation of ITCZs in CMIP phases(Oueslati and Bellon, 2015) and this section shows that these biases are also found in these CMIP6 experiments. These biases are hard to improve because the position, strength and seasonal migration of the ITCZ are controlled by ocean-atmosphere feedbacks that intertwine the local and regional circulation with cloud-radiative feedbacks and the atmospheric and oceanic transport of energy (Schneider et al., 2014; Oueslati and Bellon, 2015; Byrne and Schneider, 2016; Byrne and Zanna, 2020).

4.5 Precipitation and convection in the AMS

4.5.1 Mean seasonal precipitation

The austral summer (DJF) rainfall distribution in South America (Figure 4.7) shows several noteworthy biases in the coupled simulations compared to TRMM. The maximum austral summer rainfall in TRMM (Fig. 4.7a) is found in a northwest-southeast oriented band from the core Amazon region into southeastern Brazil, the SACZ. One main bias (Figs. 4.7e-h) is the southward displacement of the Atlantic ITCZ, observed as positive ($+5 \text{ mm day}^{-1}$) biases south of the equator and negative biases (-5 mm day^{-1}) north of the equator in the Atlantic. The models underestimate rainfall in the core Amazon basin by -3 mm day^{-1} on average, and rainfall in southeastern Brazil is overestimated by more than $+5 \text{ mm day}^{-1}$, approximately +100% of the observed rainfall in this region.

The precipitation biases are associated with a stronger northerly flow in South America, transporting moisture from the Amazon into southeastern Brazil and the La Plata Basin. The magnitude of these biases is smaller in GC3 N216 (Fig. 4.7f) than in the low resolution

simulations, such as UKESM1-hist. The ensemble mean GC3 AMIP (Fig. 4.7d) shows a better representation of the austral summer rainfall and circulation patterns, removing the

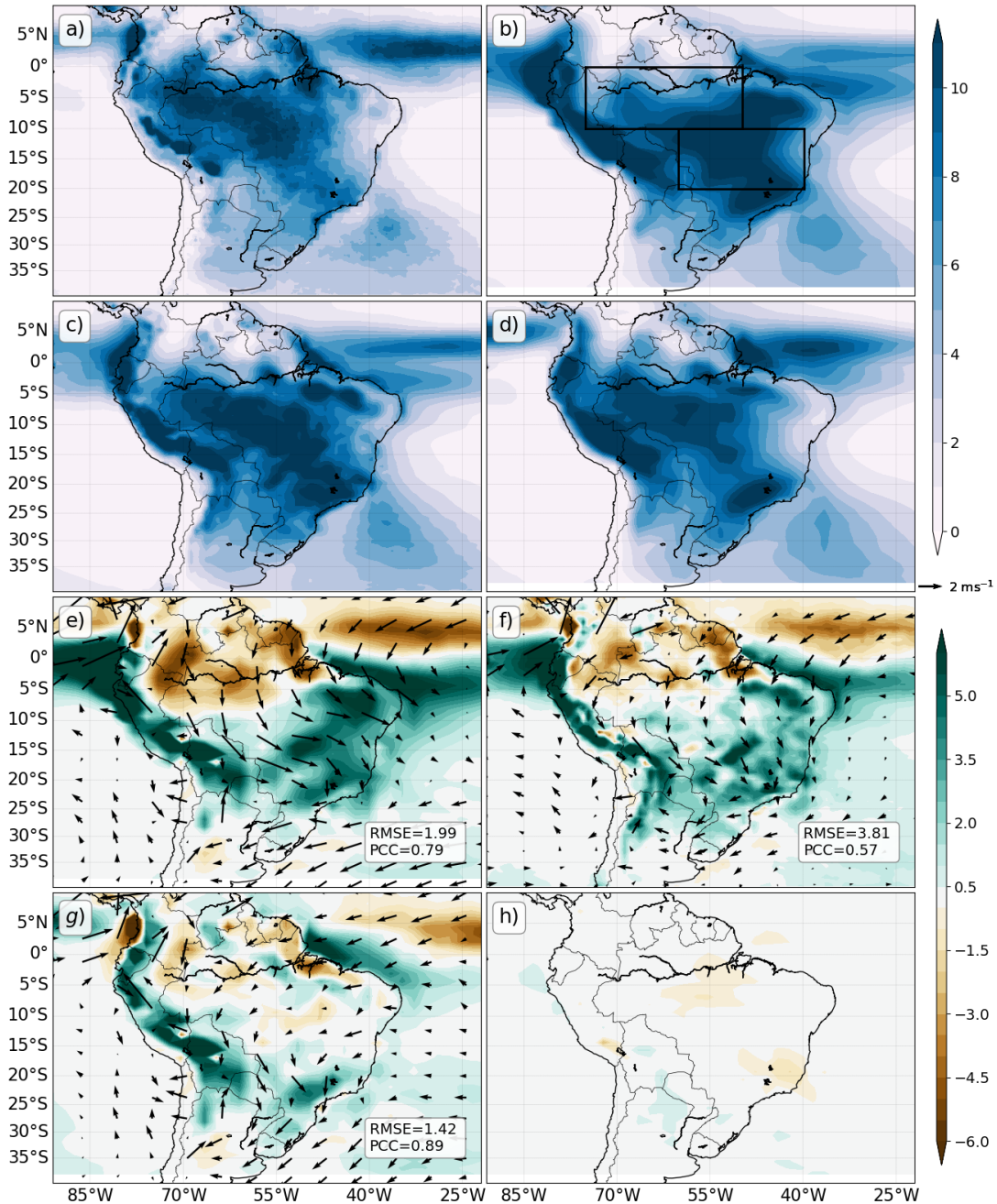


Figure 4.7: DJF mean rainfall [mm day⁻¹] from (a) TRMM, (b) UKESM1-historical, (c) GC3 N216-pi and (d) GC3-amip. (e, f, g) show the statistically significant biases, i.e., differences between panels (b, c ,d) and (a) TRMM. (h) Precipitation difference between UKESM-historical and UKESM1-pi, only statistically significant differences (95% confidence level) are shown. In (e-g) in the 850-hPa wind biases are shown as vectors.

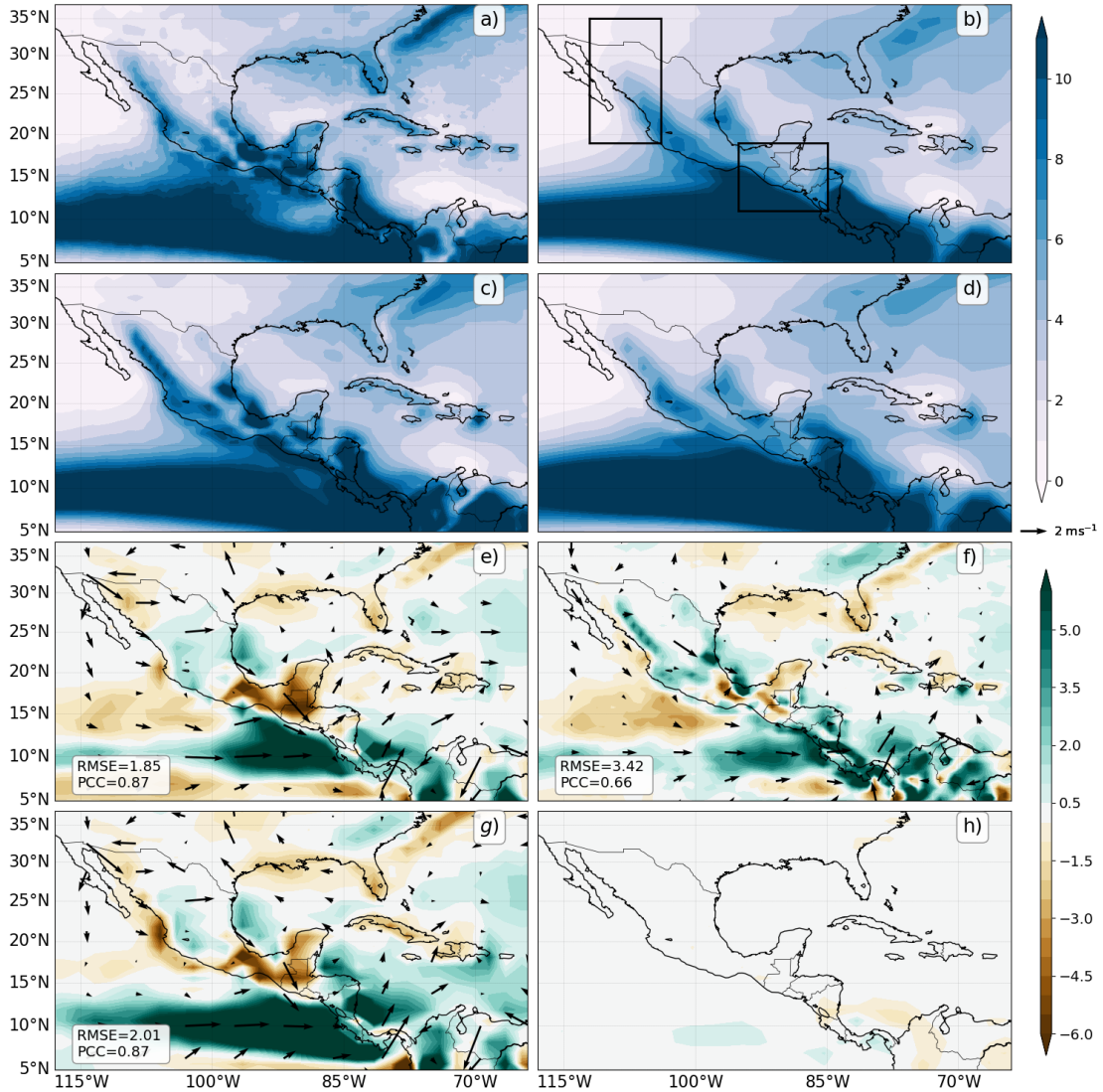


Figure 4.8: As in Figure 4.7 but for JJA in the northern part of subtropical America.

main circulation biases (Fig. 4.7g) of the coupled simulations. The response to historical forcing, illustrated by the difference between UKESM1-hist and UKESM1-pi (Fig. 4.7h), is much weaker than the magnitude of the biases and is characterized by a weak drying of the Amazon and southeastern Brazil. Therefore, the magnitude of these biases are too large to have confidence in these drying responses to historical forcing.

The modelled and observed JJA mean rainfall and biases for Mexico and Central America are shown in Figure 4.8. The main feature is the East Pacific (EP) ITCZ which extends north to 15°N near the western coast of Mexico as a broad band of rainfall ($>11 \text{ mm day}^{-1}$). The modelled EP ITCZ (Figures 4.8e, f, g) rainfall is overestimated by more than 5 mm

day⁻¹, especially in GC3-amip. This wet bias is associated with a westerly bias in the low-level circulation, suggesting a weaker flow from the Caribbean into the East Pacific.

The North American Monsoon can be observed as a band of precipitation across western Mexico. In the core monsoon region, near the Sierra Madre Occidental (Adams and Comrie, 1997; Zhou et al., 2016), the JJA-mean rainfall is higher than 8 mm day⁻¹. The distribution of rainfall in the North American Monsoon region is relatively well represented in all the simulations, as only a moderate wet bias (+2 mm day⁻¹) in western Mexico is observed. The northernmost part of the North American Monsoon (southwestern US) is best simulated by GC3 N216-pi, as the other simulations show a dry bias in this region. The low-resolution simulations (Figure 4.8e) underestimate rainfall (-5 mm day⁻¹) over land in southern Mexico, Guatemala and Belize. Rainfall in the Caribbean islands and Florida is underestimated (-1 mm day⁻¹) in all simulations.

In most cases for JJA in this region, the precipitation and wind biases were reduced in the medium-resolution simulation (Figure 4.8f) and little-to-no difference was observed between UKESM1-hist and GC3 N96-hist (not shown). The precipitation response to historical forcing is much lower than the biases (Figure 4.8h) with no significant precipitation differences over land due to the historical forcing.

4.5.2 The annual cycle of rainfall

Figure 4.9 shows the seasonal cycle of rainfall at the pentad (5-day) scale over the North American Monsoon, the Midsummer drought (MSD), the Amazon and eastern Brazil regions. The correlation between TRMM and the model and reanalysis data (ERA5) is also shown in each panel.

The seasonal cycle of precipitation in the MSD region in the simulations is well represented as all the simulations show the characteristic bimodal distribution, a feature that is difficult to simulate for a climate model (Ryu and Hayhoe, 2014). However, the magnitude of the first peak and second peaks of precipitation in the simulations are different. Most of the simulations show a wetter first peak than TRMM by 4 mm day⁻¹, and the AMIP simulation overestimates the second maximum of rainfall by 2-3 mm day⁻¹. Similarly, the differences between the first peak and the MSD and between the MSD and the second peak are more

pronounced in the simulations. The timing of the MSD period is different in the models, as the simulations show the driest period taking place 10 days after TRMM and ERA5.

In the North American Monsoon (Figure 4.9b), the observed seasonal cycle is characterized by a very long dry period from the November to June, which is followed by a sharp increase of rainfall around mid-June. The timing and strength of the onset of rainfall is well represented by all these simulations. Moreover, the modelled and observed mean precipitation rates during monsoon maturity are 4 mm day^{-1} , from mid-July until early September, which suggests the models can also reproduce the observed peak monsoon rainfall. The historical simulations show a shorter wet season characterised by an earlier retreat of the monsoon rainfall and a positive bias ($+1 \text{ mm day}^{-1}$) is found during late local fall and early winter, a feature present in most CMIP5 models (Geil et al., 2013).

The seasonal cycle of precipitation in eastern Brazil is characterised by a very wet summer ($\sim 8 \text{ mm day}^{-1}$) compared to a very dry ($\sim 0.2 \text{ mm day}^{-1}$) winter (Figure 4.9c).

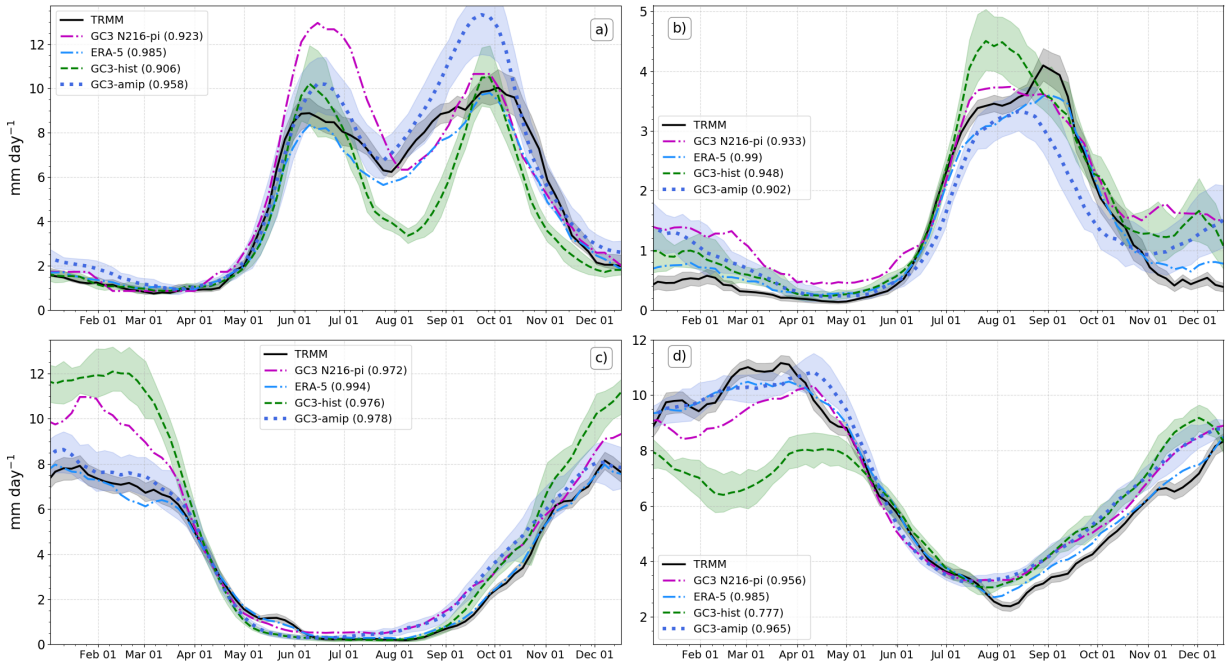


Figure 4.9: Annual cycle of pentad-mean rainfall in the regions (a) the Midsummer drought, (b) the North American Monsoon, (c) Eastern Brazil and (d) the Amazon Basin. The regions are defined as in Figure 4.3 and are illustrated in Figure 4.8b and Figure 4.9b. The shaded regions represent observational uncertainty for TRMM and ensemble spread for the historical experiments. The correlation coefficient for each of the simulated seasonal cycles with TRMM is given in brackets in each panel.

The models (Figure 4.9c) show a positive bias during monsoon maturity. This bias was found to be of $+4 \text{ mm day}^{-1}$ and $+2.5 \text{ mm day}^{-1}$ for the low and medium resolution simulations, respectively. This positive bias in the maximum rainfall is consistent with the biases shown in Figure 4.7, which showed that rainfall in southeastern Brazil is overestimated, especially in the low resolution coupled simulations. In contrast to the coupled simulations, GC3-amip shows a very good agreement with the observed maximum summer rainfall and the seasonal cycle ($r=0.978$) throughout the year.

Finally, the seasonal cycle in the Amazon (Figure 4.9d) has a weaker seasonal contrast as relatively large precipitation rates ($>2 \text{ mm day}^{-1}$) are found year-round. The coupled simulations show a dry bias during austral summer and a good agreement with the observations during austral winter. Rainfall rates in the Amazon from January to March, in both TRMM and ERA-5, are close to 10 mm day^{-1} , yet the low resolution simulations show rainfall rates of 8 mm day^{-1} in mid-February. [GC3 N216-pi shows a better agreement with observations than the low resolution coupled simulations, which points to the role of horizontal resolution](#), but still underestimates austral summer rainfall by 1 mm day^{-1} . The models, however, represent with reasonable skill the timing of the transition from early austral spring (4 mm day^{-1} in September) to summertime rainfall (6 mm day^{-1} in November).

The dry Amazon bias has been a known feature of GCMs, including the MOHC models, since CMIP3 (Li et al., 2006; Yin et al., 2013). In these simulations the dry Amazon bias is only alleviated in GC3-amip whose seasonal cycle and maximum summer rainfall agree well with observations suggesting that the Atlantic SST biases, which couple to the moisture transport between ocean and land, are the key factor for the biases in the Amazon in coupled model simulations.

4.5.3 Characteristics of convective activity

The seasonal cycles of outgoing long-wave radiation (OLR), vertical velocity (ω) and specific humidity (q) characterise how the strength and height of deep convection, as well as the moisture within the column vary with the wet season in a monsoon region. The pentad-mean annual cycle of OLR, q and ω at the 500-hPa level in four regions of

the AMS (Figure 4.10) are used as process oriented diagnostics to further evaluate the biases in the seasonal cycle of rainfall.

For the North American Monsoon the seasonal cycles of OLR, q and ω are relatively well represented in the simulations. During late boreal winter and early spring, OLR increases steadily as a result of surface warming. However, in early June, near the onset date (Douglas et al., 1993; Geil et al., 2013), OLR sharply decreases reaching a minimum value of 246 W m^{-2} by mid-July. The vertical velocity decreases steadily from January to a minimum in August, indicating ascent from May 1st until September 15th. The models show similar seasonal cycles but overestimate the summertime OLR by $\approx 6 \text{ W m}^{-2}$ and underestimate mid-level moisture by 0.3 g/kg and ω by 0.01 Pa s^{-1} which is about 5-10% overall. The simulated shallower convection and drier mid-troposphere is seemingly compensated by stronger mid-level ascent leading to reasonable precipitation rates.

In the MSD region, OLR and q show signs of convective activity from mid-April, as OLR sharply decreases and moisture increases. The characteristic MSD bimodal distribution of precipitation can also be observed as two troughs of OLR, and ω and two peaks in q separated by a period of relatively higher OLR, lower q and weaker ascent from June 15 until late August. Although arguably with a small dry bias with shallower convection after mid-July, the simulations follow closely the observed seasonal cycle.

The simulated conditions during the first peak period show similar OLR and mid-level moisture but stronger ascending motions, which may explain the positive rainfall bias in this period (Fig. 4.9a). In the period between the first peak and the MSD, the simulated OLR increases more sharply than observations from 220 W m^{-2} (June 15) to 250 W m^{-2} (early August), with similar behaviour in ω and q , which may also be related to the strong variations of precipitation within the rainy season in the simulations. The period during the second peak of rainfall in September shows signs of shallower convection and a drier mid-level when compared to ERA5.

In southeastern Brazil, the simulations reasonably follow the timings of the annual cycle of OLR, q and ω of the reanalysis, particularly during austral winter. The moisture q in ERA5 during the dry seasons of austral fall, winter and spring is reasonably simulated by all the experiments. However, during austral summer, the coupled model simulations

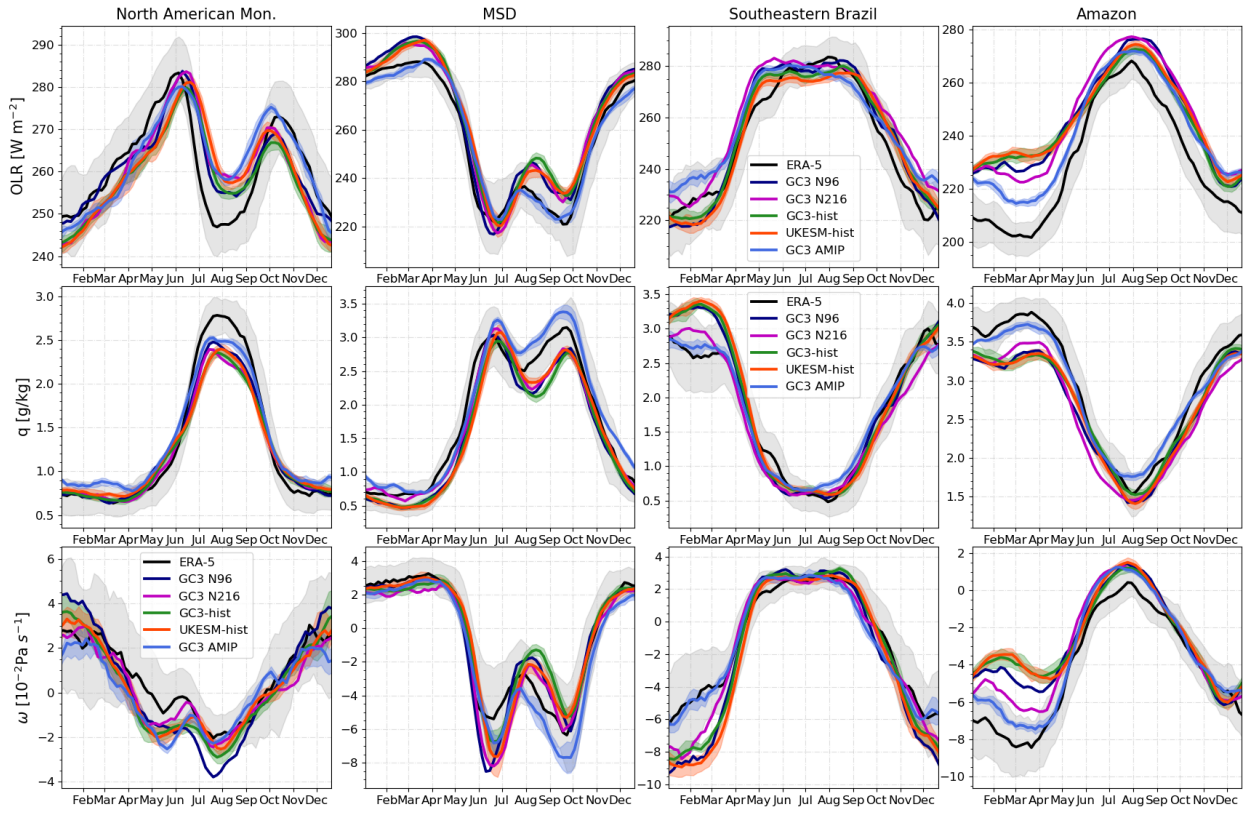


Figure 4.10: Pentad-mean (upper) outgoing long-wave radiation (OLR), (middle) specific humidity at 500-hPa and (lower) ω 500-hPa. These are shown from left to right for the North American Monsoon, the Midsummer drought, southeastern Brazil and the core Amazon. The uncertainty in ERA-5 data, shown as faint gray shading was estimating by bootstrapping with replacement the ERA-5 record 10,000 times.

show significant biases characterised by stronger ascent and increased specific humidity in the mid-levels, although the height of convection ($OLR \sim 225 \text{ W m}^{-2}$) is only modestly higher in the simulations.

The simulated OLR, q and ω exhibit the highest biases in the Amazon. During austral summer, particularly January and February, the simulated convective activity is shallower (OLR bias of $+25 \text{ W m}^{-2}$) and weaker (positive ω bias $+0.02 \text{ Pa s}^{-1}$) and the mid-level troposphere is drier (-0.5 g/kg) than in ERA5. All these biases are in agreement with the dry Amazon bias described in the previous section. Despite biases in the magnitude of OLR, q and ω during peak convective activity, the seasonal variation is very well simulated so that convective activity, as evidenced by these metrics, starts and ends in the simulations within one or two pentads of the reanalysis.

The smallest biases in the coupled simulations are those of GC3 N216-pi, for all the regions. The simulated OLR, q and ω in GC3-amip in southeastern Brazil and the Amazon show a much better agreement with the reanalysis during austral summer than the rest of the simulations. This section shows that while precipitation may be well represented in a region, e.g., the North American monsoon, competing model biases in the strength of convection and moisture may lead to a right representation of precipitation.

4.6 ENSO Impacts

El Niño-Southern Oscillation (ENSO) teleconnections are the prominent source of interannual variability for the AMS (Vera et al., 2006), as summarized in section 2.4. The response to ENSO events in UKESM1 and HadGEM3 is investigated in this section, first by investigating the mean response to ENSO events and then by analysing possible sources of non-linear teleconnections.

4.6.1 Canonical impacts to the AMS

The surface temperature and sea-level pressure (SLP) responses to ENSO events are shown in Figure 4.11 for HadGEM3, UKESM1 and ERA5 data during DJF, the season of strongest impact of ENSO events. The characteristic warm anomaly during El Niño events in the East Pacific Ocean does not extend as far east in the simulations as in the HadSST dataset or ERA5. In turn, the cold anomalies during La Niña events in the Central Pacific are colder in the simulations than in ERA5. The impact to southern North America, i.e., colder (warmer) conditions in southern (northern) North America during El Niño events is relatively well simulated. For example, the simulated and observed impacts to South America, e.g., the cold anomalies during La Niña events in northern South America are well simulated. However, the low resolution simulations show a broader and stronger than observed negative response in southeastern US to El Niño events.

The SLP response in the north Pacific and North America, known as the Pacific North-American pattern (PNA), is linked with a displacement of the subtropical jet affecting the eastward propagation of wave activity that reaches the North Atlantic (e.g. Bayr et al.,

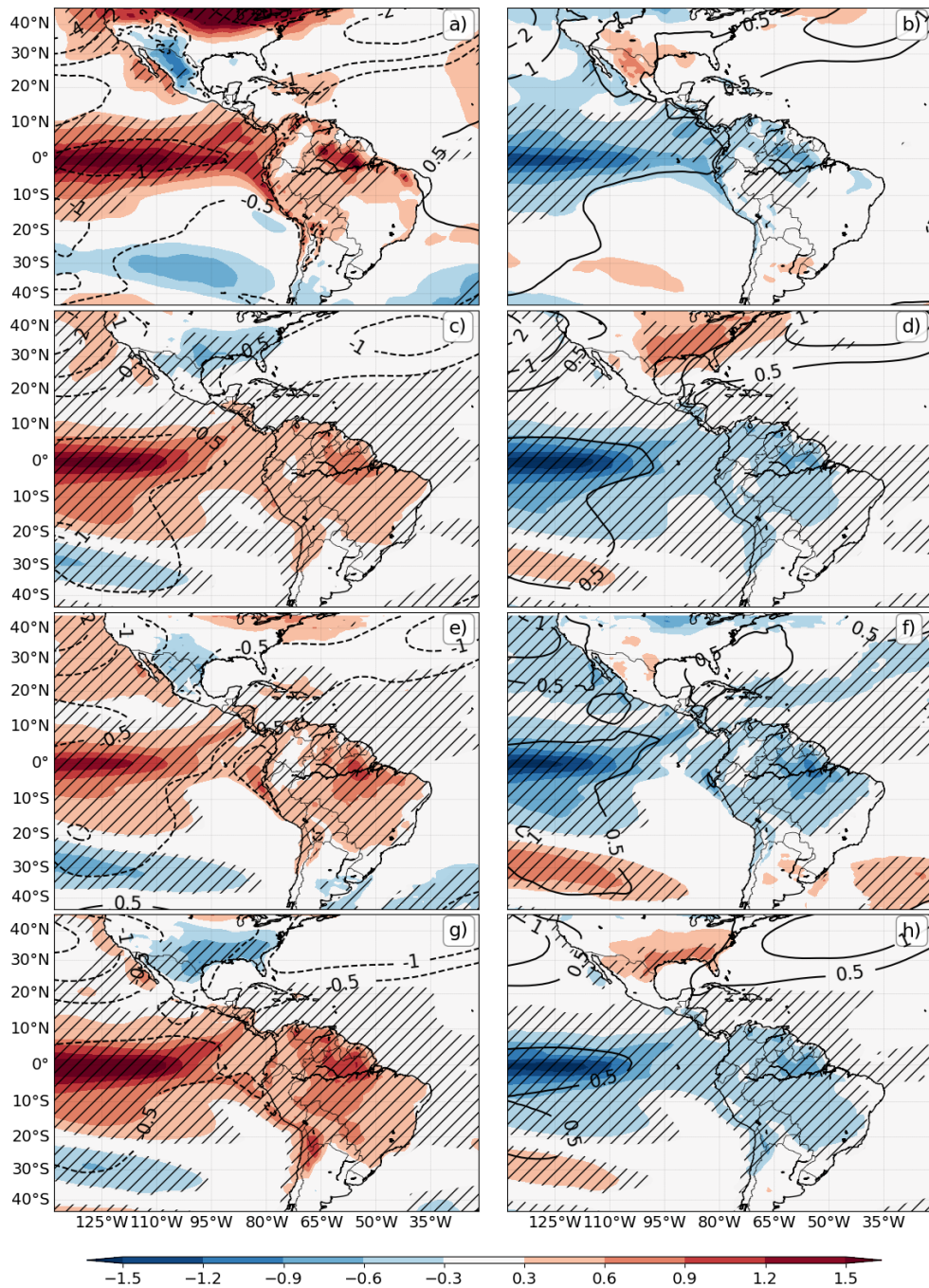


Figure 4.11: DJF Temperature anomalies (colour contours in K) and SLP (line contours in hPa) during (a, c, e, g) El Niño and (b, d, f, h) La Niña events. Results are shown for (a, b) ERA-5, (c, d) UKESM1-hist, (e, f) GC3 N96-pi and (g, h) GC3 N216-pi. The hatched regions denote differences between ENSO phases and the climatological state with significance to the 99% confidence level from a Welch t-test for the temperature field.

2019; Jiménez-Esteve and Domeisen, 2020). During El Niño events, the Aleutian Low is strengthened in ERA5, with a strong SLP anomaly (-4 hPa) off the coast of California.

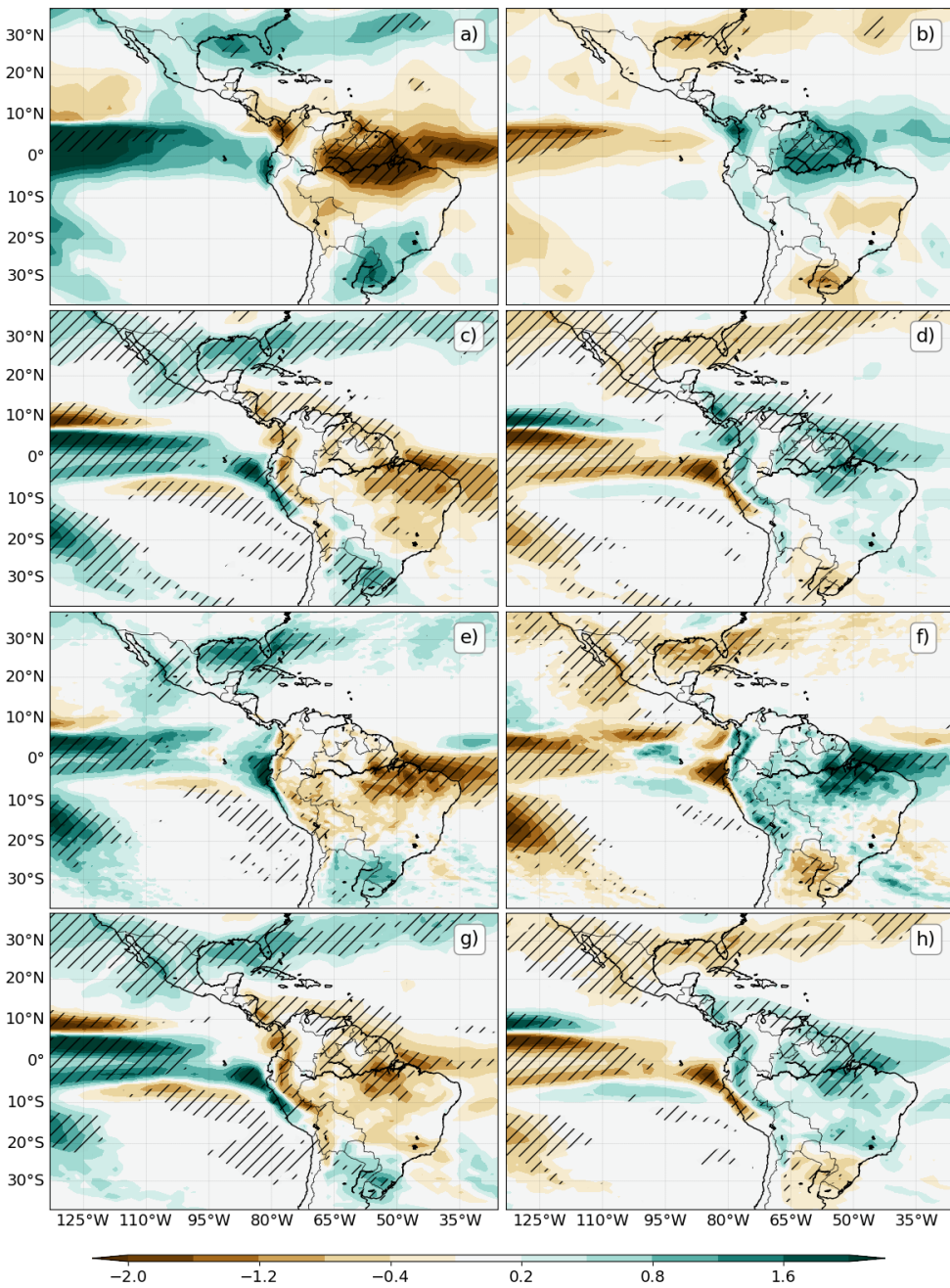


Figure 4.12: As in Figure 4.11 but for the rainfall response [mm day⁻¹] using GPCP as the observational dataset.

The models show a similar but smaller SLP response in the same region. El Niño events are associated with a negative phase of the North Atlantic Oscillation (NAO), with an opposite response for La Niña events (Fereday et al., 2020). While the models seem to be able to capture this response of the NAO, the simulated response is weaker than observed.

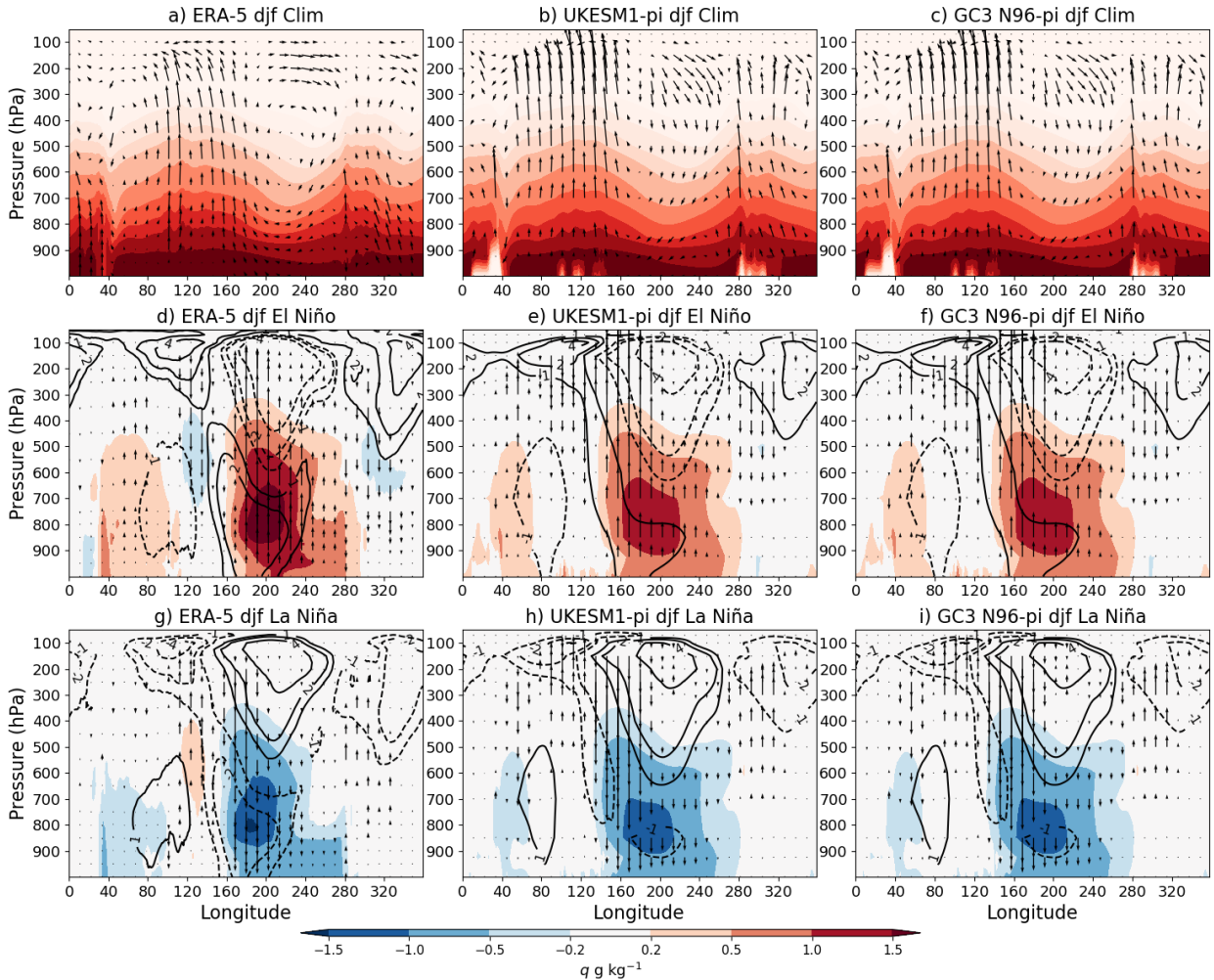


Figure 4.13: DJF Longitude-height Walker circulation (a-c) climatologies and (d-i) anomalies of specific humidity (colour-contours), ω (vectors) and zonal wind (line-contours) during (d-f) El Niño events and (g-i) La Niña events. Results are shown for ERA-5 (left), UKESM-pi (middle) and HadGEM3 N96-pi (right).

A sensible representation of the ENSO-PNA tropospheric teleconnection is important to fully simulate ENSO impacts to North America (Bayr et al., 2019) and northeast Brazil (Hastenrath, 2006; Taschetto et al., 2016).

The rainfall anomalies associated with ENSO events (Figure 4.12) show that three regions in the AMS have a significant precipitation response. In southern North America, rainfall increases (decreases) during El Niño (La Niña) events due to the effects of the PNA pattern on the subtropical jet, which influences the frequency and latitude of propagation of wintertime midlatitude disturbances which are the main source of rainfall in the region during the dry season (Vera et al., 2006; Bayr et al., 2019).

The GPCP dataset (Figure 4.12a, b) shows significant boreal winter rainfall increases in southeastern US and the Gulf of Mexico during El Niño events, and an opposite response to La Niña phases. All the simulations reproduce this impact pattern. The models also simulate the observed response in South-Eastern South America (SESA) of positive anomalies during El Niño and negative anomalies during La Niña events. This impact to SESA is due to the subsidence induced by the anomalous Walker circulation which modifies the moisture transport by the SALLJ from the Amazon to SESA (Montini et al., 2019).

The anomalies in the Amazon show the strongest response to ENSO events in the observations. Significant positive (negative) rainfall anomalies during the negative (positive) phase of ENSO in northern South America are observed in GPCP. All the simulations show a very similar and statistically significant response. This teleconnection is due to the coupling of ENSO with the Walker circulation (Vera et al., 2006; Cai et al., 2019), which is illustrated in Figure 4.13, and the effect of the ENSO-PNA teleconnection in the tropical north Atlantic.

The climatological Walker circulation during DJF shows strong ascent in the 100-160°E and the 280-310°E regions (Figure 4.13a), which correspond to the maritime continent and South America, respectively. During El Niño events, there is increased specific humidity throughout the lower troposphere in the Central and Eastern Pacific, associated with ascending motions in this region and negative low-level wind anomalies and positive upper-level wind anomalies (Figure 4.13d). In other words, an eastward shift of the Walker circulation. The wind, vertical velocity and specific humidity anomalies are the opposite during La Niña events, indicative of a stronger Walker circulation shifted west. The models seem to broadly reproduce the observed changes to the Walker circulation during ENSO events (Figure 4.13).

The anomalous descent over equatorial South America is one cause for the drying response seen during El Niño in the Amazon (Marengo et al., 2012; Cai et al., 2020). However, the ENSO-PNA teleconnection decreases in the tropical north Atlantic (Fig. 4.11), inducing a warming of the SSTs and a delay in the southward migration of the Atlantic ITCZ (Andreoli et al., 2012; Jimenez et al., 2021). Even though the models are able to simulate the ENSO-PNA SLP effect, this effect is slightly weaker than observed, particularly for El Niño events.

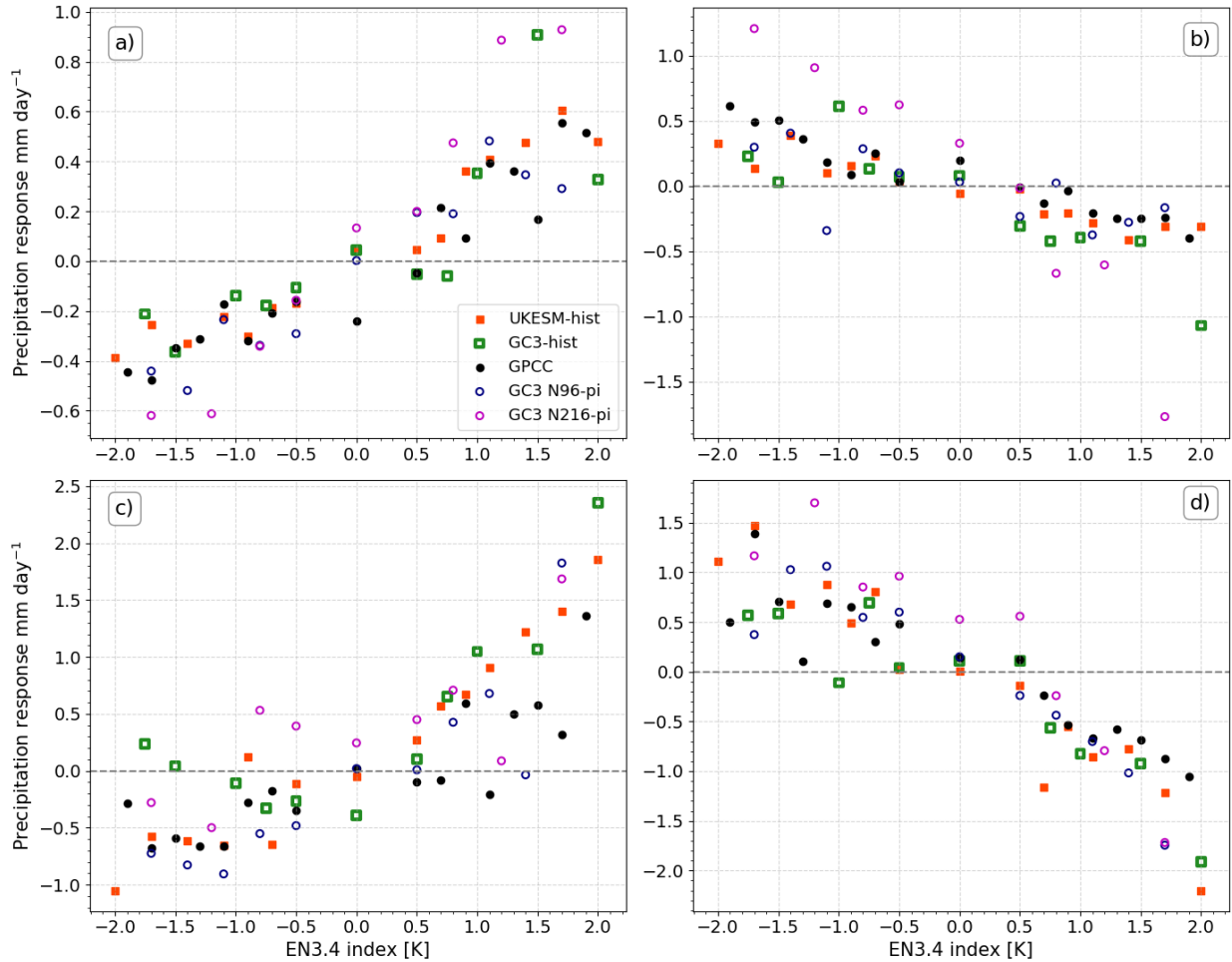


Figure 4.14: Precipitation response [mm day^{-1}] as a function of the El Niño 3.4 index (see text) for (a) southwestern North America [$20\text{--}37^\circ\text{N}, 112\text{--}98^\circ\text{W}$], (b) Central America and southern Mexico [$5\text{--}19^\circ\text{N}, 95\text{--}83^\circ\text{W}$], (c) Sout-Eastern South America [$35\text{--}25^\circ\text{S}, 60\text{--}50^\circ\text{W}$], and (d) the Amazon [$10\text{--}0^\circ\text{S}, 70\text{--}45^\circ\text{W}$]. The observation scatter points are from GPCC in the period of 1940–2013.

Figure 4.14 shows the observed and simulated precipitation responses in four regions of the AMS binned by the magnitude of ENSO events, measured by the EN3.4 index. This figure aims to show the degree of linearity of ENSO teleconnections to the AMS, i.e., a precipitation response that linearly scales with the magitude of the ENSO event. Both simulated and observed responses show degrees of non-linearity in various regions. For example, the precipitation response in the Amazon to La Niña events in observations appears to be relatively constant regardless of the strength of the event whereas in GC3 N96-pi the strongest La Niña events do not produce the strongest precipitation response over this region. This evidence suggests that for some regions there are varying degrees of

non-linearity of ENSO impacts.

4.6.2 The role of ENSO flavours

As described in section 2.4, not all ENSO events are observed with the same SST pattern in the Pacific Ocean. These different SST patterns are considered to be a source of non-linearity of ENSO impacts over South America (Sulca et al., 2018; Cai et al., 2020). Figure 4.15 shows that both UKESM1 and GC3 reasonably simulate the observed SST patterns associated with EP and CP El Niño events, although the CP SST patterns in the simulations spread further to the east than the HadSST dataset. The simulations are also able to replicate very

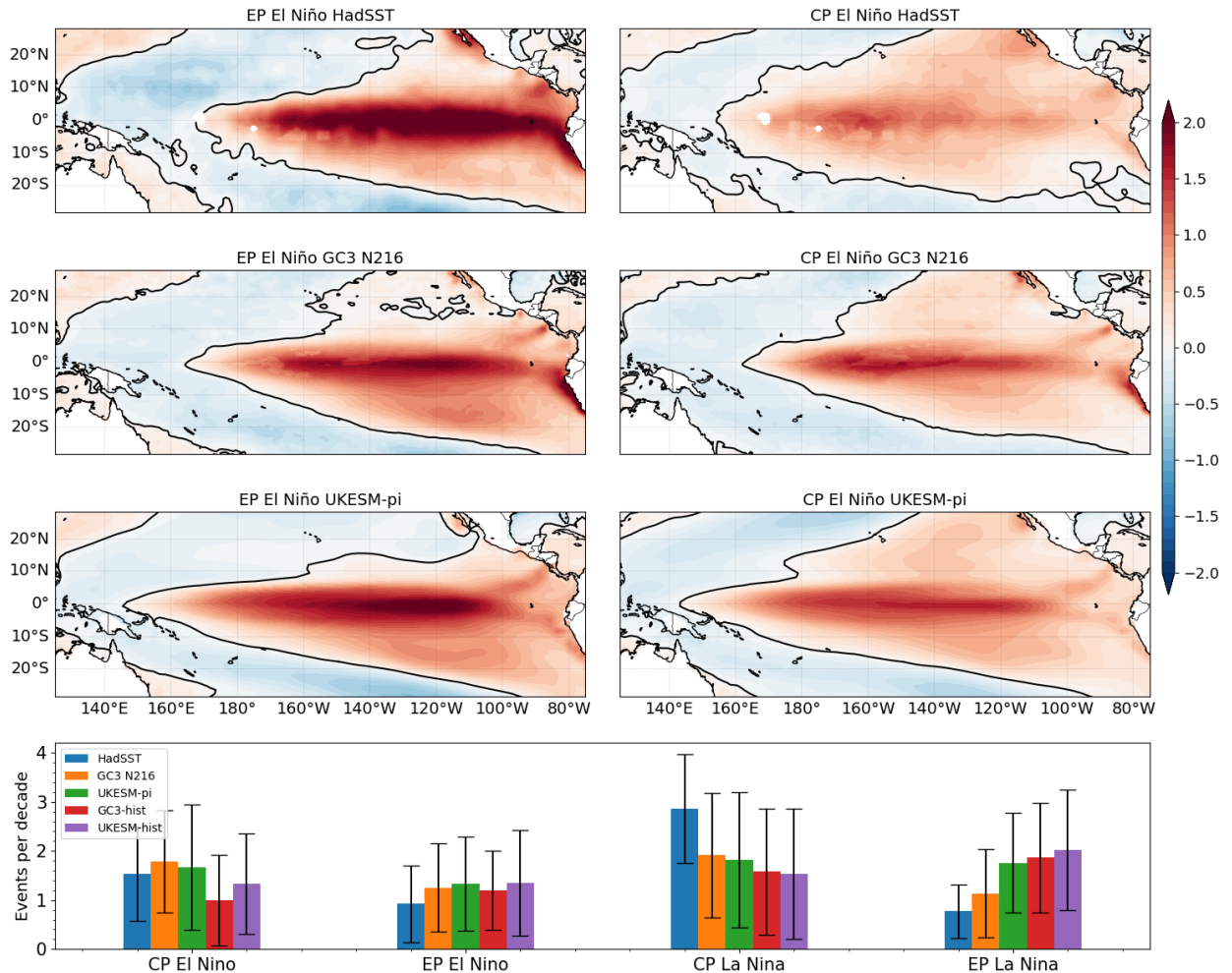


Figure 4.15: SST anomalies [K] for East Pacific (EP) and Central Pacific El Niño events in HadSST, GC3 N216 and UKESM piControl. In the bottom panel, the frequency of events per decade (with standard deviation as error bar) is shown for HadSST and the simulations used in this study.

broadly the observed differences in the frequency of each event as CP La Niña events are more frequent than EP La Niña events, while the opposite is true for El Niño events.

Furthermore, Figure 4.16 compares the precipitation anomalies for each type of ENSO event in observations with three simulations: GC3 N96-pi, GC3 N216-pi and GC3-amip. The observed precipitation response in the GPCC dataset to EP La Niña over equatorial South America is not significant and is smaller than the strong positive response to CP La Niña events in the same region. However, the simulated response in GC3 N96-pi and GC3 N216 during La Niña events appears to be more independent of the type of event. In contrast, the GC3-amip simulations shows different magnitudes of responses to different types of La Niña events, in particular a positive, and significant, anomaly for CP La Niña events in the Amazon and weaker but not significant anomalies during EP events, which agrees with observations.

The observed response to El Niño events in GPCC is also dependent on the type of event. EP EL Niño events show significant negative anomalies over the Amazon and positive anomalies over SESA whereas CP events only show significant anomalies (-1 mm day^{-1}) over northeastern South America. While the coupled models (GC3 N96-pi and GC3 N216) show a stronger response to EP EL Niño events than to CP events. In contrast, the response in GC3-amip agrees with observations, as stronger negative responses to EP El Niño events are observed in the Amazon compared to CP events in which the response is much weaker and is only significant in northeastern South America. In other words, GC3-amip agrees well with the observed non-linear impacts whereas the teleconnections in the coupled models do not seem to depend so strongly on the type of ENSO event.

4.6.3 A possible influence of the QBO on tropical ENSO teleconnections

Section 2.5 discusses the observational and modelling evidence that suggest a role for the stratospheric quasi-biennial oscillation (QBO) in modulating the determine interannual variability of the Walker circulation and monsoons (Giorgetta et al., 1999; Collimore et al., 2003; Liess and Geller, 2012). This section evaluates whether the simulations analysed in this chapter, as well as observations, show signs of an influence of the QBO on the AMS. In

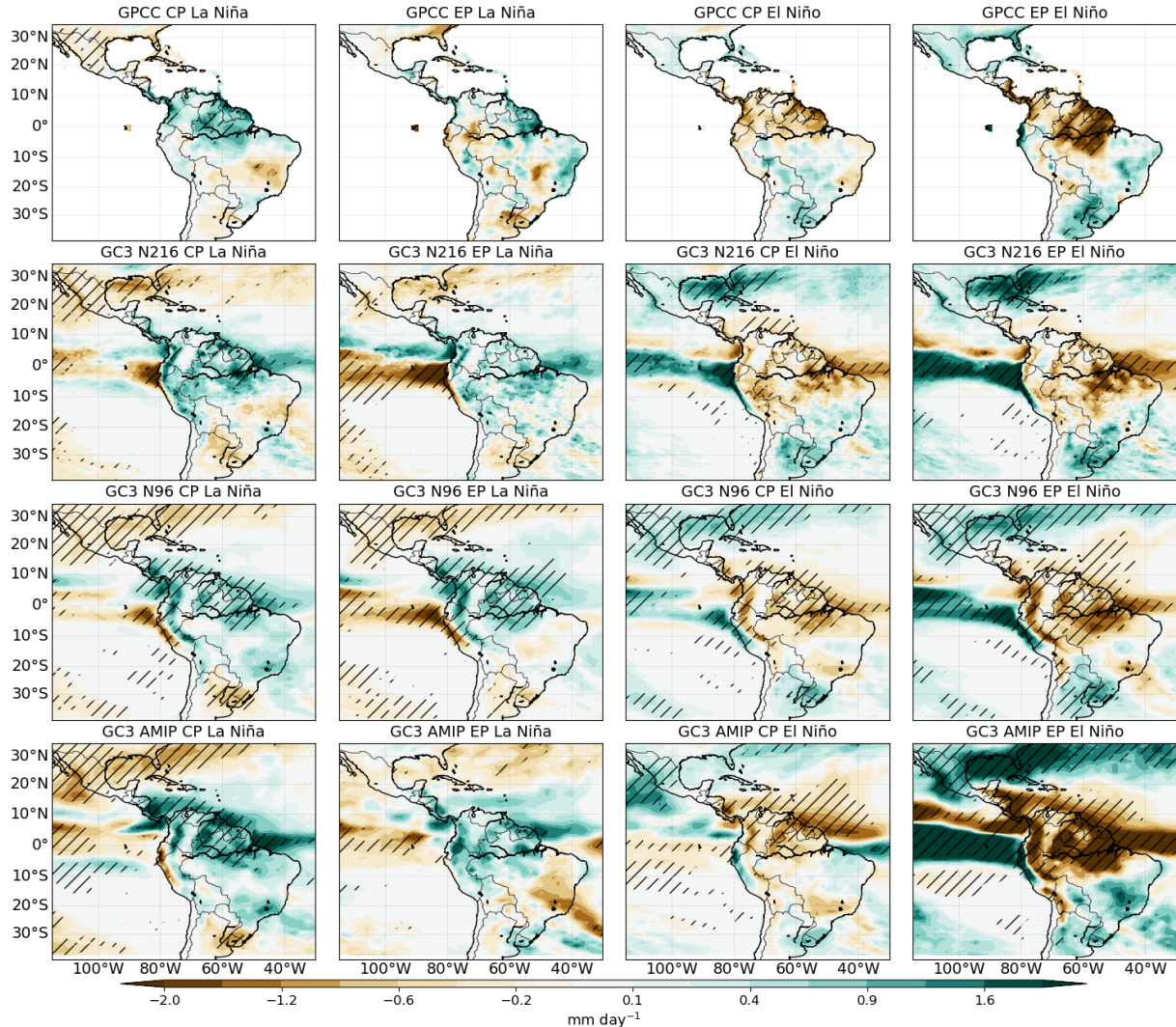


Figure 4.16: Precipitation anomalies in GPCC 1940-2013, GC3 N216-pi, GC3 N96-pi and GC3 AMIP for the four different types of ENSO events, as defined by Cai et al. (2020). Statistically significant anomalies (95% confidence level) are hatched.

particular, the analysis aims to understand whether the QBO may be a source of non-linearity for the teleconnections of ENSO associated with deep convection and the Walker circulation.

Composites of the precipitation response to La Niña (LN) events in Figure 4.17 show that the phase of the QBO may determine the strength and location of the impact. While the precipitation difference in the western Pacific is relatively similar during QBOe than during QBOw in observations and simulations, the teleconnections to Australia, South America and the maritime continent are notably different depending on the QBO phase. In the GPCP dataset, the composite difference QBOe-QBOw during LN events suggests

that the characteristic positive precipitation response during LN events in the Amazon, is largely associated with QBOw phases, whereas LN events during QBOe appear to have

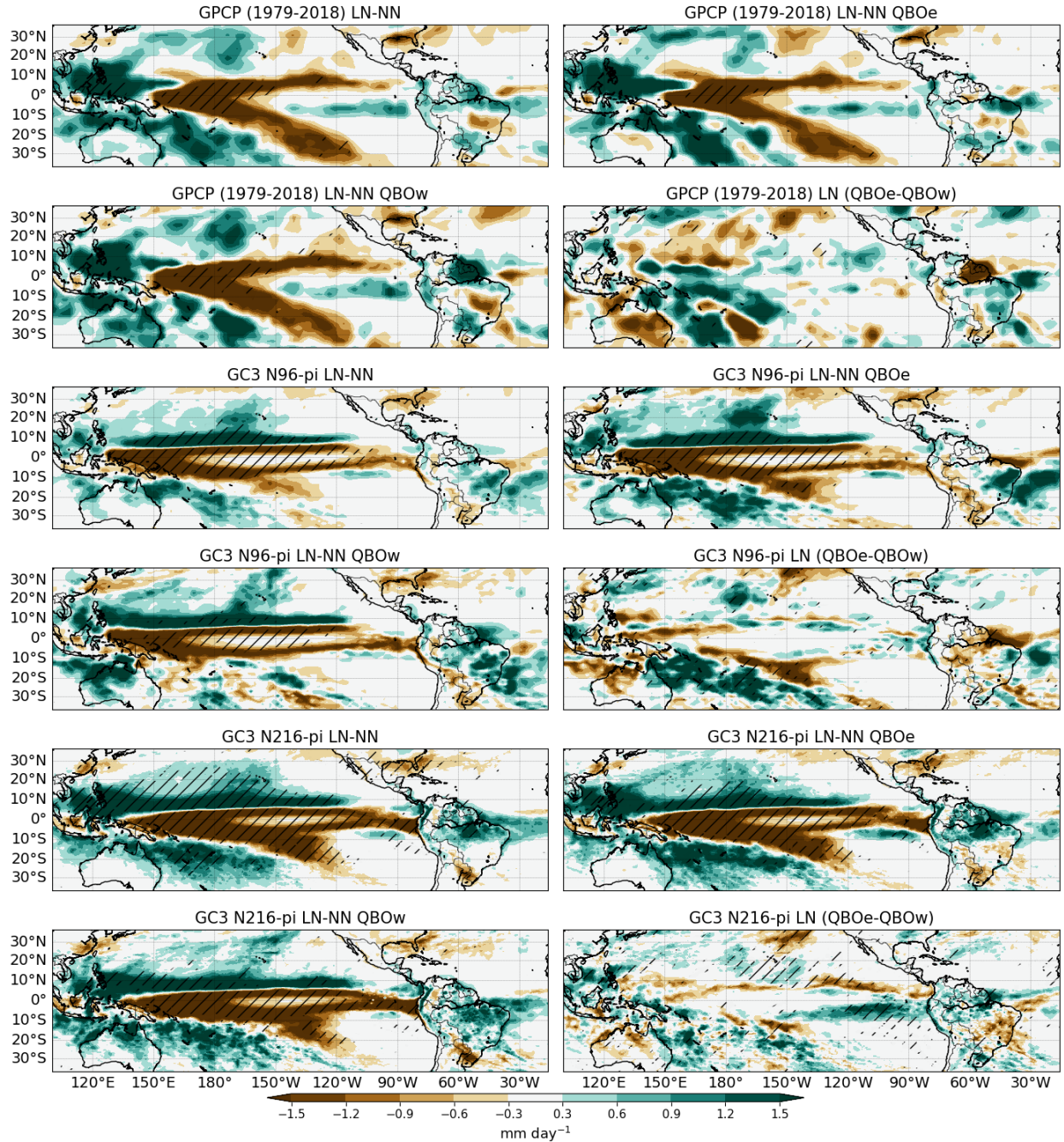


Figure 4.17: Composite precipitation differences during JFMA in GPCP (1979-2018), GC3 N216-pi and GC3 N96-pi between (top) La Niña and Neutral ENSO conditions. The two middle panels show a subset of the top panel, by separating the La Niña composite based on the phase of the QBO. The lower panel shows the differences QBO E-W during La Niña periods. Statistically significant anomalies (95% confidence level) are hatched.

little effect over South America. A similar result is obtained for GC3 N96-pi.

These precipitation responses are further investigated by changes in the overturning circulation (Figure 4.18). As depicted in Figure 4.13, La Niña events are associated with a westward shift in the Walker circulation with a strengthening of the low-level easterlies in the Pacific Ocean. Figure 4.18 shows that during LN the tropical troposphere cools and the UTLS region in the Central Pacific warms. The zonal wind anomalies in the upper-troposphere associated with LN events show different patterns and strengths during QBOw than during QBOe. The mean teleconnections during LN show positive zonal wind

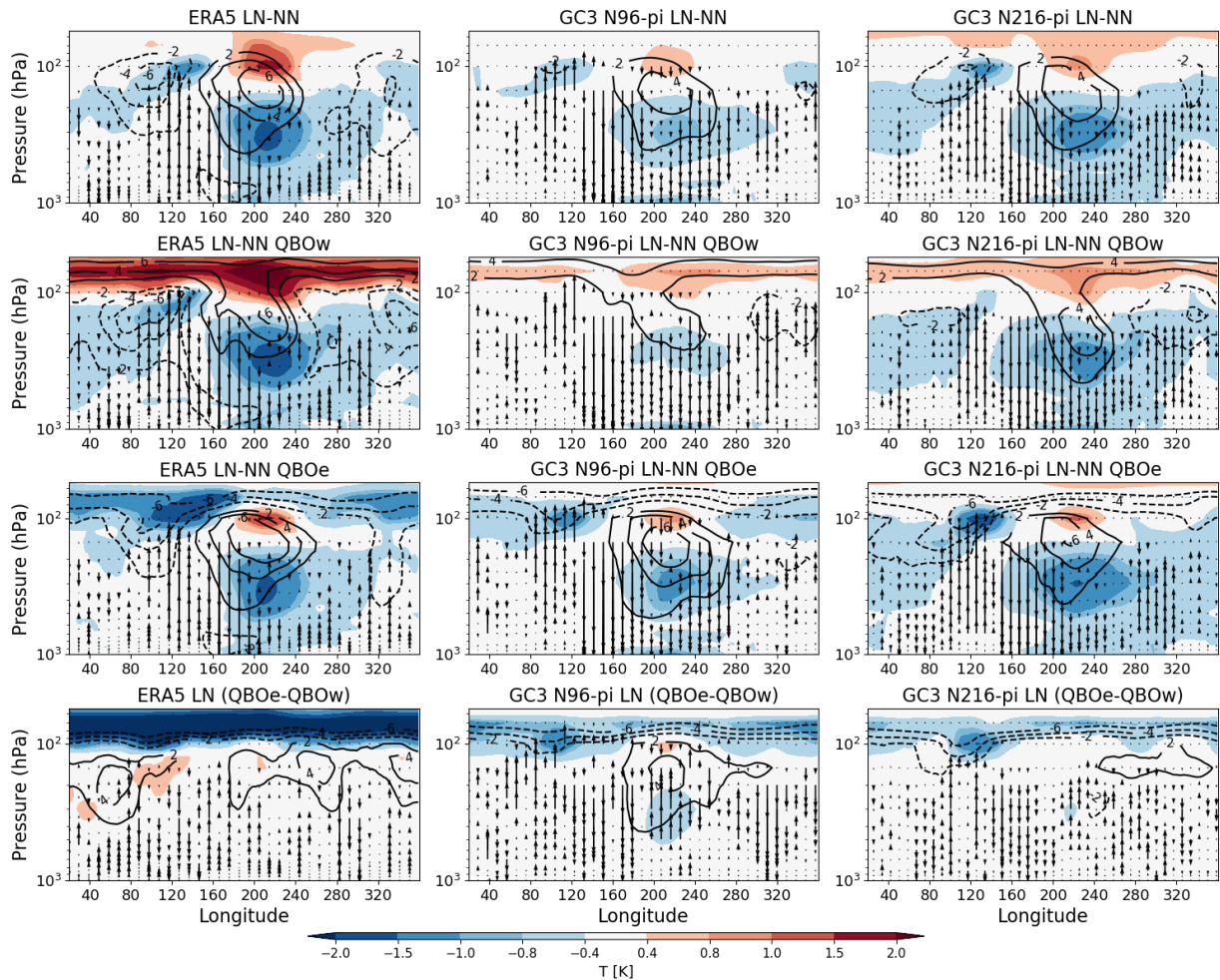


Figure 4.18: Longitude-height differences (JFMA) of equatorial (10S-10N) air temperature (color shading), zonal wind (contours) and vertical velocity (ω - vectors). The differences shown from top to bottom are between all La Niña (LN) periods and Neutral conditions (NN), between LN and NN during QBOw, LN-NN during QBOe, and the difference between LN events on different QBO phases (LN QBOe-QBOw).

anomalies in the upper troposphere of the Pacific Ocean, but these anomalies are stronger during QBOe than during QBOw in ERA5 and the two simulations shown. In ERA5, most of the upper troposphere shows positive zonal wind differences in the QBOe-QBOw panel.

The effect of LN over ascending and descending motions is also affected by the QBO phase (Fig. 4.18). In ERA5 and the simulations, the anomalous ascent observed in South America during LN events is mostly associated with QBOw, whereas only small anomalous ascent is observed during QBOe. However, ERA5 disagrees with the simulations in the western Pacific region (140-180°E), as the simulations suggest larger anomalous descent during QBOe than during QBOw, whereas in ERA5 these descending anomalies are larger during QBOw.

The effect of the QBO during the positive and the neutral phases of ENSO were also evaluated but these results are not shown because, although tentative suggestions were found that the QBO may play a role during these other phases of ENSO, there was little agreement between the models and ERA5/observations. Model biases in the representation of the QBO, specially the temperature signal associated with circulation of the QBO, most clearly seen in the bottom panels of Figure 4.18, in addition to short record of the reanalysis evidence (ERA5) or presented in this chapter warrants both caution and future work.

4.7 Summary and discussion

This chapter assessed the contributions to CMIP6 from the models HadGEM3 and UKESM1 for their representation of the AMS climate and associated large-scale tropical circulation. These CMIP6 experiments allow the comparison of the effect of including Earth System processes or increasing resolution for representing regional monsoon rainfall. A schematic in Figure 4.19 shows the primary components of the AMS climate and summarises the main biases found in these simulations and this chapter.

Rainfall in the North American Monsoon was particularly well simulated by the models. The seasonal cycle, peak monsoon rainfall rates and timings of monsoon onset and retreat in the simulations agreed well with TRMM. The historical experiments overestimate the mean temperature in most of the Americas by 1.5 K, but particularly in boreal summer in southwestern North America (+4 K). Despite this warm bias, the seasonal cycles of

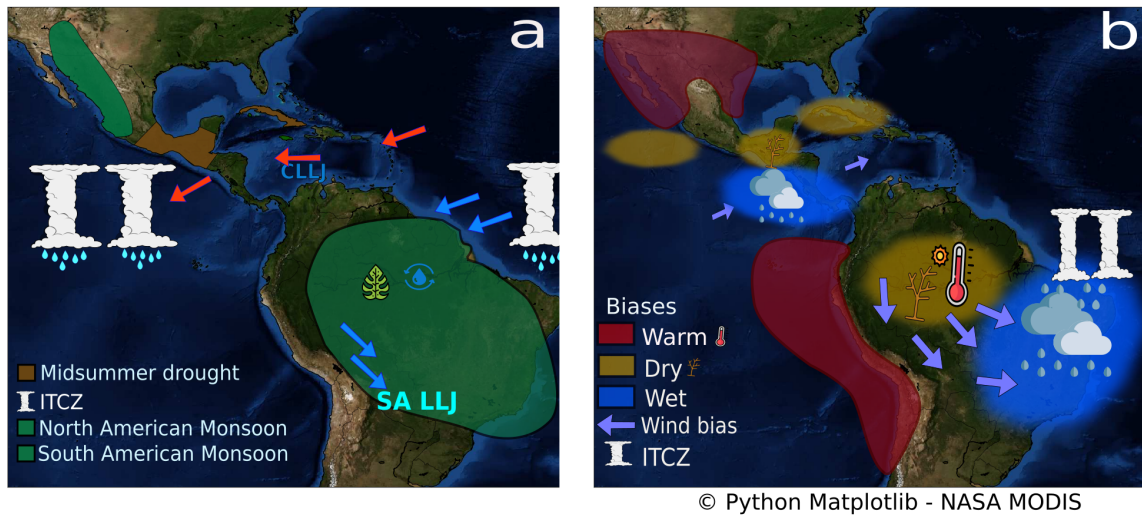


Figure 4.19: Schematics of (a) the main features in the AMS and (b) the main biases in UKESM1 and HadGEM3. In (a) the boreal summer easterlies (red) and austral summer circulation (blue) are shown with the Caribbean and South American Bolivian Low-level Jets (CLLJ and SALLJ, respectively). In (b) the biases are shown for the respective northern and southern Hemisphere summers. The ITCZ bias in (b) refers to the southward displacement bias of the Atlantic ITCZ in the simulations.

precipitation and surface temperature are well represented by these models. These results suggest model improvement of the simulation of the North American Monsoon from previous versions of the MOHC models (Arritt et al., 2000), and most of the model cohorts of CMIP3 and CMIP5 (Geil et al., 2013). However, these models continue to show biases during monsoon retreat as rainfall does not decrease as sharply as in observations after mid-September, which suggests a continued bias in the winter-time precipitation associated with cold-fronts (Adams and Comrie, 1997).

The Midsummer Drought (MSD) of southern Mexico and Central America is a regional feature of precipitation that most CMIP5 models do not capture (Ryu and Hayhoe, 2014). The MSD in UKESM1 and HadGEM3 is relatively well represented. However, the experiments analysed in this chapter simulate a wetter-than-observed first peak of precipitation and a drier MSD period, therefore simulating a larger difference between the first peak and the dry period. Rainfall during the first peak has been too wet in these models since CMIP3, suggesting a persistent wet bias in this region, likely associated with the bias in East Pacific ITCZ also shown in this chapter and in recent studies (Ryu and Hayhoe, 2014;

Mulcahy et al., 2018). In contrast, the so-called second peak of precipitation, observed in late August, is simulated in close agreement with TRMM, except in the GC3 AMIP experiment, which has a wet bias of 2 mm day^{-1} at this stage. The relative skill of UKESM1 and HadGEM to simulate this bimodal regime of precipitation makes these simulations ideal to understand the mechanisms underpinning the MSD, an outstanding question (see Section 2.3).

The East Pacific ITCZ migration and position is relatively well represented by the models (Figs. 4.4 and 4.5). However, the models overestimate the boreal summer rainfall near the coast of Central America (Figure 4.9). These biases are associated with an easterly wind bias at low levels, suggesting a bias in the flow from the Caribbean Sea into the Eastern Pacific. The simulations also show that the position of the Atlantic ITCZ is biased south of the observed ITCZ during boreal winter (Figure 4.5), particularly in the low-resolution coupled configuration.

The dry Amazon bias persists in these CMIP6 experiments. The simulations show a warm bias (+2 K) during austral spring and summer in the Amazon, a bias that exists since CMIP5 (Jones and Carvalho, 2013), and a colder than observed southeastern Brazil. These biases were linked with decreased cloud cover and less rainfall over the Amazon and more convective clouds and rainfall in southeastern Brazil (Figures 4.8 and 4.10). The low cloud cover, warm and dry Amazon biases are intertwined with the low-level circulation from the Atlantic into the South American continent. The biases in the circulation during austral summer were observed as a northerly flow anomaly over the central and southern Amazon, a feature that has been associated with a stronger moisture transport away from the Amazon (Marengo et al., 2012; Jones and Carvalho, 2018).

During the period of maximum rainfall rates in February, the simulations overestimate rainfall by 3 mm day^{-1} in southeastern Brazil and underestimate rainfall in the Amazon by a similar rate. The historical experiments show a small drying response to historical forcing in the Amazon but this response is much smaller than the magnitude of the biases, increasing the uncertainty in the response. The AMIP simulation improved the representation of the Atlantic ITCZ and the precipitation, cloud cover and temperature biases over the South American Monsoon. The improvement in the circulation and precipitation biases in the AMIP simulation suggest that the origin of the dry Amazon bias are the biases in the Atlantic SSTs.

The canonical ENSO teleconnections of temperature, SLP and precipitation in the AMS are well represented in these models. The simulated spatial patterns and strength of the positive (negative) precipitation anomalies observed in northern Mexico and South-Eastern South America during El Niño (La Niña) agree well with observations and reanalysis. Similarly, the teleconnection to the Amazon is well represented for both phases of ENSO, despite the biases in the mean state of the South American monsoon discussed above.

ENSO teleconnections in these simulations were found to be approximately linear, i.e., the precipitation response is linearly related to the magnitude of the SST anomaly in the EN3.4 region. These experiments also show symmetric teleconnections as positive and negative phases produce the opposite and equivalent precipitation response in the AMS. In contrast to observations and the GC3 AMIP simulation, the precipitation response in the coupled models appears to be independent of the type or flavour of ENSO events, i.e., between Central and East Pacific events. The fact that these models show a reasonable representation of ENSO diversity in SST patterns but the models do not replicate the observed non-linear dependence to ENSO events warrants further analysis.

The QBO appears to be a source of non-linearity for ENSO teleconnections to the Amazon. La Niña teleconnections in the Amazon are characterized by a stronger ascent associated with a stronger Walker circulation. The La Niña teleconnection pattern occurs primarily during the westerly phase of the QBO, whereas the teleconnection during the easterly phase is much weaker and barely different from the climatological mean-state. Whether the stratospheric QBO modulates the main source of interannual variability (ENSO events) for monsoon rainfall in the Amazon merits a separate chapter of this thesis (Chapter 7).

The main biases (Fig. 4.19) in these experiments are generally smaller in the medium-resolution GC3 N216 compared to the low-resolution experiments (N96), which suggests improved model performance with increased horizontal resolution. In contrast, including Earth System processes in the UM model only affects the surface temperature response to historical forcing and not the dynamical biases that drive the precipitation and ITCZ biases. In general, UKESM1-hist shows a stronger temperature response to forcing than GC3 N96-hist, as UKESM1 has been reported to have a greater climate sensitivity than GC3 N96 (Andrews et al., 2019a; Sellar et al., 2019).

The improvement in the medium-resolution simulation compared to the low-resolution simulations may be attributed to the improved dynamics of the ocean and the atmosphere. For example, the Atlantic ITCZ biases have been shown to be directly affected by processes in the convective scheme (Bellucci et al., 2010), such as the treatment of entrainment and moisture-cloud feedbacks (Oueslati and Bellon, 2013; Li and Xie, 2014). The resolution of the ocean model has been shown to impact the eddy heat flux parametrisation and the associated heat uptake and transport of the ocean (Kuhlbrodt et al., 2018). The improvement in the Atlantic SSTs and ITCZ and the associated dynamics in GC3 N216-pi also improves the associated circulation biases and moisture transport in the South American Monsoon. In other words, the oceanic resolution may play an important role in the cross-equatorial heat and moisture transport which largely control the SST gradients over the equatorial Atlantic. The SST biases in the Atlantic are likely the dominant factor to accurately simulate the spatial distribution of rainfall in South America.

5

A wavelet transform method to determine monsoon onset and retreat

This chapter describes a new method to determine monsoon onset and retreat timings using wavelet transform methodology applied to precipitation time-series at the pentad scale. The use of the method is illustrated for the North American Monsoon and the Indian Monsoon using four different precipitation datasets and climate model output. An extension of the method is used to identify the timings and strength of the Midsummer Drought of southern Mexico, Central America and the Caribbean. This chapter is based on the publication: García-Franco et al. (2021) in which all the analysis was performed by the lead author.

5.1 Introduction

The timing and strength of the rainy season are key aspects of the climate of monsoon regions as the onset or start and the retreat or end of the monsoon rainfall greatly influences sectors such as agriculture (Sultan et al., 2005; Gadgil and Rupa Kumar, 2006; Jain et al., 2015; Harvey et al., 2018) and water management (Turner and Annamalai, 2012; Bussmann et al., 2016). Scientific and societal motivation has led climate and weather research to objectively determine onset and retreat dates for purposes such as the characterisation of variability

and trends, and forecasting (e.g. Kitoh and Uchiyama, 2006; Cook and Buckley, 2009; Lucas-Picher et al., 2011; Nieto-Ferreira and Rickenbach, 2011; Htway and Matsumoto, 2011).

For this reason, a wide range of methods exist to diagnose the onset and retreat dates from a number of variables and datasets. Bombardi et al. (2020) provide a recent review of these methods and highlight the technical differences and purposes of each. Methods can be divided into those that evaluate monsoon onset and retreat on a regional scale (e.g. Webster and Yang, 1992; Fasullo and Webster, 2003; Garcia and Kayano, 2013) or at a local or grid-box scale (e.g. Liebmann and Marengo, 2001; Cook and Buckley, 2009).

Threshold methods are the most commonly used local-scale methods that typically diagnose onset and retreat from a precipitation time-series (Bombardi et al., 2020). These methods evaluate the accumulated (Liebmann and Marengo, 2001) or daily/pentad-mean rainfall rates (Geil et al., 2013) and determine the onset and retreat dates when the time-series exceeds or falls below a pre-defined value (threshold) for a given amount of time (persistence). The persistence parameter aims to decrease the effect of the noise of precipitation time series in the calculation. The threshold parameter can be a statistical measure of the seasonal cycle such as the total annual mean rainfall (Arias et al., 2012) or tuned to a specific dataset (e.g. Geil et al., 2013).

In other words, for a given purpose each threshold method is tailored to a monsoon region using a specific dataset and a specific variable. This characteristic of the threshold methods poses various shortcomings. Firstly, practical shortcomings of the threshold methods, particularly rigid thresholds, include false hits (Moron and Robertson, 2014) or some years not meeting the threshold and persistence criteria (Arias et al., 2012) requiring further relaxation of the parameters. Secondly, given that threshold methods are tailored to a specific dataset in a given region, statistical corrections are needed to implement the same threshold method in a different dataset or in another region.

CMIP assessments of monsoon onset and retreat typically use precipitation threshold methods due to the lack of data with high temporal or vertical resolution from all models to estimate vertically integrated quantities required for some methods (e.g. Geil et al., 2013; Zou and Zhou, 2015; Ha et al., 2020). Threshold methods have multiple shortcomings for CMIP assessments as the persistence and threshold parameters are tuned for observations

with a specific seasonal cycle but models have a range of biases in the seasonality, magnitude and spatial distribution of rainfall (Pascale et al., 2019; García-Franco et al., 2020). The use of pre-defined threshold values may also not be suitable to compare different model experiments with changes in forcing where the climatological mean rainfall or the seasonal cycle may change within the model run. These shortcomings are relevant because a proper diagnosis of the seasonal cycle in CMIP assessments is key to understand and diagnose current and future changes to monsoon seasonality as a result of greenhouse forcing (Zhou et al., 2016; Wang et al., 2017).

The objective diagnosis of shorter time-scale rainfall variability, such as bimodal regimes and active and break phases of a monsoon, also requires methods that can separate relatively drier and wetter periods within the rainy season. For example, for the MSD of Central America and the Caribbean (section 2.3) the objective determination of the strength, spatial distribution and robustness of the bimodal signals is not straightforward. For example, the global method used in Bombardi et al. (2020) fails to diagnose the region of southern Mexico, Central America and the Caribbean as a bi-modal regime.

The majority of existing methods to diagnose bimodal signals in the MSD region use geometric or statistical measures of the monthly-mean rainfall that measure the difference between the months of maximum rainfall and the drier months. However, this approach fails to capture the shorter-scale changes that have been shown to occur in both observations and model data, as the MSD does not start or end exactly on given calendar months (Magaña et al., 1999; García-Franco et al., 2020). Zhao and Zhang (2021) review and compare several methods to detect and measure the MSD, finding that using monthly-mean data and prior assumptions of the dates of the first and second peaks can lead to errors.

In short, multiple methods exist to diagnose monsoon onset and retreat as well as bimodal signals, each with various parameters fit for different purposes, but these methods present shortcomings for studies that compare results from multiple datasets or investigate model experiments where the climatological rainfall and the seasonal cycle are non-stationary. Both the objective determination of monsoon onset and retreat and the timings of bimodal regimes require a method that can analyse temporal changes to precipitation on several scales and that can be used on any gridded dataset.

The purpose of this chapter is then to present an objective approach that is more portable across datasets, regions, less prone to false hits and robust for various purposes. This chapter introduces a wavelet transform method to determine monsoon onset and retreat dates using pentad-mean precipitation time series. Wavelet algorithms have been extensively used in atmospheric research for multiple purposes, such as the detection of the boundary layer height (e.g. Brooks, 2003), as well as to analyse time-frequency features of a signal (e.g. Whitcher et al., 2000; Dimdore-Miles et al., 2021). In fact, Allen and Mapes (2017) used wavelet analysis to determine monsoon onset and retreat using daily OLR data.

The remainder of this chapter is organised as follows: section 2 describes the methods and datasets. Section 3 shows the results of applying the method to the Indian and North American Monsoons and the MSD. [The method is illustrated in the North American Monsoon to compare the proposed method to threshold methods of precipitation, and for the Indian Monsoon region to compare the method to a well known index of the regional moisture transport, which is a more physically-based method.](#) In this way, we test the wavelet transform method against existing methods of multiple [Section 4 summarises the method and discusses the results.](#)

5.2 Data

5.2.1 Precipitation datasets and reanalysis data

This chapter uses three gridded precipitation datasets described in chapter 3: the TRMM v7 3B42, the CHIRPS, and the CMAP datasets. These three precipitation datasets are merged products, TRMM and CMAP mainly use microwave satellite measurements complemented by several other sensors and calibrated with rain-gauge data whereas CHIRPS uses several products from TRMM, as well as high-resolution station data. These datasets also differ in their end-product horizontal resolutions.

The precipitation output from the latest ECMWF reanalysis, ERA5, is used, which has been shown to exhibit a relatively good representation of the temporal characteristics of rainfall in the AMS in chapter 4. Other variables from ERA5 used to diagnose changes

to the circulation associated with monsoon onset were daily-mean geopotential height at 500 hPa and wind speed (\vec{u}) at several vertical levels.

5.2.2 Model data

Daily precipitation data from the CMIP6 archive are used and retrieved from: <https://esgf-index1.ceda.ac.uk/projects/cmip6-ceda/>, to illustrate the method using standard climate model output. In particular, we use results from the piControl and historical simulations of HadGEM3 GC3.1 and UKESM1, described in chapter 3. The daily precipitation data were converted to pentad-scales.

5.3 The wavelet transform method

Wavelets are band-limited wave-like functions with specific mathematical properties that include finite energy and zero-mean (Whitcher et al., 2000; Addison, 2017). The wavelet function is defined using two parameters, a dilation (a width or temporal scale) and a translation (centroid in time/space).

Wavelet transforms are the result of the inner product (convolution) of a wavelet function with a time series or a signal (Addison, 2017). The wavelet transform (WT) can be thought of as a local comparison between the wavelet function and the observed signal for different frequencies. The information provided by a WT largely depends on the characteristics of the wavelet function, such that different wavelet functions are used for different purposes (Addison, 2017). For the purpose of finding the onset and retreat dates, the wavelet-based on the Haar function is useful as this wavelet finds sudden changes in a signal, acting as a time filter of the data (Addison, 2017; Brooks, 2003). The Haar wavelet is defined as the non-continuous piece-wise function:

$$\psi\left(\frac{t-b}{a}\right) = \begin{cases} 1 & b \leq t < b + \frac{a}{2} \\ -1 & b - \frac{a}{2} \leq t < b \\ 0 & elsewhere, \end{cases} \quad (5.1)$$

where a is the dilation coefficient, b is the centre of the wavelet or the translation coefficient and t is the time coordinate.

The wavelet covariant transform is then the inner product of the Haar wavelet with a timeseries (Brooks, 2003), as follows:

$$W_f(a, b) = \frac{1}{a} \int_{t_i}^{t_f} pr(t) \psi\left(\frac{t-b}{a}\right) dt, \quad (5.2)$$

where $pr(t)$ is a time series of precipitation, either on daily or pentad scales and $W_f(a, b)$ is the matrix of the covariant transform and t_i and t_f are the start and end time-points. No statistical treatment, normalization or anomaly, *a priori*, is calculated on the precipitation time series $pr(t)$ so the units of W_f are the same as the precipitation time series (e.g. mm d⁻¹).

Monsoon timings can be observed as sharp changes to precipitation, i.e., rainfall sharply increases at onset and sharply decreases at retreat. However, measuring these changes can be difficult since precipitation time series are typically noisy. The Haar wavelet is useful in these cases for signal detection since the WT is interpreted as gradients across different temporal scales and can smooth out the high-frequency variability using sufficiently large dilation scales. In other words, the wavelet covariant transform ($W_f(a, b)$) filters the time series $pr(t)$ using a temporal scaling of a , or measures gradients on a scale a for each time-step (b).

Figure 5.1 shows the Haar wavelet and one year of observed precipitation in the North American Monsoon from the CMAP dataset. Figure 5.1a illustrates how the wavelet function compares the observed signal in the interval $b \leq t < b + \frac{a}{2}$ with the values of the signal in the interval $b - \frac{a}{2} \leq t < b$ where b in this case is a pentad time step. The WT coefficient for dilation $a = 20$ pentads at the translation of $b = 35$, i.e., pentad 35, is a measure of the precipitation difference between the sum of the observed rainfall 10 pentads after pentad 35 and the sum of the observed rainfall 10 pentads before pentad 35 as illustrated in Figure 5.1b.

Figure 5.2 shows an example of the WT application using the observed climatological precipitation in the North American Monsoon in four different precipitation datasets. The mean climatological rainfall rates (upper panel) differ in their peak summer rainfall rates but qualitatively show similarities in the start and end dates of the rainy season. The WT coefficients ($W_f(a, b)$ in the middle panel) for a small dilation $a = 4$ are relatively noisy but show a clear maximum and minimum that correspond well with the maximum and minimum of longer dilations ($a = 14, 20$). The sum of these four coefficients at each

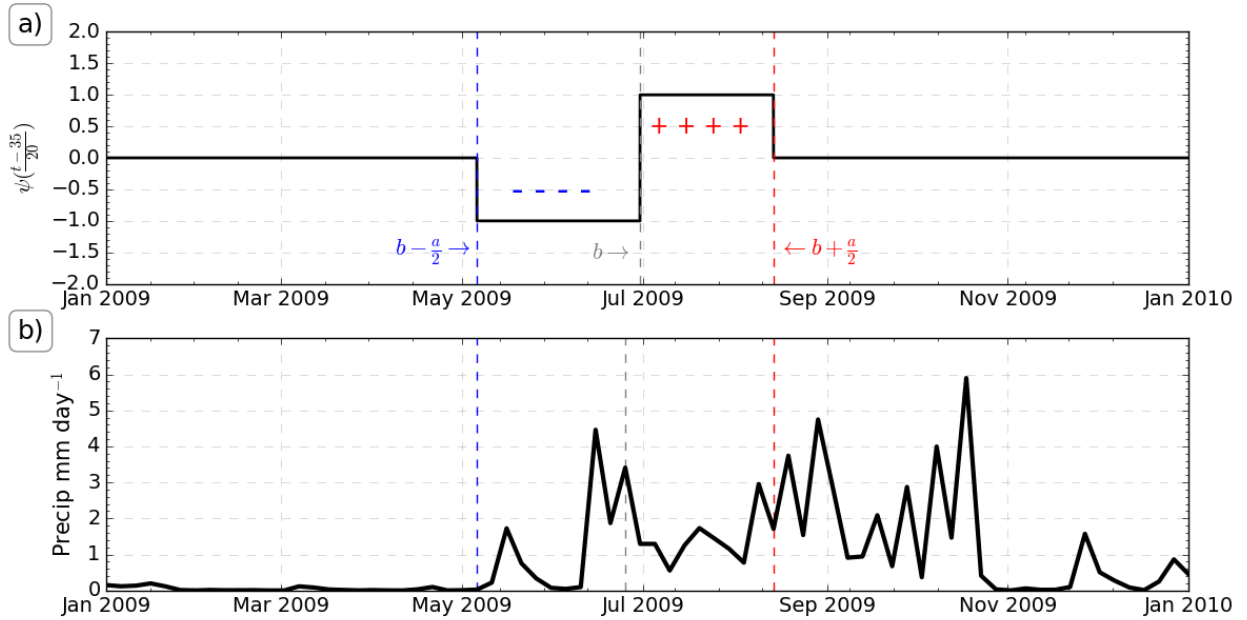


Figure 5.1: (a) Haar wavelet at a dilation $a = 20$ and translation $b = 35$, which is the 35th pentad around June 22. The positive and negative parts of the wavelet are highlighted in red and blue, respectively. (b) CMAP precipitation in 2009 in the North American Monsoon [20-27°N, 110-103°W].

translation or pentad b , highlight a maximum found around June 22 and a minimum found around September 21, which agree well with previous results of mean onset and retreat dates in the North American Monsoon (e.g. Arias et al., 2012; Geil et al., 2013).

5.3.1 Identification of Monsoon Onset and Retreat

Local maxima in the WT highlight positive steps in the precipitation time series with a coherent scale of a pentad steps. This interpretation is then extended to diagnose monsoon onset. The pentad (b^*) corresponding to the maximum of the sum of the transform over a set of scales is defined as monsoon onset (MO), i.e.:

$$MO = b^* \Leftrightarrow \sum_{a_0}^{a_f} W_f(a, b^*) = \max \left(\sum_{a_0}^{a_f} W_f(a, b) \right). \quad (5.3)$$

where a_0 and a_f are the limits of the pentad scales, i.e., the dilation coefficients, b^* is the pentad of maximum $\sum W_f(a, b)$ and the monsoon onset pentad. Similarly, the monsoon retreat pentad is found at the minimum of the sum of the WTs, i.e.,

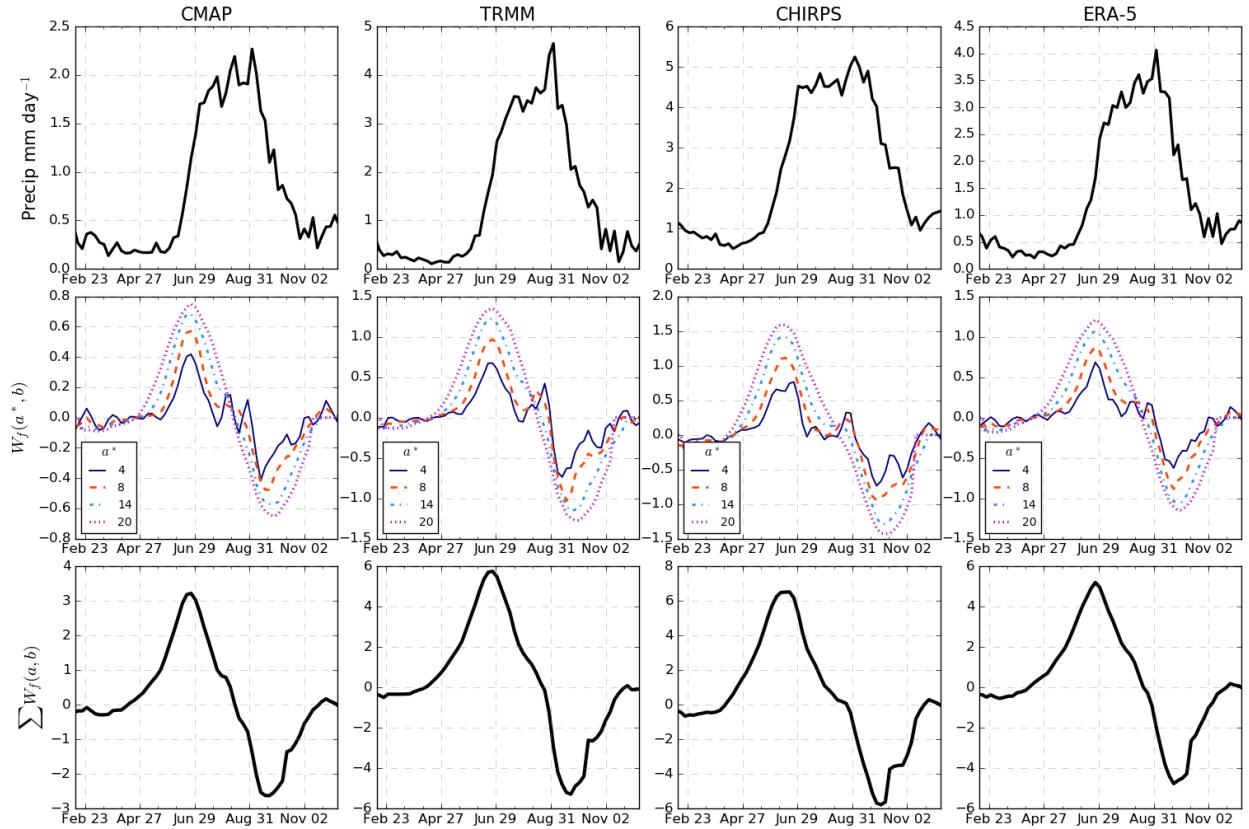


Figure 5.2: (upper) Climatological pentad-mean precipitation in four different observational datasets in the North American Monsoon [19–35°N, 110–103°W]. (middle) The wavelet transform coefficients (mm d^{-1}) for four different dilations a . (lower) The sum of the WT coefficients (mm d^{-1}) over dilations $a = 4, 8, 14, 20$.

$$MR = b^* \Leftrightarrow \sum_{a_0}^{a_f} W_f(a, b^*) = \min \left(\sum_{a_0}^{a_f} W_f(a, b) \right). \quad (5.4)$$

In other words, we seek to find monsoon onset and retreat using the maximum and minimum the wavelet power spectrum over a range of temporal scales. Several sensitivity tests were performed with different dilation coefficients (a) in the different observational datasets, models and regions and a set or vector of dilation scales was found to be optimal. The set of dilation coefficients $\vec{a} = (28, 30, \dots, 54)$ was found to be robust, i.e., was able to capture the onset and retreat dates in all the datasets.

Monsoon onset is defined as the maximum sum of wavelet coefficients, capturing positive gradients within the scales of 14 to 27 pentads (half of the elements of vector a defined above). Monsoon Retreat has a similar definition, capturing the greatest negative gradient

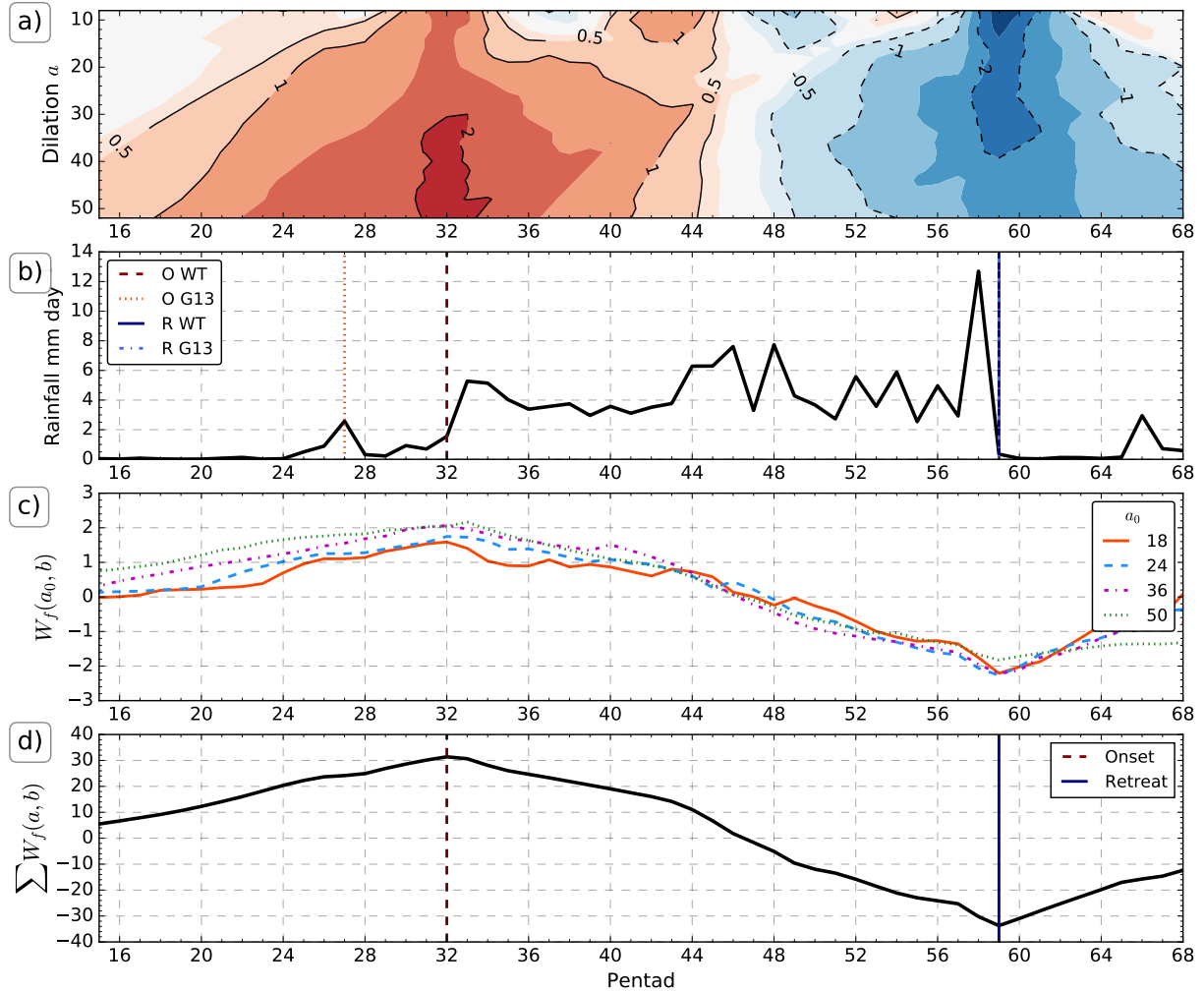


Figure 5.3: Example determination of monsoon onset and retreat dates for the North American Monsoon [20-27°N, 109-103°W] in the TRMM dataset for 2009. (a) WT coefficient matrix ($\text{mm } d^{-1}$) as a function of time and dilation coefficient a . The shading is from -3 to 3 $\text{mm } d^{-1}$ with an interval of 0.5 $\text{mm } d^{-1}$. (b) Observed precipitation, the onset and retreat dates as determined by the WT method (dashed) and the threshold method of Geil et al. (2013) (solid) are shown. Note that the date of retreat is diagnosed to be the same between the two methods. (c) The WT coefficients for different dilations. (d) The sum of the WT ($\sum W_f(a, b)$) ($\text{mm } d^{-1}$); the maximum and minimum are shown in red and blue, representing onset and retreat pentads, respectively.

of precipitation over the same pentad scales.

For example, Figure 5.3 illustrates the method in the North American Monsoon in the TRMM dataset for 2009. Figure 5.3a shows the WT coefficient matrix, showing the changes in precipitation for dilations ranging from 10 to 50. A clear signal of positive coefficients is observed between pentads 28 to 34 and a similar negative signal observed in pentads 56 to 60. Figure 5.3b shows the time series of the observed precipitation, which suggests that monsoon

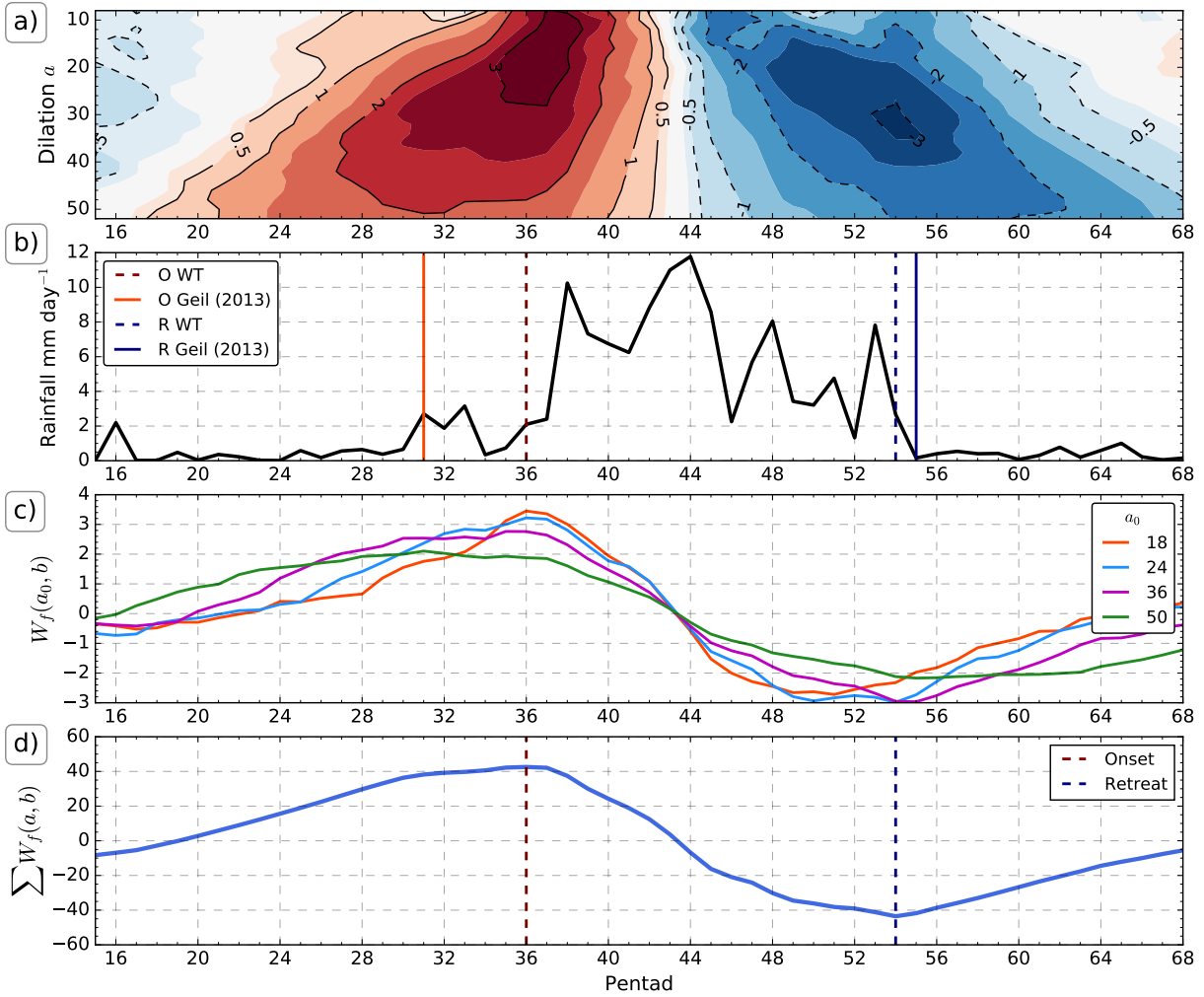


Figure 5.4: As in Figure 5.3, but for a year (1875) in the HadGEMGC3.1 N216 pre-industrial control simulation.

onset occurs sometime between pentads 28 and 34. Observed rainfall rapidly decreases after pentad 59 suggesting that monsoon retreat can be diagnosed around this pentad.

Figure 5.3c shows the WT coefficients as a function of pentad for several dilations (a_0). The coefficients for all scales seem to follow a very similar behaviour, increasing during spring to reach a maximum around pentad 32 and thereafter decreasing to a minimum around pentad 59. When the sum of the wavelet transform coefficients across the dilations is computed (Figure 5.3d) this behaviour becomes much clearer. The maximum and minimum are found at pentads 32 and 59, respectively and these pentads define the onset and retreat times. For comparison, the results from the method of Geil et al. (2013) are shown in Figure

5.3b, indicating that this method may have found an earlier onset.

As a proof of concept, Figure 5.4 shows a similar example using precipitation area-averaged in the same region but using model data from the piControl simulation of HadGEM3 GC3.1 N216. The results show that the WT method can capture the onset and retreat dates with relatively high skill and that these dates are different from the dates computed using the method of G13, with the threshold method suggesting an earlier onset and a later retreat.

5.3.2 Extension for Application to the MSD signal

The wavelet method can be extended to characterise the shorter scale variations of precipitation of the MSD in Central America and the Caribbean. First, the monsoon onset and retreat dates are determined in the time series from the area-averaged precipitation in the MSD region via the approach described in the previous section. Once the onset and retreat dates are established, an additional wavelet analysis determines the dates in which the MSD starts and ends. The onset and end of the drier period of the MSD can be found by computing the wavelet transform again but using smaller dilations and over a limited temporal range. In particular, the WT is only calculated in the 20 pentads before and after the dates defining monsoon retreat and onset, respectively. The MSD Onset (MSDO) and MSD End (MSDE) are defined as the minimum and maximum, respectively, of the sum of the wavelet transforms (equations 5.3 and 5.4) using dilation coefficients $\vec{a}^* = (10, 12, \dots, 24)$. The diagnosis of the onset and end of the MSD is also robust to using other dilation coefficients of similar magnitude.

Figure 5.5d illustrates the use of the WT method to determine the dates of MSDO and MSDE for the precipitation of 2017 in ERA-5. Figure 5.5a depicts the wavelet covariant transform matrix, showing the W_f coefficients for each dilation a at each pentad b . The onset of rainfall is diagnosed around the time-steps of highest positive W_f coefficients – around pentads 24 to 32 for almost all dilations. These positive coefficients are followed by a period of negative values from pentad 32 to pentad 40, which represent the decrease in precipitation, or relative drought, in the midsummer. The MSD is followed by another period of positive coefficients from pentad 44 to pentad 52, illustrating the so-called second peak of precipitation and, finally, a period of negative coefficients associated with monsoon retreat.

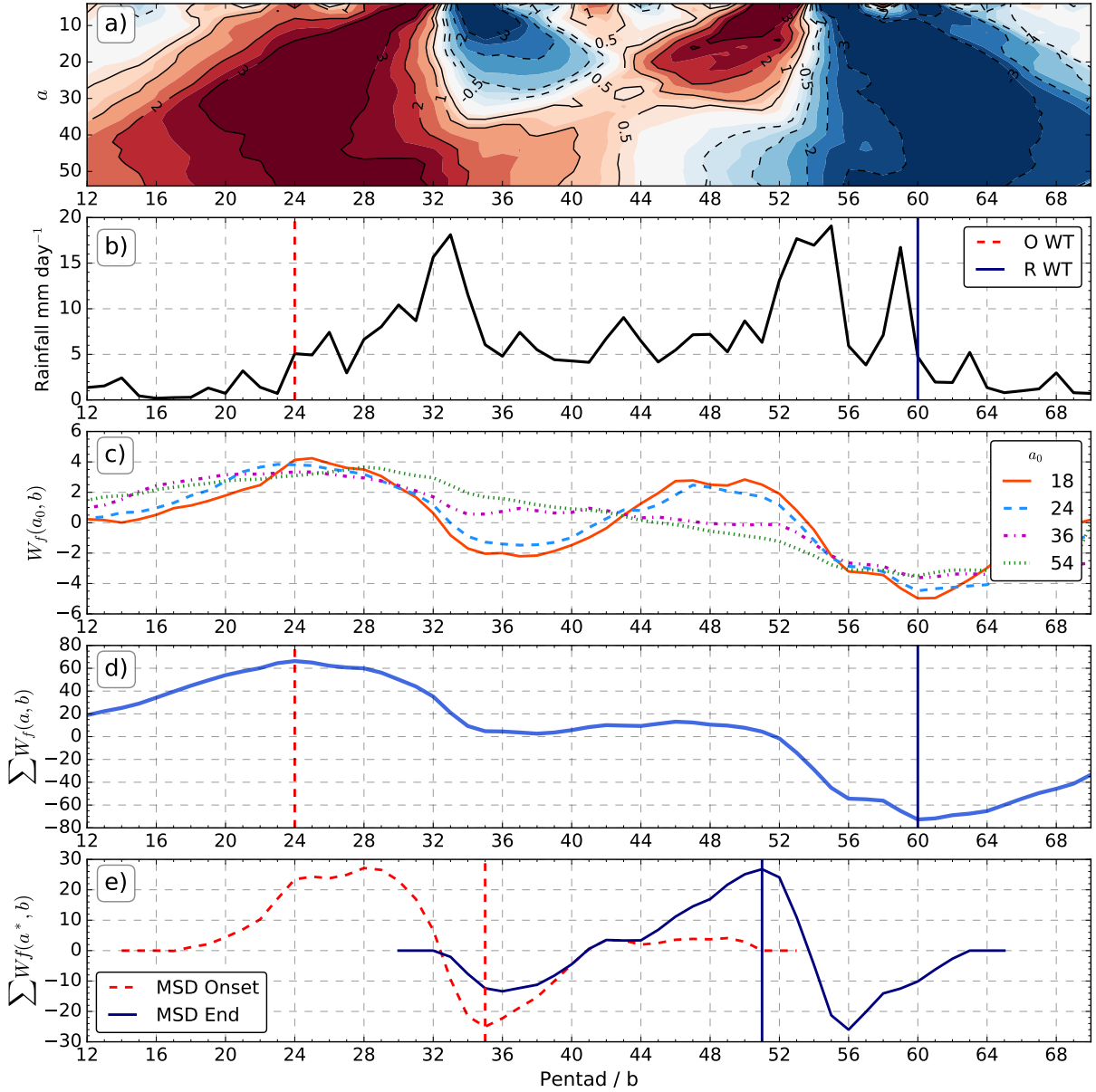


Figure 5.5: Example characterisation of the MSD [11-19°N, 95-85°W] using ERA-5 data for 2017. (a) Wavelet transform spectra, (b) observed precipitation with the onset and retreat pentads shown in red and blue, respectively. (c) Wavelet transform coefficients for four different dilations (mm d^{-1}). (d) The sum of the wavelet transform coefficients (mm d^{-1}) for $a = 28, \dots, 51$. (e) The sum of $W_f(a, b)$ (mm d^{-1}) for dilation coefficients $a = 12, \dots, 24$ showing the start (MSD Onset) and end (MSD End) of the midsummer drought.

The coefficients of the wavelet transform ($W_f(a_0, b)$) for selected dilations a_0 (Figure 5.5c) show that the smaller dilations are more sensitive to smaller scale variations in the time series and longer dilations better highlight the long-term change of the time series. For example

$a_0 = 18$ shows signs of a MSD by showing two local maxima and two local minima, whereas $a_0 = 54$ only shows a local maximum and a local minimum associated with onset and retreat.

The maximum and minimum of the sum over all dilations (Figure 5.5) depict the rainfall onset and retreat dates, respectively. The second wavelet transform $W_f(a^*, b)$ is computed over smaller dilation coefficients (a^*) near the onset and retreat dates as described above to highlight the MSDO and the MSDE. Figure 5.5e shows the sum of the wavelet transform coefficients $W_f(a^*, b)$ and the pentad of the MSDO, 34, and MSDE, 49, corresponding to the minimum and maximum of the sum of these wavelet transform coefficients, respectively.

The strength of the MSD can be measured through the maximum and minimum sum of the coefficients $\sum W_f(a^*, b)$ used to define the start and end dates of the MSD. For example, in Figure 5.5e the minimum of the $\sum W_f(a^*, b)$ was -20 mm d^{-1} found at pentad 35 and an opposite local maximum of $+20 \text{ mm d}^{-1}$ at pentad 49. These two values, hereafter *coef1* and *coef2*, provide a quantitative measure of the strength of the MSD for this year in this dataset and will be used to measure the spatial and temporal variability of the magnitude of the MSD in the different datasets.

5.3.3 Comparative Methodologies

For validation purposes, the wavelet transform method is compared with existing methods which determine onset and retreat in the North American and Indian monsoons. The threshold methods of Geil et al. (2013) (hereafter G13) and Arias et al. (2012) (hereafter A12) are compared to the results of the wavelet transform in the North American Monsoon. G13 used a threshold of 1.3 mm day^{-1} for at least 3 days for onset and 7 days for retreat for daily TRMM observations. This study, in contrast, analyses most of the data on the pentad-scale, so we adapt this method for TRMM to the same threshold value, but the onset pentad is the first pentad above the threshold whereas for retreat, we require rainfall to be below the threshold for two consecutive pentads. The method of A12 defines onset with two conditions. The first condition to find the onset pentad is that six out of the eight subsequent pentads must have rain-rates above the annual-mean climatological rainfall. The second condition is that at least six out of the eight previous pentads must be below the annual-mean climatological rainfall. The opposite definition is used to determine the pentad of monsoon retreat.

In relation for the Indian Monsoon region, a commonly used metric is the hydrological onset and withdrawal index (HOWI) which is based on moisture transport over the Arabian Sea (Fasullo and Webster, 2003; Sahana et al., 2015; Chevuturi et al., 2019). To compute the HOWI index, first, the vertically integrated moisture transport (χ) is computed from daily ERA-5 data in the Arabian sea, as described by Fasullo and Webster (2003), i.e.:

$$\chi = \frac{1}{g} \int_{p_0}^0 q \mathbf{V} dp, \quad (5.5)$$

where g is the gravitational acceleration, p are the pressure levels, q is the specific humidity and \mathbf{V} is the wind vector. The VIMT is then normalized using the transformation:

$$HOWI = 2 \left(\frac{\chi - \min(\bar{\chi})}{\max(\bar{\chi}) - \min(\bar{\chi})} \right) \quad (5.6)$$

where χ is the unnormalized time series, $\bar{\chi}$ is the mean seasonal cycle of the unnormalized index and HOWI is the normalized index. The onset date is defined as the first day of each year where the HOWI index is greater than zero and the retreat date is the first day after the onset date that the HOWI index is negative (Fasullo and Webster, 2003; Sahana et al., 2015). The necessary daily data of moisture and wind speed on sufficient vertical levels to compute the HOWI index in the MOHC submissions to CMIP6 was not available, so the HOWI index can only be computed using ERA5 and will be compared to the WT method used on the observational gridded datasets.

5.4 Results

The monsoon onset and retreat dates were determined for each year in each observational and model dataset for the Indian, North American and MSD regions using the methods described in the previous section. The calculations were performed for area-averaged precipitation time series representative of the core regions defining these monsoons. [Several tests show there is little sensitivity to the performance of the WT to the size of the box, relative to other methods, however, the mean values of retreat and onset dates are very sensitive to the regions chosen for the averaging.](#) Calculations were also made at grid-box scales to illustrate the spatial distribution of the onset and retreat dates.

5.4.1 The North American Monsoon

Table 5.1 shows the mean onset and retreat dates estimated using the G13, A12 and WT methods for precipitation time series averaged over the North American monsoon. The table reports the results for three observational datasets, ERA-5 reanalysis and five climate model experiments. The observations agree that the onset date is found at pentad 33 (around June 15), according to the WT and the method by G13. However, the method of G13 reports a mean retreat date that is one pentad later than the WT method, i.e., around October 7th for G13 method and October 2nd for the WT. The method by A12 disagrees with G13 and the WT methods for both onset and retreat mean pentads, in both cases finding an earlier onset (pentad 30) and retreat (pentad 54) for all the observational datasets.

The climate models reasonably represent the mean onset and retreat dates, as only the

Table 5.1: Mean (standard deviation) pentads of monsoon onset (O) and retreat (R) in the North American Monsoon [110°-103°W, 20°-27°N] for observational datasets, reanalysis and model output with the wavelet transform method WT, G13's and A14's method. Pentad 34 corresponds to the period between June 17-22 and pentad 54 to the period Sep 27 - Oct 1. The results from the WT method in the model experiments which are statistically different to both the CMAP and CHIRPS results at the 95% confidence level, according to a Welch's t-test, are shown in bold.

Dataset / Experiment	WT O	WT R	G13 O	G13 R	A12 O	A12 R
TRMM	33.3 [±1.8]	55.8 [±1.9]	33.0 [±1.7]	56.6 [±1.4]	30.4 [±1.7]	53.8 [±2.0]
CMAP	33.2 [±1.6]	55.0 [±2.1]	36.0 [±3.3]	55.7 [±1.8]	31.7 [±3.0]	54.5 [±3.3]
CHIRPS	32.5 [±1.5]	54.7 [±1.9]	33.6 [±1.7]	56.1 [±1.4]	30.1 [±1.7]	53.6 [±2.5]
ERA-5	33.5 [±1.8]	55.5 [±2.0]	33.6 [±1.8]	56.4 [±1.4]	30.9 [±1.7]	53.3 [±2.3]
GC3 N216-pi	33.7 [±2.0]	55.1 [±1.8]	32.6 [±2.5]	55.9 [±2.3]	32.4 [±2.5]	53.8 [±3.8]
GC3 N96-pi	33.7 [±2.2]	55.0 [±2.1]	32.7 [±2.9]	56.3 [±2.0]	31.9 [±2.6]	54.1 [±4.1]
GC3-hist	33.8 [±2.3]	55.1 [±2.1]	33.3 [±2.9]	56.0 [±2.2]	31.9 [±2.6]	53.7 [±4.0]
UKESM-pi	34.5 [±2.1]	54.8 [±2.1]	34.1 [±2.9]	56.1 [±1.9]	33 [±2.6]	53.9 [±4]
UKESM-hist	34.3 [±2.2]	54.3 [±2.2]	34.4 [±3.2]	55.6 [±2.1]	33.1 [±3.0]	53.2 [±4.2]

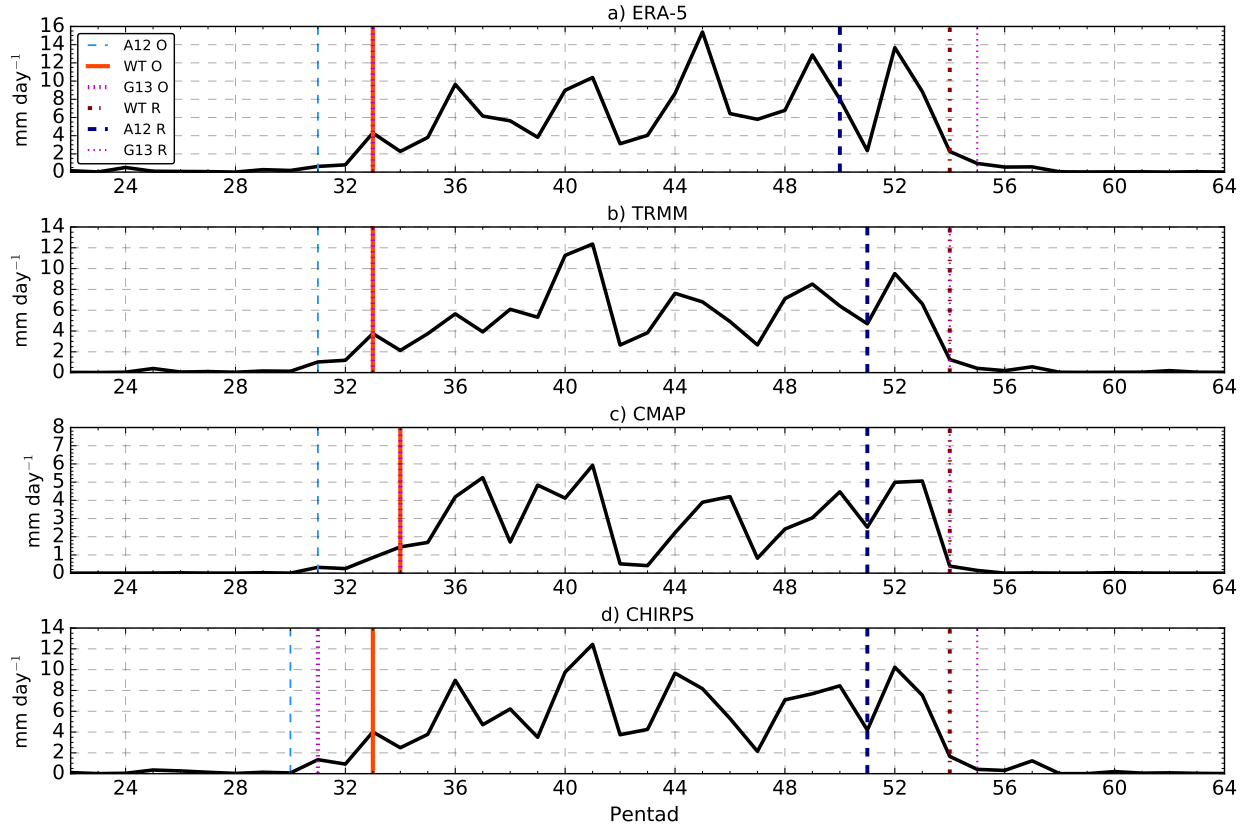


Figure 5.6: Pentad-mean precipitation for the North American Monsoon in 2010 in four precipitation datasets showing the onset and retreat pentads as diagnosed by the WT, the A12 and G13 methods. The area used to average the precipitation is illustrated in in Figure 5.7b).

onset dates from both experiments of UKESM1 are statistically different to the results of CMAP and CHIRPS. The similarities in onset and retreat dates confirm that the seasonal cycle in the North American monsoon is very well represented by these models, as suggested by chapter 4. In the results of the simulations, A12 also produces an earlier onset and retreat dates when compared to the other two methods of about 1.5 pentads, but this difference is within the uncertainty range given by the interannual variability of the model data which is largest for A12.

Figure 5.6 compares the estimated onset and retreat dates using the three methods for the 2010 North American Monsoon using the three observational datasets and ERA5. A12 shows an earlier onset and retreat in all the datasets compared with the WT and G13 which agree in almost every dataset. The WT method estimates the retreat and onset dates more consistently across datasets relative to the other methods.

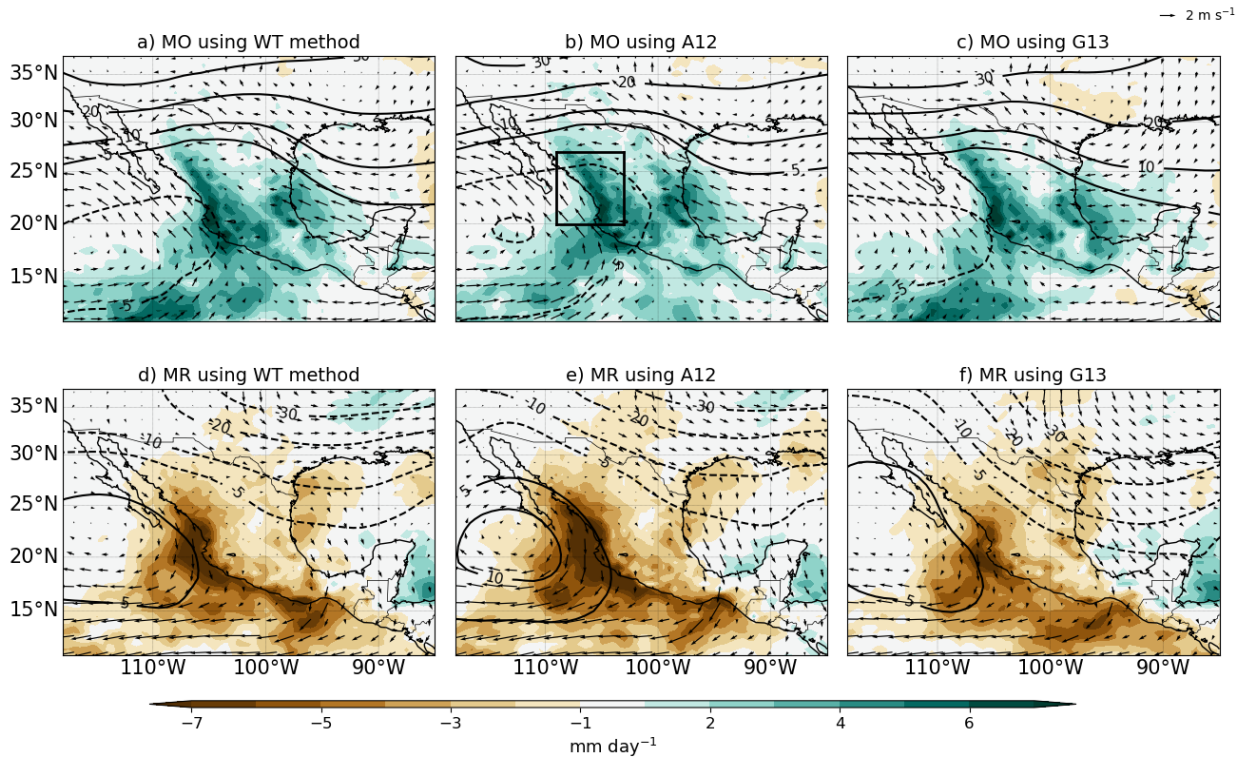


Figure 5.7: Precipitation (color contours), low level wind at 850-hPa and geopotential height (line contours) at 500 hPa anomalies for (a, b, c) the difference between the 10 days after monsoon onset and 10 days prior to onset (MO) using onset dates from (a) the WT (b) Arias et al. (2012) and (c) Geil et al. (2013). (d, e, f) are as in (a, b, c) but for monsoon retreat. The data and dates are obtained from ERA-5, and the area for the average is shown in the box in b).

The meteorological changes associated with onset and retreat of the North American Monsoon (Figure 5.7) are illustrated as the composite differences of the precipitation, wind and geopotential changes 10 days prior to and after onset and retreat. These changes to the circulation and precipitation are reasonably similar for all the three methods. The impact of monsoon onset in precipitation is diagnosed to be slightly stronger by A12 compared to WT or G13. The WT method shows a very similar pattern and magnitude of the circulation and precipitation anomalies of onset and retreat when compared to the other two methods. The method by G13 produces the weakest anomalies, particularly of precipitation whereas the method by A12 produces the strongest precipitation and geopotential anomalies, particularly at retreat.

Figure 5.8 shows the spatial distribution of the mean onset and retreat dates in the North American Monsoon region for various datasets. There is high agreement between

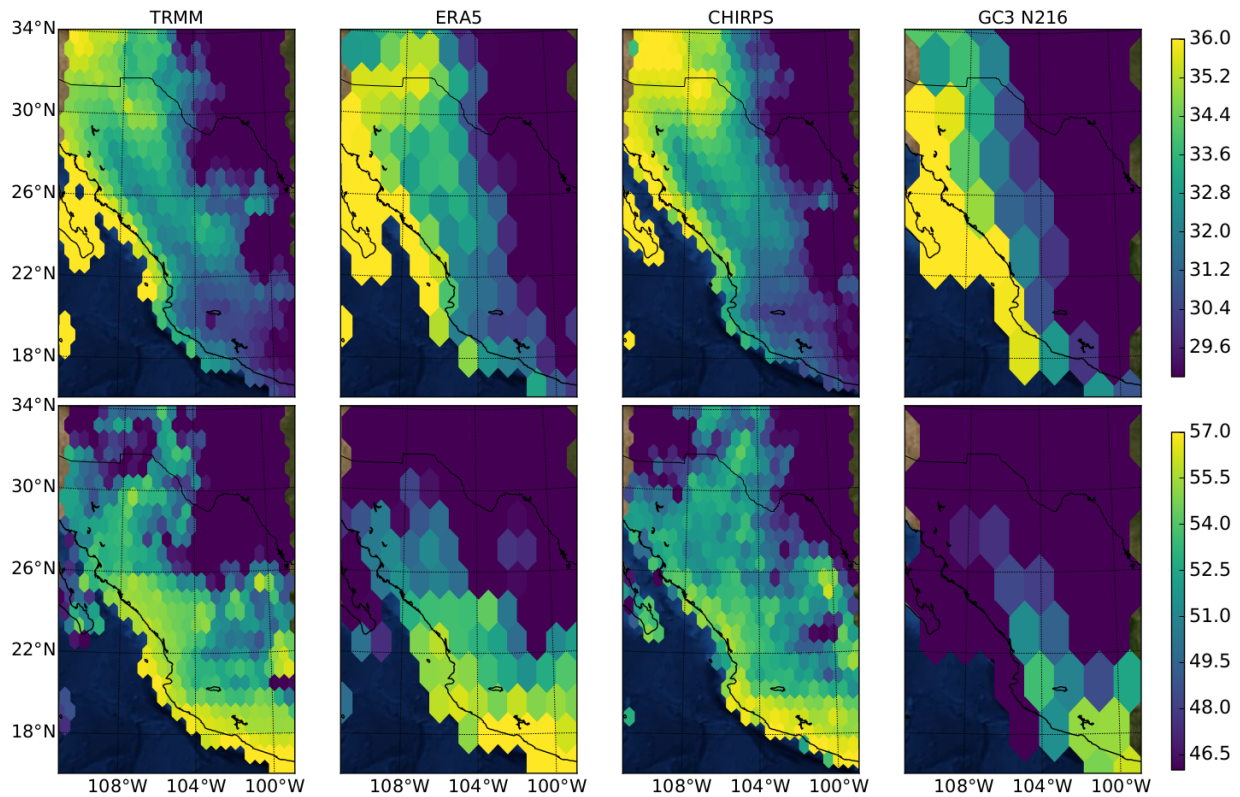


Figure 5.8: Rainfall onset (upper) and retreat (lower) mean pentads in the North American Monsoon for observations and a climate model output using the WT method.

TRMM, CHIRPS and ERA5 on the spatial pattern of mean onset and retreat dates. Onset in western Mexico is around pentad 31 (around June 1st), whereas in Chihuahua and Sonora the rainy season begins shortly after pentad 35 (June 22). The pattern in the medium-resolution simulation GC3 N216 piControl is consistent with observations, particularly during onset. However, the spatial pattern of the mean retreat dates in the northern regions of the monsoon show an earlier than observed retreat, possibly associated with the dry bias in this region in these models (see chapter 4).

5.4.2 The Indian Monsoon

Table 5.2 compares the mean onset and retreat dates of the Indian Monsoon as computed from the HOWI index using ERA5 data, and the WT used for gridded precipitation datasets. The onset and retreat dates from the HOWI index were converted from the daily to the pentad-scale to compare with the WT. The mean onset date for the HOWI index is May 27th

between pentads 29 and 30, and retreat is between pentads 49 and 50, around September 3rd. The mean onset date found using the WT method for the four observational datasets was pentad 32, about two pentads later than the HOWI index. The mean retreat date for the WT method (pentad 53) was two pentads later than the HOWI results.

Overall, the models exhibited later than observed onset (+4 pentads) and earlier retreat (-2 pentads) dates. The differences between the hydrological determination of onset and retreat dates, through HOWI, and the WT method on gridded precipitation datasets is statistically significant, according to a Welch's t-test comparing the HOWI and all the gridded datasets. These differences may be due to the different regions where each method is defined, i.e., HOWI is defined over the whole of the Arabian Sea where an earlier onset would be expected when compared to rainfall over mainland India, where the WT method was applied.

Figure 5.9 shows the differences between the WT (based on ERA5 precipitation) and HOWI methods in their characterisation of the meteorological changes associated with onset and retreat. The comparison of precipitation and moisture fluxes at 850 hPa anomalies 10 days prior to and following monsoon onset and retreat show that the HOWI index better captures the moisture transport in the Arabian Sea whereas the WT method best captures precipitation differences over mainland India. The HOWI index characterisation of the

Table 5.2: Mean (standard deviation) pentads of monsoon onset (MO) and retreat (MR) in the Indian Monsoon using the WT method on observed, reanalysed and modelled time series as well as for the HOWI index. The region over which precipitation was area-averaged for the WT method was [75°-83°E, 18°-24°N]. The mean onset and retreat dates that are significantly different to the 99% confidence level to the CMAP dataset are shown in bold.

Dataset	MO	MR
TRMM	31.6 [± 1.8]	53.2 [± 1.9]
CMAP	31.8 [± 1.6]	53.3 [± 2.6]
CHIRPS	31.5 [± 1.4]	53.4 [± 1.9]
ERA-5	31.8 [± 1.9]	52.7 [± 2.6]
GC3 N216-pi	34.4 [± 1.3]	50.5 [± 1.9]
UKESM-pi	36.1 [± 3.1]	51.9 [± 3.2]
UKESM-hist	36.0 [± 3.9]	51.8 [± 3.3]
GC3 N96-pi	35.5 [± 1.8]	51.8 [± 2.3]
GC3-hist	35.7 [± 2.1]	51.5 [± 2.8]
HOWI (ERA5)	29.5 [± 2.3]	49.3 [± 2.4]

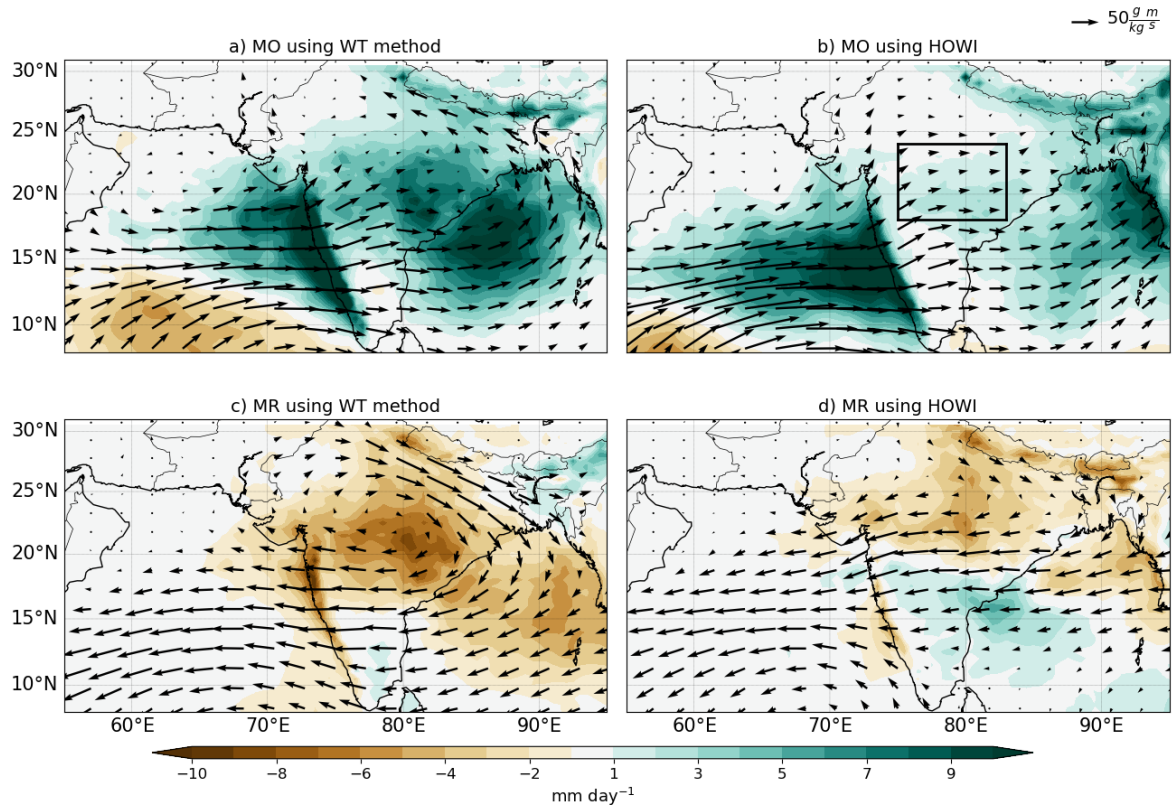


Figure 5.9: Precipitation anomalies (color contours) and the moisture flux vectors calculated from the product of specific humidity (q) and wind (\vec{u}) at 850 hPa. (a, b) shows the difference between the 10 days after monsoon onset and 10 days prior to MO using (a) the WT and (b) the dates estimated using the HOWI index. (c, d) are as defined in (a, b) but for MR. The dates are calculated from ERA5 data averaged over the box in panel b).

moisture flux in the Arabian Sea may be out-of-phase with precipitation over mainland India, and this lag could possibly explain some of the results of Table 5.2.

The WT method is also able to capture onset and retreat dates and the associated anomalies within the climate model output. Figure 5.10 shows the precipitation and moisture transport anomalies around the onset and retreat of the Indian monsoon in three different climate model experiments. While the models show significant biases in the timings of the monsoon, according to a Welch's t-test (Table 5.2), the patterns of rainfall and moisture transport anomalies to the observations around both onset and retreat agree well with reanalysis.

The spatial distribution of the mean onset and retreat dates of the Indian monsoon as characterized by the WT method (Figure 5.11) shows that the mean onset and retreat

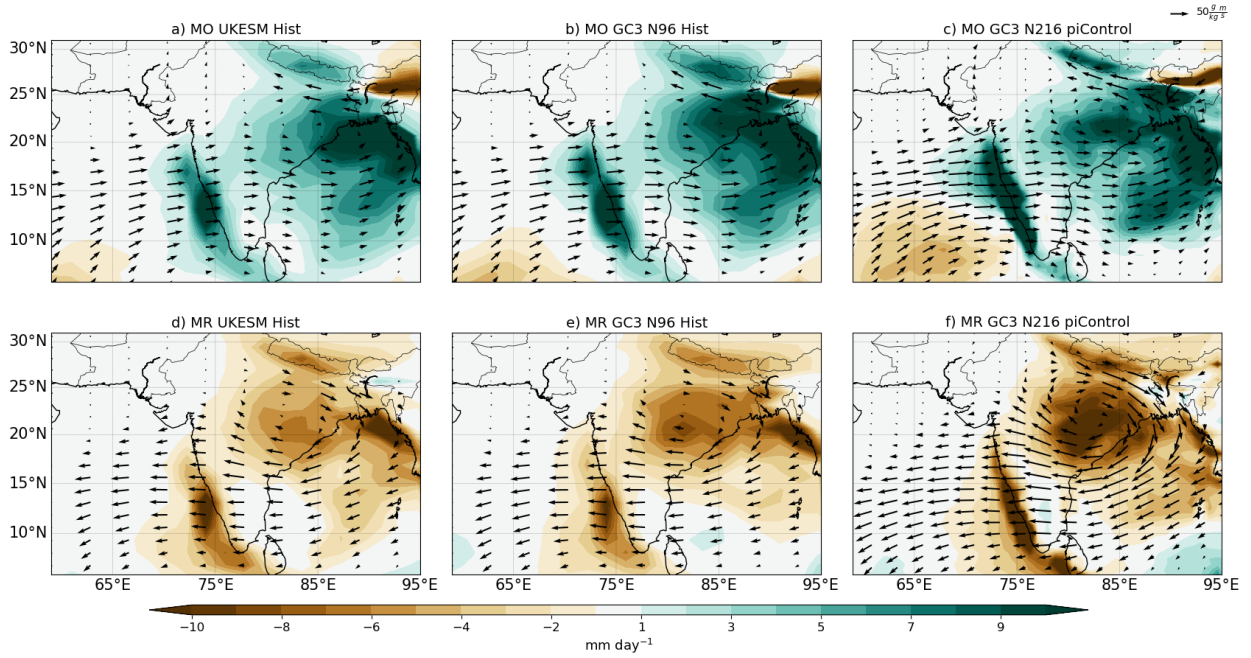


Figure 5.10: As in Figure 5.9 but showing onset and retreat for three different climate model experiments: (a, d) UKESM1 historical, (b, e) HadGEM3 GC3.1 N96 historical, (c, f) HadGEM3 GC3.1 N216 piControl.

dates vary greatly spatially on the southern tip of the subcontinent. While most of northern India has a mean onset date around pentad 33, the western coast shows an earlier onset by about one or two pentads. There is high agreement in the onset date between the three observational datasets and the reanalysis over mainland India and between TRMM and ERA5 over the western coast of India. The earliest onset is found on the western coast around pentad 25-27 and extending to central India by pentad 31. The GC3 N216 simulation, however, shows a later onset than observed by about two pentads in most regions. In contrast, the spatial pattern for the mean retreat date shows higher spatial variability between the western and eastern coasts of India. CHIRPS shows the latest retreat dates over the south-central states when compared to TRMM and ERA-5.

5.4.3 The midsummer drought

Results from the application of the wavelet transform to the MSD, including the mean onset and retreat dates as well as the start and end dates of the MSD period, are reported in Table 5.3. The mean onset date in the observations is around pentad 27 (May 14), whereas

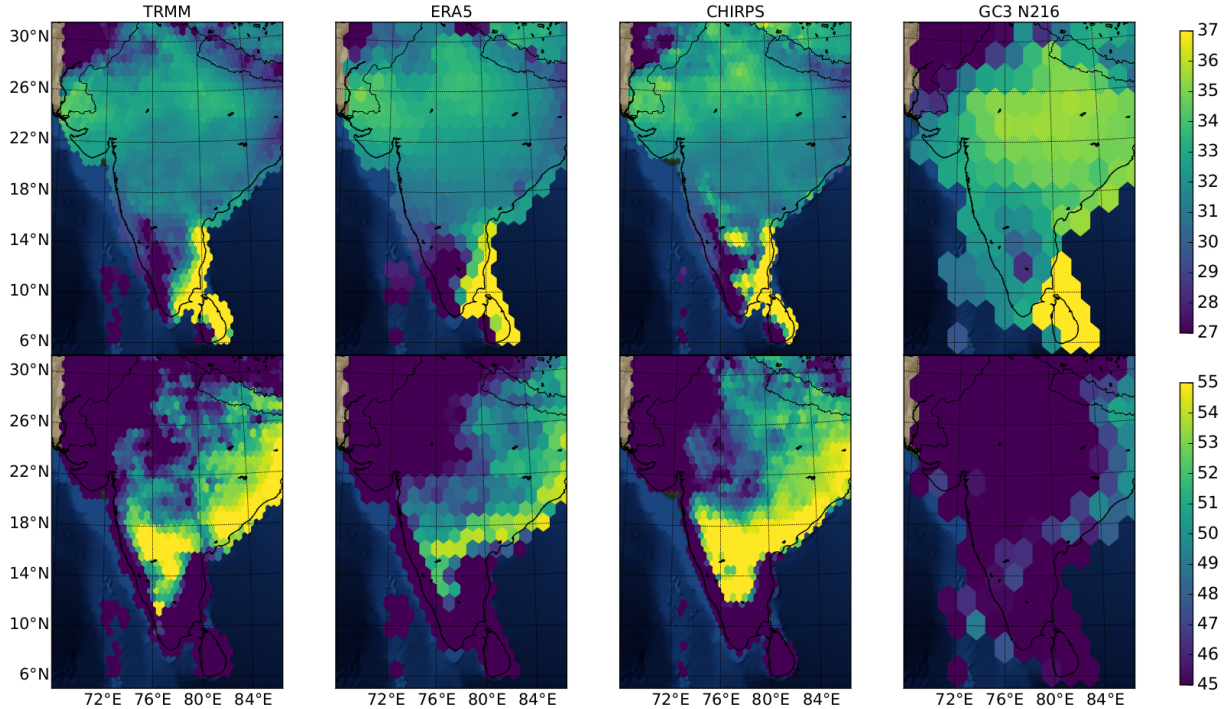


Figure 5.11: As in Figure 5.7 but for the Indian Monsoon.

the retreat date is around pentad 61 (October 31). The end of the so-called first-peak period, or start of the relatively drier period (MSD), referred to in this thesis as MSD onset (MSDO) is consistently found in all the observed datasets to be around pentad 36 (around June 29). The end of the drier period or start of the second peak, referred to in this thesis as MSD end (MSDE) is also consistently determined to be between pentads 48 to 49 in the four observational datasets. In other words, the MSD has a mean duration of 12 pentads, or around two months, from late June to late August. In the MOHC simulations, the MSD starts slightly later than observed by about two pentads, and ends about one pentad later than observed around September 10.

Figure 5.12 shows the rainfall anomalies associated with the different periods (stages) of the rainy season in southern Mexico and Central America. These include monsoon onset and retreat, and the start and end of the MSD, the MSDO and MSDE, respectively. For each stage, we compared the anomalies computed by separating the stages using the WT method or the dates of the climatological monsoon onset, retreat, MSDO and MSDE as found in Table 5.3. In this way, the ability of the WT method to characterise rainfall variations is

Table 5.3: Mean pentads of monsoon onset (MO), rainfall retreat (MR), MSD Onset (MSDO) and MSD End (MSDE) in the MSD region [11-19°N, 95-85°W, illustrated in Figure 5.12a.] estimated through the WT method. Pentad 35 corresponds to the period between June 22-27 and pentad 52 to the period Sep 13-18. The model dates shown in bold are statistically different from CMAP and CHIRPS results to the 99% confidence level according to a Welch's t-test.

Dataset	MO	MR	MSDO	MSDE	coef1	coef2
TRMM	25.8 [±2.2]	61.6 [±3.1]	35.9 [±2.4]	49.0 [±4.1]	-9.5 [±4.2]	10.4 [±5.4]
CMAP	26.7 [±1.9]	60.6 [±3.3]	36.5 [±2.6]	48.0 [±4.2]	-7.1 [±4.2]	7.7 [±4.3]
CHIRPS	26.7 [±2.3]	61.4 [±3.1]	36.5 [±2.7]	48.3 [±3.5]	-4.7 [±2.7]	5.5 [±3.2]
ERA-5	26.5 [±2.2]	61.8 [±3.2]	36.1 [±2.7]	48.8 [±3.5]	-10.7 [±5.4]	11.8 [±6.6]
UKESM-pi	27.4 [±2.4]	61.9 [±3.2]	38.2 [±2.7]	49.1 [±2.7]	-18.2 [±8.7]	14.6 [±8.0]
GC3 N96-pi	26.9 [±2.6]	62.3 [±3.5]	37.8 [±2.1]	49.9 [±3.1]	-21.7 [±9.4]	16.8 [±8.0]
GC3 N216-pi	26.9 [±2.3]	62.2 [±3.5]	38.4 [±2.1]	50.0 [±2.7]	-23.5 [±8.0]	14.1 [±6.7]
GC3-hist	26.9 [±2.7]	62.8 [±3.7]	37.8 [±2.4]	50.3 [±2.6]	-19 [±8.7]	17.1 [±8.4]
UKESM-hist	28.5 [±2.7]	62.8 [±3.5]	38.7 [±2.8]	50.1 [±2.7]	-20.3 [±10.1]	14.9 [±8.3]

tested against a first best guess – the climatological mean dates.

Overall, using the dates for MSDO and MSDE from the climatological dates results in weaker anomalies than compositing via the specific dates for each year obtained with the WT method. Even though the area-averaged signal used to diagnose the different MSD stages focuses on a small region of southern Mexico and northern Central America, the anomalies associated with the onset and end of the MSD (Figures 5.12f, h) extend across the East Pacific warm pool, most of the western coast of Mexico and into to the Caribbean Sea and Cuba. This result suggests that the MSD is not the result of micro-scale processes but the relatively large extent of the MSD precipitation pattern indicates this is a regional feature associated with regional-scale processes. This result suggests that the MSD is part of a regional-scale process on the result of local-scale processes.

The analysis of individual years of observed precipitation in the selected area-averaged

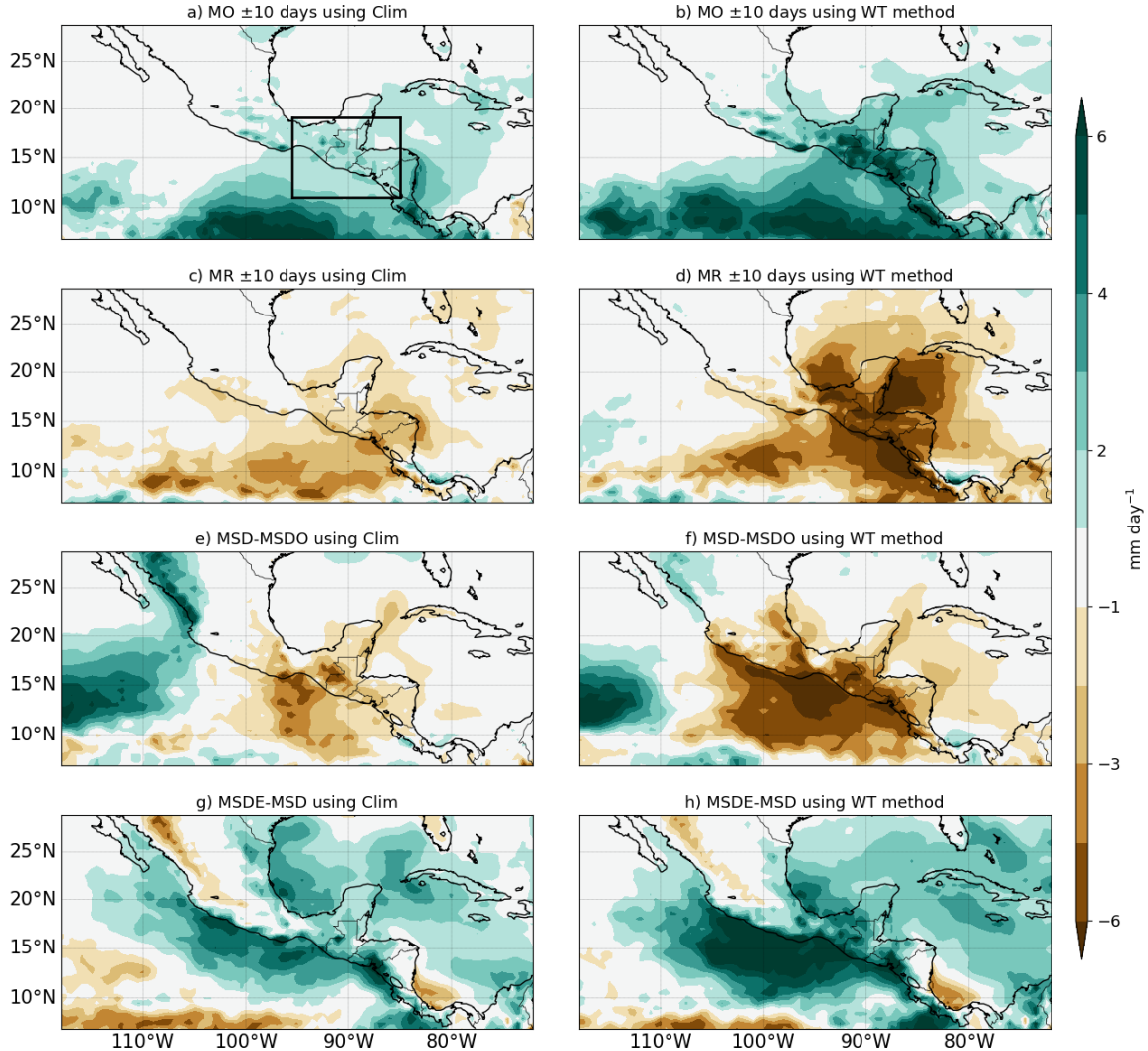


Figure 5.12: Precipitation anomalies for (a, b) the difference between the 10 days after monsoon onset and 10 days prior to onset (MO) using (a) the climatological dates of onset and (b) the dates estimated using the WT method. (c, d) are as in (a, b) but for monsoon retreat. (e, f) Difference between the Midsummer Drought (MSD) and the 10-day mean prior to the onset of the MSD (MSDO). (g, h) as in (e, f) but showing the difference between the end of the MSD (MSDE) and MSD. The data and calculations are from ERA-5. The black rectangle in a) shows the MSD area used to average the precipitation throughout this study.

time series showed that not all years showed a bimodal signal in the area-averaged precipitation (Fig. 5.13). In fact, a given year could be classified as having (1) a canonical two-peak structure separated by an MSD, (2) only having a first peak and an MSD but no second peak, (3) only having a second peak but no clear MSD or (4) a plateau-like monsoon season with no MSD-type variations (see Fig. 5.13).

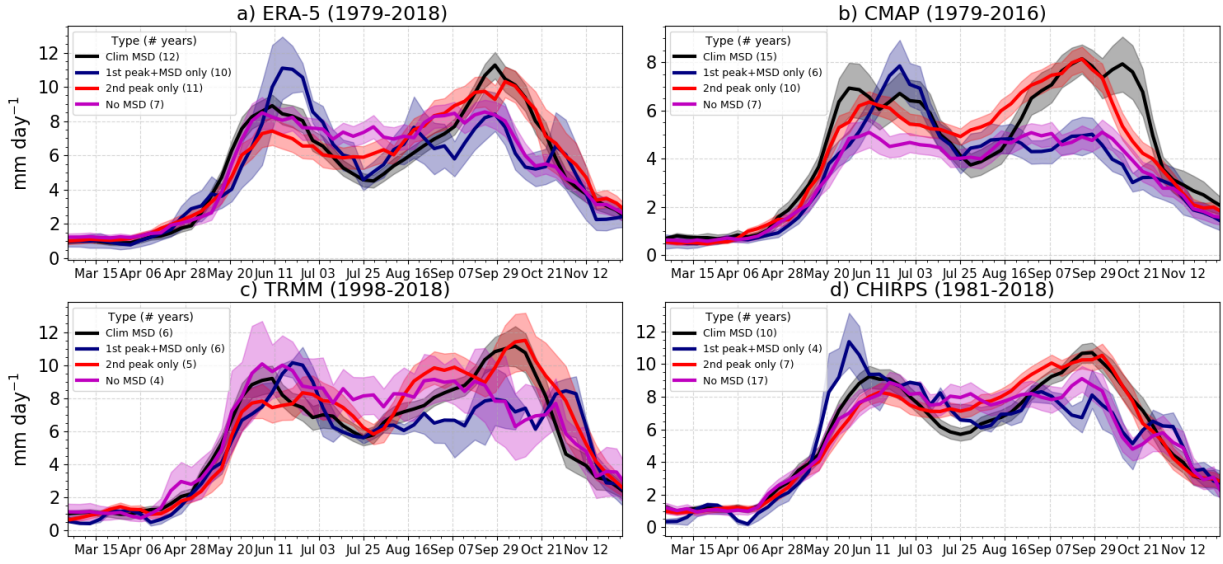


Figure 5.13: Pentad-mean precipitation in years differentiated by MSD characteristics in four datasets: (a) ERA-5, (b) CMAP, (c) TRMM and (d) CHIRPS. The shading for each line represents first to third quantile of the distribution provided a bootstrapping with replacement all the years in each composite 10000 times.

Due to this year-to-year variability in the characteristics of the seasonal cycle, an objective measure was defined to determine whether a signal presented a robust MSD-bimodal seasonal cycle. For this purpose, the WT algorithm was applied to randomly generated precipitation time series. The random time series are constructed by randomly sampling observations in the wet and dry seasons. The pentad-mean onset and retreat dates from Table 5.3 were used to composite the observations into dry and wet distributions.

For a random time series that aims to mimic one year of precipitation, the rainfall values for each pentad in the year are randomly selected from the dry or wet distributions, depending on the pentad. In this way, the value of a given pentad of the random time series may have been observed at a different pentad; the only constraint is that the random values come from pentads that were observed in the same season: dry or wet. The logic behind this approach is that in most monsoon regions, the peak monsoon rainfall should follow a plateau, see for example the North and South American monsoons in Figure 4.9 in the previous chapter. However, a bimodal regime would show a notable decrease in precipitation in the middle of the rainy season, such that it cannot be explained by the inherent short-scale variability of rainfall.

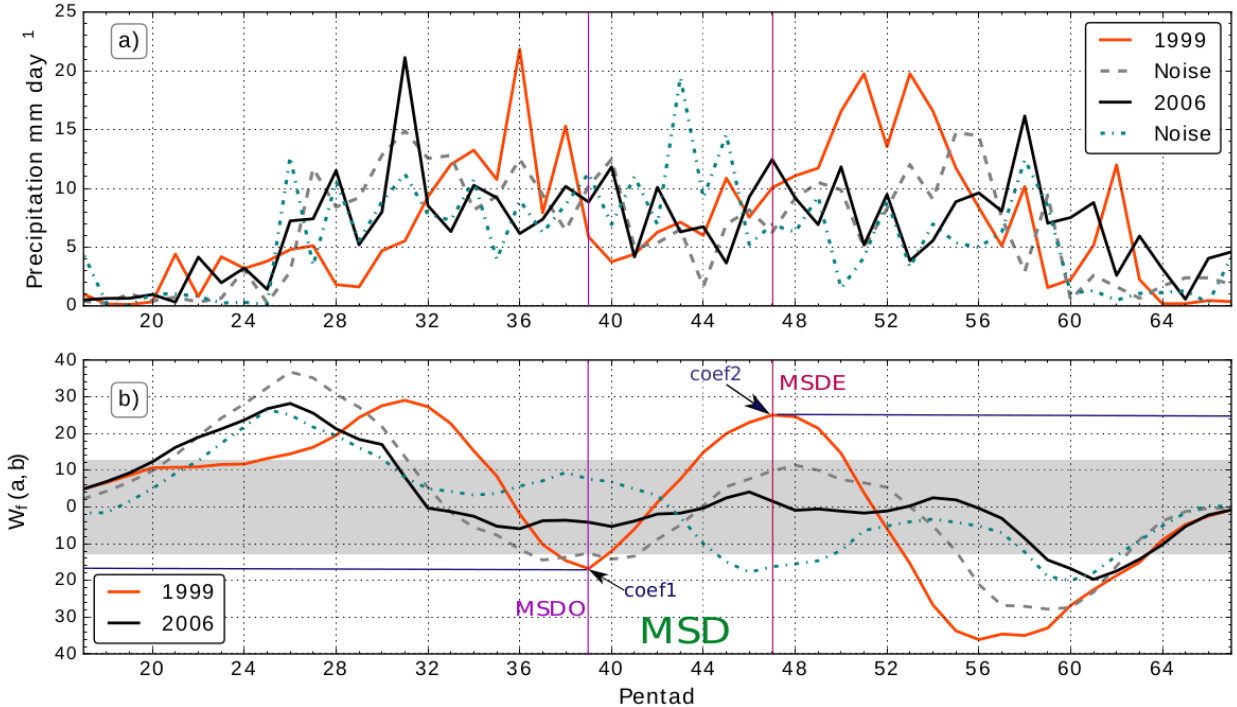


Figure 5.14: (a) Pentad-mean precipitation in two years of TRMM data: 1999 and 2006 and two randomly generated precipitation time series (see text). (b) Sum of the wavelet transforms of the time series in (a). The shaded region in gray in (b) corresponds to the interval between the first quantile of *coef1* and the third quantile of *coef2* of 10,000 random timeseries constructed with TRMM data. The onset (MSDO) and end (MSDE) of the relatively drier period, as well as the location and values of *coef1* and *coef2* for 1999 are labelled in (b).

This approach has two advantages. First, that the random time series impose a monsoon-like feature with a sharp wet-dry season contrast but secondly, the random selection in the wet season removes the possible signal of the MSD in the climatological rainfall. The random time series are then constructed by randomly drawing values at each pentad from the wet or dry season distributions of each dataset. Then, the WT method was used on 10,000 of these random-time series. This approach rendered a distribution of coefficients (*coef1* and *coef2*) essentially representing the variability of the WT method applied to noise.

Figure 5.14 shows the pentad-mean time series from two years in the TRMM dataset, and two randomly generated time series. The coefficients *coef1* and *coef2*, illustrated in Figure 5.14b, measure the difference in precipitation between the first peak and the MSD period and the MSD and the second peak, respectively. The first quantile of *coef1* and the third quantile of *coef2* provide a measure of robustness for the observed *coef1* and *coef2*.

In other words, for a year to be classified as having a robust MSD signal, the resulting $coef1$ and $coef2$ of the WT procedure must be lower and higher, respectively, than those obtained for a random time series. The analysis of $coef1$ then determines the existence of a first-peak MSD type variability and $coef2$ determines the robustness of a possible second-peak for that year. By this procedure, a given year could fit into four categories:

- Canonical MSD: $coef1$ lower than the first quartile (25%) of random $coef1$ and $coef2$ higher than the third quartile (75%) of random $coef2$.
- 1st peak+MSD: $coef1$ lower than the first quartile of random $coef1$ but $coef2$ lower than the third quartile of random $coef2$. In other words, the second peak is not distinguishable from noise.
- 2nd peak only: $coef1$ higher than the first quartile of random $coef1$ but $coef2$ higher than the third quartile of random $coef2$. In other words, the second peak is distinguishable from noise, but there is no first-peak + MSD structure.
- No MSD: $coef1$ higher than the first quartile of random $coef1$ and $coef2$ lower than the third quartile of random $coef2$. In other words, the precipitation time series shows no robust signal of an MSD regime, with a first or second peak.

Figure 5.13 shows how separating years into these categories affects the pentad-mean seasonal cycle of precipitation in southern Mexico and Central America in four observational datasets. This figure also validates the above procedure as the WT method is able to robustly separate years into the different categories.

For each dataset we determine those grid-points showing a robust MSD. We use the method outlined above to construct the random time series for each grid-point and estimate the random values of $coef1$ and $coef2$, repeating the procedure 10,000 times. A given grid-point is diagnosed to have a robust MSD when the value of $coef2 - coef1$ is higher than the third quartile of the PDF of the random time series. The value of $coef2 - coef1$ is a measure of the magnitude of the MSD since $coef2$ measures the relative strength of the second-peak compared to the MSD and therefore positive in an MSD grid-point

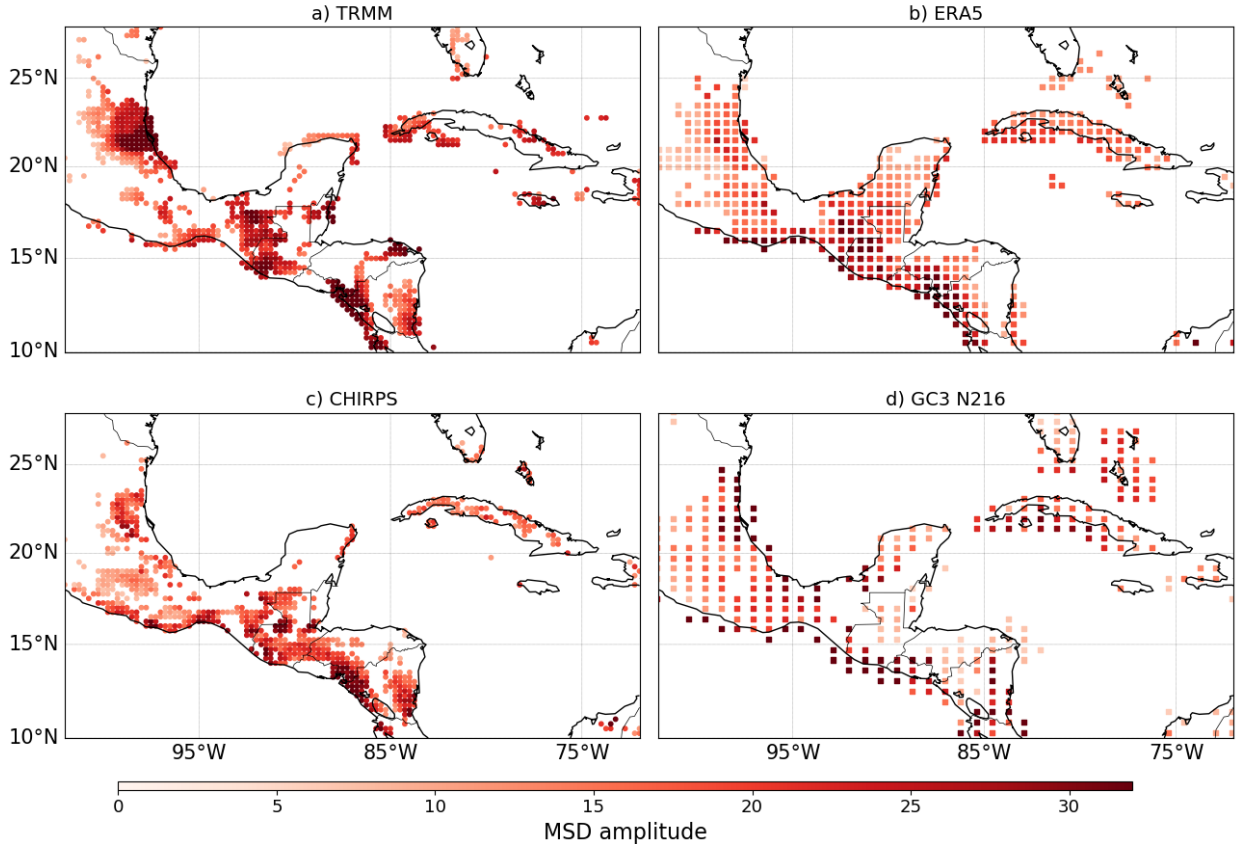


Figure 5.15: Grid points where the MSD is significantly different, i.e. outside the first and second quartiles of the random distribution, from noise (see section 3.3) for a) TRMM, b) ERA5, c) CHIRPS and d) GC3 N216-pi. The magnitude of the MSD, measured as $coef2 - coef1$ is shown in colour shading.

and $coef1$ compares how dry the MSD is relative to the first-peak and thus negative if an MSD regime is observed at that grid point.

Figure 5.15 shows the regions where the climatological rainfall shows a MSD signal that is distinguishable from noise, i.e., regions where the values of $coef2 - coef1$ exceed the third quartile of the distribution composited with random time series, as well as the magnitude of the MSD for the TRMM, ERA5, CHIRPS and the GC3 N216 piControl simulation. Cuba, western Central America and most of southern and central-eastern Mexico exhibit a robust MSD signal. This map also shows that the strongest MSD signal is found on the western coast of northern Central America and northeastern Mexico. The high correspondence between the three observational datasets shows that the method is robust across datasets. These results agree well with previous studies on the spatial distribution of the MSD (Magaña

et al., 1999; Perdigón-Morales et al., 2018; Anderson et al., 2019; Zhao and Zhang, 2021). In particular, the method is able to replicate the previously reported MSD signal in the Pacific Mexican coast and the stronger MSD signal in northeastern Mexico.

Figure 5.16 shows the spatial distribution of the mean onset and retreat pentads and the start and end of the MSD, in the grid-points where the signal is significant as in Fig. 5.15. The earliest rainfall onset is found on the western coast of southern Mexico, Guatemala and El Salvador, as well as in Cuba, at pentad 25, whereas onset in the Yucatan peninsula is found at pentad 28 and even later, around pentad 31, in the eastern states of Mexico. In

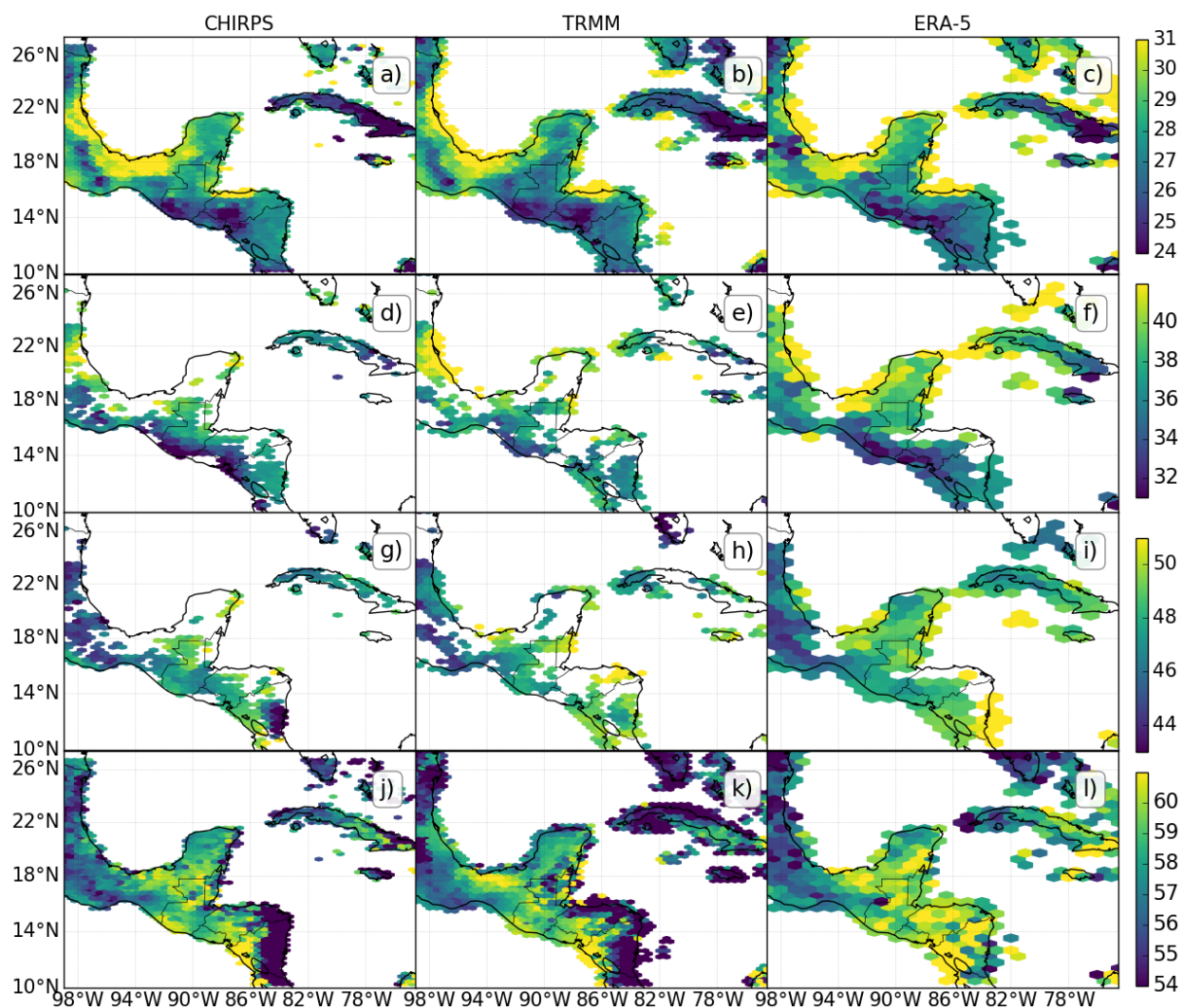


Figure 5.16: Spatial distribution of pentad dates of the timings of the summer rainfall season in the MSD region, showing (a-c) MO dates and (d-f) MSDO dates, (g-i) MSDE and (j-l) MR for (left) CHIRPS, (middle) TRMM and (right) ERA-5.

contrast, the retreat date seems spatially more homogeneous as northern Central American has a mean retreat date around pentad 59 and central Mexico around pentad 54. The MSD coherently starts over the western coast of Guatemala and Chiapas around pentad 33. In contrast, the MSD on the eastern Mexican states of Veracruz and Campeche begins after pentad 40. The earliest MSD end (Figs. 5.16h-j) is found in central and northeastern Mexico, around pentad 42 whereas the MSD in Guatemala ends around pentad 48.

5.5 Summary and discussion

The assessment of the AMS in the MOHC submissions to CMIP6 in Chapter 4 lacked a robust analysis of the representation of the timings of the monsoon. The principal reason for this shortcoming was the lack of a robust, widespread method to diagnose onset and retreat dates in the various regions of the AMS with the various datasets available. This chapter aimed to address this issue by developing a new method to compute onset and retreat dates for the purpose of intercomparison between multiple observational and model data.

The novel method described in this chapter uses pentad-mean precipitation data to compute a wavelet transform over multiple temporal scales from which a set of coefficients and diagnostics are used to determine onset and retreat dates. The wavelet function used is the Haar wavelet, a wavelet typically used to find abrupt changes in signals. Onset is defined as the maximum of the sum of the coefficients of the wavelet transform computed over a range of temporal scales or dilations. These dilations were found to provide the best results in a range from 28 to 54 pentads. Monsoon retreat is similarly defined but uses the minimum of this sum of wavelet transform coefficients. The use of this method is illustrated using multiple observational datasets and climate model output. The method is compared to existing methods to find onset and retreat dates in three monsoon regions.

The method performs favourably to existing methods that use precipitation thresholds in the North American Monsoon, as shown by the anomalies of precipitation, wind and geopotential around the onset and retreat dates. The spatial distribution of monsoon onset and retreat in this region was found to be sensibly captured by the wavelet algorithm, illustrating the earlier onset in central-western Mexico and the later onset in northwestern

Mexico, Arizona and New Mexico. The spatial distribution of onset and retreat dates was diagnosed to be very similar between the TRMM, CHIRPS and ERA5 datasets, which suggests that the method produces similar results in datasets with different resolutions and climatologies. These results confirm that these models reasonably simulate the seasonal cycle of precipitation in the North American monsoon. This result also suggests that the method is robust to be used at the grid-box scale, and not just for region-averaged time series.

The WT method also compares well to a hydrologically defined index (HOWI) in the Indian Monsoon, although the WT better captures the precipitation variations whilst HOWI better captures changes to the moisture transport. However, the WT method is also able to capture strong differences in moisture transport around the onset and retreat dates, in both models and observations. The WT method obtains a later onset and retreat as compared to the HOWI index, which is possibly associated with a lag between the moisture transport about the Arabian Sea (as diagnosed by HOWI) and the precipitation over mainland India (as measured by the WT method). The spatial distribution of onset and retreat dates in the Indian Monsoon region, diagnosed using the WT method seems to be relatively consistent and coherent amongst the observational datasets, as the mean onset date in mainland India was found at pentad 32. Onset is earliest on the western coast of India and the onset date appears to be very homogeneous in central India.

The WT method was extended to characterise the timings and strength of the Midsummer Drought (MSD), using the same principle as for determining onset in the Indian monsoon, but computing the WT over smaller dilations around the onset and retreat dates. By using randomly-generated time series, the spatial distribution of grid-points displaying a robust MSD signal was found in Cuba, the northwestern coast of Central America and several regions of south and north-eastern Mexico. The MSD in southern Mexico and northern Central America is found to start around pentads 35 and 36 (last week of June) and end around pentad 48 (mid-August) in most observational datasets and the ERA5 reanalysis. To our knowledge, this extension of the WT method provides one of the very few methods for characterising the MSD on sub-monthly scales.

The WT method is in many ways similar to the agronomical and threshold methods (e.g. Liebmann and Marengo, 2001; Moron and Robertson, 2014), as the implementation of the

method uses a subjective determination of the dilation scales; these scales are comparable to the persistence and window parameters of the threshold methods. However, the WT method presented has three main advantages over most threshold methods. First, the method produces robust results for the Indian and North American monsoon of onset and retreat, and spatial distributions comparable to previous methods (Moron and Robertson, 2014) while not being subject to 'false hits' nor years without an identification of the onset and retreat dates. In other words, the method provides robust results without requiring further treatment of years with false hits or undetermined years.

The second advantage of the method is portability, or utility, as the method shows robust and consistent results for three observational datasets, a reanalysis and climate model experiments with varying climate forcing but without any constraint or treatment of the data beforehand and in three different regions with different seasonal cycles. In other words, this method is robust across datasets and regions. In contrast to rigid threshold techniques (e.g. Liebmann and Marengo, 2001), the identification of onset and retreat for each time series, e.g. at each grid-point, is based upon coherent temporal changes within each precipitation time series while not using parameters determined *a priori* specifically for a region. The WT method can then be used in any time series, regardless of the origin of the time series, without any further change or consideration than those established by the dilations scales determined in section 2.2.1. The portability of the method also means that the method can be implemented as a *local-scale* method applied at the grid-box scale for high-resolution datasets such as CHIRPS as well as for regional scales using area-averaged time series.

Third, and in contrast to typical threshold methods, the wavelet method can be applied to climate model output straightforward using the same configuration of dilation scales, a feature of the method that is illustrated by our analysis of several experiments using the Hadley Centre models. The treatment of the data does not require any normalisation or statistical treatment even when used for grid-point time series for different regions or experiments with varying forcing where the seasonal cycle or total annual rainfall may change notably within the model time series. **The method may be used for other purposes such as finding active and break phases of a monsoon, however, due to the constraints of the WT, the method cannot be used for forecasting purposes, or real-time identification of the onset and retreat.**

This chapter provides the main tool for the following chapter, which aims to better understand the physical mechanisms behind the MSD, a question that would be difficult to address without the existence of a robust method for determining the timings of the MSD at the pentad-scale.

6

The Midsummer drought in the MOHC CMIP6 experiments

This chapter investigates the mechanisms associated with the bimodal seasonal cycle of precipitation, also known as Midsummer drought (MSD), of southern Mexico and Central America using CMIP6 experiments produced by the Met Office Hadley Centre. The chapter evaluates three theories for the MSD that exist in the literature: SST and cloud-radiative feedbacks, the double crossing of the solar declination angle and the moisture transport associated with the Caribbean Low-Level Jet (CLLJ).

6.1 Introduction

A bimodal signal in the climatological seasonal cycle of precipitation has been documented in several regions of southern Mexico, Central America and the Caribbean; most commonly referred to as Midsummer drought (MSD Mosiño and García, 1966; Magaña et al., 1999; Gamble et al., 2008; Perdigón-Morales et al., 2018; Zhao et al., 2020). Since the first observational descriptions of the MSD, research has aimed to understand the physical mechanisms that cause the two-peak structure of precipitation (e.g. Hastenrath, 1967; Magaña et al., 1999; Curtis, 2002; Herrera et al., 2015; Maldonado et al., 2017; Straffon

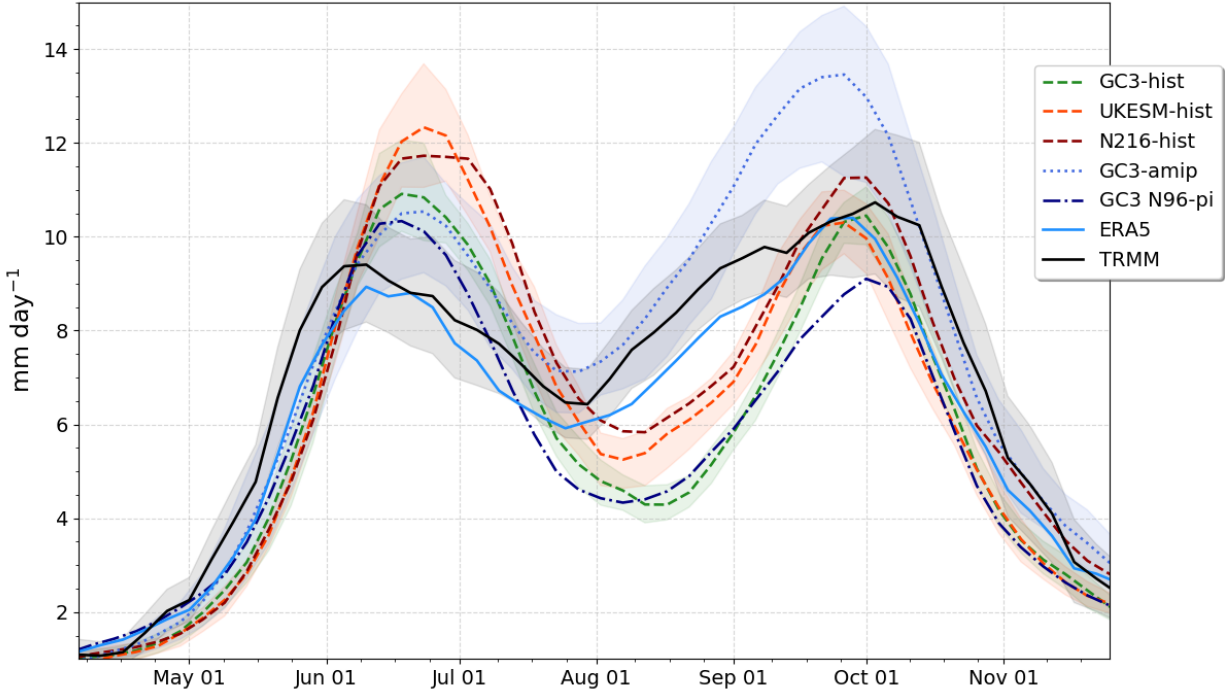


Figure 6.1: Pentad-mean precipitation in southern Mexico and northern Central America [95–86°W, 11–19°N]. The shading for the TRMM dataset is a measure of observational uncertainty obtained by bootstrapping the interannual variability whereas the shading for the CMIP6 experiments show the ensemble spread where multiple ensemble members were available.

et al., 2019; Perdigón-Morales et al., 2019; Zermeño-Díaz, 2019). Section 2.3 summarises the literature on the theories for mechanisms for the MSD and their limitations.

Moreover, most global climate models from the CMIP5 cohort struggle to reasonably reproduce the seasonal cycle of precipitation in the region (Rauscher et al., 2008; Ryu and Hayhoe, 2014) which has led other studies to use regional climate models to understand mechanisms and future projections (Fuentes-Franco et al., 2015; Cavazos et al., 2020). Less attention has been given as to why some GCMs reproduce or not the bimodal seasonal cycle; for instance, Ryu and Hayhoe (2014) only analysed how biases in large-scale features of CMIP3/5 models such as the North Atlantic Sub-Tropical High (NASH) could influence the representation of the MSD. Chapters 4 and 5 show that the CMIP6 MOHC simulations reproduce the timings and strength of the bimodal signal of precipitation with reasonable skill (Figure 6.1), albeit with a stronger first peak and a later onset of the MSD.

The lack of agreement in the literature on the leading mechanism for the bimodal seasonal

cycle of precipitation and the good representation of the spatial and temporal characteristics of the MSD in the MOHC CMIP6 experiments are the main motivation for this chapter. This chapter aims to increase our understanding of the physical mechanisms associated with the MSD of southern Mexico and northern Central America, also referred to as Mesoamerica, by diagnosing relevant processes that are represented in these MOHC CMIP6 experiments.

Three leading hypotheses (section 2.3) are investigated for the MSD of southern Mexico and Central America: the SST-cloud-radiative feedback proposed by Magaña et al. (1999), the solar declination angle hypothesis (Karnauskas et al., 2013) and the CLLJ as a modulator for moisture transport and convective activity in Mesoamerica (Herrera et al., 2015; Zermeño-Díaz, 2019). The main features of the three mechanisms are illustrated in Figure 6.2. The SST cloud-radiative feedback mechanism (Fig. 6.2a) proposes that the peaks and trough of precipitation in the seasonal cycle are a result of a similar seasonality in the East Pacific SSTs and surface humidity. During the first peak of precipitation, cloud radiative effects (CREs) block shortwave radiation from reaching the surface in addition to increased latent heat fluxes from the ocean to the atmosphere which cool the SSTs and lead to a decrease in convective activity and precipitation. During this drier period with less cloud cover, incoming shortwave increases again and raises East Pacific SSTs above 29°C and surface humidity leading to the second peak of precipitation.

The solar declination angle hypothesis (Fig. 6.2b) argues that total shortwave radiation absorption at the surface is the key element that controls the surface energy balance and the strongest control of the seasonal cycle of incoming shortwave is the solar declination angle. The total shortwave absorption by the surface modifies the surface moist static energy, specifically the surface moisture, which in this framework is the ultimate control of precipitation. In Central America, the solar declination angle crosses twice during the summer, once at the start and once at the end, and evidence by Karnauskas et al. (2013) suggests that precipitation follows the solar declination angle and surface moist static energy with a lag of a few weeks.

Finally, the third mechanism investigated in this chapter argues that the seasonal cycle of the CLLJ, possibly influenced by the seasonal variations to the NASH, modifies moisture transport in the region (Fig. 6.2c). Studies have noted that the increase in the jet strength

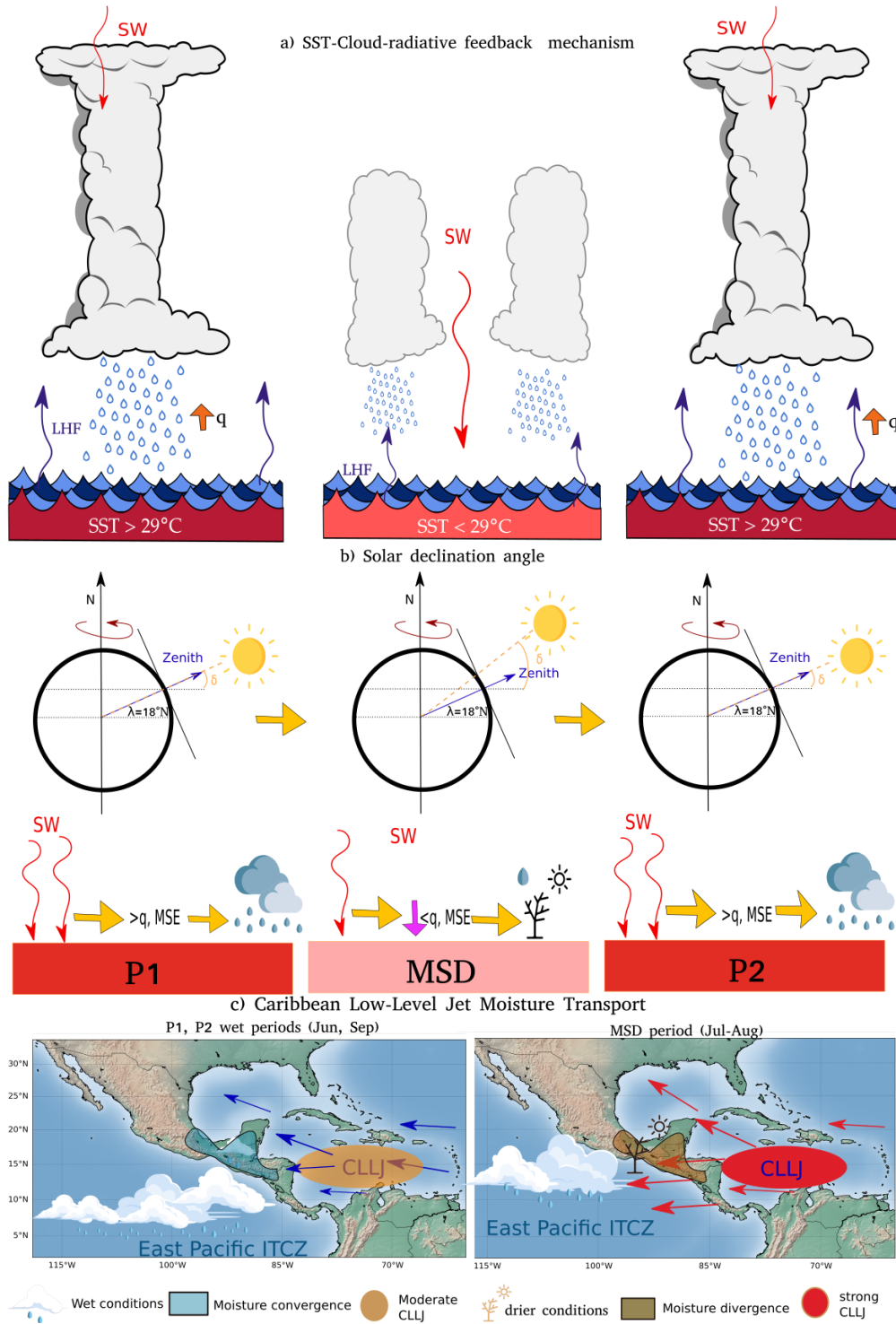


Figure 6.2: Schematic of the three mechanisms analysed in this chapter, a) the SST cloud-radiative mechanism, (b) the solar declination angle and (c) the moisture divergence mechanism driven by the CLLJ. In all panels, three stages of the MSD are represented (left) the first peak period, (middle) MSD and (right) the second peak period.

at the midsummer coincides with a reduction of rainfall over mainland. This argument appears more frequently in studies to explain the MSD of the Caribbean (e.g. Martinez et al., 2019), but suggestions have also been made that the CLLJ variations could control the total moisture transport over the continent (Herrera et al., 2015). Specifically, the hypothesis is that in July the strengthening of the CLLJ decreases the convergence of moisture over the continent and the total water content over western Central America, explaining the slight decrease in precipitation during the MSD period.

The remainder of this chapter is presented as follows. Section 2 describes the observational data and the CMIP6 experiments and summarises how the WT method is implemented to diagnose the timings of MSD. Section 3 evaluates the representation of the key features of the regional climate in the CMIP6 experiments and in ERA5. Then, the roles of the East Pacific SSTs (section 4), cloud-radiative effects and surface shortwave absorption (section 5) and the CLLJ and moisture transport (section 6) are investigated using composite and regression analysis. Finally, a short investigation of the MSD using the moist static energy budget is given in section 7. A summary and discussion is presented in the final section of this chapter.

6.2 Data and methods

6.2.1 Observations and reanalysis data

All the data used in this chapter are described in more detail in Chapter 3. This chapter uses the precipitation datasets of TRMM and CHIRPS. The remaining diagnostics are taken from ERA5 at the 0.75° resolution and for the period 1979-2019. ERA5 precipitation data is used throughout this chapter to compare against the models, and not observed datasets, because of two reasons. Firstly, observational (satellite or surface station) data of all diagnostics are not available on long periods at the daily resolutions required for this study, for example of the wind flow or moisture profiles over the ocean region. Secondly, ERA5 precipitation in the MSD region closely follows TRMM and CHIRPS (Fig. 6.1), and the previous chapter shows that ERA5 reasonably reproduces the mean timings for the MSD compared to TRMM and CHIRPS. Therefore, ERA5 can be compared to the simulations as another model; one that is more realistic as the reanalysis is partially driven

by the observed state of the atmosphere through the assimilations of radiosondes taken in the region as well as satellite data of various quantities (Hersbach et al., 2020).

6.2.2 CMIP6 data

This chapter uses the output from realizations of the HadGEM3 GC3.1 run at two resolutions at N96 and N216 and from UKESM1. These experiments are described in section 3.2.2 and summarised in Table 3.2. The main experiments used in this chapter are the pre-industrial control (piControl), AMIP, and historical experiments. The pre-industrial control experiments use a constant external forcing for the year 1850, and are relatively longer integrations (Menary et al., 2018), whereas the historical experiments use our best estimate of the time-varying aerosol and greenhouse gas emissions from 1850 to 2014 (Eyring et al., 2016; Andrews et al., 2020). The AMIP experiments use the same external forcing as the historical experiments but also "nudge" the SSTs using observational products, thereby decoupling the atmosphere from the ocean and removing SST biases (Eyring et al., 2016).

In addition to these deck experiments used in previous chapters, this chapter uses experiments from the Cloud-Feedback MIP (CFMIP) (Webb et al., 2017) and ScenarioMIP (O'Neill et al., 2016) activities of CMIP6 (see Table 3.2). The experiments from CFMIP are the GC3-amip lwoff in which longwave radiative effects are turned off and amip-p4K and amip-m4K in which the SSTs are increased and decreased 4 K, respectively, globally from the main amip experiment. The runs used from the ScenarioMIP are forced using the Shared Socioeconomic Pathways (SSPs): SSP1, SSP2 and SSP5 which correspond to Sustainability, Middle of the Road and Fossil-fuel development narratives, respectively (O'Neill et al., 2017). In these scenarios, global mean temperatures increase at the end of the 21st century, relative to pre-industrial levels, between 0.40 to 2.05°C, 1.27 and 3.00°C for SSP2 and 2.40 and 5.57°C for SSP5 (Tebaldi et al., 2021).

6.2.3 Determination of the timings of the MSD

Chapter 5 describes a wavelet transform (WT) method that can determine the timings of the MSD in observational gridded datasets, reanalysis and climate model precipitation time series. This chapter uses the WT method to determine the onset (MO) and retreat

(MR) of the monsoon rainy season, as well as the onset (MSDO) and end (MSDE) of the MSD. MO and MR are determined by the maximum and minimum sum of WT coefficients computed from a dilation scale vector ranging from 24 to 54 pentads. After MO and MR are determined, a second WT is computed with dilation scales from 10 to 24 pentads and the minimum sum of the WT coefficients corresponds to the onset of the MSD and the maximum to the end of the MSD (MSDE). Similarly, the timings of the first (P1) and second (P2) peaks of precipitation are determined from the results of the WT method: P1 is defined as the period between the MSDO and the preceding 4 pentads or 20 days, whereas the second peak is defined as the period between the date of MSDE and the subsequent 4 pentads.

An example of this separation of the MSD timings for each year is given in Figure 6.3, for precipitation observed from TRMM in 2017 over the study region. The area of study of this chapter is in southern Mexico and northwestern Central America (depicted in Figure 6.4) a region with strong and robust MSD signals (see Chapter 5). The WT method was applied to the TRMM, CHIRPS and ERA5 datasets and in the model precipitation time series area-averaged over the study region.

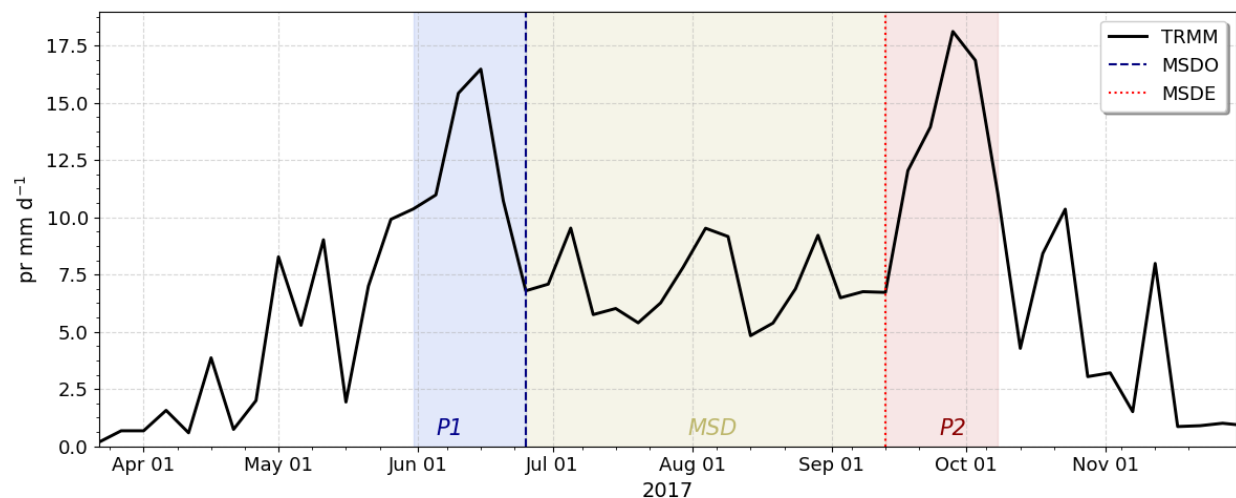


Figure 6.3: Pentad-mean precipitation averaged over the study region [95–86°W, 11–19°N] in the TRMM dataset for the summer of 2017. The timings of the onset (MSDO) and end (MSDE) of the MSD, as well as the first (P1) and second (P2) peak periods and the MSD periods are highlighted.

6.3 Climatological features

The seasonal cycle of precipitation in the MSD region (Figure 6.1) is reasonably well simulated by the CMIP6 experiments and by ERA5, as shown in previous chapters. The two-peak structure of the MSD is observed in TRMM and ERA5 as two precipitation maxima, the first peak found during early to mid-June and the second peak at the end of September, separated by a drier period that spans from late June to late August. The precipitation in ERA5 agrees well with the seasonal variation of TRMM and the mean rates during the first peak, the MSD and second peak periods.

The MSDO in the CMIP6 experiments is diagnosed one or two pentads after TRMM and ERA5 and the experiments show a stronger variation of precipitation between the first

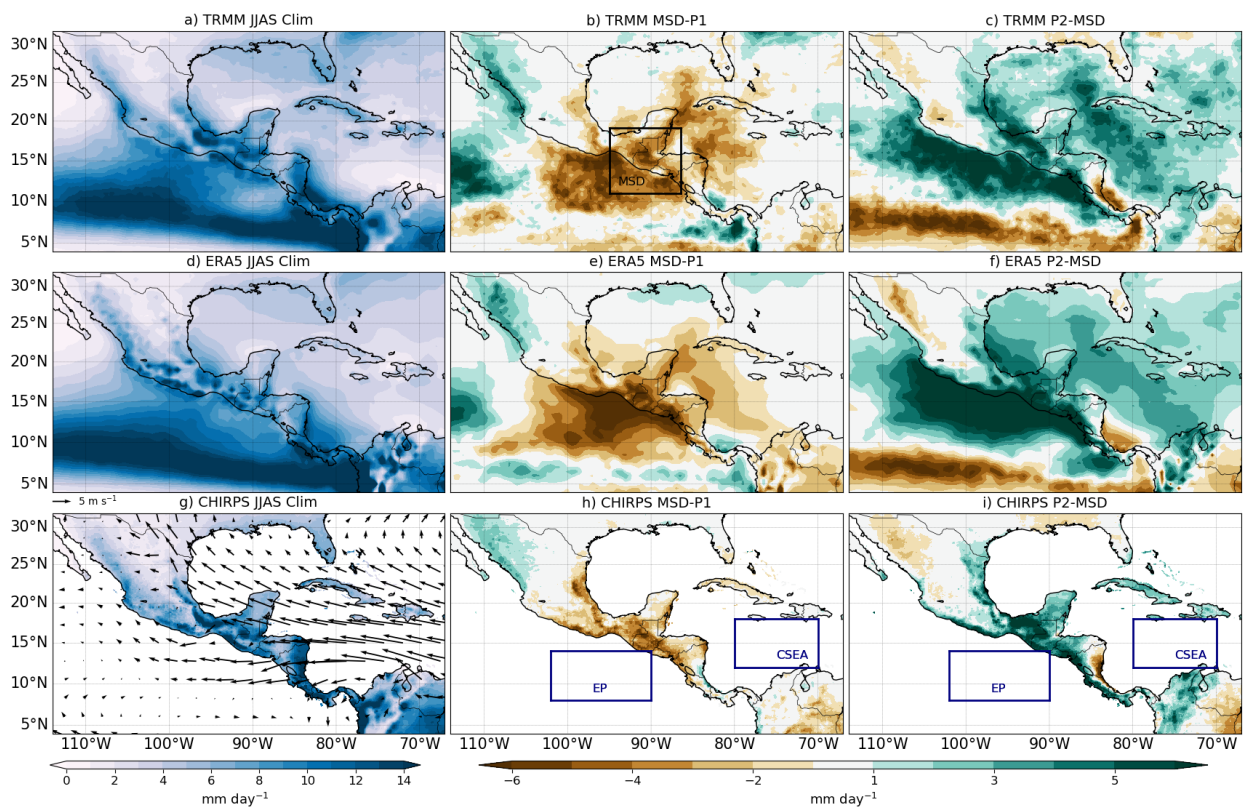


Figure 6.4: (a, d, g) Climatological JJAS rainfall and the difference between (b, e, h) the midsummer drought and the first peak (MSD-P1) periods and (c, f, i) between the second peak and the midsummer drought (P2-MSD) periods for (a-c) TRMM, (d-f) ERA5 and (g-i) CHIRPS. The climatological low-level winds (at 850 hPa) for JJAS in ERA5 are shown in c). The boxes in panels b, h and i show the definitions of the MSD, EP and CSEA regions that are used throughout this chapter.

peak and the MSD. A noteworthy feature is that most experiments simulate a drier MSD period but wetter peak periods. In particular, the pre-industrial control experiments show a higher magnitude of precipitation during the first peak and the MSD period whereas GC3-amip experiments are characterized by a wetter second peak.

The climatological distribution of precipitation and the temporal differences within the MSD timings in ERA5 agrees well with TRMM and CHIRPS (Figure 6.4). ERA5 reasonably captures the climatology of precipitation over land over the East Pacific ITCZ. The biases of JJAS-mean precipitation in ERA5 (Figure 6.5) are positive over the East Pacific Ocean and western Mexico, and negative over land in southern Mexico and Central America.

The patterns of the MSD-P1 and P2-MSD differences in ERA5 (Fig. 6.4) also agree well with TRMM. The precipitation differences associated with the MSD timings within the box in Figure 6.4b extend well outside the study region comprising the easternmost Pacific Ocean, the entrance to the Gulf of Mexico and western Caribbean Sea, particularly in the P2-MSD panel. The interannual variability of mean boreal summer rainfall, and P1 and P2 magnitudes between ERA5, TRMM and CHIRPS are also very similar (not shown). This means that ERA5 may be used to investigate what processes best explain the interannual variability of precipitation of the reanalysis, specifically, what factors modulate the variations of the P1-MSD from one year to the next.

The simulations (Figure 6.6) have important biases in the magnitude of the precipitation in the East Pacific ITCZ with a positive bias of 3-6 mm day⁻¹ as well as a dry bias over

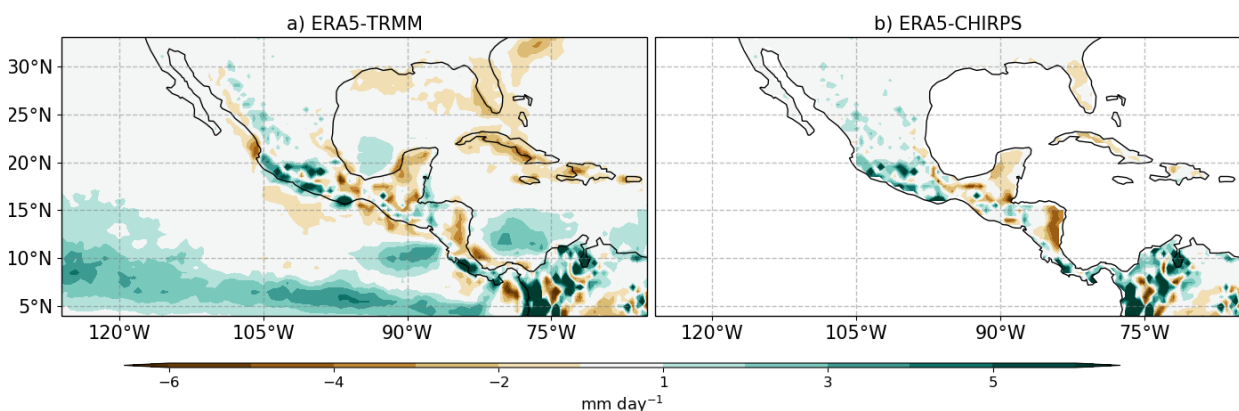


Figure 6.5: (a, b) JJAS precipitation biases in ERA5 when compared to (a) TRMM and (b) CHIRPS.

southern Mexico and Central America, as shown in chapter 4. These biases are much larger in the simulations than in ERA5. The simulations capture the spatial patterns associated with the MSD stages, characterised by the highest differences found on the west coast of southern Mexico and northwestern Central America. In agreement with ERA5 and TRMM, the precipitation differences in the MSD region in the simulations are always opposite to that of the North American monsoon region, e.g., in Figures 6.4 and 6.6 the North American monsoon is wetter when the dry period begins in the MSD regions.

The mean rainfall observed in the three periods (P1, P2 and the MSD) in the simulations varies notably between experiments with different configurations and with external forcing (Figure 6.7). The scatter of the first and second peak and the MSD mean rainfall rates show that the mean precipitation rate at each stage is not necessarily linearly related to another, i.e., a larger magnitude of the first peak of precipitation does not imply a wetter or drier

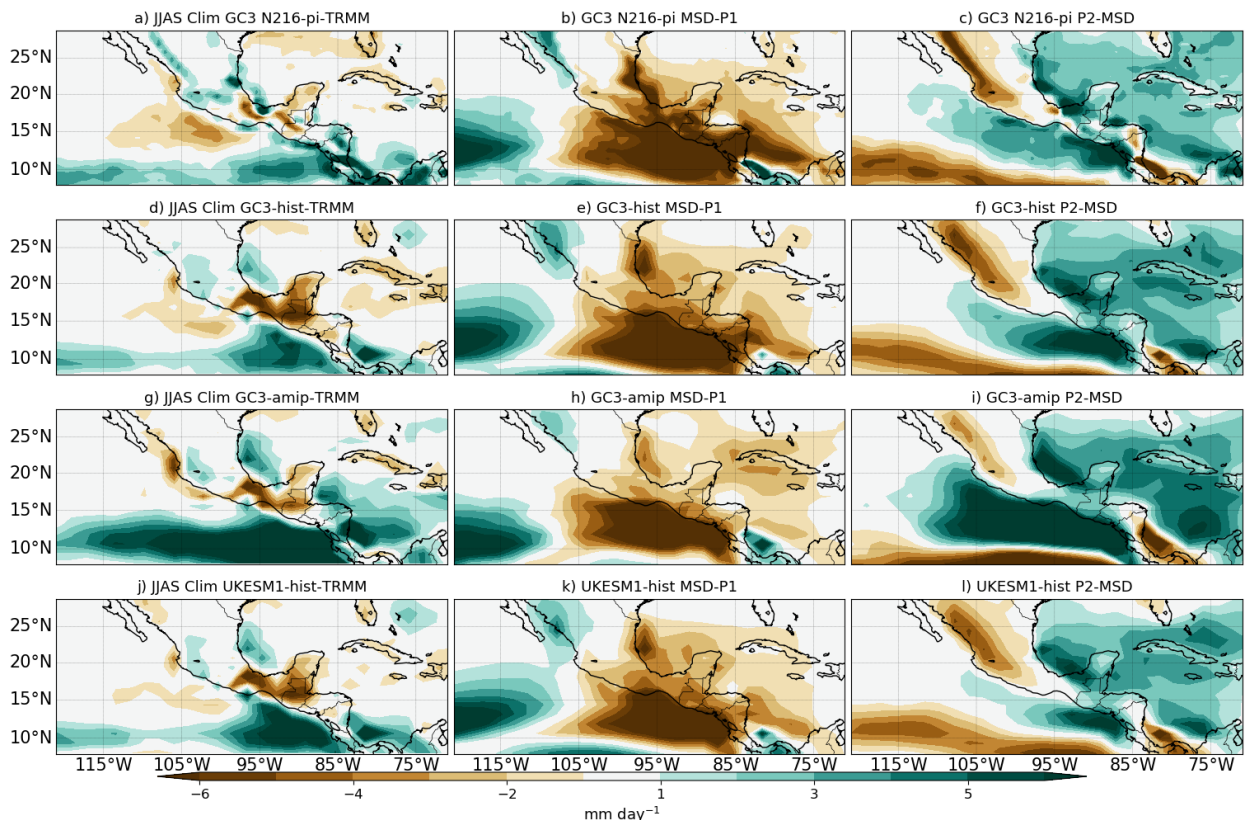


Figure 6.6: (a, d, g, j) JJAS model bias compared to TRMM and the difference between (b, e, h, k) the midsummer drought and the first peak periods and (c, f, i, l) between the second peak and the midsummer drought periods for four different simulations.

MSD period. The atmosphere-only runs, GC3-amip, are a good example of this behaviour as the mean rainfall during P1 is roughly the same as in the rest of the simulations but the mean rainfall during the MSD is slightly larger than in the rest of the simulations.

The magnitude of the first decrease in rainfall (MSD-P1) and the late-summer increase (P2-MSD) also show a significant spread amongst experiments (Figs. 6.7c-d), which also suggest that there is only a modest relationship between the magnitude of the MSD and the magnitudes of the two peaks of precipitation in these simulations. The scatter of ERA5 in all panels is notably close to that of TRMM and CHIRPS, which is further evidence that

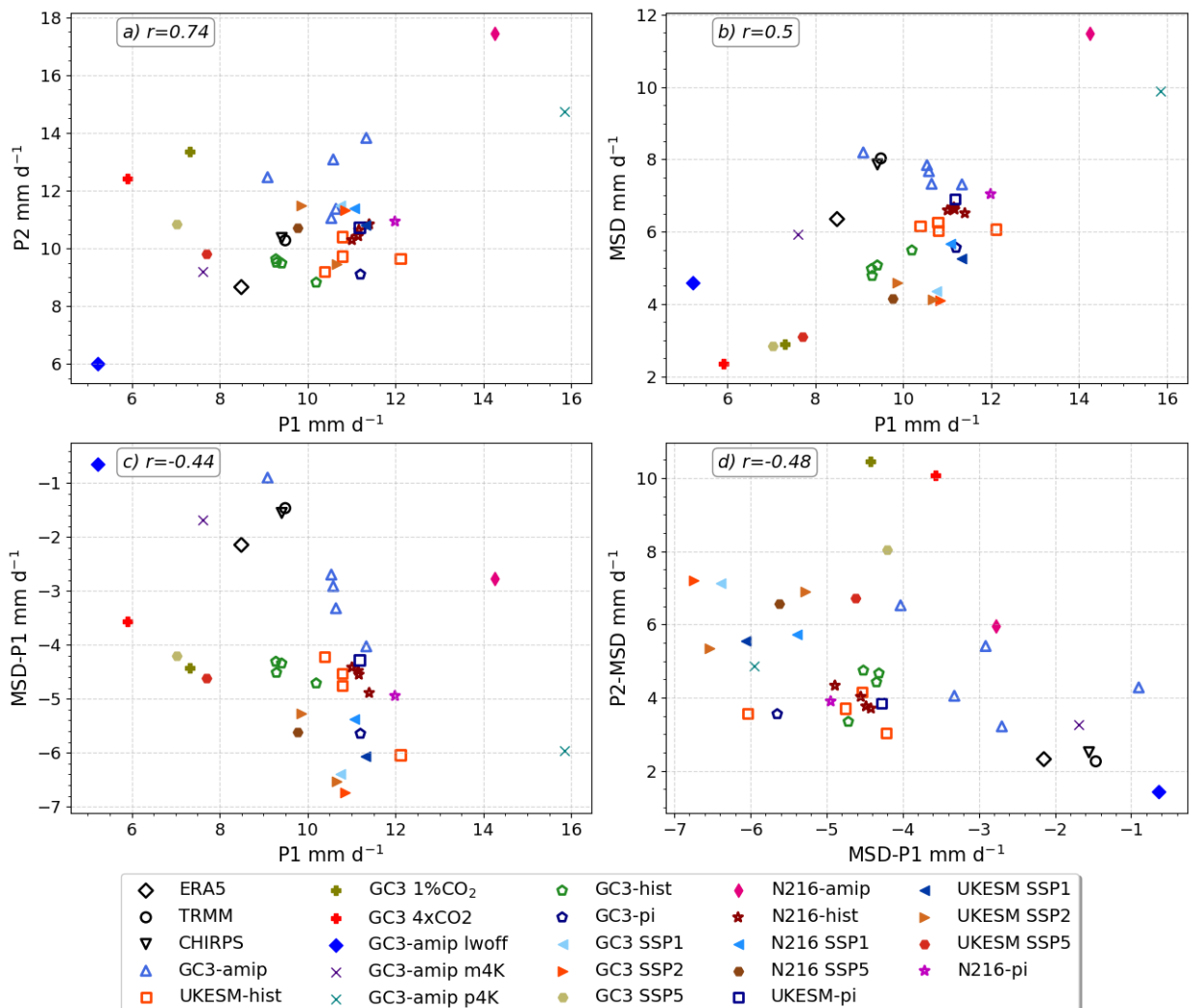


Figure 6.7: (a, b) Scatter plots of the mean values of precipitation [mm day⁻¹] for TRMM, ERA5, CHIRPS and the CMIP6 experiments (see 6.2.2) during the first peak (P1), the MSD and the second peak (P2) periods and (c, d) the precipitation differences between the three periods. The region used for this averages is illustrated in Figure 6.4.

the timings and strength of the MSD is well represented by this reanalysis. In contrast, the medium-resolution atmosphere-only run (N216-amip) shows the highest bias in precipitation throughout the three stages of the wet season.

This result is noteworthy because this configuration uses a higher resolution than GC3 N96 and is forced by observed SSTs, yet the simulation cannot capture the observed precipitation rates and is strikingly the worst simulation overall. One explanation for this result is that in the low-resolution simulations there are notable dry biases over land (Figs 6.6) and wet biases over the ocean, and the medium-resolution simulation improves the dry bias over land more so than the wet bias over the ocean leading to an overall increase of the bias over the whole region.

The outgoing long-wave radiation (OLR) and vertical velocity (ω at 500 hPa) differences associated with the MSD were computed using the WT method for each dataset (Figure 6.8). These composite results confirm that the MSD is not a local-scale feature but convective activity varies coherently in neighbouring regions. From the first peak period to the MSD, OLR and ω , increase in the easternmost Pacific, southern Mexico and northern Central America and extend into the Caribbean islands and Sea; because ω is defined as $\omega = DP/Dt$ these positive anomalies are indicative of weaker ascent.

In contrast, two regions show opposite responses to the MSD. A region several degrees west into the East Pacific Ocean (125°W) and another region north of the study region, i.e., the North American monsoon region, show signs of negative OLR and ω anomalies, in the MSD-P1 panels. These negative anomalies are indicative that, simultaneously to the onset of the MSD, convection is observed stronger and deeper in the North American Monsoon region and in the Pacific region west of the continent. The OLR and ω variations associated with the end of the MSD show a relatively opposite picture to the MSD-P1 differences. Note that several of these features have been described previously by Herrera et al. (2015), who argues that ascending and descending anomalies in the MSD are closely related to the 125°W East Pacific region.

The literature suggests that a number of climatological features of the region play key roles for the MSD (Section 2.3). These climate features include the seasonal cycle of the East Pacific (EP) SSTs, the Caribbean Sea SSTs, the EP zonal wind flow and the CLLJ

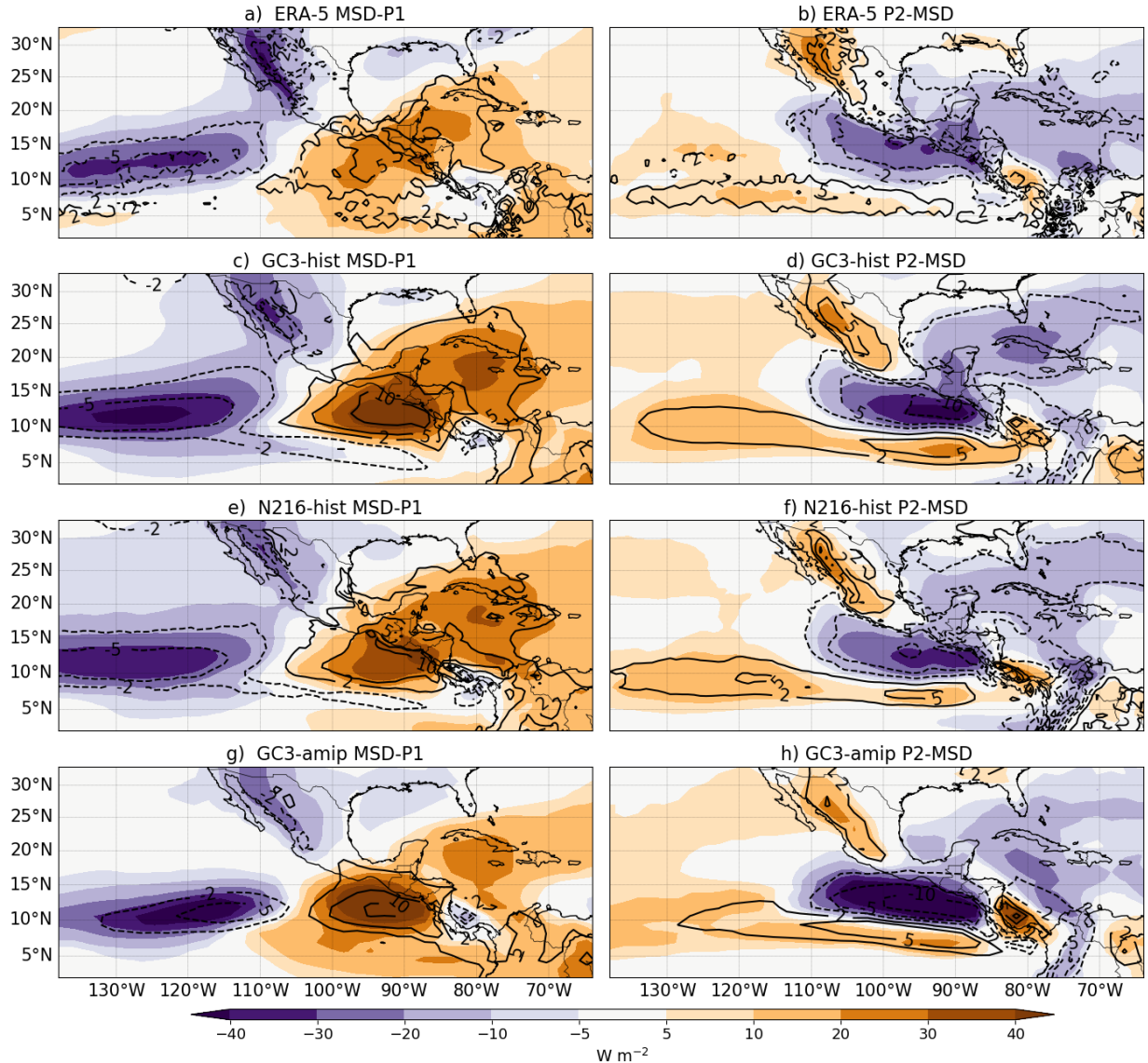


Figure 6.8: Outgoing long-wave radiation (OLR) [W m^{-2}] (shaded) and ω 500-hPa [$10^{-2} \text{ Pa s}^{-1}$] (line contours) differences between the MSD and first peak and the second peak and MSD.

(Magaña et al., 1999; Amador, 2008; Herrera et al., 2015; Straffon et al., 2019; García-Martínez and Bollasina, 2020). The seasonal cycle of these features in ERA5 and the simulations (Figure 6.9) shows that the models are able to replicate the seasonal variations of the SSTs and the zonal wind flow of the region.

The seasonal cycle of EP SSTs (Figure 6.9a) show that the maximum SSTs are found in late May, prior to the first peak of precipitation in Mesoamerica. In contrast, the Caribbean SSTs peak in early fall, about five months later, during late September. After the peak

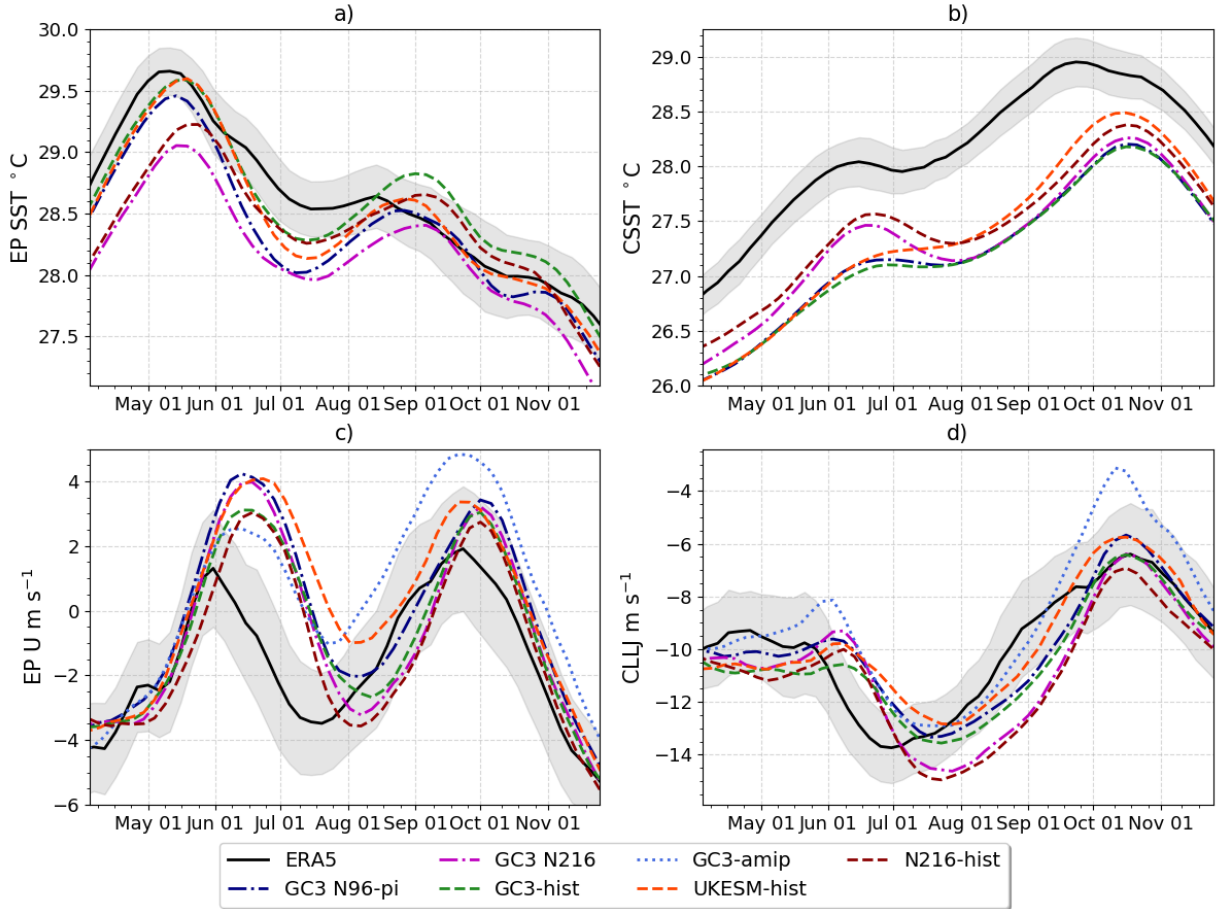


Figure 6.9: Pentad-mean seasonal march of the (a, b) SSTs [$^{\circ}\text{C}$] and (c, d) the low-level (925-hPa) zonal wind flow [m s^{-1}] in (a, c) the easternmost equatorial Pacific and (b, d) the Caribbean Sea. The transparent shading is as in Figure 6.1. The regions used for EP and CSEA averages are illustrated in Figure 6.4h.

SST period in the EP, SSTs decrease to a local minimum found in July both for ERA5 and the simulations. The models show a cold bias in the SSTs in both regions, but this bias is most pronounced in the Caribbean Sea.

The low-level wind flow in the EP shows a bimodal seasonal cycle in ERA5 and the simulations (Fig. 6.9c). The easterly flow in the EP during the spring becomes weaker turning westerly at the end of May and reaching a local maximum in early June in ERA5 and mid-June in the simulations. This local maximum then decreases during June and early July as the zonal wind becomes easterly again. The easterly flow peaks in mid July in ERA5 and two to three weeks later in the simulations. The strength of this easterly flow magnitude is more different between experiments during July and August than in other months. After the

easterly flow peaks in the midsummer, the zonal wind becomes westerly again peaking at the end of September in both ERA5 and simulations. This seasonality of the zonal wind in the EP is similar to the seasonal cycle of precipitation in the region in the models and simulations.

The CLLJ seasonal cycle (Figure 6.9d) is reasonably replicated by the simulations, compared to ERA5, although the peak strength of the CLLJ, which is found during the last week of June in ERA5, is delayed in the simulations by about three weeks, as the simulated CLLJ peaks in mid-July in all the simulations. The simulations follow closely the evolution of the CLLJ in late summer and fall, except for a notable bias in GC3-amip in Oct-Nov characterised by a weaker than observed CLLJ.

6.4 The role of East Pacific SSTs

The EP SSTs are a key element of mechanism proposed by Magaña et al. (1999), which argues that the EP SSTs, surface moisture, cloud radiative effects and surface fluxes are part of a feedback mechanism that explains the two peak structure of the MSD. A key prediction of this mechanism is that EP SSTs, surface moisture and turbulent fluxes exhibit a bimodal seasonal cycle in which EP SSTs and surface fluxes decrease during the first peak period and increase during the Midsummer drought period. In other words, this hypothesis predicts that the seasonal cycle of EP SSTs should be similar to the evolution of precipitation but out-of-phase, with the SSTs leading the precipitation. This section aims to evaluate these predictions for ERA5 and for the CMIP6 experiments.

According to the feedback mechanism, the EP SSTs cool down during or slightly prior to the onset of the MSD and then increase during the MSD period which then enhances precipitation and causes the second peak in late summer. However, in ERA5 the EP SSTs only very slightly increase during the MSD (Jul-Aug) and cool notably in late August and September in synchrony with the second peak in deep convection and precipitation (Figs. 6.1 and 6.9a). In the models, there is indeed a second peak in EP SSTs in late summer found in early September and therefore nearly synchronous to the second peak of precipitation. While EP SSTs clearly lead precipitation in May-June, the SST-precipitation relationship in mid and late summer is less obvious. In the models, the second peak of

SSTs is nearly synchronous to the second peak in precipitation, which seems to contrast with the predictions of the SST-radiative-convective feedback mechanism.

In order to better understand the relationship between EP SSTs and precipitation over the MSD region, the WT method is used to composite SSTs and surface humidity in the P1, MSD and P2 periods. The spatial distribution of SST and surface humidity changes associated with the MSD (Figure 6.10) suggest that the EP SSTs south of 10°N cool slightly between the P1 and MSD periods, meanwhile the Gulf of California and the northern eastern

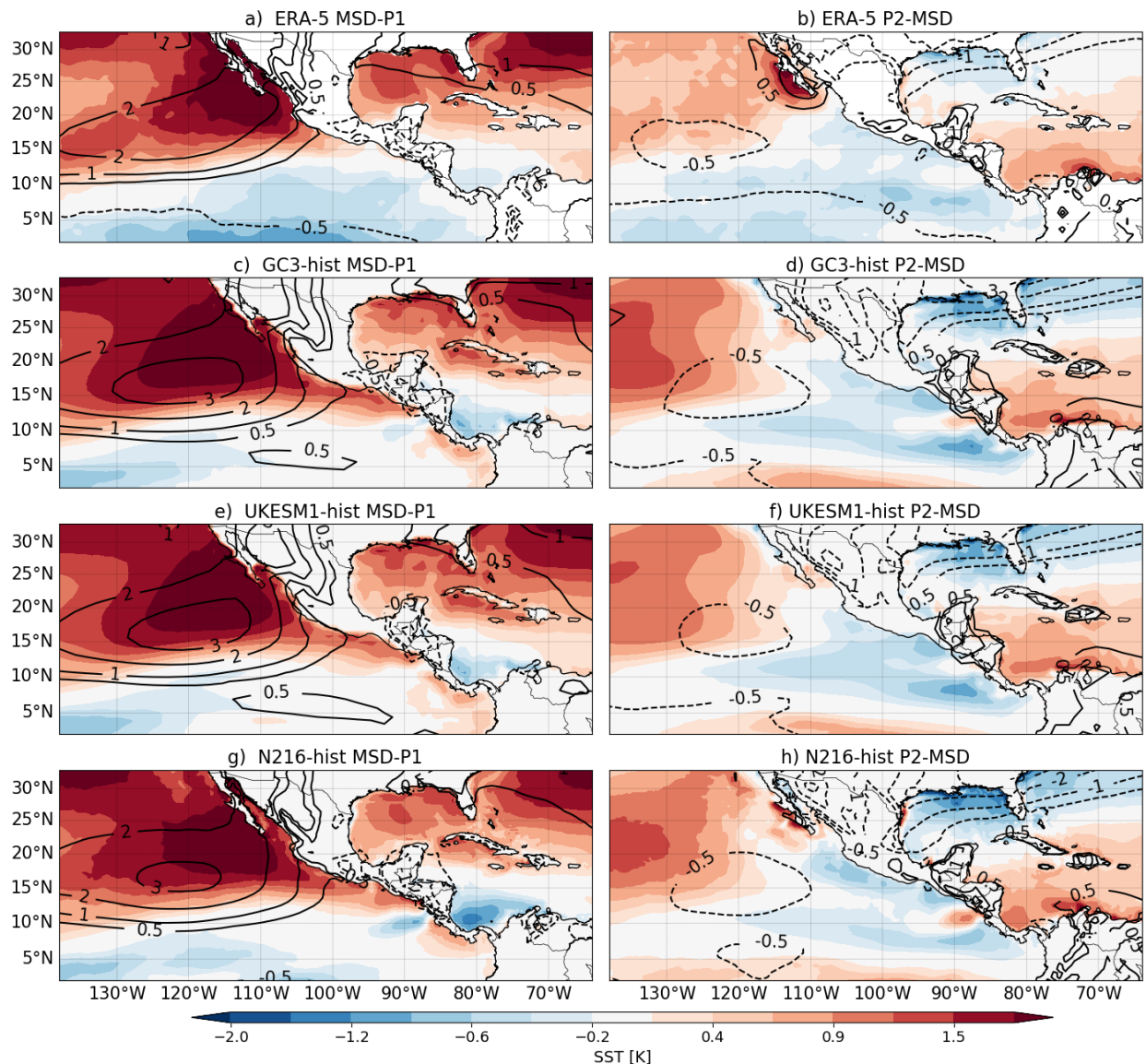


Figure 6.10: As in Figure 6.8 but the anomalies are shown for SSTs [K] (contours) and surface humidity [g kg^{-1}] (line-contours).

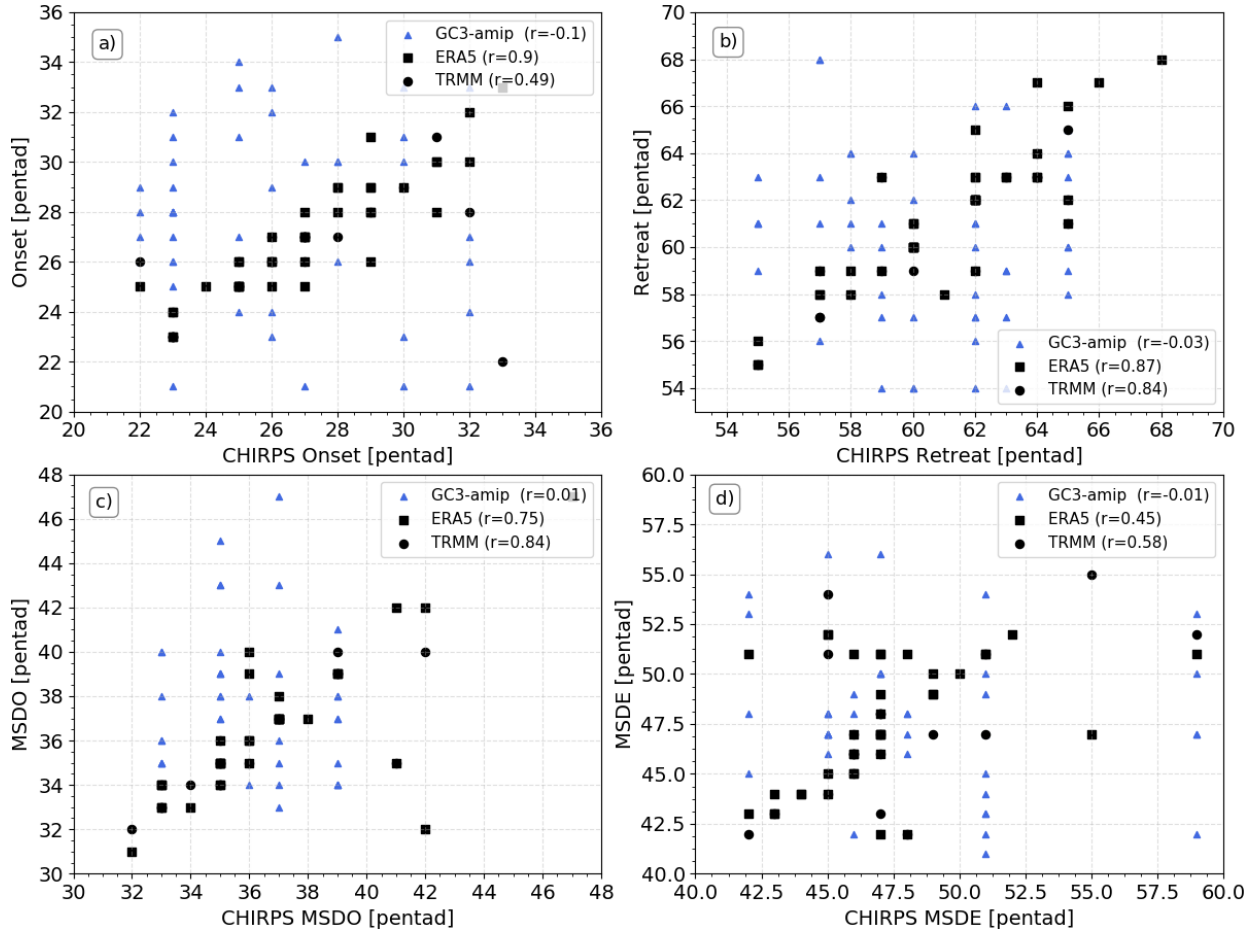


Figure 6.11: Scatterplots of the pentads diagnosed by the WT method as the dates of (a) monsoon onset (MO), (b) monsoon retreat (MR), (c) MSDO and (d) MSDE where the results of the CHIRPS dataset, on the x-axis, are compared with ERA5, TRMM and the GC3-amip simulation, on the y-axis. The legend shows the Pearson r coefficient for each comparison.

Pacific significantly warms. At the end of the MSD (P2-MSD), the EP SSTs decrease in both ERA5 and the simulations. The P2-MSD panels show that the Caribbean SSTs increase, as Caribbean SSTs peak at the end of the summer (Fig. 6.9b).

The historical simulations generally agree with the composite differences of ERA5, with no appreciable warming in the EP region in the MSD-P1 panels, and cooling in the EP and the Gulf of Mexico and warming in the Caribbean Sea in the P2-MSD panels. These results suggest that while the seasonal cycle of EP SSTs show a bimodal signal, when the timings of the MSD in each year of each simulation are examined more closely using the WT method, the EP SSTs do not synchronously warm during or after the MSD, contradicting the radiative-convective feedback mechanism.

Another element of the convective-radiative feedback mechanism is that the SST variability would force changes to the surface humidity and surface humidity would modify precipitation. The surface humidity in the EP and MSD regions, however, is unchanged (less than 0.5 g kg^{-1}) during the various stages of the MSD (Figure 6.10), even though precipitation varies notably during these periods. Instead, the greatest variations in surface humidity are observed west of Baja California and in the North American Monsoon region, both from the P1 to the MSD and from the MSD to the P2 periods. The surface humidity variations in the simulations also agree well with those of ERA5 and are very similar amongst the realizations.

If the EP SSTs play a dominant role in the timings and strength of the MSD, as implied previously (Magaña et al., 1999; Magaña and Caetano, 2005; Herrera et al., 2015), then the simulations with imposed SSTs taken from observations, e.g., the GC3-amip experiment, may be further explored to evaluate the links between SSTs and the timings or strength of the MSD. A scatter plot of the dates (pentads) of the MO, MR, MSDO and MSDE (Figure 6.11) for matching years between the CHIRPS dataset and TRMM, ERA5 and the five ensemble members of GC3-amip shows that the timings of the MSD in GC3-amip are unrelated to CHIRPS and ERA5. The timings from ERA5 agree very well with the CHIRPS and TRMM datasets. This evidence would suggest that the SSTs forcing the model in GC3-amip are not the dominant factor controlling the timings of the MSD in these atmosphere-only runs.

Alternatively, the interannual variability in ERA5 and the differences amongst the MOHC CMIP6 experiments may be further explored to understand whether differences in EP SSTs are related to changes of precipitation in the MSD region. For this purpose, composite differences between the P1, MSD and P2 periods were computed for each variable for each year in each dataset and then averaged to provide a mean value that relates changes in precipitation to different diagnostics in different stages of the rainy season. These results are presented in scatter plots that aim to diagnose emergent properties and physical relationships that explain the different representations of the MSD. [The interannual variability of ERA5 is examined by comparing how each variable can explain the year-to-year differences in P1, P2 and MSD precipitation rates.](#)

The mean difference in SSTs (Figure 6.12a) between the P1 and the MSD periods indicate cooling of the EP for ERA5 associated with the precipitation reduction. In contrast,

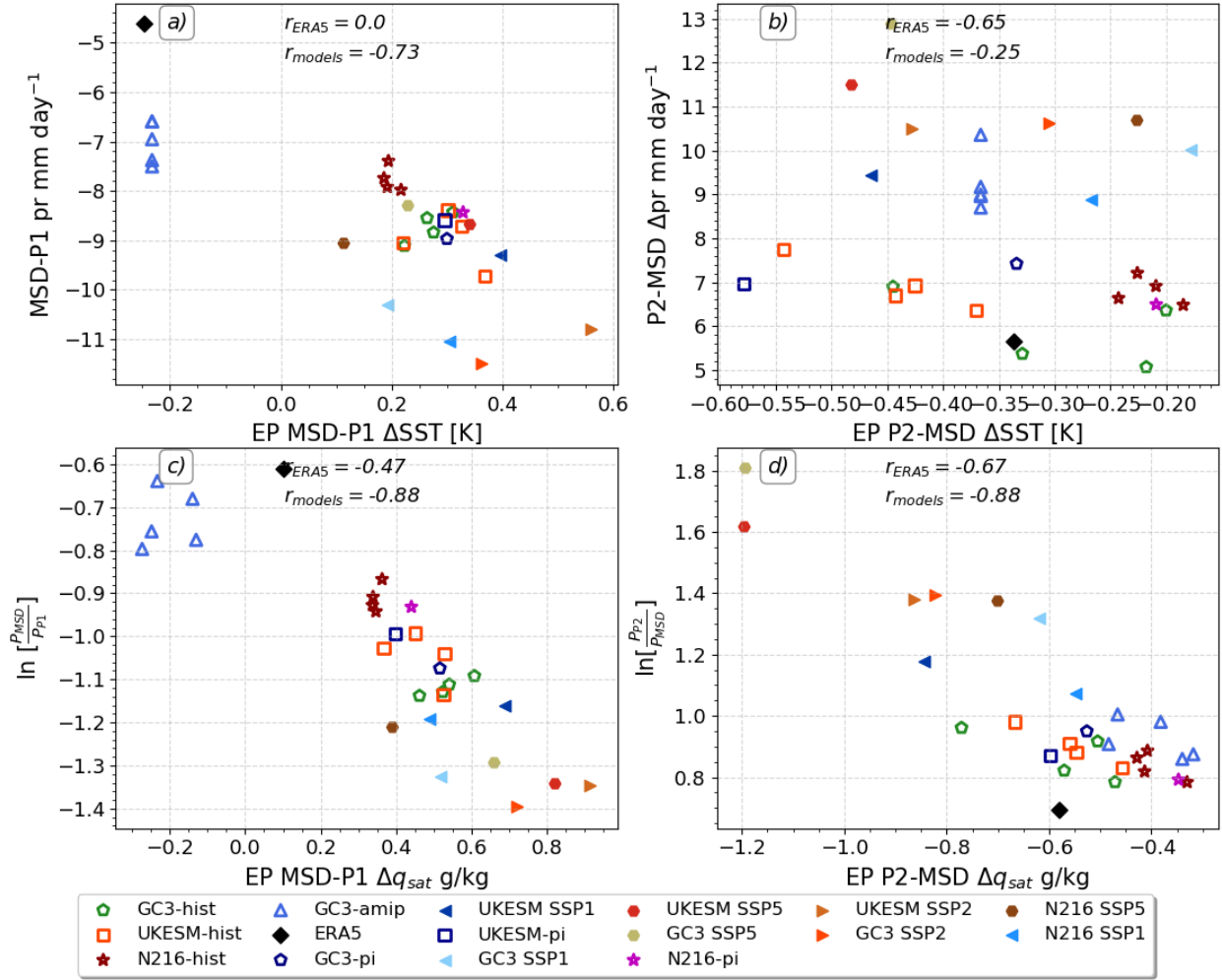


Figure 6.12: Scatterplots of the mean changes in the East Pacific (a, b) sea-surface temperatures (SSTs) and (c, d) surface saturation specific humidity q_{sat} in the x-axis with respect to precipitation variations in the MSD region on the y-axis for the (a, c) MSD-P1 and (b, d) P2-MSD periods. The correlation coefficient of the interannual spread in ERA5 and the multi-experiment correlation coefficient are shown in each panel. Only the mean values of ERA5 are shown but the correlation was calculated for the 40 years in the period of the reanalysis.

the coupled model simulations show a positive SST difference (warming) and a greater precipitation reduction from the P1 to the MSD period. The slight warming signal in the MSD-P1 difference (Figure 6.12a) in the coupled-model experiments suggests that in the models as precipitation decreases during the MSD, the EP SSTs warm by 0.2 K.

During the second peak, the EP SSTs cool (Figure 6.12b) associated with a positive increase in precipitation, suggesting an inverse relationship between EP SSTs and precipitation. However, the relationship does not seem to explain the inter-experiment spread or the

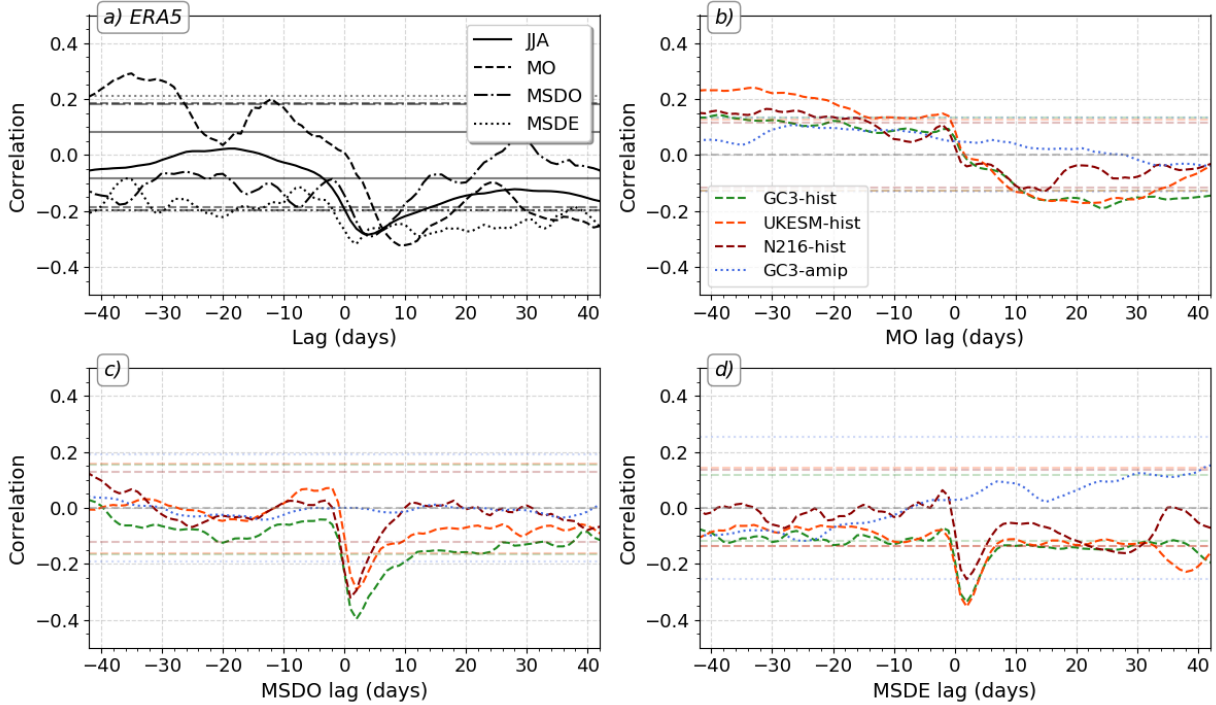


Figure 6.13: Lagged correlations between East Pacific SSTs and precipitation in the MSD region for (a) ERA-5 where the lag 0 date was used in four different ways: first, all the boreal summer JJAS SSTs and precipitation pairings, then lag 0 represents the monsoon onset (MO), MSD onset (MSDO) and MSDE dates. (b-d) as in (a) but for the simulations where the correlations are computed with the SST-precipitation timeseries lagged with respect to the b) monsoon onset date, the c) MSDO date and the d) MSDE date.

inter-annual variability in ERA5 as the correlation coefficients are low and not significant, i.e., a stronger second peak is not associated with a cooler EP SSTs in late summer.

Furthermore, evidence shows that the surface saturation specific humidity q_{sat} , which measures the maximum moisture that a parcel can hold, provides a strong link between precipitation and SSTs on seasonal time-scales over tropical oceans (Yang et al., 2019; Good et al., 2021). For these reasons, Figure 6.12 also shows the relationship between the saturation specific humidity at the surface and precipitation. The temporal changes to q_{sat} associated with the MSD timings (Figure 6.12c,d) are not positively related to changes in the precipitation over the MSD region. Although the inter-annual variability of q_{sat} changes during the MSD-P1 period in ERA5 shows a positive correlation, the mean changes to q_{sat} during this stage are very small compared to the differences in the experiments and, furthermore, the simulations shows an opposite relationship (negative correlation).

For the P2-MSD differences, there is a negative correlation for both ERA5 and the experiments, which means that the strongest second peaks of precipitation are associated with cooler SSTs. A more direct relationship was examined between the EP q_{sat} and EP pr . This analysis (not shown) resulted in a weaker (and negative) relationship in both regions between q_{sat} which suggests that changes to q_{sat} are not key to explain the variability of precipitation.

The previous results have analysed synchronous changes between the EP SSTs, surface humidity, q_{sat} and precipitation over the MSD region, but these relationships may exist with some lags and as suggested by the radiative-convective feedback mechanism, the SSTs should be leading precipitation. Lag-lead correlations (Fig. 6.13) of the EP SSTs and the precipitation in the MSD region show that only during monsoon onset are these two fields significantly positively correlated at lags of \approx -35 days in ERA5 and -40 to -20 days in the historical experiments.

In ERA5, the correlation for all the boreal summer (JJAS) sample is only significant for the SSTs leading precipitation region for negative lags from 30 to 40 days and is only significant (negative correlation) at positive lags at lag +5 days, indicative of an inverse SST-precipitation relationship where the SSTs follow precipitation. In the models (Fig. 6.13b-d), very similar results are found where significant positive correlations at negative lags, indicative of SSTs leading precipitation, are only found for the MO panel, whereas for MSDO and MSDE panels, the correlations are only significant at positive lags and for negative correlations, indicative of the precipitation leading the SSTs on the scale of 3-5 days and SSTs decreasing with increased precipitation.

This section investigated the radiative-convective feedback hypothesis by Magaña et al. (1999). Results in this section show that in observations, the EP SSTs do not exhibit a double-peak seasonal cycle, so the second peak of precipitation over the MSD region cannot be driven by a second peak in EP SSTs in late summer. Furthermore, evidence shows that the variations of precipitation during the midsummer are not statistically related to variations in EP SSTs in ERA5 or in the CMIP6 simulations, contradicting the main arguments of this hypothesis.

6.5 The role of cloud-radiative effects

The mechanisms proposed by Magaña et al. (1999) and Karnauskas et al. (2013) suggest that the net shortwave energy absorbed by the surface is key in the driving mechanism of the MSD. Magaña et al. (1999) argue that tall convective clouds influence the net shortwave (SW) flux at the surface and suggest that the cloud-radiative effects (CREs) experience seasonal changes that occur at the same as the MSD and are linked to the bimodal signal of precipitation. In turn, Karnauskas et al. (2013) argue that the seasonal march of solar insolation determined by the solar declination angle controls the net SW absorbed by the surface and this absorption of SW energy modulates the seasonal cycle of the surface energy balance and of precipitation. This section evaluates the predictions of these theories concerning CRE and the SW absorbed by the surface.

CREs are coupled to the tropical circulation (Bony et al., 2004; Webb et al., 2017) and influence the timing and strength of monsoons (Guo et al., 2015; Byrne and Zanna, 2020). The longwave (LW) CRE play an important role in the convective heating and moistening of the tropical atmospheric column whereas the SW CRE controls the surface absorption of energy (Allan, 2011). These studies motivate an investigation of the relationships between CRE, and the timing and strength of the MSD. The surface cloud radiative effect (CRE_{surf}) is computed from daily-mean fields following Allan (2011), as the sum of the LW and SW CREs, i.e.:

$$\begin{aligned} \text{CRE}_{surf} &= \text{LWC}\text{RE}_{surf} + \text{SWC}\text{RE}_{surf} \\ &= \text{LDS} - \text{LUS} - (\text{LDS}_{cs} - \text{LUS}_{cs}) + \text{SDS} - \text{SUS} - (\text{SDS}_{cs} - \text{SUS}_{cs}), \end{aligned} \quad (6.1)$$

where the fluxes are depicted as long-wave (L) or short-wave (S) and downwelling (D) or upwelling (U) at the surface (S) and the subscript $_{cs}$ denotes under clear-sky conditions. The long-wave upwelling at the surface (LUS) virtually cancels with the LUS_{cs} because the long-wave emission from the surface is minimally dependent on the presence of clouds (Allan, 2011). The net CRE at the surface is then given by:

$$\text{CRE}_{surf} = \text{LDS} - \text{LDS}_{cs} + \text{SDS} - \text{SUS} - \text{SDS}_{cs} + \text{SUS}_{cs}. \quad (6.2)$$

The CRE_{surf} during P1, MSD and P2 periods (Fig. 6.14) is negative and the minimum values are found in the East Pacific ITCZ region. The differences between the MSD timings closely follow the precipitation changes during these periods as the minimum CRE in the EP and the Mesoamerican region is found during the two peaks of precipitation with a weaker CRE over the Mesoamerican region and nearby basins during the MSD. The smallest CRE is found over the Baja California Peninsula. The results of the two historical experiments closely follow the results of ERA5, and the only notable difference is that the CREs are generally stronger in GC3-hist than in N216-hist.

The comparison of the individual contributions of the SW and LW surface CREs show that the dominant term in the EP and Mesoamerican regions is the SW term (Fig. 6.15). The negative SW CRE is strongest in the EP ITCZ region and the pattern of SW CRE varies temporally in similar fashion to the net CRE, i.e., in the MSD region, the SW term is notably larger ($<-90 \text{ W m}^{-2}$) during the two peak periods of precipitation than during

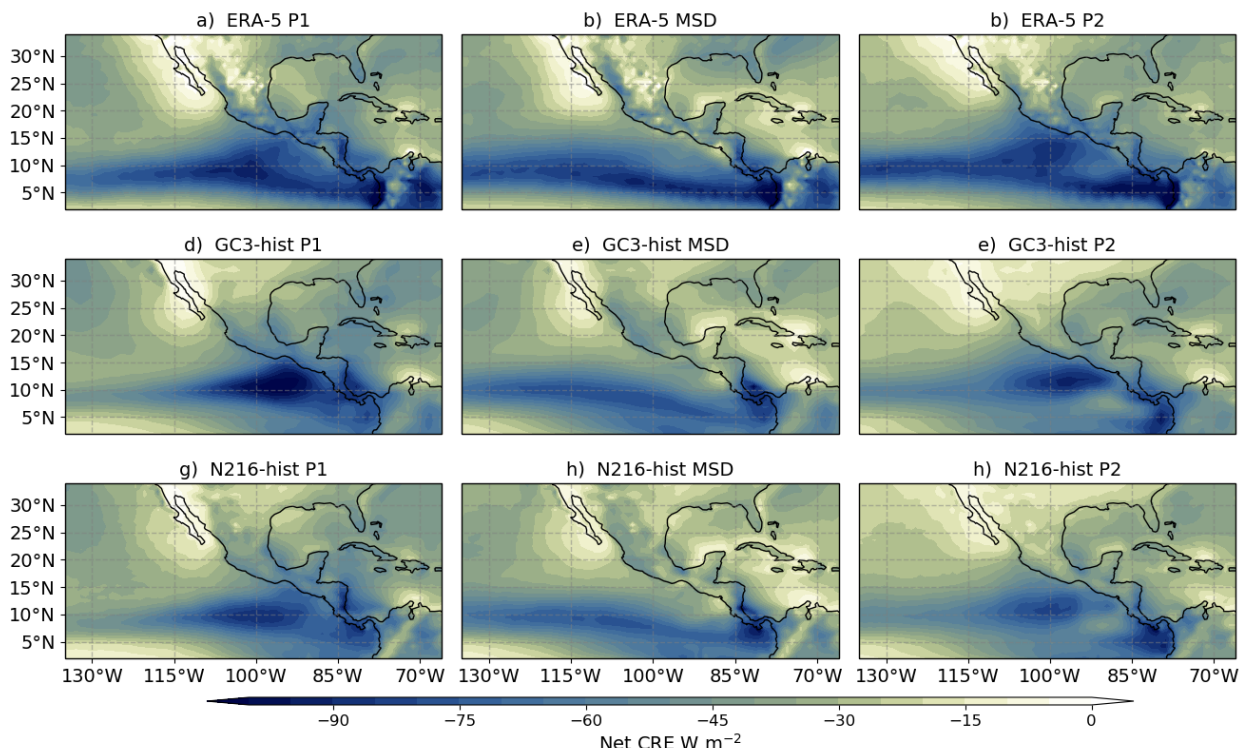


Figure 6.14: Composite mean net CRE at the surface [W m^{-2}] during the periods of onset of the MSD, the MSD and the end of the MSD for (a-c) ERA5, and the ensemble mean of (d-f) GC3-hist and (g-h) N216-hist.

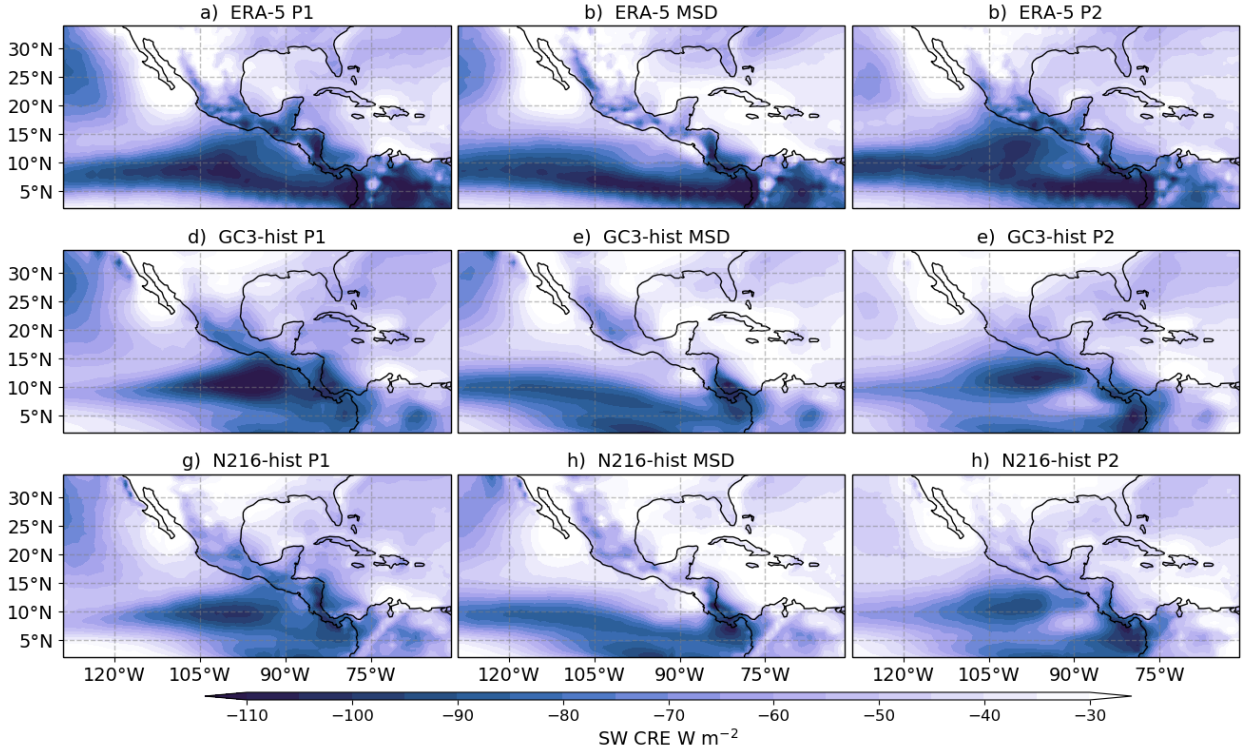


Figure 6.15: As in Fig. 6.14 but for the short-wave radiative effect.

the MSD. In the historical experiments, the SW CRE is strongest in the EP ITCZ region and the SW CRE over the MSD region varies notably in the three stages of the rainy season. In contrast, the LW term (not shown), is generally smaller in magnitude than the SW term and is largest over land and in the ocean west of the California. Over the EP and CSEA regions, the LW term shows very small horizontal gradients, indicative of fairly weak horizontal gradients in the LW effect of clouds.

These composites depict how the spatial distribution of the CRE synchronously varies with the MSD, but how these terms actually within the season in the MSD region is not obvious. The seasonal cycles of the SW, LW and net CREs (Figure 6.16a-c) show bimodal signals characterized by stronger CREs during the two peak periods during June and September and a relative minimum in between found in late July in ERA5 and early August in the simulations. The simulations reasonably simulate the magnitude of the net and SW CRE during the early summer season but overestimate the decrease in the net SW and LW CRE during the midsummer, very likely associated with the underestimation of precipitation over this same period (Figure 6.1).

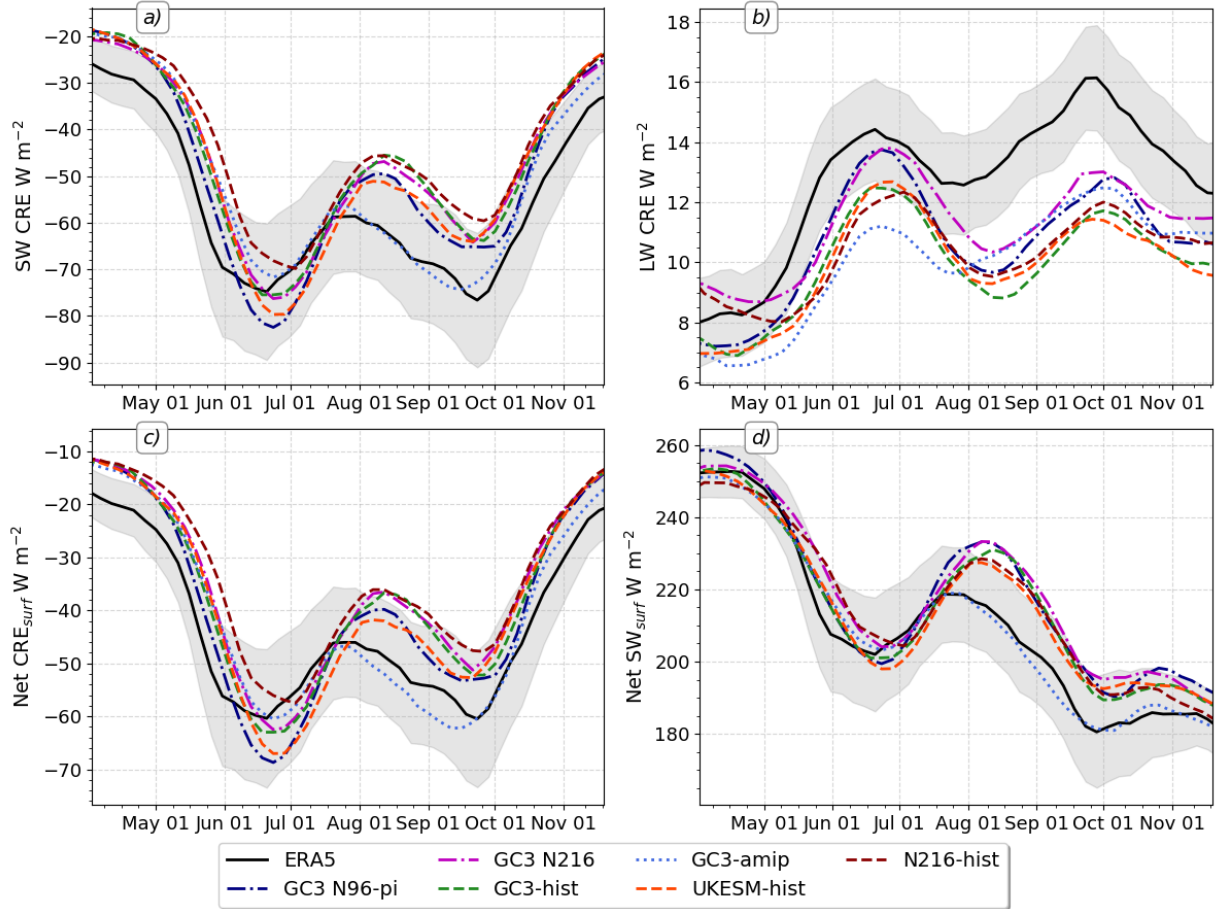


Figure 6.16: Pentad-mean seasonal cycle of the (a) SW and (b) LW CREs, (c) the net CRE, and (d) the net SW at the surface, signed positive to indicate surface absorption of SW radiation.

Regardless of CREs, according to Magaña et al. (1999) and Karnauskas et al. (2013), the net SW (the difference between upwelling and downwelling shortwave fluxes) at the surface should also have a bimodal seasonal cycle. In both ERA5 and the simulations, the net SW (Figure 6.16d) seasonal cycle is characterized by a first peak in late May, which coincides with the peak in East Pacific SSTs. This peak in surface SW is followed by a local minimum during June which is followed by a secondary increase in July in ERA5 and in August in the simulations. After this second local maximum, there is another sharp decrease of net SW at the end of the summer, which coincides with the second peak of precipitation, which agrees with previous hypotheses.

The spatial distribution of changes to the net SW at the surface (Figure 6.17) show that from the first peak to the MSD there is a positive difference in net SW, indicative of more

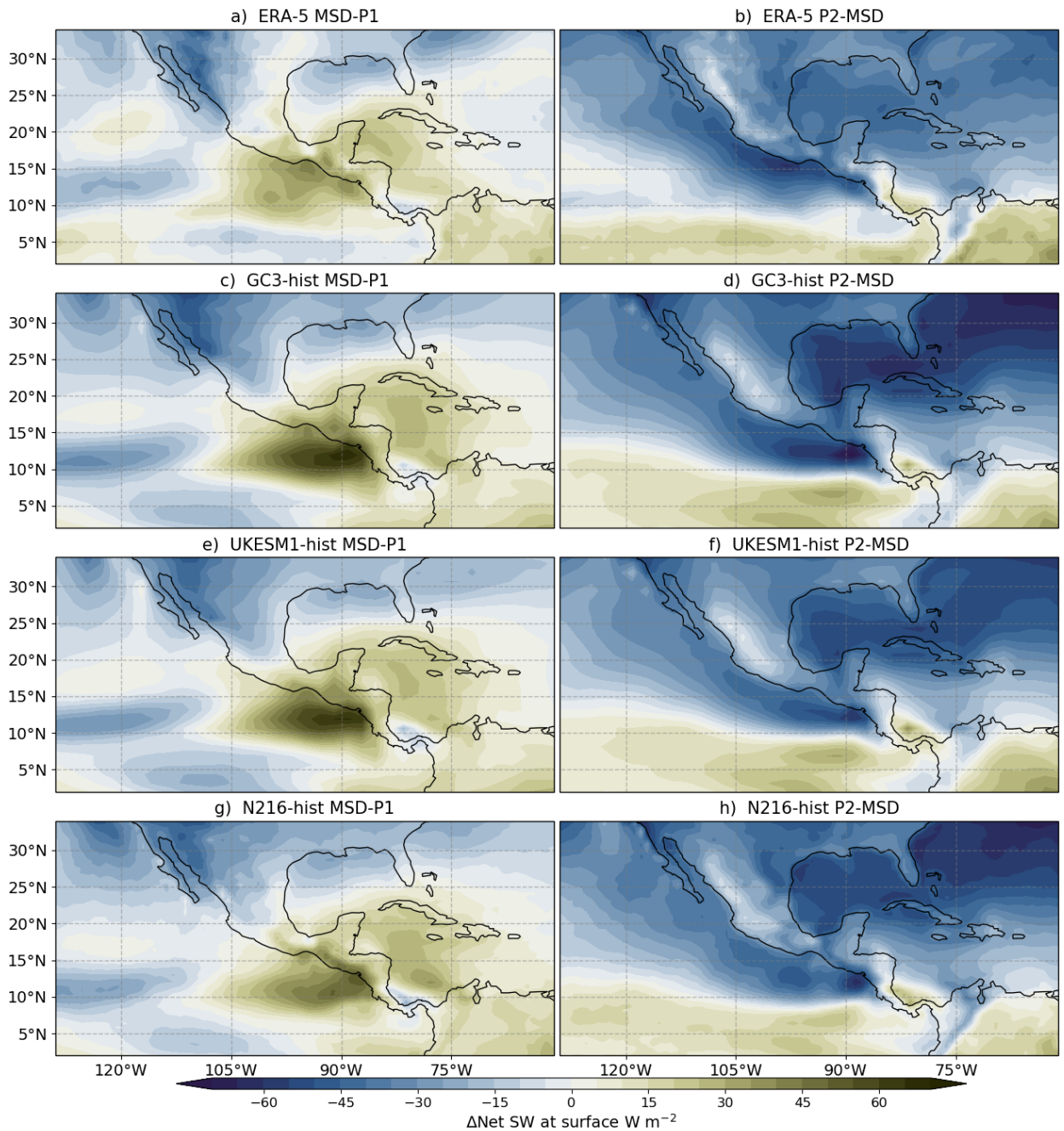


Figure 6.17: As in Fig. 6.8, but for the net shortwave radiation [W m^{-2}] at the surface.

SW energy absorption at the surface, of about 30 W m^{-2} in ERA5 and 40 W m^{-2} in the simulations. In contrast, for the P2-MSD differences, a notable reduction in net SW energy is observed throughout the North American continent but the maximum reduction is found on the western coast of southern Mexico. One might reasonably then suspect that the increased SW absorption during the MSD may indeed be the cause or part of the mechanism for the

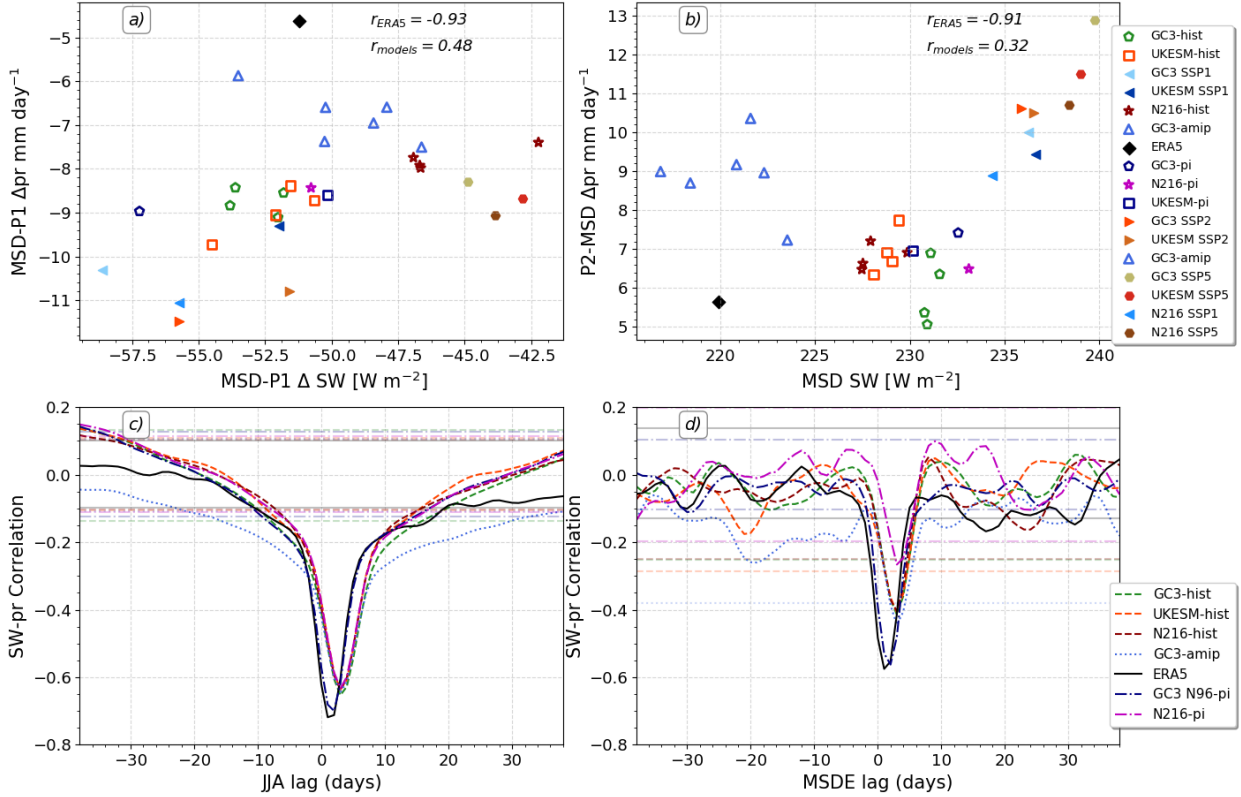


Figure 6.18: (a, b) Scatter of the mean changes to the net short-wave (SW) at the surface (abscissa) with respect to changes in precipitation for different MSD stages. (c, d) Lagged-regression coefficients between the net shortwave absorption in the East Pacific and precipitation over the MSD region for the (c) the JJA season and (d) around the MSDE date.

second peak of precipitation, as suggested by both Magaña et al. (1999) and Karnauskas et al. (2013). However, this could just be a correlation that highlights the coupling between clouds, radiation and precipitation and not necessarily that SW heating is the driving mechanism.

These hypotheses are further tested through scatter and lag-lead regression analysis (Figure 6.18). The changes to the net SW at the surface are unrelated to the interannual variability of precipitation in ERA5. The reduction in SW in the MSD-P1 periods shows a null correlation with the changes of precipitation during the same stages, whereas the net SW absorbed in the EP during the MSD period is negatively correlated with precipitation during the second peak. In other words, years where less shortwave is absorbed in the EP are years stronger second peaks in the MSD region, in contrast to previous hypotheses.

Furthermore, in the MOHC CMIP6 experiments there appears to be only a modest relationship between net SW and precipitation. The changes to SW during the MSD-P1 are

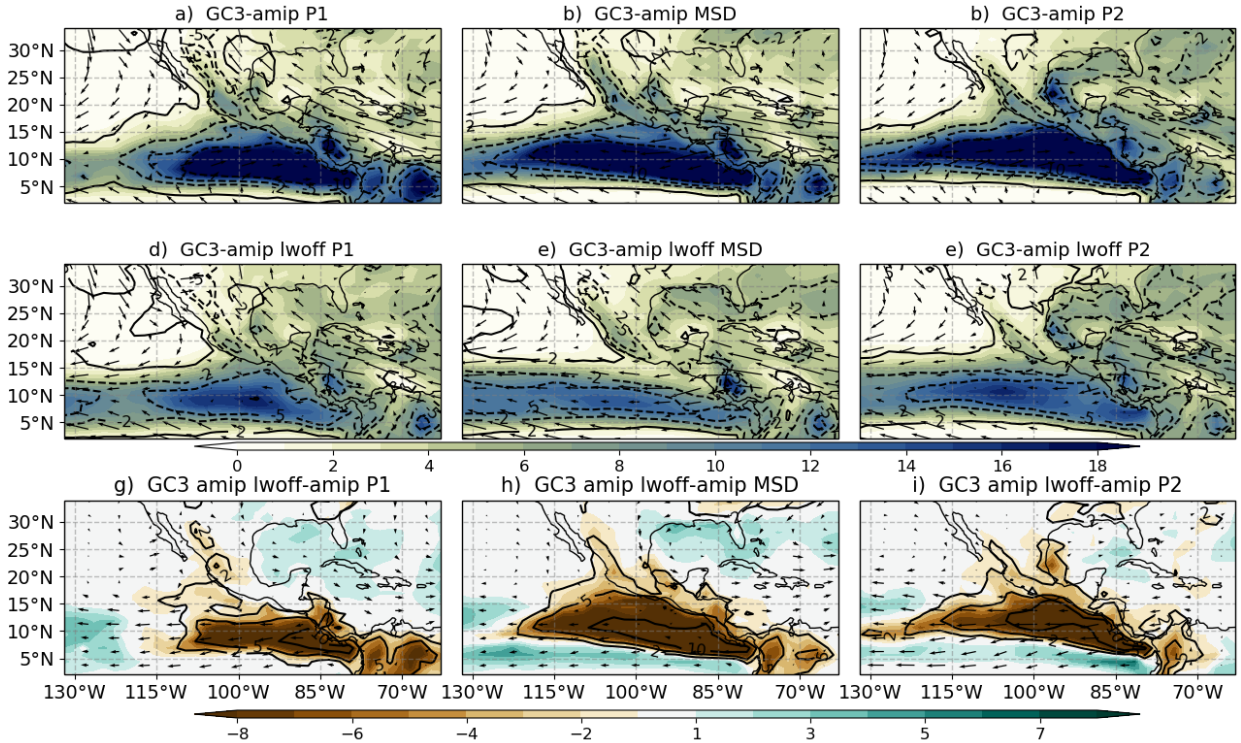


Figure 6.19: Composite mean precipitation (shading in mm day^{-1}), vertical velocity (contours in $10^{-2} \text{ Pa s}^{-1}$) and 850 hPa wind speed (vectors) for the P1, MSD and P2 periods in the (a-c) GC3-amip and (d-f) GC3-amip lwoff experiment. (g-i) shows the difference between the lwoff-amip and the amip experiments.

only modestly related to precipitation as simulations that have the smallest changes to net SW in this period do not exhibit the smallest changes to precipitation. Similarly, a very weak relationship between SW and precipitation is found within the different experiments to relate the net SW at the surface during the MSD and the strength of the second peak.

Lag-lead relationships (Figure 6.18c, d) confirm that there is a strong negative correlation between SW and precipitation at lag 0. This negative correlation illustrates that strong precipitation periods are associated with less shortwave absorbed by the surface, due to the high clouds blocking incoming SW. Correlations are not significant outside of lag -5 to 5 days near the MSDE date, although they appear significant for some coupled simulations at lags of -40 days when the entire JJA season is considered. These results are contradictory with the argument of Karnauskas et al. (2013) who argued a lagged relationship between shortwave absorption at the surface and precipitation at the end of the MSD.

Finally, while the incoming SW radiation plays an important role in several theories

for the MSD, the LW effects have important consequences in monsoon dynamics (Guo et al., 2015; Byrne and Zanna, 2020). The GC3-amip lwoff experiment is part of the contributions from the Cloud Feedback MIP (CFMIP) (Webb et al., 2017) to CMIP6. This experiment is identical to the GC3-amip experiment except that the treatment of the LW in the radiation code in the model is not affected by the presence of clouds. The radiation code does not assummes all LW fluxes to be under clear-sky conditions and routines that account for the effect of clouds are not called. In other words LW heating is independent from clouds, so the radiation-cloud coupling is removed and radiative fluxes do not depend on the characteristics of convective clouds.

The impact of the LW CRE for precipitation in the Mesomerican region is critical (Figure 6.19). When the LW CREs of clouds are ignored, precipitation over the whole domain is greatly reduced (50-80%), ascent becomes weaker and the low-level circulation also weakens. These results are in agreement with previous studies (Guo et al., 2015; Byrne and Zanna, 2020) that show that cloud radiative heating strengthens the local and regional circulation in a monsoon. The circulation and precipitation is so diminished in GC3 amip-lwoff that this is the driest simulation found in this chapter (Figure 6.7) and the variations between the MSD and the two peak periods of precipitation are almost undistinguishable.

This section diagnoses the seasonal cycle and spatial variability of CRE at the surface as depicted by ERA5 and the CMIP6 simulations. The net CRE at the surface is dominated by the SW term, indicating the strong effect that convective clouds have to block SW radiation from reaching the surface throughout the rainy season. The total absorbed SW shows a double-peak structure, with the second peak appearing at the end of the MSD period for both ERA5 and CMIP6 simulations, as suggested in the solar declination angle hypothesis Karnauskas et al. (2013). However, the strength and timing of the changes to the SW absorption suggest that the relationship between SW heating and precipitation is more of a correlation than a causal link from the SW to the precipitation.

6.6 The role of the Caribbean Low-Level Jet

The previous sections evaluate the SST radiative-convective feedback and the solar declination angle hypotheses whereas this section examines the role of the Caribbean Low-Level Jet (CLLJ) for the MSD of Mesoamerica. Section 6.3 shows that the seasonal cycle of the CLLJ, is well represented by the simulations (see Figure 6.9d), but the timing of the peak magnitude of the CLLJ in the models is delayed by about three weeks with respect to ERA5. The timing of the start of the MSD is notably also delayed in the models by around 10 days, according to Table 5.3 in the previous chapter. This evidence is suggestive that the CLLJ may be playing a role in the timings of the MSD in the simulations, which would be consistent with previous hypotheses (e.g. Herrera et al., 2015; Martinez et al., 2019).

The main dynamical argument that links the MSD in southern Mexico and Central America and the CLLJ is centred around variations in the moisture flux convergence (MFC), and subsequently in the total water content (TWC) (see e.g. Gamble et al., 2008; Herrera et al., 2015; Martinez et al., 2019; Zermeño-Díaz, 2019). For this reason, this section examines the CLLJ magnitude as measured by the 850 hPa zonal wind in the Caribbean Sea (see box in Figure 6.4), and the integrated moisture flux convergence (IMFC) and TWC in the MSD region. The IMFC was calculated using the following equation from daily ERA5 data and daily data from the simulations:

$$IMFC = -\left\langle \nabla \cdot \vec{u}q \right\rangle, \quad (6.3)$$

where q is the specific humidity at each pressure level, \vec{u} is the wind vector and ∇ is the horizontal divergence operator and the $\langle \rangle$ operator denotes column integrals in the troposphere.

The seasonal cycle of the IMFC and TWC (Figure 6.20) averaged over the region of the MSD shows a strong bimodal signal, with two maxima in IMFC and TWC occurring roughly at the same time as the two peaks in precipitation and a minimum found during Midsummer. The simulations follow closely the variations of the seasonal cycle of ERA5, but with a weaker IMFC over the region in all the simulations, particularly after the period of the first peak of precipitation.

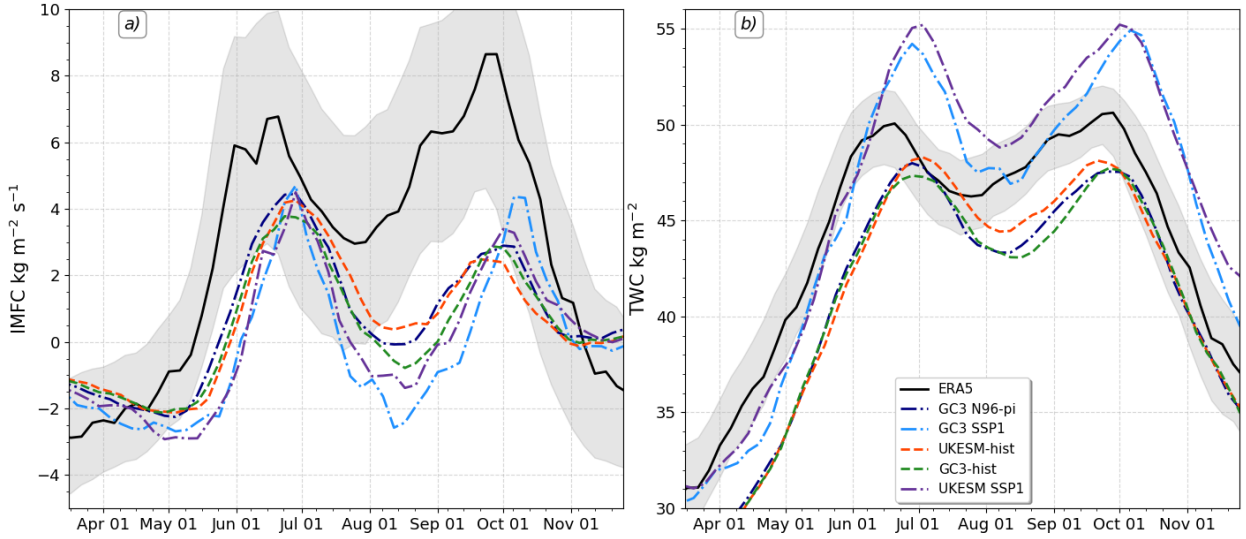


Figure 6.20: Seasonal cycle of (a) IMFC and (b) TWC averaged over the MSD region.

The magnitude of the two peaks of IMFC is fairly similar for all the simulations, in contrast with the asymmetry between the first and second peaks of precipitation, e.g., the historical experiments show a wetter first peak than the second peak. The IMFC during MSD, in contrast, shows notable differences amongst experiments, with the SSP1 experiments showing a smaller IMFC compared to the historical and piControl experiments, in fact in early August the IMFC is negative (indicative of moisture divergence) in the SSP1 experiments.

The magnitude and timings of the two peaks in TWC is fairly similar amongst the piControl and historical experiments and ERA5, albeit some differences. The drying of the column in the simulations during midsummer occurs weeks after the drying in ERA5, which agrees with the differences in the seasonal cycle of precipitation. The low-emission scenario (SSP1) experiment show a higher TWC indicative of a moistening of the column throughout all the seasons for a relatively low greenhouse forcing compared to the historical experiments.

The IMFC, TWC and 850-hPa wind variations associated with the MSD (MSD-P1 and P2-MSD) are shown in Figure 6.21 for ERA5 and two simulations. The patterns observed in the low-level wind vectors associated with the MSD timings follow closely the previously reported "MSD patterns" described by Zermeño-Díaz (2019); Zhao et al. (2020), which confirms that the WT method is able to extract similar patterns in the low-level wind associated with the MSD to other techniques. The wind flow pattern in the MSD-P1 panel is

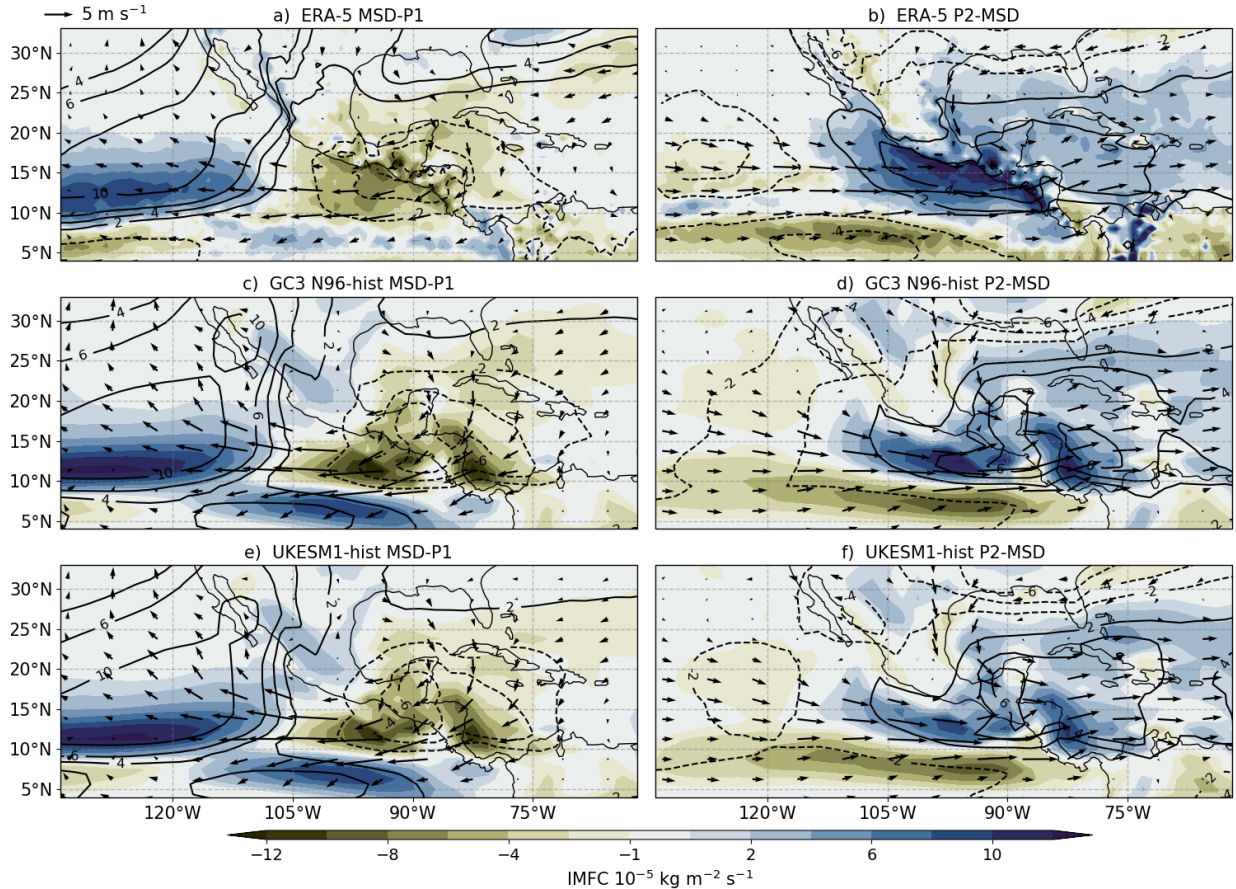


Figure 6.21: As in Figure 6.10, but showing variations in the IMFC (shading), TWC (contours in units of kg m^{-2}) and 850-hPa wind (vectors).

characterised, both in ERA5 and the simulations, by modest northeasterly anomalies in the Gulf of Mexico and the CSEA and strong easterly anomalies over the EP region. These wind anomalies indicate that as the wetter first peak period transitions to the drier MSD, the wind field changes from a weak low-level westerly wind to an easterly wind (see also Figure 6.9c). At the end of the MSD, the wind direction changes again to a westerly direction in the East Pacific, whereas the wind anomalies in the CSEA turn to westerlies indicative of a weakening of the CLLJ, coincident with the second peak of precipitation observed in the MSD region.

The IMFC and TWC show coherent variations with the timings of the seasonal cycle of precipitation in the MSD region, with less moisture convergence and precipitable water in the column during the drier period compared to the two peak periods. In contrast, west of the coast at around the 125°W , during the MSD there is increased TWC and IMFC in ERA5 and

in the simulations, in agreement with the previous sections which showed increased convective activity in this region. Simultaneous to the drying of southern Mexico and Central America during the MSD, the North American monsoon region moistens (increased TWC and IMFC).

The IMFC and TWC anomalies associated with the end of the MSD period, depicted by the P2-MSD panel, show positive differences in the MSD region and negative anomalies southward, suggesting increased IMFC and TWC over southern Mexico and northern Central America, in agreement with the secondary increase in precipitation. Positive TWC and IMFC differences extend from the MSD region to the east into Cuba, the Caribbean Sea and the Gulf of Mexico. This moistening coincides with increased moisture divergence to the south of the MSD region in the East Pacific (120-90°W, 3-10°N) and decreased TWC.

A scatter plot of the mean changes to the IMFD, TWC and the CLLJ and their relationship to the synchronous variations in precipitation (Figure 6.22) confirm that these diagnostics are deeply related to the timings and strength of the seasonal cycle of precipitation.

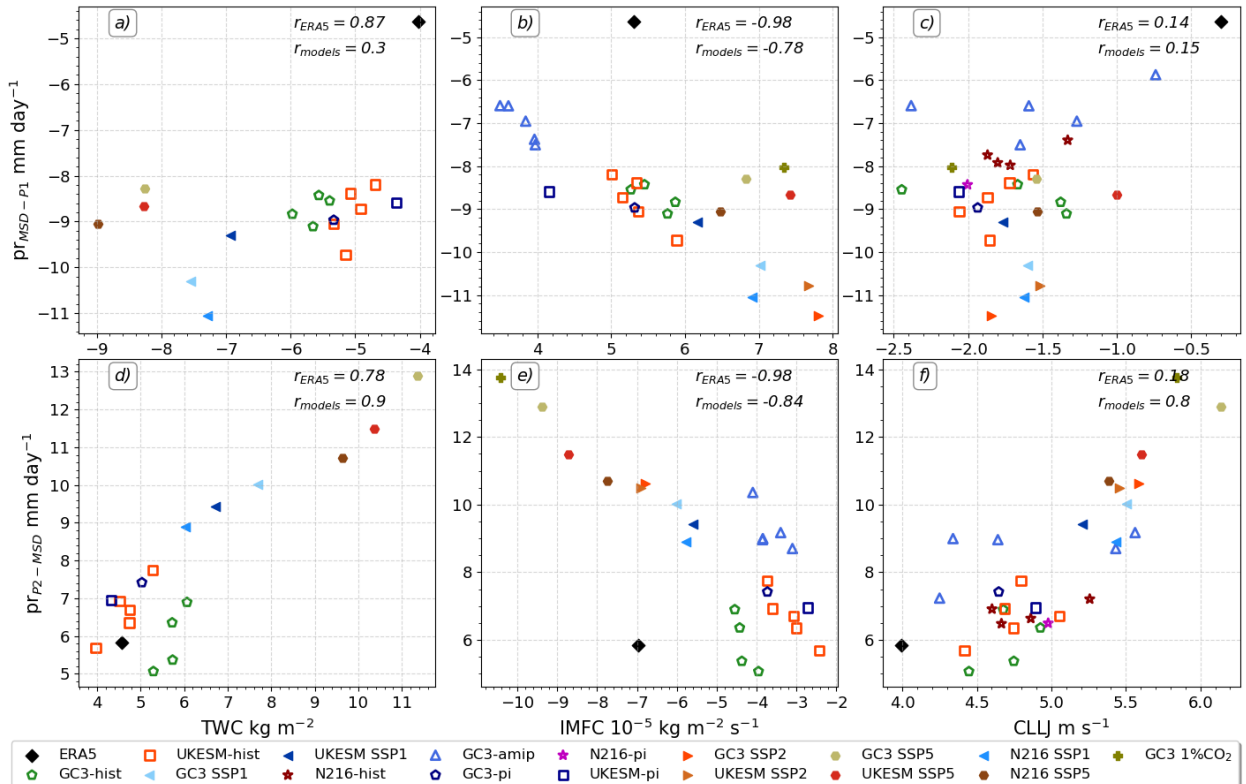


Figure 6.22: As in Figure 6.12, showing the scatter of mean changes (a-c) MSD-P1 and (d-f) P2-MSD periods, but using the (a, d) IMFD and (b, e) TWC in the MSD region and the (c, f) CLLJ on the x-axis and precipitation in the MSD region in the y-axis.

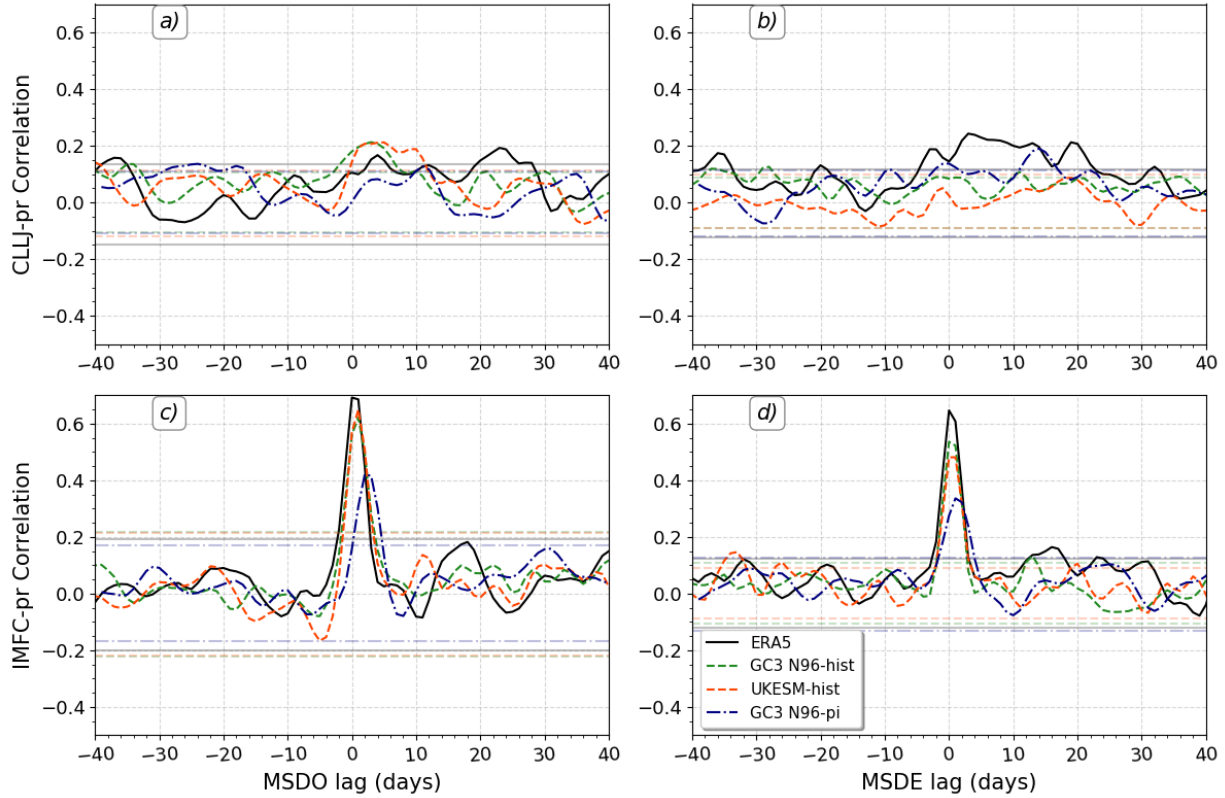


Figure 6.23: Lagged correlations between precipitation in the MSD and the (a, b) CLLJ, defined as the 925 hPa zonal wind averaged over the CSEA region, and (c, d) the IMFC over the MSD region. Correlations are shown with lags computed with respect to the (a, c) onset and (b, d) end dates.

The interannual variability of the precipitation differences MSD-P1 in ERA5 are very well explained by the variability of the TWC ($r = 0.87$) and the IMFC ($r = -0.98$) but less so by the CLLJ ($r = 0.14$). The inter-experiment MSD-P1 precipitation differences can largely be explained by the differences in IMFC changes during the MSD-P1 periods ($r = 0.78$). However, the changes in the CLLJ and IMFC in the simulations can not explain the precipitation differences between the runs in the MSD-P1 periods.

The changes from the MSD to the second peak of precipitation (Fig. 6.22) in the simulations are very well explained by the mean variations to the CLLJ, the TWC and the IMFC. However, for the interannual variability of ERA5, only changes to the TWC and IMFC show significant and relatively high correlations. These results would suggest that variability in the CLLJ can explain several differences in the magnitude of the P2-MSD differences in the models, possibly through the modulation of the CLLJ on the TWC and

the IMFD over the continent; nevertheless, the observed interannual variability of the CLLJ cannot explain the interannual variability in the strength of the second peak.

The synchronous relationship found in the previous scatterplot is further tested via lagged correlations (Figure 6.23). These correlations do not show any evidence of robust relationship between the CLLJ or the IMFC with precipitation at any lags. In particular, the correlations of precipitation with the CLLJ are not higher than 0.3 at any lag and only become significant for a few days in some simulations. In particular, around the MSDE date, no correlation at negative lags is significant and positive which is at odds with the hypothesis that CLLJ is responsible for the end of the MSD.

However, the strength of the CLLJ may not be the relevant factor, but rather the influence of the CLLJ on the IMFC. The correlation of IMFC with precipitation shows a strong positive correlation, both at MSDO and MSDE in reanalysis and models around lag 0, and similar results are found for TWC-pr correlations (not shown). However, there is little evidence that this relationship is of a lagged nature, as the correlations are not significant away from the 0 lag.

6.7 A short look at the MSD through the lens of the moist static energy budget

The results in the previous sections suggest that only some elements of the CLLJ hypothesis can explain the interannual variability in the strength of the MSD in reanalysis and the differences in the CMIP6 experiments. To further explore the processes that control the start of the MSD, the moist static energy (MSE) budget is used in this section to disentangle how the column MSE budget terms vary over the wet season. The MSE budget terms are obtained, as described in section 3.3, from daily-mean values at all available levels within the troposphere for reanalysis and climate model output. Note that the radiative heating terms are not available from the CMIP archive on daily scales.

The seasonal cycle of the budget terms, as well as the boundary layer or near-surface MSE (h_b), is shown in Figure 6.24 with some quantities shown for the EP region and others for the MSD region. The vertical advection of dry (s) and moist (h) static energy show a

bimodal seasonal cycle, with two peaks at the start and end of the summer season, separated by a local minimum that occurs at the end of July or early August. The simulated vertical advection of MSE corresponds well with ERA5 during boreal summer for all the simulations, although the vertical advection of s is smaller in the historical and SSP1 experiments during the MSD and second peak periods. The vertical advection of s is higher in the GC3 amip experiment during late summer compared to other experiments, which is important because this simulation has the wettest second peak.

The sum of the latent and sensible heat fluxes in the EP region show a clear bimodal signal in the experiments but not in ERA5. The experiments also show very large positive

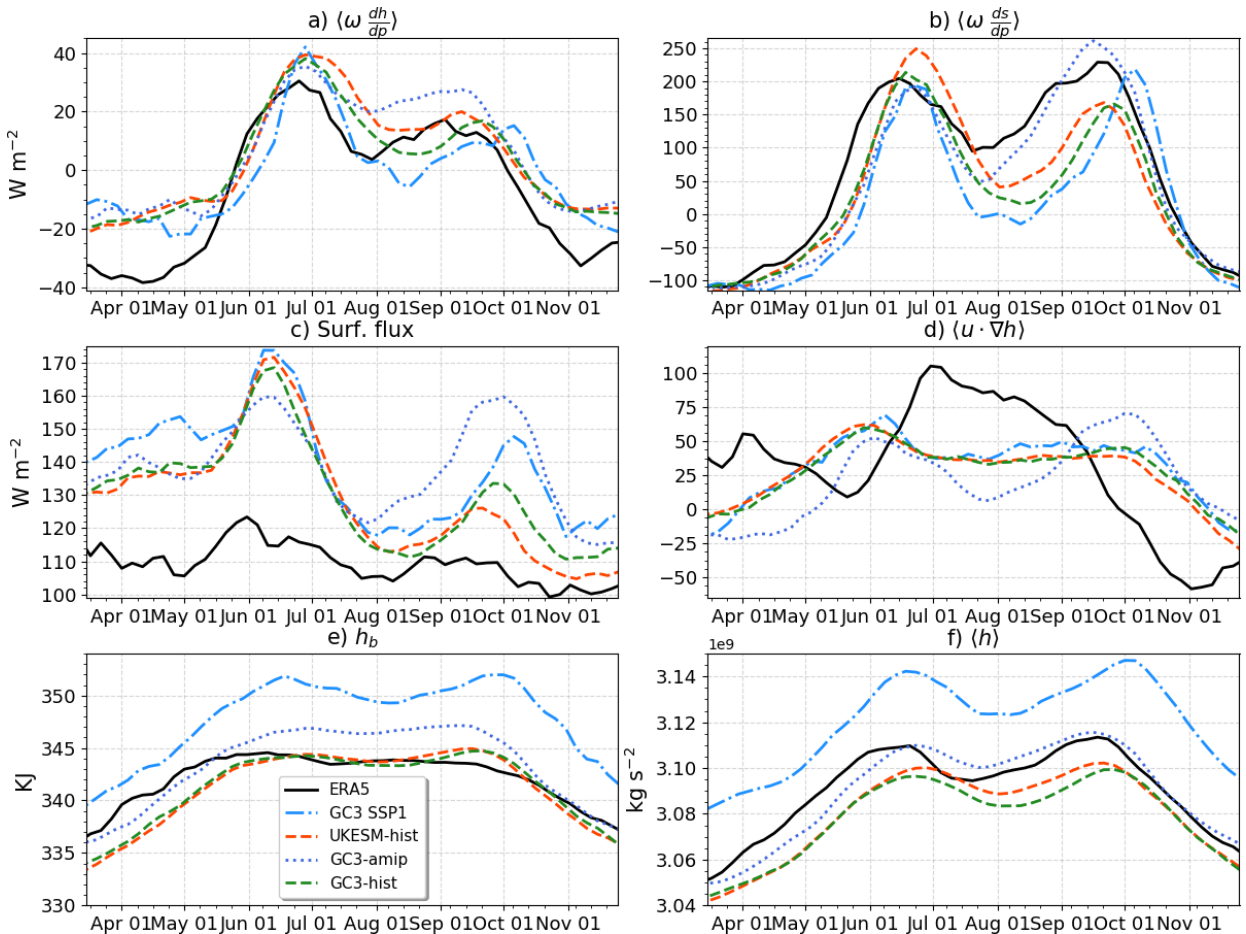


Figure 6.24: Pentad-mean seasonal cycle of the moist static energy budget terms. Vertical advection of (a) moist and (b) dry static energy, (c) the sum of the latent and sensible heat fluxes, (d) horizontal advection of MSE, (e) boundary layer MSE (h_b) and total column MSE ($\langle h \rangle$). The quantities in panels c,d were averaged over the EP region and the rest of the panels over the MSD region.

biases in surface fluxes during both periods of peak precipitation, especially the GC3 amip experiment. These biases in the surface fluxes in the EP are possibly one of the reasons for the very wet bias found in the EP ITCZ in these models.

The theory by Karnauskas et al. (2013) suggests that the net shortwave surface energy balance being strongly modulates the various stages of the MSD, through an influence on the surface or boundary layer MSE (Fig. 6.24e). However, in most of the simulations and ERA5, h_b in the MSD region follows a plateau-like seasonal cycle with a clear increase during spring, a plateau during summer and a sharp decrease in October at the end of the rainy season. The SSP1 experiment shows a decrease in h_b in August but this is fairly modest compared to the magnitude of the change in h_b at the end and start of the summer.

Similarly, the total column h shows a modest bimodal seasonality in reanalysis and simulations, i.e., $\langle h \rangle$ decreases at the midsummer. The low-emission scenario shows a notable increase in total column h compared to historical and pre-industrial experiments. In spite of this increase in total column h in SSP1, the total precipitation is not increased uniformly over all the stages of the wet season in scenario experiments (see Fig. 6.7), so changes to TWC do not explain variations to precipitation throughout the wet season in this region.

The spatial distribution of the mean $\langle \omega dh/dp \rangle$ and $\langle \omega ds/dp \rangle$ (Figure 6.25) during the three stages of the MSD seasonal cycle show a good agreement between the experiments and reanalysis. The highest values of $\langle \omega ds/dp \rangle$ are found on the western coast of northern Central America, in the easternmost position of the ITCZ. Positive values of $\langle \omega dh/dp \rangle$ are found in the Caribbean Sea, the Gulf of Mexico and over the MSD region throughout the three stages of the MSD. Negative values of $\langle \omega dh/dp \rangle$ and $\langle \omega ds/dp \rangle$ are found over the coast of California throughout the wet season.

The changes to the $\langle \omega dh/dp \rangle$ and $\langle \omega ds/dp \rangle$ during the MSD periods (Figure 6.26) show that in the MSD region, $\langle \omega dh/dp \rangle$ and $\langle \omega ds/dp \rangle$ are reduced during the MSD period compared to the P1 period, this difference is maximized right at the exit of the Gulf of Tehuantepec, in southwestern Mexico. Simultaneously, from the P1 to the MSD period, $\langle \omega ds/dp \rangle$ increases west of the MSD region near the 125°W region whereas $\langle \omega dh/dp \rangle$ increases in northern Mexico and in the Gulf of California.

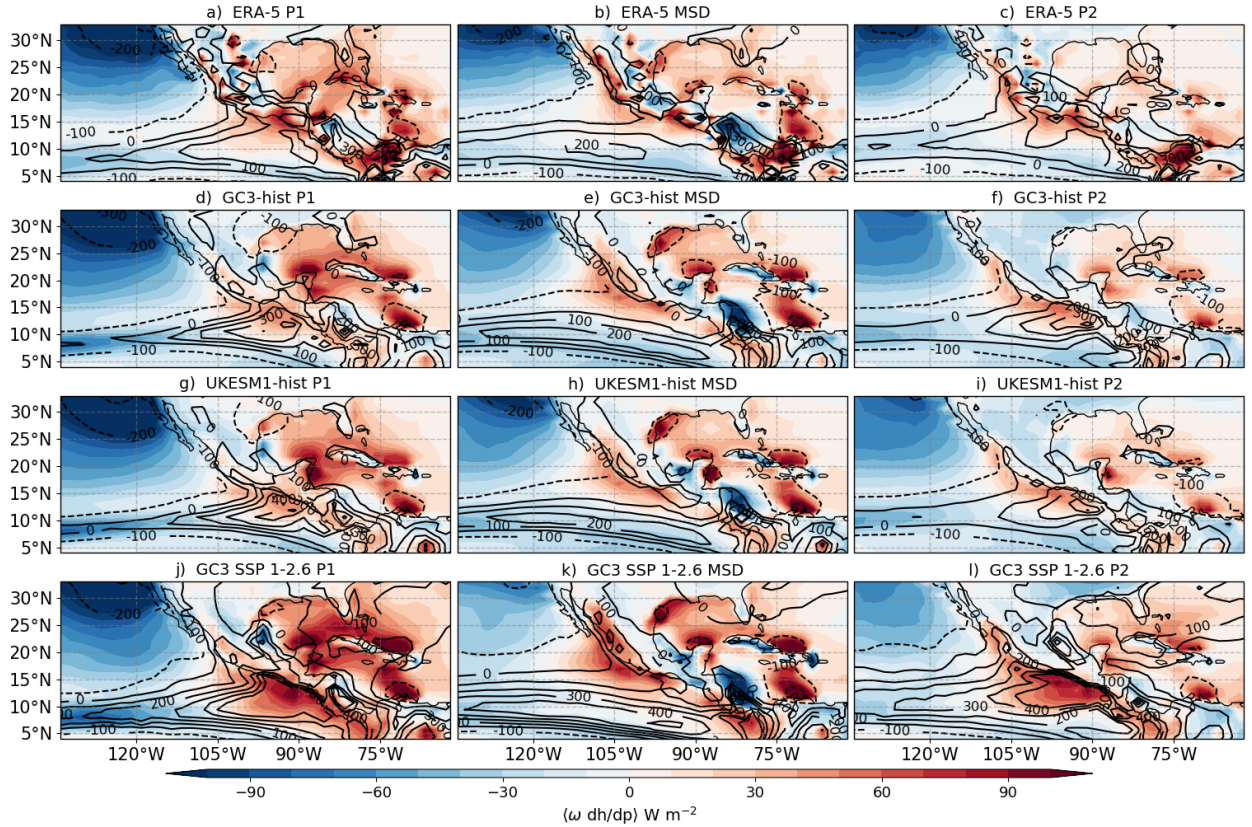


Figure 6.25: Composites of mean $\langle \omega dh/dp \rangle$ (shading in W m^{-2}) and $\langle \omega ds/dp \rangle$ (contours in W m^{-2}).

At the end of the MSD (Figure 6.26), $\langle \omega dh/dp \rangle$ and $\langle \omega ds/dp \rangle$ increase in the MSD region. Again, the maximum difference of $\langle \omega ds/dp \rangle$ is found in the Gulf of Tehuantepec region. The North American monsoon region shows a decrease in both $\langle \omega dh/dp \rangle$ and $\langle \omega ds/dp \rangle$. Both for the P2-MSD and MSD-P1 panels, the experiments are able to reproduce the spatial patterns of these changes to these budget terms. Furthermore, the SSP1 experiment shows larger differences between the MSD stages compared to the historical experiments.

The horizontal advection term and the surface fluxes also show notable differences associated with the MSD timings (Figure 6.27). In the MSD-P1 period, decreased surface fluxes in the easternmost Pacific Ocean are observed in the three simulations and, to a lesser degree, in ERA5. These differences suggest that in the models, surface fluxes decrease as precipitation decreases from the wet first peak period to the dry MSD period. In the simulations, these negative surface flux anomalies are collocated with negative differences of the horizontal advection of MSE term. The opposite patterns appear for both $\langle \vec{u} \cdot \nabla h \rangle$

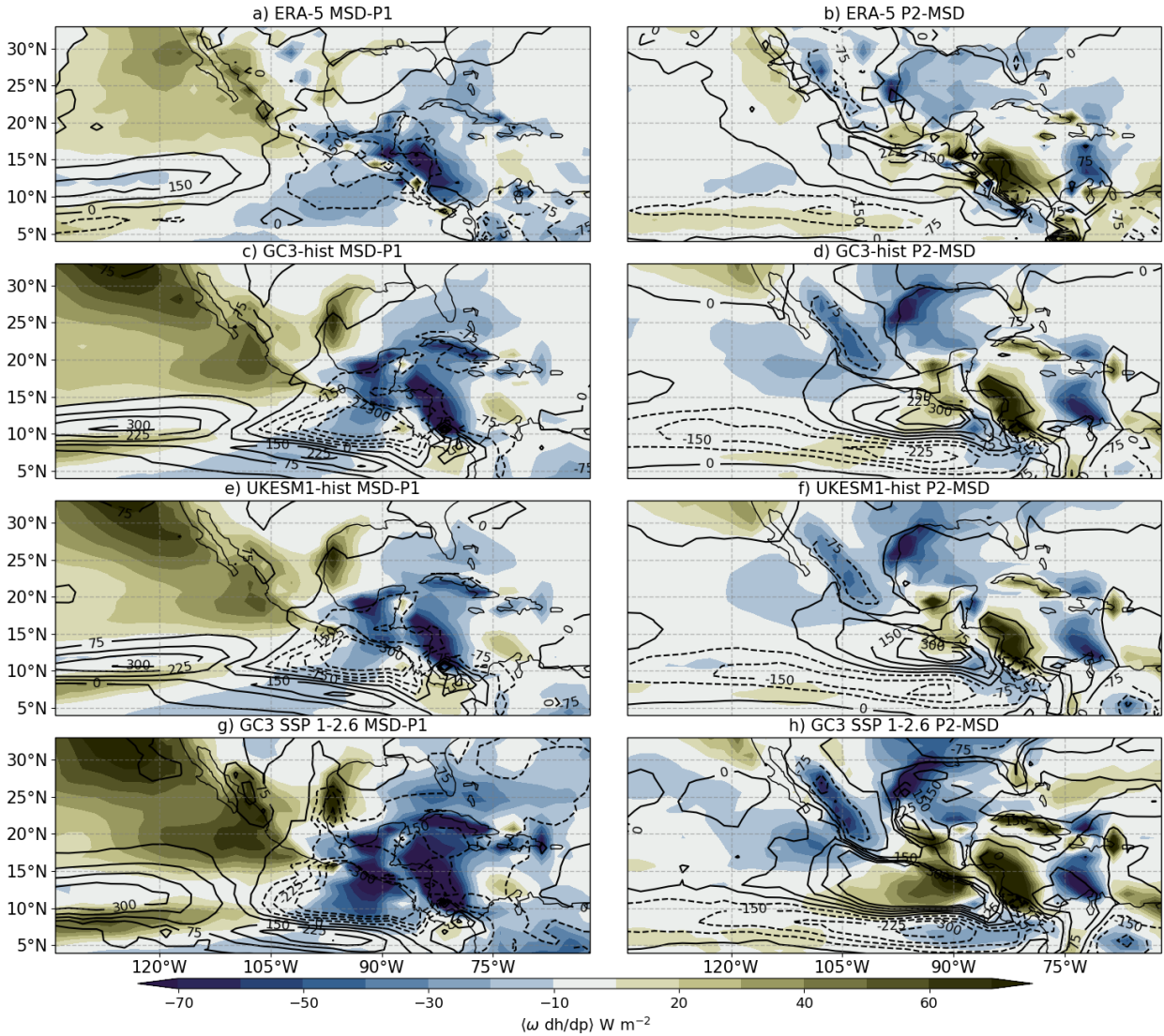


Figure 6.26: Composites of the differences (a, c, e, g) MSD-P1 and (b, d, f, h) P2-MSD of $\langle \omega dh/dp \rangle$ (shading in $W m^{-2}$) and $\langle \omega ds/dp \rangle$ (contours in $W m^{-2}$).

and surface fluxes in the P2-MSD differences.

The scatter of the relationship between precipitation and the vertical advection of dry and moist static energy during the wet season (Figure 6.28) indicates that the vertical advection term is strongly linked to precipitation variations, both in ERA5 as in the simulations. Figure 6.28 shows that the interannual variability of vertical advection of dry and moist static energy in ERA5 is strongly related to interannual variations in the precipitation changes during the MSD. Negative differences of $\langle \omega dh/dp \rangle$ and $\langle \omega ds/dp \rangle$ are observed in MSD-P1 panel whereas increases of these terms occur from the MSD period to the second peak period in ERA5

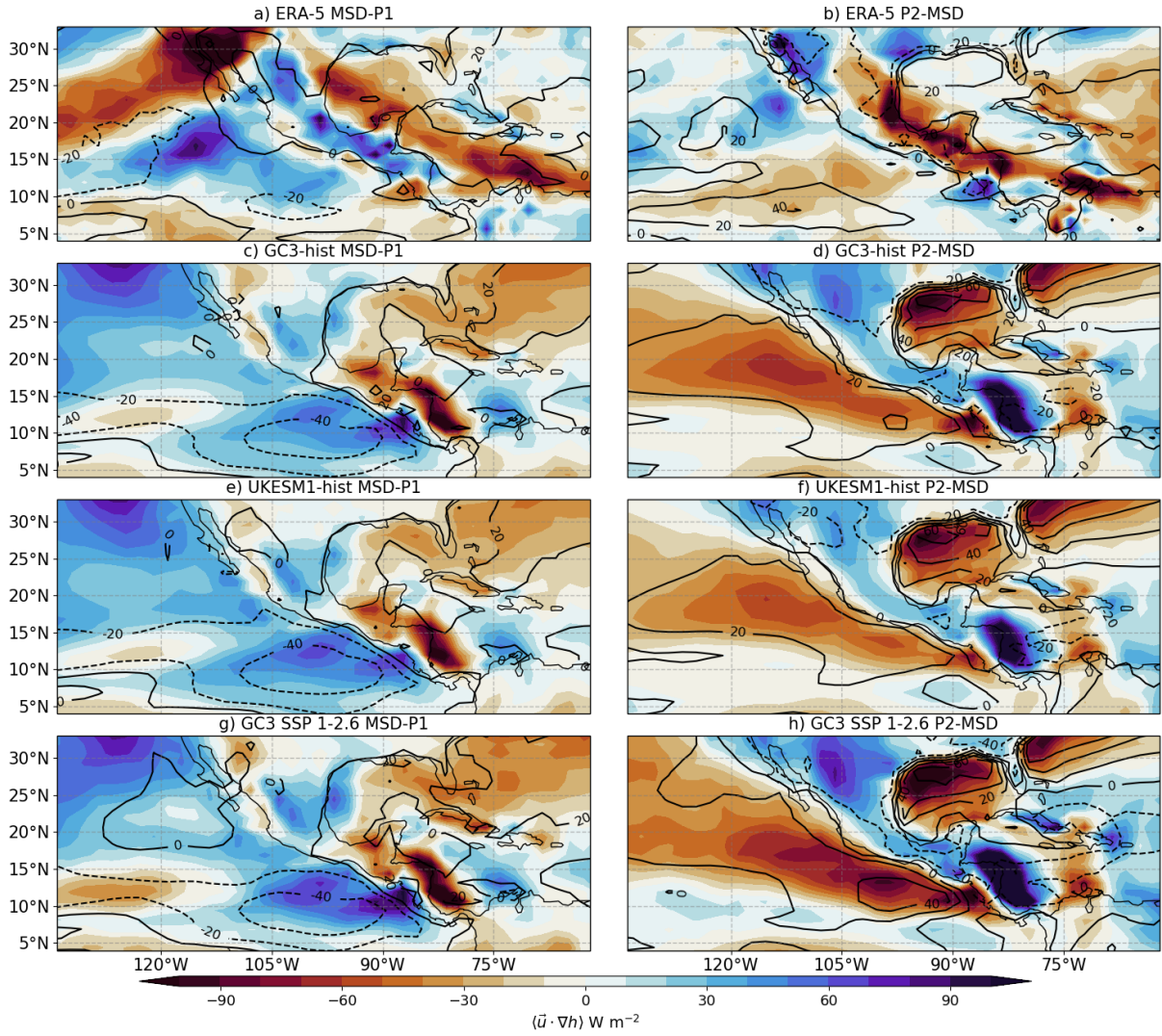


Figure 6.27: Composites of the differences (a, c, e, g) MSD-P1 and (b, d, f, h) P2-MSD of $\langle \vec{u} \cdot \nabla h \rangle$ (shading in W m^{-2}) and total surface fluxes (F) (contours in W m^{-2}).

and in the experiments. Specifically, $\langle \omega ds/dp \rangle$ is the term that best explains interannual variability of the strength of the MSD, measured by the difference MSD-P1 in ERA5.

A key question then is how the MSE budget equation is balanced in the different stages of the seasonal cycle, i.e., which terms balance the changes to the vertical advection of MSE and how this balance changes from the early and late wet periods compared to the MSD period. Figure 6.29 shows the mean values of each budget term in the MSD region in ERA5 and the simulations. The results in the simulations are shown as monthly-mean values because the radiative heating data from the CMIP6 archive was only available for monthly-mean frequencies.

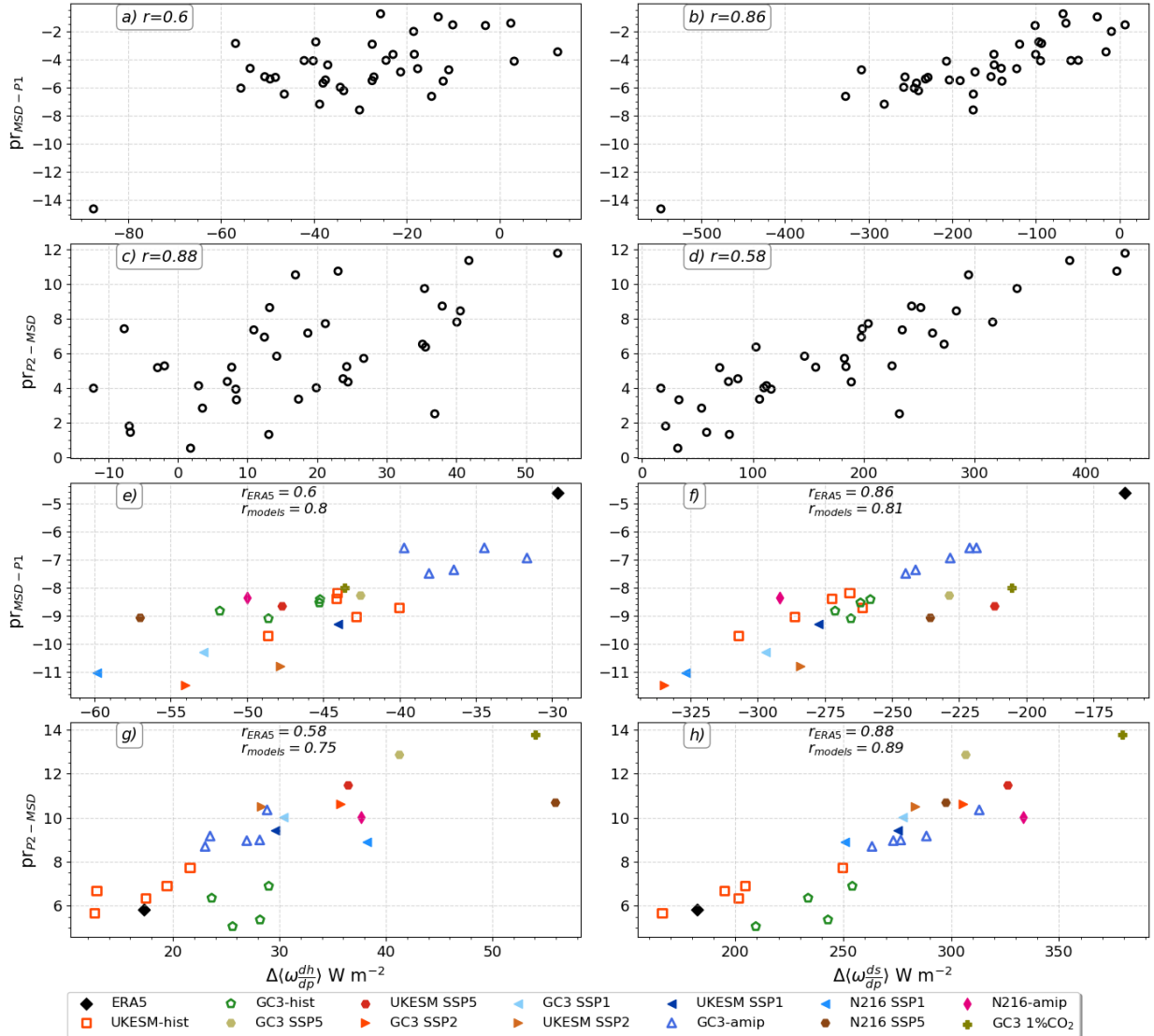


Figure 6.28: Scatterplot of the relationship between the area-averaged mean vertical advection of dry and moist static energy and precipitation over the MSD region. (left) Differences in $\langle \omega dh/dp \rangle$ and (right) in $\langle \omega ds/dp \rangle$ on the x-axis with corresponding differences in precipitation on the y-axis computed for differences amongst MSD-P1 and P2-MSD periods, as indicated on the y-axis label. (a-d) Interannual variability of ERA5 where each dot represents one year in ERA5. In (e-h) the differences represent the mean values for all years in each dataset.

In ERA5 (Fig. 6.29a), the positive contributions of MSE from the shortwave heating and the surface fluxes are balanced mostly by the negative contribution from the longwave heating (radiative cooling of the column) and to second order by the horizontal and vertical advection terms. The differences in the budget terms between the P1, MSD and P2 periods (Fig. 6.30) are most pronounced for the vertical and horizontal advection terms,

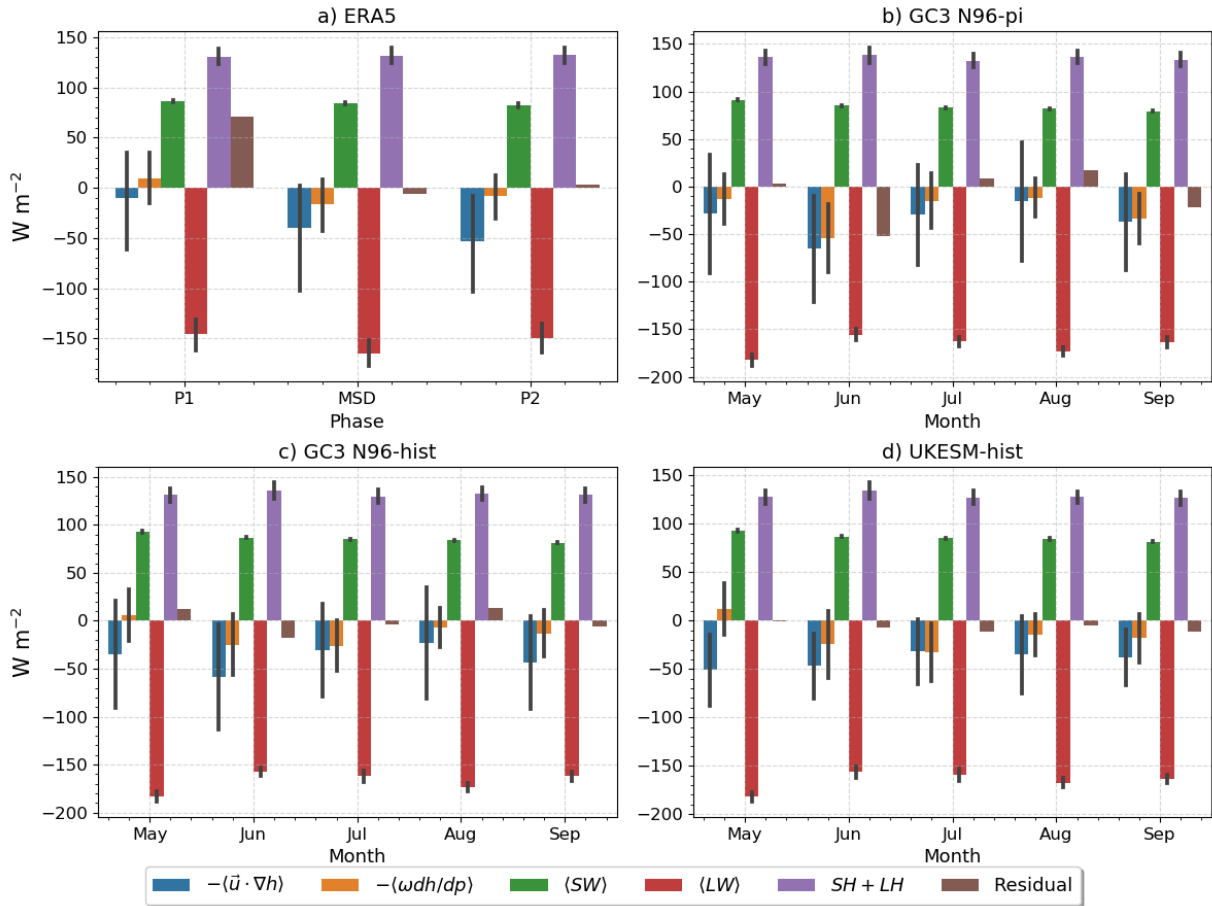


Figure 6.29: Barplots of the area and time-averaged MSE budget terms: horizontal advection ($\langle \vec{u} \cdot \nabla h \rangle$) and vertical advection ($\langle \omega dh/dp \rangle$), longwave ($\langle LW \rangle$) and shortwave ($\langle SW \rangle$) heating and the sum of sensible (SH) and latent heat (LH) fluxes. The residual or addition of all the terms is also shown in each panel. (a) Budget terms computed from ERA5 in the MSD region in the P1, MSD and P2 periods and (b-d) show the monthly-mean values of the budget terms from three CMIP6 simulations. [The error bars indicate the standard deviation for each month/phase.](#)

and the LW heating term. The horizontal advection term increases absolute magnitude (more negative contribution) and the vertical advection term changes sign (from positive to negative) during the MSD compared to the first peak period. However, from P1 to the MSD stage, the longwave radiative heating notably decreases and increases again from the MSD to P2 periods whereas the shortwave heating term appears to change very little between the stages of the rainy season.

In the CMIP6 simulations (Fig. 6.29b-d), a similar balance is observed with the largest contributions arising from the radiative heating and surface flux terms. From May to September some seasonal variations in each term are observed (Fig. 6.30b-d), for example,

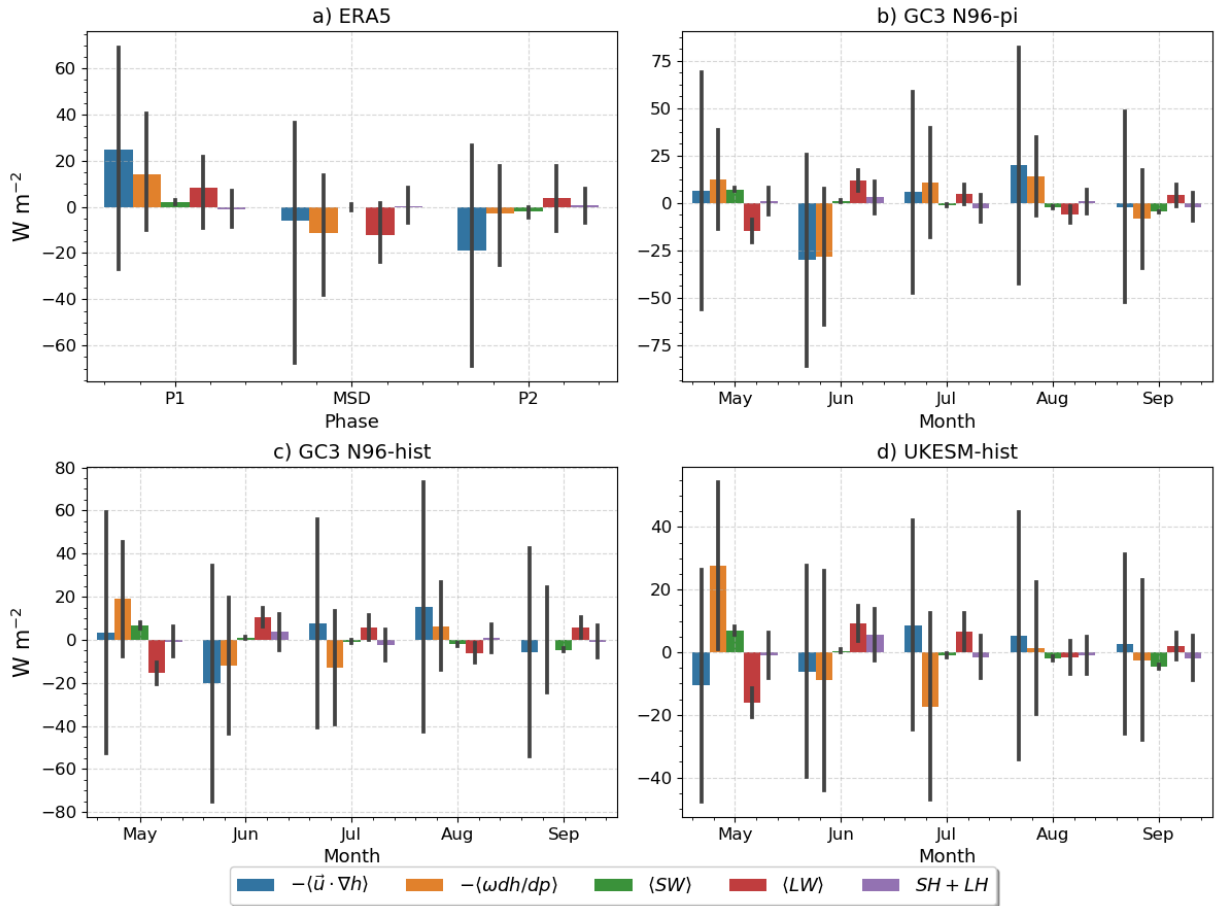


Figure 6.30: As in Figure 6.29 but each term is shown as anomalies from the wet season (JJAS) mean.

stronger longwave cooling in May than in June-July. The vertical advection term becomes negative during the early rainy season (June-July). As in ERA, the absolute contribution from the vertical advection term increases during the MSD with minima found in June or July in all the simulations. The contribution from the horizontal advection term increases during the months of the two peaks of precipitation (May and September) and decreases during the MSD.

The MSE budget analysis is able to show what terms vary more coherently with the timing of the MSD, as well as what terms explain better the variability of the strength of the MSD. First, this section shows that vertical advection terms show a bimodal seasonal cycle, which points to the strong relationship between ω and precipitation. However, the surface h remains relatively constant throughout the rainy season, in contrast to the suggestions by Karnauskas et al. (2013). The patterns of anomalous vertical and horizontal

transport of h also show strong variations synchronous to the MSD stages, suggesting that precipitation follows closely variations in h .

The comparison of individual terms shows that the variability of the horizontal advection and longwave heating terms within the rainy season is stronger than for the shortwave heating and surface fluxes (Fig. 6.30). This evidence (Fig. 6.30) suggests that LW heating and CRE, and moisture transport may be more important than the variations in surface fluxes or the shortwave heating because their variations are more strongly linked to the MSD variations of precipitation. The horizontal advection fluctuations partially support the mechanism that links the moisture transport from the CLLJ to the precipitation in the MSD, however, further work is needed to link the CLLJ to the horizontal advection term.

6.8 Summary and discussion

The Midsummer drought (MSD) is a key element of past, present and future climates of southern Mexico, northern Central America and the Caribbean with important implications for agriculture and water management (Hellin et al., 2017; de Sousa et al., 2018; Harvey et al., 2018). However, there is no complete description of the physical mechanisms that explain the spatial and temporal variability of the MSD. This lack of understanding is magnified when investigating the MSD in global climate models used for projections of future climate, as little is known as to why only some models can reproduce the MSD (Ryu and Hayhoe, 2014).

This chapter tackled these shortcomings in the literature by investigating the processes that are linked to the MSD in CMIP6 experiments of the MOHC models, an investigation that was motivated by the two previous chapters which showed that these models reasonably reproduced the main features of the MSD signal. The first contribution of this chapter is the diagnosis of MSD timings and patterns on a sub-monthly scale, a step forward from previous studies that diagnosed the MSD on monthly-mean timescales, possibly missing key information in the process. For this purpose, the wavelet transform method (WT; Chapter 5) was used to determine the timings of the MSD on a 5-day (pentad) scale.

The WT method proved useful to separate the wet season in each dataset into three stages: the first and second peak periods (P1 and P2) and the drier period (MSD). This approach

was able to reproduce the so-called MSD pattern reported in previous studies (Zermeño-Díaz, 2019; Zhao et al., 2020) using various diagnostics such as OLR, ω and the low-level wind flow. This pattern is characterised by a strong change of the zonal wind flow crossing from the Caribbean Sea into the easternmost Pacific Ocean, as well as by anomalous vertical velocities found west of the coast at around 125°W (Herrera et al., 2015; Zermeño-Díaz, 2019).

The chapter first evaluates key climate features in the region such as the seasonal cycle of the CLLJ and East Pacific SSTs. Results show that the simulations agree well with the observed seasonal cycle and that the experiments show very similar MSD patterns to ERA5. The following sections in the chapter test three hypotheses put forth to explain the MSD, which is the second key contribution from this chapter. Each hypothesis is evaluated using the WT method in two different ways. The first question was whether a hypothesis could explain the interannual variability in the strength and timing of the MSD in ERA5. The second approach focused on the CMIP6 experiments and aimed to test whether the elements of each hypothesis could explain the differences in precipitation at each stage of the seasonal cycle between the experiments.

The first mechanism proposed by Magaña et al. (1999) argues that SST-cloud-radiative feedbacks explain the MSD. In this hypothesis, the SSTs in the East Pacific should also exhibit a bimodal seasonal cycle, with a second peak in SSTs found in September. Even though Magaña and Caetano (2005) analysed this for a specific year and found no evidence of a second peak in SSTs, no study to date robustly evaluated whether observations or models confirm their hypothesis. This chapter provides evidence that in ERA5, SSTs not only do not increase at the later stages of the summer but rather decrease. While the seasonal cycle in the simulations do show a two peak structure, the composite analysis shows that as precipitation transitions from the drier MSD to the second peak periods, SSTs decrease in the Pacific coast of Central America, in contrast to the prediction of the SST-cloud feedback mechanism. No evidence is found that the variability of the East Pacific SSTs is directly associated with the precipitation over the MSD region in ERA5 or in the CMIP6 experiments.

The feedback mechanism also suggests that the second peak is a result of a second increase in downwelling shortwave radiation at the surface that results from cloud cover during the drier MSD. The solar declination angle mechanism of Karnauskas et al. (2013)

also suggests that shortwave absorption has two peaks in the seasonal cycle, which leads to the two precipitation peaks. The shortwave absorption at the surface does show a bimodal seasonal cycle in ERA5 and in the simulations, as predicted by these two mechanisms.

However, the interannual variability in ERA5 and inter-experiment differences in the absorbed shortwave at the different stages of the seasonal cycle cannot explain the changes over precipitation. Moreover, no significantly positive correlation is found between the shortwave absorption at the surface and precipitation at any lags but rather a strong anticorrelation signal is found, which is a result of stronger convective activity leading to more cloud cover and less downwelling shortwave at the surface. Therefore, while this chapter found some evidence of strong correlations between SW and precipitation, there is little evidence found that the SW drives precipitation, as argued by the solar declination angle mechanism.

Cloud-radiative effects (CRE) are known to be key for precipitation in monsoon regions and the central argument of Magaña et al. (1999) is that precipitation and CRE (at the surface) are part of a feedback mechanism that explains the MSD. This chapter presents the first regional evaluation of the net CRE at the surface as well as the long-wave and short-wave contributions. The net CRE at the surface over the wet season is negative in the regions of high precipitation, i.e., the East Pacific ITCZ and the MSD region reaching values of -100 W m^{-2} over the core ITCZ region in both the models and ERA5.

The net CRE is dominated by the short-wave component that acts to cool the surface due to the effect of cloud cover associated with convection. Over the MSD region, the net, shortwave and longwave CRE at the surface show a bimodal regime that closely follows the evolution of precipitation. Finally, an experiment part of CFMIP in which the long-wave effects of clouds are turned-off from the radiative scheme shows that the longwave radiative effects are key for monsoon precipitation in Central America and southern Mexico, where longwave effects are decoupled from the simulation, shows that the long-wave component of CRE are key for sustaining the monsoon circulation and precipitation irrespective of the bimodal MSD signal.

This section showed that CRE have a strong seasonal cycle associated with the MSD in ERA5 and the MOHC experiments. However, further research into CRE in present and future climates in the region is warranted, for example, further work could include a

detailed examination of the CRE at the top of atmosphere and at the surface in the MSD, particularly to understand the relationship between CRE and the large-scale circulation, and how this relationship is different over land in Mesoamerica than over the Caribbean Sea and the East Pacific Ocean.

One alternative hypothesis is that the MSD is caused by the modulation of the transport of moisture by the CLLJ (Herrera et al., 2015; Zermeño-Díaz, 2019; Martinez et al., 2019). The integrated moisture flux convergence and the total column water content are found to better explain observed and simulated differences in precipitation, compared to the previous hypotheses. Evidence is presented that the low-level wind flow variations on the west coast of Central America is linked to the variations in the strength and direction of the CLLJ. Changes to the CLLJ and moisture convergence allow skillful predictions of precipitation changes at the end of the MSD period but these are less skilful for changes at the start of the MSD.

A moist static energy (MSE) budget is implemented to investigate whether this technique could provide additional insight into the mechanisms of the MSD. The total column MSE, as well as the vertical advection terms of the budget show a clear bimodal signal that closely follows that of precipitation. The vertical advection of dry and moist static energy are found to have the strongest relationship to the interannual variability and the inter-experiment differences of precipitation in the MSD region. In particular, $\langle \omega ds/dp \rangle$ is able to better explain interannual variability in ERA5 as well as the precipitation differences between the range of experiments considered in this chapter.

The horizontal advection term does exhibit strong variations during the wet season over land and over the ocean, with increased divergence of h during the MSD, suggesting that the moisture transport hypothesis may be more relevant than the other theories. However, further research is required to better understand whether the vertical velocity profile changes during the rainy season or whether the strong relationship between the vertical advection term and precipitation is best explained by changes to the vertical profiles of h and s , as well as more research on how the horizontal advection term may be related to the CLLJ.

The findings of this chapter support the CLLJ hypothesis more than the first two hypotheses which are more radiative-thermodynamic in principle. Recent work (Boos and Pascale, 2021; Fu et al., 2021) has shown that mechanical forcing and the moisture and

MSE transport by the low-level wind flow are leading mechanisms to enhance convective activity over land and the coastlines of Mexico. Our results are in line with this recent work as the radiative effects over convection seem less important than the IMFC, which seems to be the leading cause for changes in the MSD precipitation.

7

The tropical route of QBO teleconnections in UKESM1 and HadGEM3

This chapter examines the influence of the stratospheric QBO on the tropical circulation and surface using pre-industrial control experiments of CMIP6 of the MOHC models and targeted model experiments. The relationship between the QBO and the tropical circulation, monsoons and the ITCZ is diagnosed and results are discussed in the context of existing hypotheses that could explain a downward influence from the stratosphere to the troposphere.

7.1 Introduction

Long-distance effects or teleconnections associated with the stratospheric quasi-biennial oscillation (QBO) have been well documented in the subtropics and extratropics, for example for the stratospheric polar vortex (Holton and Tan, 1980; Anstey and Shepherd, 2014; Lu et al., 2020), the subtropical jets (Garfinkel and Hartmann, 2011; Hansen et al., 2016) and the North Atlantic Oscillation (Hansen et al., 2016; Gray et al., 2018; Andrews et al., 2019b). Observational and modelling have also found evidence for a tropical route of influence of the QBO to surface climate (Gray et al., 2018; Hitchman et al., 2021). In particular, impacts related to the QBO have been shown in features of tropical climate such as monsoons (Giorgetta et al., 1999; Claud and Terray, 2007; Liess and Geller, 2012), the

ITCZ (Gray et al., 2018), tropical sea-surface temperatures (SSTs) (Gray, 1984; Garfinkel and Hartmann, 2011; Huang et al., 2012), tropical cyclones (Ho et al., 2009; Jaramillo et al., 2021) and most recently, the Madden-Julian Oscillation (MJO) (Lee and Klingaman, 2018; Wang et al., 2019; Martin et al., 2020).

The limited observational record suggests a QBO signal over monsoon regions in satellite-derived cloud properties (Collimore et al., 2003; Liess and Geller, 2012), as well as in surface precipitation (Gray et al., 2018). However, the observational evidence shows zonally asymmetric impacts, indicative that the impact of the QBO may depend on longitude, which has been hypothesized (e.g. by Collimore et al., 2003; Liess and Geller, 2012) to work through a QBO modulation of the Walker circulation (Hitchman et al., 2021). A similarly limited amount of modelling evidence exists for the tropical route of QBO teleconnections. For instance, Giorgetta et al. (1999) shows a sensitivity of cloudiness in boreal summer monsoon regions within a GCM and Nie and Sobel (2015) find in a cloud-resolving model that the influence of the QBO may depend on the strength of convection and SST forcing, suggesting a non-linear effect of the QBO over a convective profile. See section 2.5.2 and recent reviews on stratospheric-tropospheric coupling in the tropics (Hitchman et al., 2021; Haynes et al., 2021) for more detail on evidence for the tropical route of QBO teleconnections.

Although the polar and subtropical routes of QBO teleconnections are relatively well established, the impact of the QBO over tropical convective phenomena remains less well understood for various reasons. First, the short observational record limits the confidence in any analysis that seeks to investigate differences between the two QBO phases in a 30-40-yr long dataset. Tropical circulation variability on QBO time-scales is largely dominated by ENSO and there is also evidence that ENSO and convection in the tropical Pacific influence the QBO, which makes it difficult to separate the cause and effects of ENSO and the QBO (Schirber, 2015; Christiansen et al., 2016; Gray et al., 2018).

Furthermore, the specific physical mechanisms through which the QBO could influence tropical convection at the grid-scale or the large-scale tropical circulation are also not well understood. While early studies (Gray, 1984; Collimore et al., 2003) suggest that changes to the vertical wind shear or static stability in the upper-troposphere lower-stratosphere (UTLS) region are the cause of these teleconnections, there is a lack of evidence in the

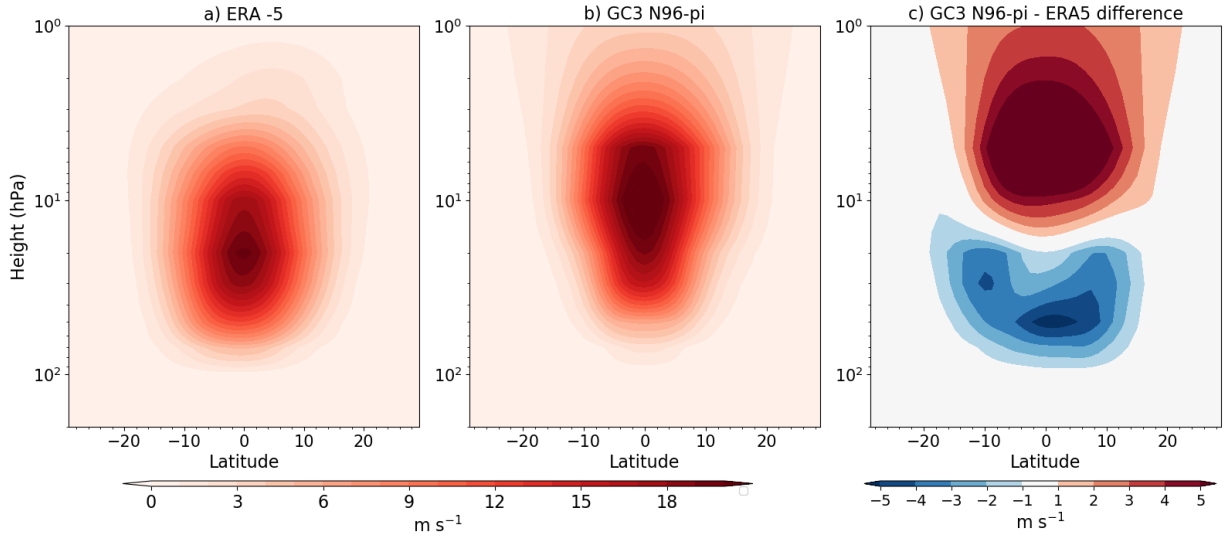


Figure 7.1: Latitude-pressure plot of the amplitude [m s^{-1}] of the QBO for (a) ERA5 and (b) GC3 N96-pi. (c) The difference in amplitude between the (b) model and reanalysis. Obtained from the zonal mean zonal wind fourier spectrum magnitude within the QBO periods, as in Schenzinger et al. (2017).

literature to support any mechanism over another as zonally asymmetric impacts are diagnosed in observations (Hitchman et al., 2021). As such, studies have struggled to pin-point direct impacts and mechanisms by which the QBO may modulate any aspect of tropical surface climate.

The leading hypothesis to explain an impact from the QBO on tropical deep convection suggests that changes to the UTLS static stability, caused by the QBO residual circulation, modifies the strength of convection (Collimore et al., 2003; Liess and Geller, 2012; Nie and Sobel, 2015). However, most of the existing climate models underestimate the amplitude of the QBO in the lowermost stratosphere (Figure 7.1) and by consequence the variability of the UTLS static stability associated with the QBO is lower in state-of-the-art GCMs (Schenzinger et al., 2017; Richter et al., 2020; Bushell et al., 2020). For example, the observed relationships between the QBO and the MJO have not been found in GCMs (Lee and Klingaman, 2018; Kim et al., 2020) and one reason for these results may be the underestimation of the UTLS temperature variability associated with the QBO in current GCMs.

In addition, only a relatively small number of studies have analysed tropical QBO teleconnections in a GCM, specifically in CMIP5/CMIP6 models (Serva et al., submitted),

as most CMIP analyses focus on the polar and subtropical routes of QBO influence (Richter et al., 2020; Anstey et al., 2021). Biases in the stratosphere of GCMs such as the weaker amplitude of the QBO in the lower stratosphere have led several studies to perform experiments in which the model stratosphere is relaxed towards an observed or idealized state, more commonly known as nudging (e.g. Garfinkel and Hartmann, 2011; Lee and Klingaman, 2018; Gray et al., 2020; Richter et al., 2020; Martin et al., 2021a). The nudging technique has proven useful because the relaxation can remove biases, identify causal pathways and test specific hypotheses regarding the mechanisms (Gray et al., 2020; Martin et al., 2021a; Haynes et al., 2021).

In short, there is a lack of robust evidence for QBO surface impacts in the tropics as QBO-related anomalies in observations may be the result of chance or the upward effect of tropical convection on the characteristics of the QBO. Moreover, there is little modelling evidence of QBO impacts in the tropics, particularly with state-of-the-art GCMs. The Met Office Hadley Centre (MOHC) Unified Model (UM) exhibits an internally generated QBO that is reasonably similar to observations, except for the weak amplitude bias in the lower stratosphere (Richter et al., 2020). Moreover, nudging has been successfully applied to this model in previous studies (Telford et al., 2008; Gray et al., 2020). For these reasons, the UM is ideal to investigate whether there are any surface impacts in the tropics associated with the QBO and what mechanisms may be at play in the observed stratospheric-tropospheric coupling.

This chapter first investigates QBO tropical teleconnections in the pre-industrial control simulations of the MOHC from CMIP6. This part examines whether there is any evidence of modelled QBO impacts at the surface in the tropics and whether they are consistent with the available rainfall observations. We then systematically explore evidence for a QBO impact on the major modelled tropical climate circulations, taking advantage of the extremely long simulations that can provide improved estimates of statistical significance when compared with the relatively short observational and reanalysis datasets.

Nudging experiments feature in the second part of the chapter. Atmosphere-only and coupled model simulations are analysed to evaluate the effect of improving the biases of the QBO amplitude on the surface response. Specifically, these experiments test the UTLS static stability hypothesis, so that stronger effects would be expected in a model with a

stronger UTLS temperature variability associated with the QBO compared to a model with a weaker UTLS static stability effect of the QBO.

The methodology and data used in this chapter are presented first, including the details on the nudging experimental setup. Then, the QBO impacts in the CMIP6 experiments are diagnosed and described which leads to the examination of the nudging experiments. A discussion and conclusions are presented at the end of the chapter.

7.2 Methods and data

The observational datasets and reanalysis (ERA5) used in this chapter are described in more detail in section 3.1 and consist of the HadSST3 dataset for SST, GPCP for precipitation and ERA5 for the rest of the diagnostics that include the zonal and meridional winds, air temperature, etc.

7.2.1 CMIP6 data

The three pre-industrial control experiments of the MOHC submitted to CMIP6 are used in this chapter: GC3 N96-pi, GC3 N216-pi and UKESM-pi. UKESM-pi and GC3 N96-pi are run with the same resolution (N96) of $1.875^\circ \times 1.25^\circ$ and GC3 N216-pi is considered a medium-resolution simulation (N216) with atmospheric resolution of $0.83^\circ \times 0.56^\circ$. The period of 1850-2350 (500 years) is used for GC3 N96-pi and GC3 N216-pi and 2050-2650 (600 years) for the UKESM-pi. The three simulations chosen use the same model setup, with constant year 1850 forcing, but differ in their horizontal resolution or the treatment of aerosol-chemistry processes and land-surface interactions (see section 3.2).

Pre-industrial control experiments are fit for the purpose of examining the internal variability of a model due to the constant forcing and their length. Multiple studies have used this type of experiments to investigate teleconnections and variability (Watanabe et al., 2012; Zanchettin et al., 2014; Palmer and McNeall, 2014; Menary et al., 2018; Dimdore-Miles et al., 2021).. For the purposes of this chapter, the QBO effect can be examined in the model as various cycles of decadal variability are sampled throughout the 500 yr of the integration. Note that the variability of the pre-industrial control experiments is

compared against the variability of observations with the caveat the greenhouse forcing may play a role for the observed responses.

7.2.2 Indices

For the QBO, the monthly-mean equatorially averaged [5°S-5°N] zonal mean zonal wind at 70 hPa is used and each phase of the QBO is defined using the threshold of 2 m s⁻¹ (Garfinkel and Hartmann, 2010), so the westerly phase (QBOW) is defined for months with an index value above 2 m s⁻¹ and the easterly phase (QBOE) for index values below -2 m s⁻¹. For ENSO, the EN3.4 SST index is used, with a running-mean of 5 months and a threshold of ±0.5 K used to define positive or negative events. Neutral months are defined where the running-mean of EN3.4 index is smaller than ±0.5 K.

The amplitude and descent rates of the QBO are calculated using the deseasonalized zonal mean equatorially averaged in equatorial latitudes for all levels. The amplitude (A) of the QBO is defined using the first and second principal components (PCs) empirical orthogonal function (EOF) decomposition of the 10-70 hPa wind time-series (Serva et al., 2020) as $A = \sqrt{PC1^2 + PC2^2}$. The descent rates are calculated following Schenzinger et al. (2017) for descending westerly and easterly phases individually by finding the level of the zero wind line ($u = 0$) for each month and computing the difference between consecutive months. These definitions of the amplitude and descent rates were chosen to evaluate the influence of ENSO on the whole profile of the QBO and not just one single level.

An index for the Indian Ocean Dipole (IOD) was also required and this chapter uses a convective precipitation index of the zonal gradient in the Indian Ocean (convective IOD Index), defined as the difference of the deseasonalized area-averaged convective precipitation between the western [50-70°E] and eastern [80-100°E] equatorial [10°S-10°N] Indian Ocean, which is in a similar region as the standard SST IOD index (Wang and Wang, 2014). This convective precipitation is used to define IOD events with a 1 standard deviation threshold to define positive and negative events.

7.2.3 Analysis techniques

Composite analysis is the preferred technique used throughout this chapter. For each QBO or ENSO phase, composite samples are drawn for specific seasons using the indices and definitions mentioned above. Statistical significance is estimated in various ways, in some cases through standard Student or Welch t-test's where specified, and in some other cases a randomised resampling or bootstrapping method is also implemented in several sections of the chapter. The bootstrapping method is performed in all cases by drawing random samples from the entire simulation and repeating the process 10,000 times to evaluate the likelihood of obtaining a relationship by chance.

Linear regression analysis has proven useful to understand the effect of one or more aspects of the climate over a region or a time-series, and was used to investigate the surface impacts of the QBO in observations by Gray et al. (2018). A simple linear regression model can be written as:

$$Y(t) = X_0 + X_i(t)\beta_i + \epsilon, \quad (7.1)$$

where Y is the measured or dependent variable, X_0 is a constant coefficient, β_i is the regression coefficient between X_i and Y and ϵ represents random error or a residual. In all cases, the models solved using an ordinary least-squares (OLS) method. A multivariate regression model can be used to study the joint effect of two or more predictors over a variable (Y) such that the model can be written as:

$$Y(t) = X_0 + \sum_j^N X_j(t)\beta_j + \epsilon \quad (7.2)$$

where $X_j(t)$ is any predictor with an associated regression coefficient β_j . As in previous studies (Gray et al., 2018; Misios et al., 2019), the regression coefficient can be rescaled to evaluate the total effect that a predictor (X_j) can have on the variance of the measured variable (Y) using the standard deviation (σ_j) and the maximum ($X_{j,max}$) and minimum ($X_{j,min}$) values of X_j so that the rescaled coefficient β'_j can be written as:

$$\beta'_j = \beta_j \frac{X_{j,max} - X_{j,min}}{\sigma_j}. \quad (7.3)$$

7.2.4 Nudging experimental setup

This section describes the experimental setup for the nudging experiments. The GC3.1 configuration of the UM model is used (model version 11.4), using an atmospheric horizontal resolution of N96 (corresponding to the low-resolution version of the MOHC CMIP6 simulations). Both atmosphere-only and ocean-atmosphere coupled experiments were conducted for the period 1981-2015, using a present-day climate setup where all external forcings, including greenhouse gas and aerosol emissions, are set constant to those of the year 2000.

Nudging refers to the relaxation of a model variable towards a specified state which can be from reanalysis, observations or idealized states (Gray et al., 2020; Martin et al., 2021a). In the UM setup, three variables can be relaxed, air temperature (T) and the zonal (u) and meridional (v) components of the wind. The relaxation is applied at each grid-point, in contrast to the setup in other models (e.g. Martin et al., 2021a) where the relaxation is performed in a zonal-mean sense. Specifically, the UM uses a Newtonian relaxation technique (Telford et al., 2008; Gray et al., 2020) which sets the field to be relaxed (F) at each time-step through the following equation:

$$\Delta F = G\Delta t(F_{ndg} - F_{model}), \quad (7.4)$$

where ΔF is the discrete change of F at each time-step, G is the relaxation parameter, Δt is the time-step size, F_{ndg} is the value of the field from the nudging data and F_{model} is the model value of the field at the last time-step (Telford et al., 2008).

The relaxation parameter G sets the strength of the relaxation and is linked with the relaxation timescale (τ) by $G = 1/\tau$. In the UM model, the relaxation timescale is given by the temporal resolution of the nudging data, which is 6-h (Telford et al., 2008; Gray et al., 2020), so that $G = \frac{1}{6} \text{ h}^{-1}$. This relaxation parameter has been shown to be sufficiently strong to constraint the stratospheric state of the model (Gray et al., 2020) and so the same parameter was used for the simulations of this chapter.

Furthermore, the nudging can be performed between specified vertical levels and in selected latitude/longitude regions with *tapering*. The tapering refers to a linear interpolation

Table 7.1: Experimental setup indicating the model configuration, the period, ensemble members, acronym and relaxation details.

Setup	Period	Ensembles	Name	Nudging
Atmosphere-only	1981-2015	3	AMIP	ERA5. U-only 90 hPa
Atmosphere-only	1981-2015	2	AMIP-Control	No
Atmosphere-only	1981-2015	3	AMIP-Shifted	ERA5. U-only, 90 hPa. Relaxation shifted -1 year.
Coupled	1981-2015	6	Coupled Nudged	ERA5. U-only 90 hPa.
Coupled	1981-2015	2	Coupled Control	No.

between the maximum G and zero nudging ($G = 0$). For example, a tapering of 4 vertical levels was applied in our simulations which means that there was a linearly increasing G from a bottom level with no nudging to the level where the specified G is implemented; the same linear interpolation works for latitudinal nudging and tapering.

The experimental design chosen was to relax the zonal wind (u) in the model levels that correspond to 90 hPa to 4 hPa, with a tapering of 4 levels, which means that full nudging was only working from 70 hPa to 10 hPa. The nudging was done at all longitudes in the latitude band of 10°S-10°N with a latitudinal tapering of 10 degrees on both sides, which means that at 20°N the relaxation parameter was 0. The experimental setup aims to reasonably simulate the observed variability of the zonal wind leaving the meridional component of the wind and the temperature to respond freely within the model.

Atmosphere-only and coupled ocean-atmosphere simulations were performed with this nudging setup, with corresponding control simulations in which there was no relaxation of any kind (Table 7.1). The atmosphere-only (AMIP) experiments were run with observed SSTs using the CMIP6 SST dataset used for AMIP experiments, note the surface boundary SSTs are used at all latitudes. The coupled experiments use an oceanic resolution of 0.25° (ORCA025) using the NEMO model (Storkey et al., 2018). Each ensemble member was initialized from different ocean/atmosphere initial conditions in order to decrease the role that internal variability may have on these simulations. For each of the nudged experiments several ensemble members were performed, three for the atmosphere-only configuration and six for the coupled ocean-atmosphere configuration.

Note that the coupled experiments differ only slightly from the setup used in the CMIP6 piControl experiments, with the atmospheric resolution matching the resolution of GC3 N96-pi ($1.875^\circ \times 1.25^\circ$) and the oceanic resolution being the same as GC3 N216-pi (0.25°). The forcing is constant in both types of runs, except that in the piControl experiments, the forcing represents conditions of the year 1850 and in these experiments the forcing is for the year 2000.

In addition to the nudged and control coupled and AMIP experiments, we performed another type of atmosphere-only experiment. In the normal AMIP Nudged experiment, the SST driving data corresponds to the same year as the imposed zonal wind in the equatorial stratosphere that was observed in the real-world. To explore possible feedback processes between QBO winds and the SSTs, we performed an AMIP Shifted experiment, where the nudging data was shifted with a -1 year lag from the SSTs. In this experiment, e.g., the model year 1997 was run using 1997 SSTs but zonal winds in the stratosphere corresponding to 1996 of ERA5. In this way we have minimised any in-phase relationship between the QBO phase and the SSTs. An alternative approach would be to *shuffle* the SSTs so that each year is run with randomly selected SSTs. However, since we are performing multi-year simulations shuffling has associated issues of how to join the randomly-selected SSTs at the year-boundary to form a coherent multi-year SST time-series. To avoid this issue we decided to simply shift the SSTs by one year so the QBO phase and SSTs were not aligned.

7.3 Teleconnections in the pre-industrial control experiments

This section examines the tropical route of QBO teleconnections in a GCM, specifically, whether there is any surface impact of the QBO in the tropics in the MOHC piControl experiments. The medium resolution version of the model (GC3 N216-pi) arguably best represents the tropospheric dynamics, particularly in some monsoon regions (García-Franco et al., 2020), so results are shown primarily for GC3 N216-pi. The other two simulations were also analyzed and we note where there is agreement or not between the three simulations.

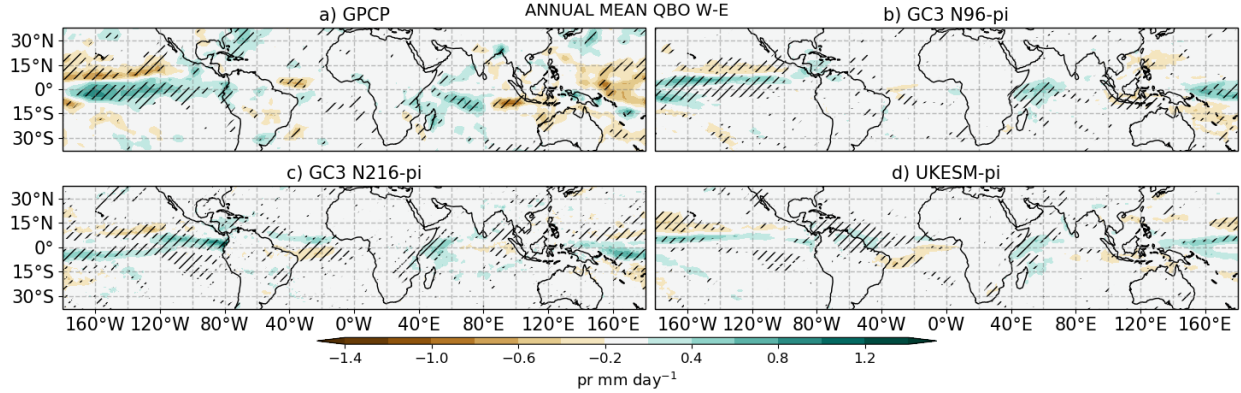


Figure 7.2: Annual mean precipitation difference between QBO W-E phases in (a) GPCP, (b) GC3 N96-pi, (c) GC3 N216-pi and (d) UKESM-pi. Hatching denotes statistical significance to the 95% confidence level using bootstrapping with replacement for each composite sample.

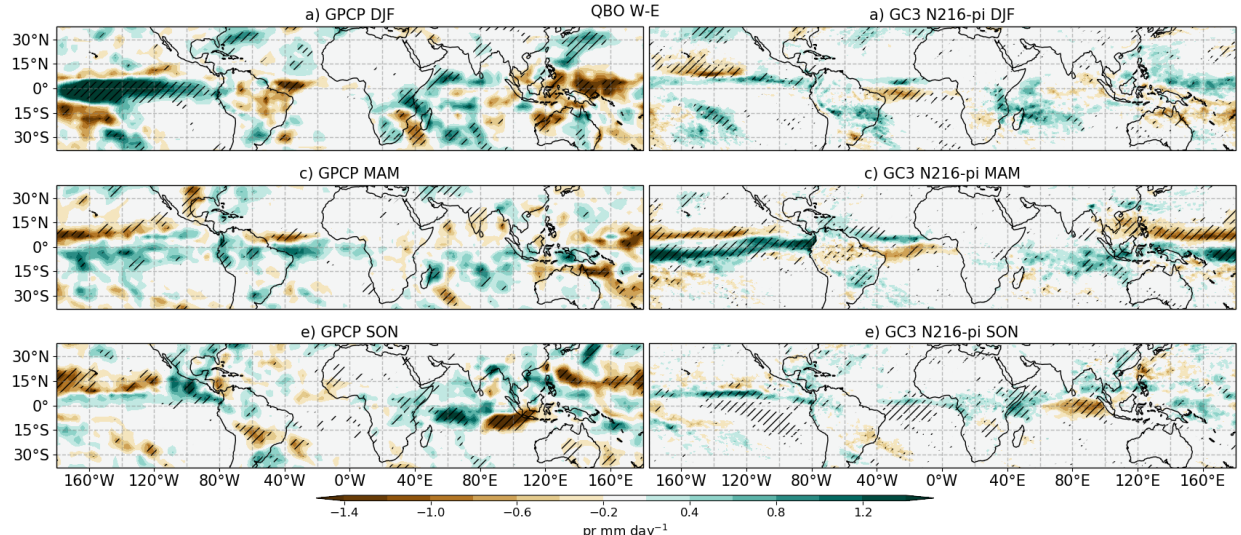


Figure 7.3: As in Figure 7.2, but showing QBO W-E differences in specific seasons for GPCP and GC3 N216-pi.

7.3.1 Precipitation and SST response

The composite differences in annual mean precipitation between QBO W and E phases (Figure 7.2) in observations (GPCP) are largest and significant in the tropical Pacific, equatorial Atlantic and the Indian Oceans, which generally agrees with previous observational findings (Liess and Geller, 2012; Gray et al., 2018). The three simulations generally agree with the results of GPCP, with positive differences (QBO W-E) found in the equatorial Central Pacific and the Indian Ocean as well as the negative differences in subtropical Pacific, albeit the differences are smaller in the simulations.

These QBO-related differences in precipitation are strongly dependent on the seasonal cycle in both models and observations (Figure 7.3). For example, during DJF (Fig. 7.3a), the positive differences in GPCP (which resemble El Niño anomalies) found over the equatorial Pacific are stronger compared to the annual mean, whereas in SON (Figure 7.3e) there are no significant differences in the same region. In contrast, in SON the largest differences in GPCP appear in the Indian Ocean.

In GC3 N216-pi, however, the positive El Niño-like differences in the equatorial Pacific are stronger in MAM (Fig. 7.3c-d) and not in DJF as in GPCP. The Atlantic ITCZ region shows a response in MAM in both observations and models (although the model response is of opposite sign to observations) but this response is muted in annual-mean differences. The responses over the Atlantic and Indian Ocean are of opposite sign, for example in DJF. This feature would suggest that if the impacts are caused by the QBO they are not zonally symmetric, and possibly support the hypothesis of a QBO modulation of the Walker circulation (Liess and Geller, 2012; Hitchman et al., 2021). UKESM-pi and GC3 N96-pi show similar precipitation patterns to GC3 N216-pi that resemble El Niño precipitation patterns in DJF, as well as tropical precipitation differences that also exhibit strong seasonal dependence (not shown).

In SON (Fig. 7.3e-f), both models and observations results show relatively large and significant differences in the Indian Ocean, characterized by a dipole of wet anomalies to the west and dry anomalies to the east. These dipole anomalies may be an indication that the QBO influences the Indian Ocean Dipole (IOD), which is characterized by a zonal gradient of SSTs and convective activity in the Indian Ocean (Saji et al., 1999; Deser et al., 2010; McKenna et al., 2020). Finally, all the models and GPCP indicate that the Caribbean Sea is wetter during QBO W compared to the QBO E in boreal summer (not shown).

The QBO W-E SST differences are consistent with the precipitation results (Figure 7.4). Results in HadSST and in the models show significant positive differences in the equatorial Pacific which are similar to El Niño patterns. In DJF, the observed SST anomaly pattern resembles an East Pacific (or 'standard') El Niño, whereas the simulated anomalies in DJF for all models are weaker and look like central Pacific El Niño (Capotondi et al., 2015). In

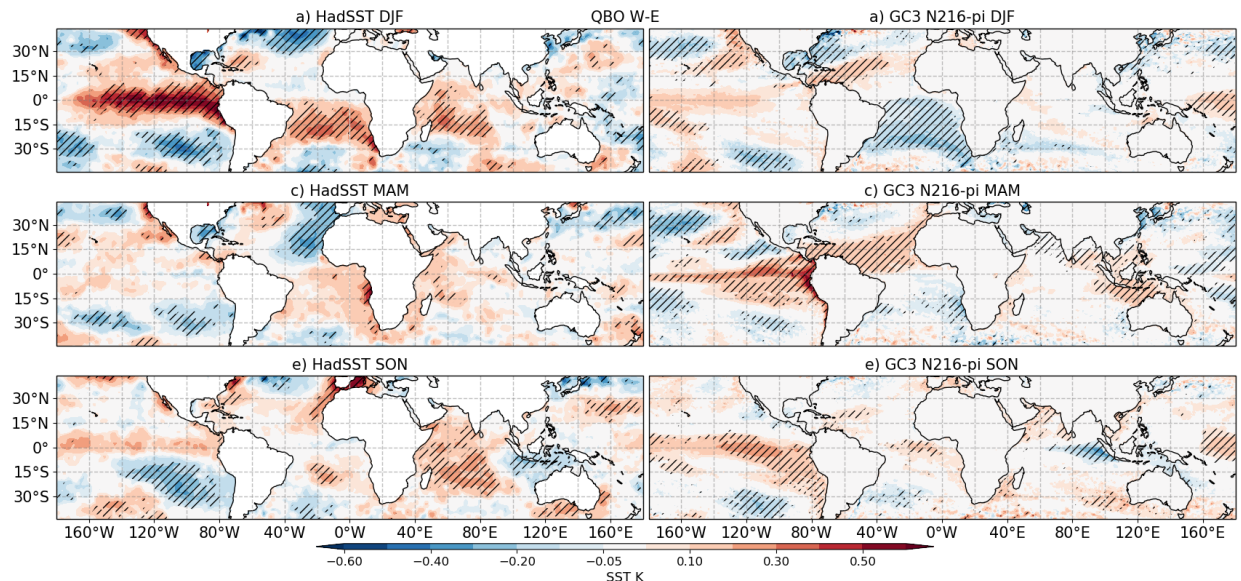


Figure 7.4: As in Figure 7.3, but for SST differences in the (a, b) annual, (c, d) DJF and (e, f) MAM means for HadSST and GC3 N216-pi.

GC3 N216-pi the largest differences are observed in MAM in the easternmost Pacific Ocean whereas in the other simulations, the El Niño-like differences also appear in DJF (not shown).

The models show a warm difference in the northern tropical Atlantic that is found in all seasons except in boreal summer and that is not observed in HadSST (Fig. 7.4). The simulated warm anomalies in the Caribbean Sea and Atlantic in DJF are accompanied by a cooling of the Gulf of Mexico, warmer SSTs over the coast of California and a cooling of the central North Pacific, all of which resemble the impact of El Niño events and the positive phase of the Pacific North American (PNA) pattern (Deser et al., 2010; Guo et al., 2017; Jiménez-Esteve and Domeisen, 2020). Alternatively, these SST patterns may be associated with the QBO influence on the PNA pattern and the subtropical jet position, independent of ENSO (Garfinkel and Hartmann, 2011), or the polar vortex route to the NAO (Gray et al., 2018).

This section investigates the precipitation and SST composite differences associated with the phase of the QBO. Evidence suggests that the strongest precipitation responses are found over the ocean, in the ITCZ regions, and that several SST and precipitation patterns look like El Niño teleconnection impacts. However, there is no hypothesis that could explain why ocean effects are larger than over land or why only oceanic convection would be affected

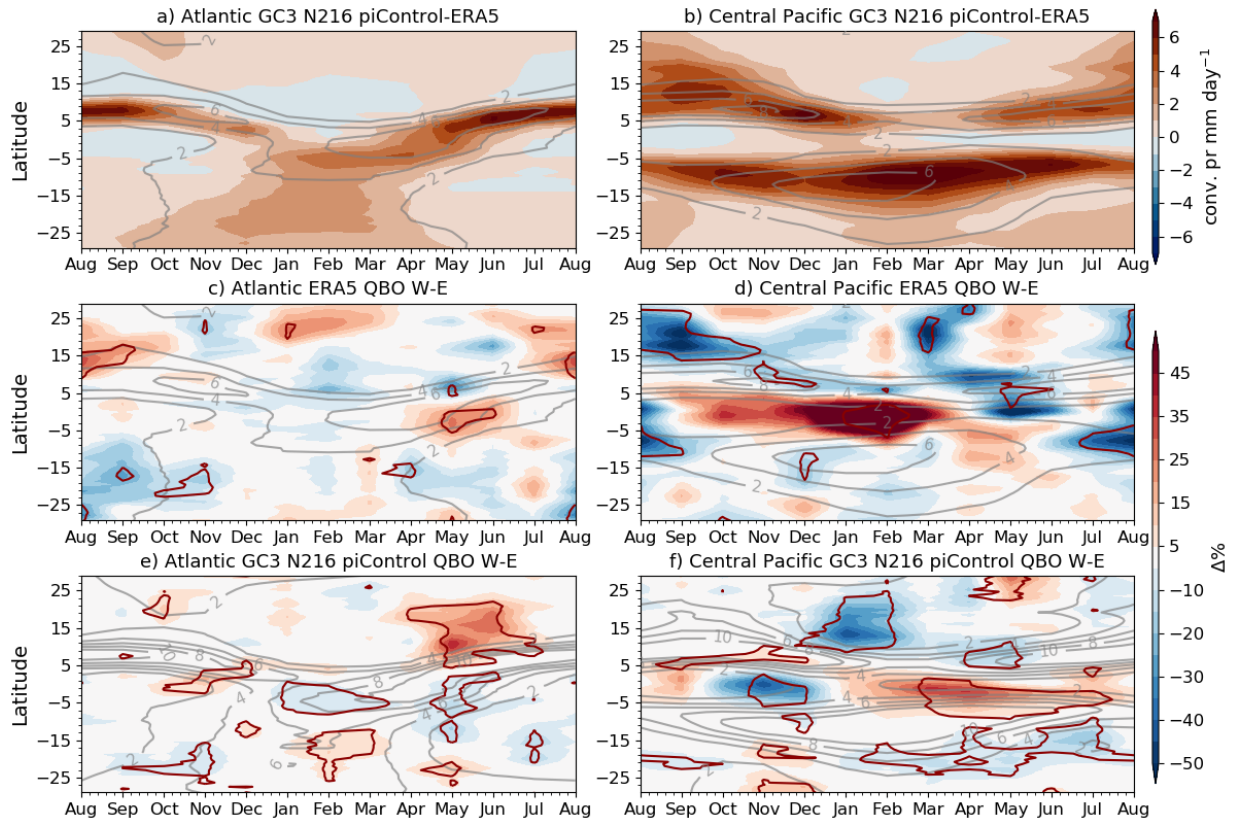


Figure 7.5: (a, b) Zonal mean biases in convective precipitation in GC3 N216-pi compared to ERA5 in the (a) Atlantic [60°W-20°W] and (b) Central Pacific [180°W-140°W] sectors. (c-f) Monthly and zonal mean QBO W-E percent (%) differences in convective precipitation where the absolute difference is weighted by the climatological value at each latitude and month. The line-contour (red) depict differences that are statistically significant to the 95% level according to a bootstrapping test and the grey lines show the climatological values.

by the QBO. These results also suggest that there seems to be some aliasing or coupling with ENSO events in these composites and that the QBO impact is not zonally symmetric. One would reasonably assume that observed ENSO-QBO aliasing would be due to the short observational record. For that reason the following sections examine more closely how the ITCZ, the Walker circulation and ENSO are related to the QBO.

7.3.2 ITCZ and monsoons

Climate model biases in the representation of the migration and dynamics of the ITCZ may modify any physical effects of the QBO over convection. In GC3 N216-pi, biases in the position and strength of the Pacific and Atlantic ITCZs are smaller than the lower resolution

versions of the UM model (see Chapter 4). However, these biases (Fig. 7.5a-b) are still noteworthy and are mainly characterized by a southward shift of the simulated Atlantic ITCZ in DJF and MAM and a wider extent of the Central Pacific ITCZ compared to ERA5.

The monthly-mean QBO W-E zonal-mean convective precipitation differences in the Pacific and Atlantic ITCZ regions (Figure 7.5) show that the ITCZ impacts are seasonally dependent. While there are no clear differences in the Atlantic sector for ERA5 in any month, in GC3 N216-pi there is a significant northward shift of the ITCZ from April to June, which is likely associated with the warm SST anomalies found in this season in the northern tropical Atlantic (Fig. 7.4).

The differences in the Pacific sector confirm previous model and observational results (Gray et al., 2018; Serva et al., submitted) that the Pacific ITCZ becomes stronger during QBOW compared to QBOE (Fig. 7.5d, f) in both ERA5 and the simulations. In ERA5, the strongest differences are found during DJF, characterized by increased precipitation over the core ITCZ region. In GC3 N216-pi, a southward shift of the ITCZ is observed from February to July, maximized in the MAM season, observed as a dipole of positive anomalies to the south and negative anomalies to the north of the equator. Very similar results for the Atlantic and Pacific sectors were observed for the other two simulations (not shown).

Note that the biases in the model are larger than the climatological values in some instances. This reduces confidence that the model response is to be expected in observations. However, impact to the strength of the East Pacific ITCZ is strikingly similar in observations (Fig. 7.2). Moreover, there is little modelling evidence of a QBO effect over the ITCZ in a model to begin with so that even though biases may play a big role, Figure 7.5 shows a robust association between the QBO and the ITCZ in a long GCM integration.

In spite of existing observational evidence (Collimore et al., 2003; Liess and Geller, 2012; Gray et al., 2018) that suggest a link between the QBO and convective activity in monsoon regions over land, the results in the previous section (Fig. 7.2) show little-to-no effect of the QBO on precipitation over land in these simulations. The precipitation response over land is examined more closely by analysing regions that fit the concept of the global monsoon. For this purpose, a monsoon region is defined where over 55% of the total annual rainfall is

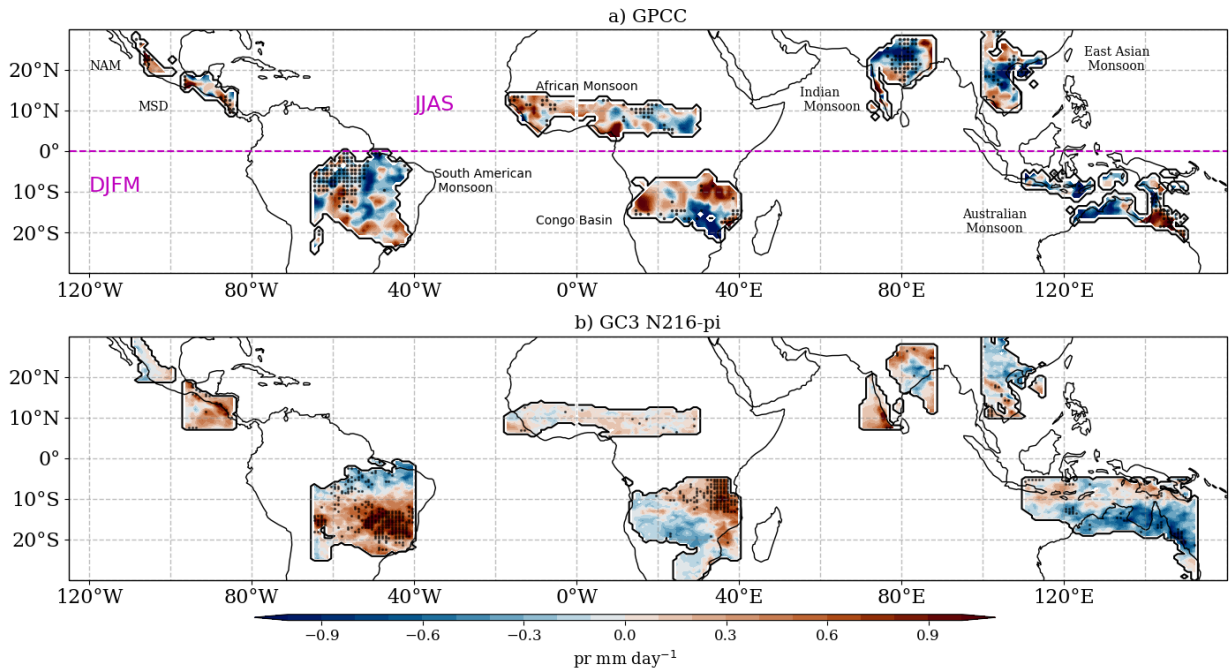


Figure 7.6: Convective precipitation differences in monsoon regions between QBO W-E phases for a) ERA5 and b) GC3 N216-pi. For monsoon regions in the Northern hemisphere, differences are shown for the JJAS period, whereas for Southern Hemisphere monsoons, results are shown for DJFM. Red dots indicate differences that are statistically significant to the 95% level according to the bootstrapping test.

observed or simulated in the respective summer season and the summer-winter rainfall rate difference is higher than 2 mm day^{-1} (Wang and Ding, 2008; Wang et al., 2017, 2021).

After defining these regions, the QBO W-E differences are computed for JJAS and DJFM for Northern and Southern Hemisphere monsoons, respectively. Figure 7.6 shows that there is no coherent response to the QBO phase in GPCC in any monsoon region. However, in GC3 N216-pi there are significant differences for Southern Hemisphere monsoons. In the South American monsoon region, the QBO W-E differences indicate a significantly wetter southeastern Brazil, where the South Atlantic Convergence Zone is located (Zilli et al., 2019). Similarly, a drier Australian monsoon and wetter conditions for East Africa are observed during QBOW compared to QBOE.

For Northern Hemisphere monsoons there are no robust or significant differences (Fig. 7.6b), however, if only Neutral ENSO months are considered, all the three simulations suggest a wetter boreal summer for Central America (not shown) in QBOW compared to QBOE. The

different responses observed for the three simulations suggest that the representation of the dynamical features of each monsoon by each model configuration is important for any response to the QBO. Furthermore, the relatively smaller differences seen for land compared to ocean features indicates that SST feedbacks are important for the QBO response in the model, and potentially less important effects are simulated by the model in land monsoon regions.

This section shows that impacts to the strength and location of the ITCZ are observed in the simulations. In particular, observational and model results suggest a stronger Pacific ITCZ for QBOW compared to QBOE, which could be due to an aliasing effect or an indication of an ENSO-QBO relationship. Shifts to the Atlantic ITCZ in the model are not seen in observations, and are likely influenced by model biases, however, this is one of the first pieces of evidence of a QBO-ITCZ relationship in a GCM. Model results also suggest a modest yet significant influence over Southern Hemisphere monsoons and a weak but robust impact over Central American precipitation and no robust impacts for other Northern Hemisphere monsoons.

7.3.3 ENSO and the IOD

A higher frequency of El Niño events during QBOW and of La Niña during QBOE has been observed since 1979 (Taguchi, 2010; Liess and Geller, 2012), however, the observational record is so short that these relationships may be explained by the statistical uncertainty. The precipitation and SST responses found over the equatorial Pacific in the three pre-industrial control simulations also resemble ENSO patterns, which may suggest an uneven frequency of ENSO events per QBO phase in these long integrations. Similarly, a dipole response in the Indian Ocean found in boreal fall closely resembles the IOD. For these reasons, we examine if the frequency of ENSO and IOD events is in any way related to the phase of the QBO. Note that ENSO and IOD indices and events are defined in section 7.2.2.

The result of this analysis shows that EN3.4 SST and convective IOD indices are significantly different for each phase of the QBO in HadSST/ERA5 and GC3 N216-pi (Figure 7.7). In particular, the mean IOD and ENSO indices are very frequently positive in QBOW and negative in QBOE months from September until January. In the model, the differences for the IOD index are largest in SOND and for the ENSO index from Feb-to-May.

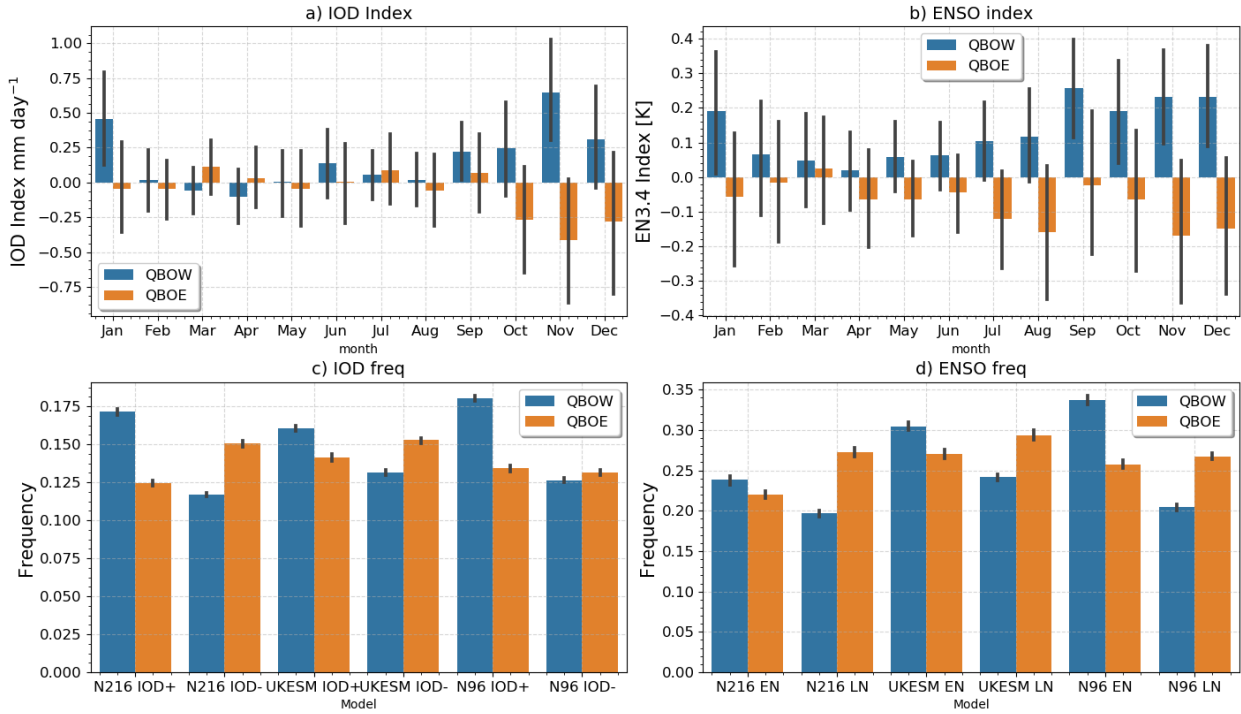


Figure 7.7: Monthly-mean (a, c) IOD-prc and (b, d) EN3.4 index separated per QBO phase in (a-b) GC3 N216-pi, and for the (c) ERA5 and (d) HadSST datasets. The error bars show the standard deviation of each index for each month.

Table 7.2: ENSO and IOD events frequency (month month⁻¹). For positive and negative events, for each mean value the error shown is the standard deviation of the distribution found by bootstrapping with replacement.

Dataset	QBO phase	IOD+	IOD-	El Niño	La Niña
GC3 N216-pi	W	0.17±0.03	0.11±0.02	0.24±0.09	0.19±0.05
GC3 N216-pi	E	0.12±0.03	0.15±0.03	0.21±0.07	0.26±0.07
ERA5/HadSST	W	0.17±0.01	0.13±0.01	0.28±0.01	0.27±0.02
ERA5/HadSST	E	0.12±0.01	0.19±0.03	0.17±0.02	0.27±0.03

In observations and reanalysis, the IOD differences are also observed from September through January, and the ENSO index differences are characterized by negative mean ENSO index for QBOE from December to April. The GC3 N96-pi and UKESM-pi results are very similar and the differences are also significant (not shown).

The frequency of ENSO and IOD events are also significantly different for each ENSO phase in both ERA5 and the three simulations (Table 7.2). El Niño events are more frequent under QBOW conditions than under QBOE and, while in the HadSST dataset, La Niña

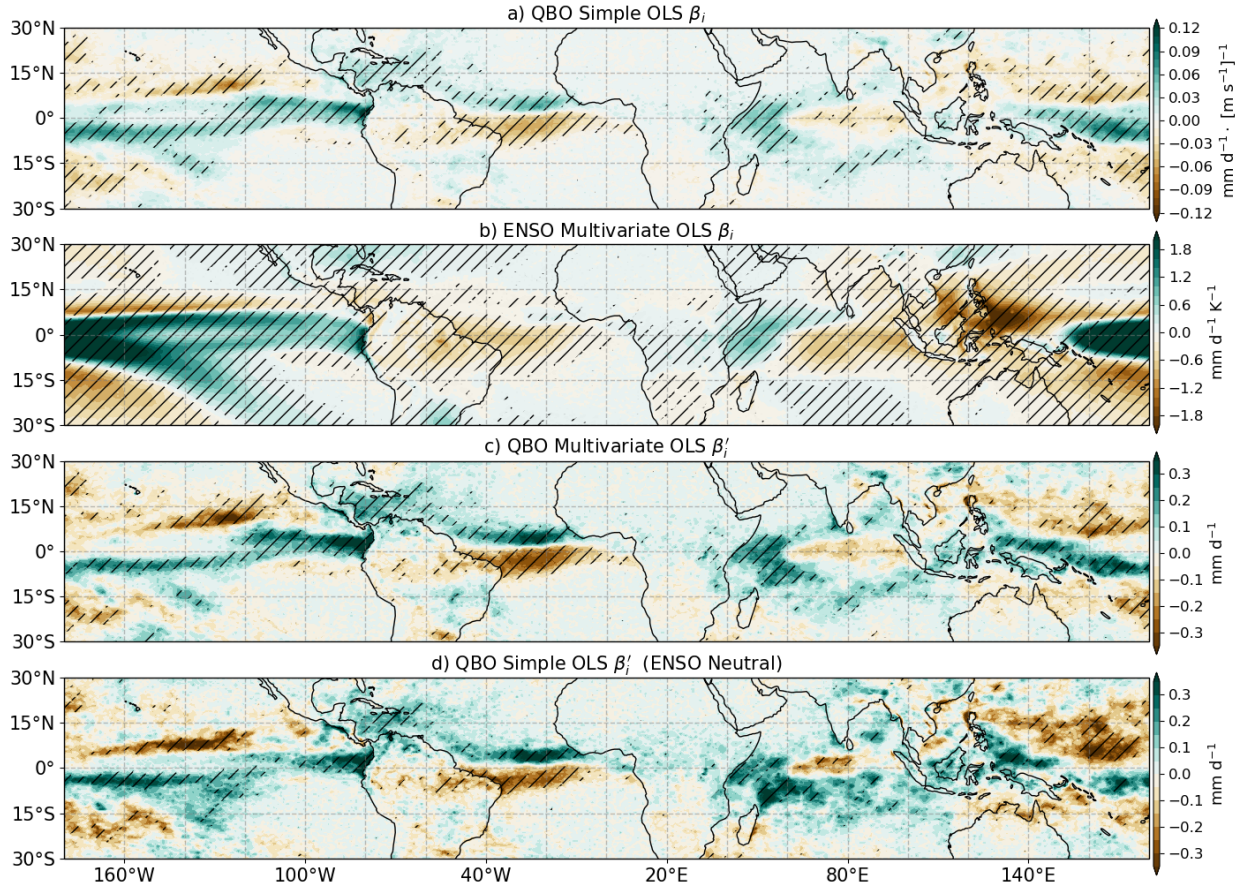


Figure 7.8: Regression model results in GC3 N216-pi for convective precipitation. (a) Regression coefficients (β_i) from a simple ordinary least-squares (OLS) regression model with the QBO index, (b, c) the regression coefficients resulting from a multivariate regression model using the ENSO and QBO indices for the (b) ENSO and (c) QBO predictors. In (c) the regression coefficients are rescaled by multiplying the regression coefficients with the ratio of maximum amplitude and standard deviation of the QBO index. (d) Rescaled regression coefficients from a simple OLS model with the QBO index, but using time-series where ENSO was classified as in a Neutral state using the EN3.4 index.

events are equally frequent in both QBO phases, in GC3 N216-pi La Niña events are more frequent under QBOE than under QBOW. The IOD event frequency is also markedly different depending on the QBO phase, with positive events more frequently observed in the westerly phase of the QBO and negative events found more frequently under QBOE, both for ERA5 and the experiments. These results evidence that in these simulations ENSO and the IOD are significantly linked to the QBO phase. The uneven frequency of ENSO and IOD events amongst QBO phases may explain the composite differences found in Figs. 7.2, and 7.3.

In order to better understand whether there is a 'true QBO' precipitation response

in the tropics, independent of ENSO, we use regression analysis as described in section 7.2.3. A simple ordinary-least squares (OLS) regression model is used to evaluate the linear relationship between the QBO phase at 70 hPa and precipitation variability. A multivariate regression model, which includes the EN3.4 index, estimates the QBO and ENSO linear relationships with precipitation, simultaneously. Based on the multi-variate regression, one can evaluate the impact of one predictor (QBO) having removed the influence of another predictor (e.g. ENSO).

The simple regression analysis (Figure 7.8a) shows very similar results to the annual-mean composite differences, suggesting increased precipitation over the equatorial Pacific when the zonal winds at 70 hPa are positive. However, these results could be due to the increased frequency of El Niño events for QBOW phases. The multivariate results, i.e., when both ENSO and QBO indices are included in the regression, show that part of the precipitation response associated with the QBO is removed compared to the simple regression, but other responses remain and are still significant (Fig. 7.8c). For example, the positive regression coefficients that suggest a northward shift of the Atlantic ITCZ and the wetter Caribbean Sea and western Indian Ocean in the simple regression model are still found in the multivariate regression analysis, as well as in a simple regression analysis when only Neutral ENSO months are considered (Fig. 7.8d).

These results highlight that there is a 'true' precipitation response or signal associated with the QBO that is independent from ENSO. The implication from these results is that the effect of ENSO must be considered not only when analysing observations but aliasing with ENSO may also occur in model simulations. Similarly, these results confirm that significant differences in the position and strength of convection in the Atlantic and Pacific ITCZs and in the Indian Ocean and Caribbean Sea regions are related to the phase of the QBO and are independent from the ENSO index.

A different question, however, is whether the impacts associated with ENSO teleconnections vary for each QBO phase. Figure 7.9a shows the QBO W-E differences in DJF-mean precipitation for all months in GC3 N216-pi. This response over all events is then split and compared to Neutral ENSO seasons only, and El Niño (EN) and La Niña (LN) seasons. The response in the Atlantic ITCZ, described in previous sections, is observed in Neutral

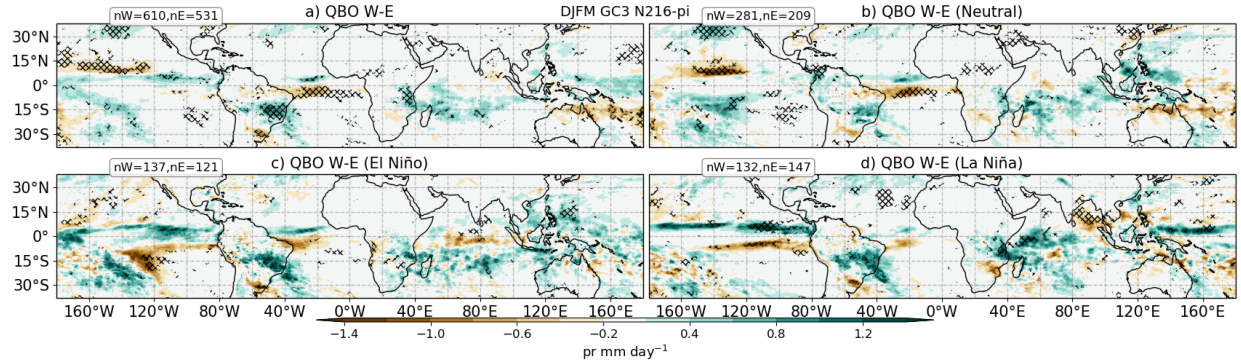


Figure 7.9: Composite QBO W-E precipitation differences in GC3 N216-pi in DJFM for (a) all the events, (b) Neutral ENSO conditions only, (c) El Niño and (d) La Niña conditions. The sample size of each composite is noted in the top left corner of each panel. Statistically significant differences to the 99% confidence level are shown through the hatching.

and EN years but this response is not observed during LN conditions. However, positive differences in the western Indian Ocean and in the western Pacific are much stronger during LN than in other ENSO phases.

These results can be interpreted as El Niño and La Niña teleconnections being slightly different for each QBO phase. For example, in southeastern Brazil, wetter conditions during QBOW compared to QBOE are found both for LN and EN conditions which indicate that in this model simulation, ENSO teleconnections to South America are also dependent on the QBO phase. Similarly, the La Niña precipitation response in the Western Pacific is significantly dependent on the QBO phase. The positive precipitation response on the west coast of California only appears during Neutral periods.

This section showed that different frequencies of ENSO and IOD events for each QBO phase are observed in the simulations and observations, which could influence the results of the previous sections. Regression analysis was used to account for the likely aliasing of ENSO impacts with the QBO surface response. Several significant impacts linked to the QBO remain even when the influence of ENSO is removed, suggesting some surface impacts associated with the QBO are independent of ENSO.

7.3.4 The Walker circulation

A number of studies have suggested a link between the QBO and the Walker circulation to explain zonally asymmetric anomalies in convective features associated with the QBO

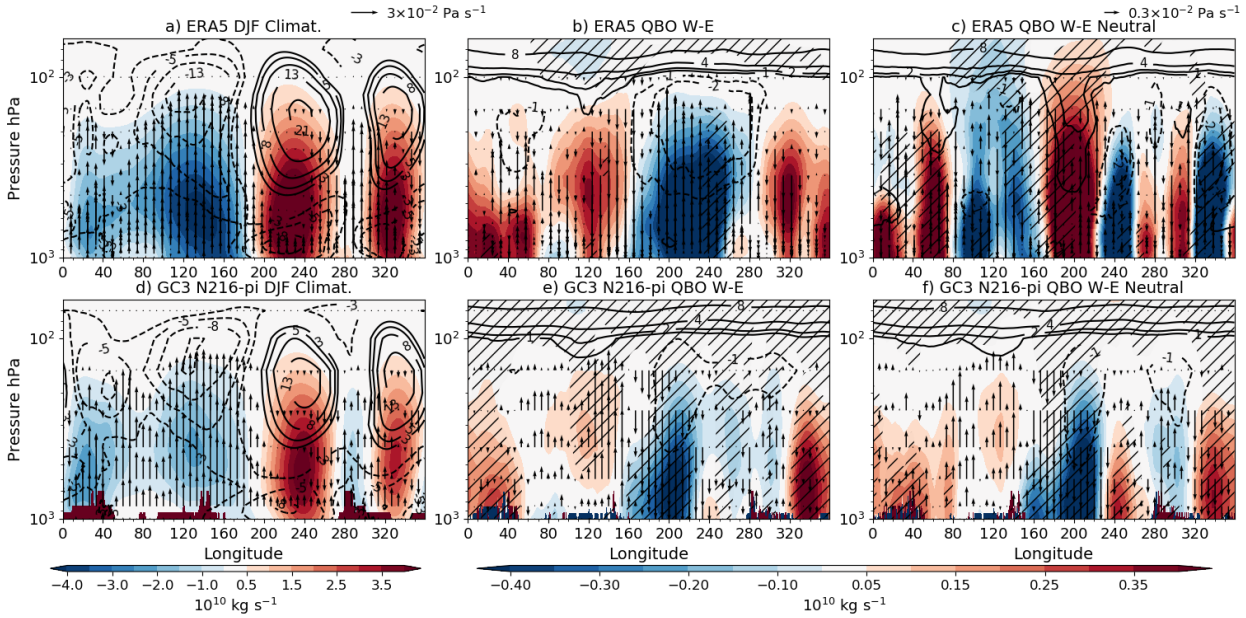


Figure 7.10: (a, d) Climatological mean-state of the Walker circulation, depicted through the zonal streamfunction (ψ) in shading, the zonal wind (contours), and vertical velocity (ω [Pa s^{-1}], vectors) during the DJF season in a) ERA5 and (d) N216-pi. (b-c, e-f) show W-E composite differences, during DJF, for the same variables only that hatching represents statistical significance to the 95% confidence level for differences in the streamfunction, and only statistically significant differences in the zonal wind and ω are shown. (g-h) are as in (d-f) but considering Neutral ENSO periods only. Example vector sizes for ω are given in the top right corners of a and c.

(e.g. Collimore et al., 2003; Liess and Geller, 2012). To evaluate this hypothesis, the zonal streamfunction is used to measure the Walker circulation (Yu and Zwiers, 2010; Bayr et al., 2014) and is defined as:

$$\psi = 2\pi \frac{a}{g} \int_0^p u_D dp, \quad (7.5)$$

where ψ is the zonal streamfunction, u_D is the divergence part of the zonal wind, a is the Earth's radius, p is the pressure coordinate and g the gravitational constant. The streamfunction is calculated by first averaging in the equatorial band of 10°S-10°N and integrating to the top level of each dataset.

Composite differences in DJF show that the streamfunction in the eastern Pacific [220-260°E] is significantly weaker during QBOE than during QBOW in ERA5 and GC3 N216-pi (Fig. 7.10). These streamfunction differences are significant even low in the troposphere in the model. The zonal wind at upper-levels (300-100 hPa) of the central eastern Pacific [200°E]

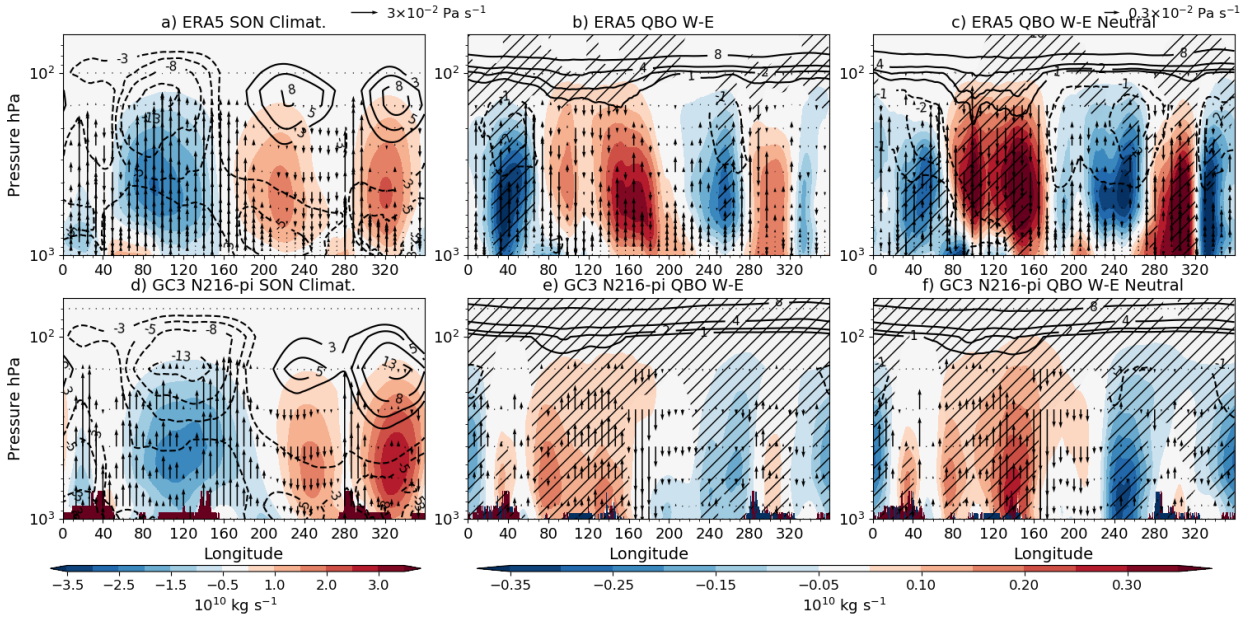


Figure 7.11: As in Figure 7.10 but for the SON season.

is also weaker in QBOW compared to QBOE in both model and reanalysis. In GC3 N216-pi, the negative ψ difference is accompanied by descending motion anomalies in the 170–220°E region, whereas anomalous ascent is observed in the Maritime continent and Indian Ocean. The differences in the other simulations agree with the results of GC3 N216-pi (not shown).

In boreal fall (Fig. 7.11), the differences are also significant and are linked to the relationships found between the IOD and the QBO. Specifically, significant positive differences in the streamfunction are found in the eastern Indian Ocean and Maritime continent and negative differences in the eastern Pacific. In GC3 N216-pi, vertical velocity anomalies indicate stronger ascent in the western Indian Ocean and in the Maritime continent whereas descending anomalies are found in the eastern Indian Ocean. These results agree with positive IOD indices found in QBOW and a mean negative index during QBOE.

The rightmost panels in Figures 7.10 and 7.11, in which only Neutral ENSO months are considered, suggest that this relationship between the QBO and the Walker circulation occurs regardless of ENSO events for GC3 N216-pi. However in ERA5, removing ENSO events changes the sign of the response, likely due to the small sample size in the observational record when only neutral months are considered. These results highlight links between

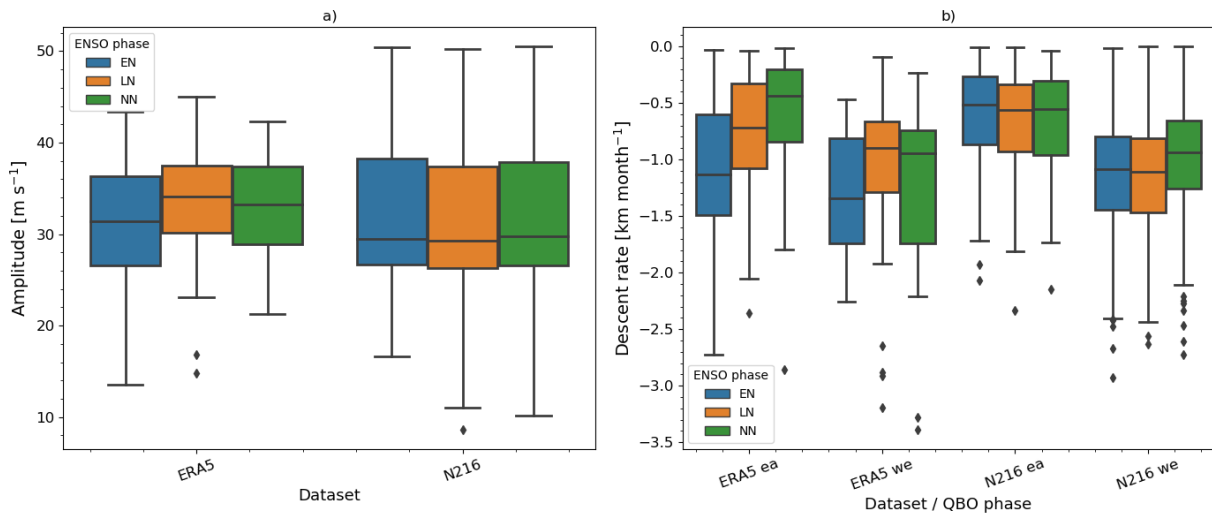


Figure 7.12: Mean QBO (a) amplitude [m s^{-1}] and (b) descent rate [km month^{-1}] separated by dataset (ERA5 and GC3 N216-pi) and ENSO phase. NN stands for Neutral ENSO. In (b) descent rates are shown for both descending easterly (ea) and westerly (we) phases following Schenzer et al. (2017).

the large-scale overturning circulation and local responses which may explain the zonally asymmetric results found in previous studies and in early sections of this chapter.

7.3.5 ENSO influence on the QBO

The causality of the relationships found between ENSO and the QBO are hard to evaluate because these relationships could be due to a QBO effect on the tropical troposphere or the opposite. To understand whether ENSO events can influence the QBO as suggested in other studies (Schirber, 2015; Serva et al., 2020), several characteristics of the QBO were analysed and composited for each ENSO phase including: the descent rate, the amplitude and the phase speed of the QBO. In ERA5, QBO descent rates and the amplitude depend on the phase of ENSO (Figure 7.12). A higher amplitude and slower descent rates are observed during La Niña phases and weaker amplitudes and faster descent rates during El Niño. Similarly, faster descent rates are observed during the westerly phase compared to the easterly phase.

In the model, the descent rates are also faster for the westerly phase, however, the relationships between the QBO characteristics and ENSO are less clear. Both the amplitudes and descent rates of the QBO are not significantly different between EN and LN phases. The only significant difference in the model is that descending westerlies are slower in Neutral

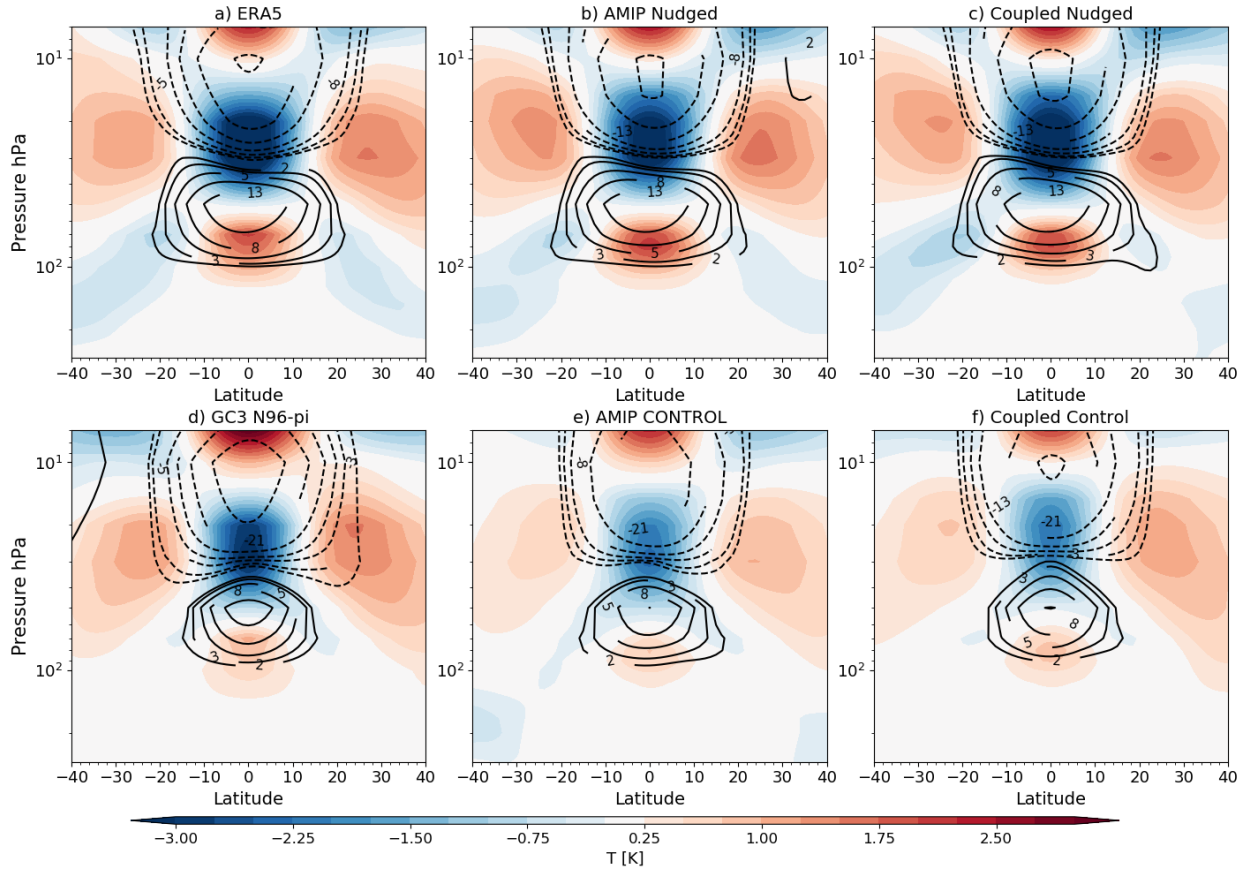


Figure 7.13: Latitude-height plot of the zonal-mean temperature (shading) zonal wind (contours in m s^{-1} differences (QBO W-E) in (a) ERA5, the nudged simulations in (b) AMIP and (c) coupled configurations and (d) GC3 N96-pi from CMIP6, the control simulations with no nudging in (e) AMIP and (f) coupled configurations, and . The black line denotes the tropopause height obtained from the model data in (b, d) and for ERA5 the tropopause height was found through the gradient threshold method. For the nudged experiments, the ensemble-mean is shown.

ENSO months compared to EN or LN conditions. A similar null relationship between ENSO and the phase speed of the QBO is found for GC3 N216-pi (not shown).

These results suggest that there is little influence of ENSO on the descent rate and amplitude of the QBO in GC3 N216-pi, which agrees with the results of Serva et al. (2020) for an older version of the HadGEM model. Therefore, there is no evidence to suggest that the QBO-ENSO relationships found in the previous sections are caused by the influence of ENSO on the QBO within the UM model, as it may be the case for observations.

7.4 The nudging experiments

This section investigates the results from the nudging experiments, in which the zonal wind was relaxed towards ERA5 between 10°S-10°N and 90 and 4 hPa. Figure 7.13 shows that the nudged experiments, both AMIP and Coupled, exhibit larger QBO W-E differences in the UTLS zonal-mean zonal wind and air temperature compared to Control experiments. The nudged experiments very closely resemble the results of ERA5, particularly in the equatorial region. The removal of the weak QBO amplitude bias suggests that these nudged experiments are suitable to investigate the surface response to the QBO and the static stability hypothesis for the tropical route of QBO teleconnections. The horizontal distribution of the 100 hPa temperature differences is also improved by the nudged experiments and resembles very closely the results from ERA5 (not shown).

7.4.1 Atmosphere-only experiments

This section describes the results of the atmosphere-only experiments: AMIP Nudged, AMIP Control and AMIP Shifted. First, an analysis of the effect of nudging on the overturning circulation shows that the Walker circulation biases in the upper troposphere of the control experiments are notably improved in the nudged experiments (Fig. 7.14). The mean state of the Walker circulation is weaker in the AMIP Control simulation and exhibits an easterly bias at upper levels compared to ERA5.

These two tropospheric biases are improved in the lower stratosphere in the Nudged experiments compared to control experiments. Even though the relaxation is only applied above 90 hPa, significant differences between control and nudged experiments are observed for the zonal wind and zonal streamfunction at 200 hP near the dateline, over South America and over the Atlantic Ocean. However, no significant differences in the streamfunction or zonal wind in the lower troposphere are observed between the AMIP Shifted and Nudged experiments which means that the mean overturning circulation is not modified by the variability of the nudging data, only by the mean-state of the nudging data.

The annual-mean difference of precipitation between W and E phases (Fig. 7.15) in the AMIP Nudged ensemble-mean matches closely the results of GPCP, characterised by an El

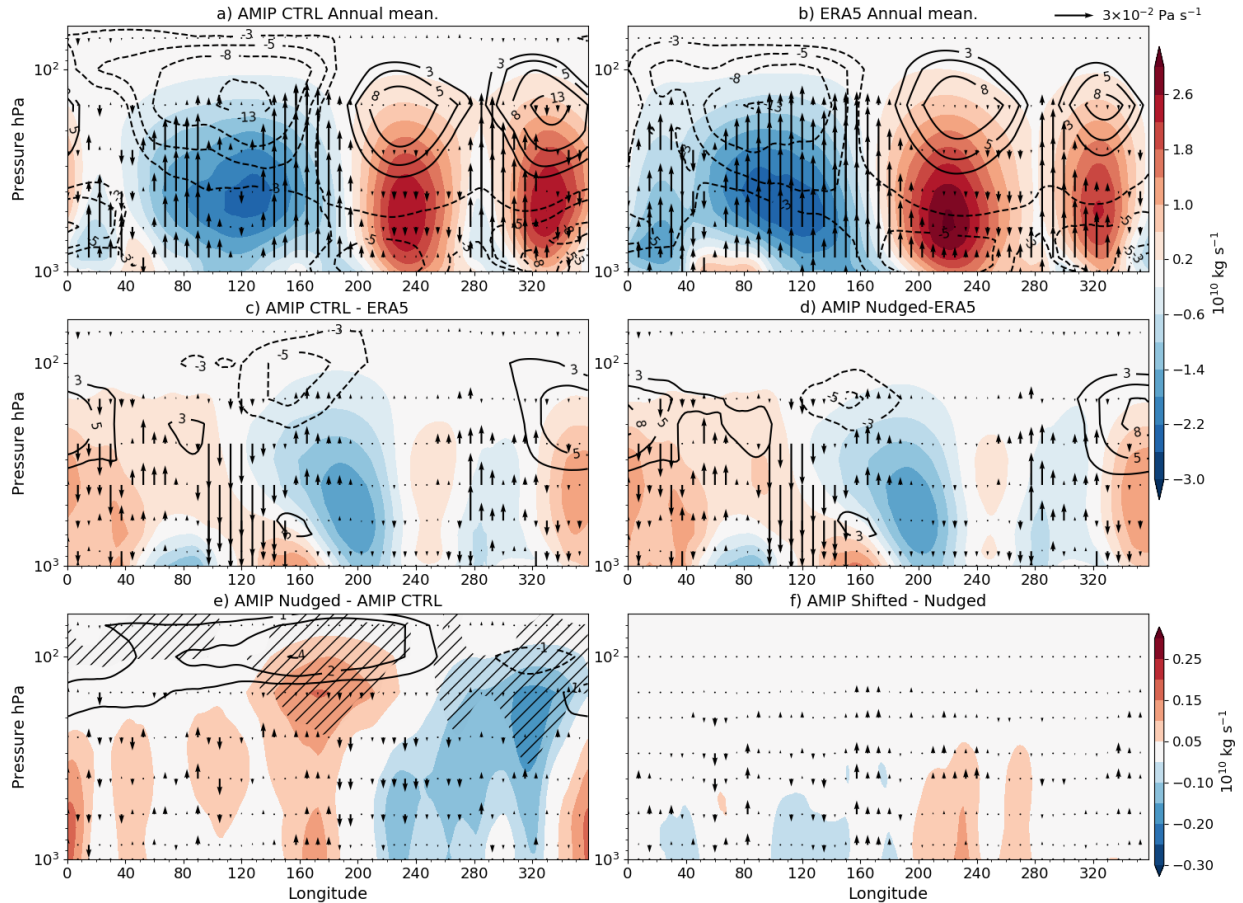


Figure 7.14: Zonal mass streamfunction (ψ in shading), zonal mean zonal wind (contours) and vertical velocity (vectors) averaged over the band 10°S-10°N. Climatological mean in the (a) AMIP Control experiment and (b) ERA5. (c-d) show biases in the (c) Control and (d) Nudged experiments with respect to ERA5 whereas (e-f) show differences between experiments, (e) AMIP Nudged-Control and (d) AMIP Shifted-Nudged. Note that the colorbar and scale of the vectors changes are different between (a-d) and (e-f). In (e-f), significant differences (95% confidence level according to a Mann-Whitney two-sided test) in the streamfunction are highlighted with hatching.

Niño pattern in the Pacific Ocean, a weaker Atlantic ITCZ and a gradient of precipitation in the Indian Ocean during QBOW compared to QBOE. In contrast, the AMIP Control and the simulations with an out-of-phase relaxation of the winds with respect to the SST driving data (AMIP Shifted) show very different responses to the AMIP Nudged experiment and observations. A similar result is found for seasonal-mean composite differences (not shown), so that the precipitation response in the simulations where the QBO index and the SSTs match exactly as in observations (AMIP Nudged) produce a very similar response to GPCP, whereas simulations where the nudged QBO winds do not match the observed

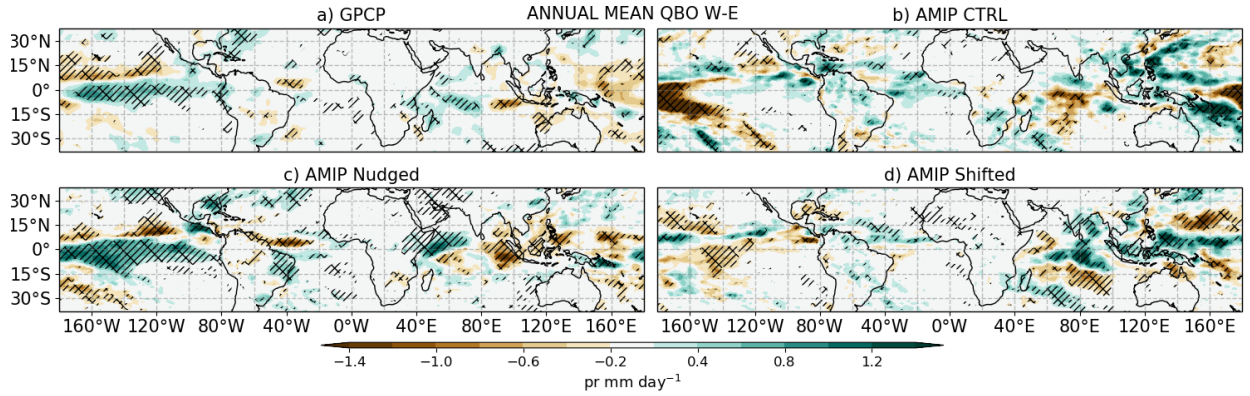


Figure 7.15: Annual-mean precipitation response (QBO W-E) in (a) GPCP, and atmosphere-only experiments: (b) AMIP CTRL, (c) AMIP Nudged and (d) AMIP Shifted.

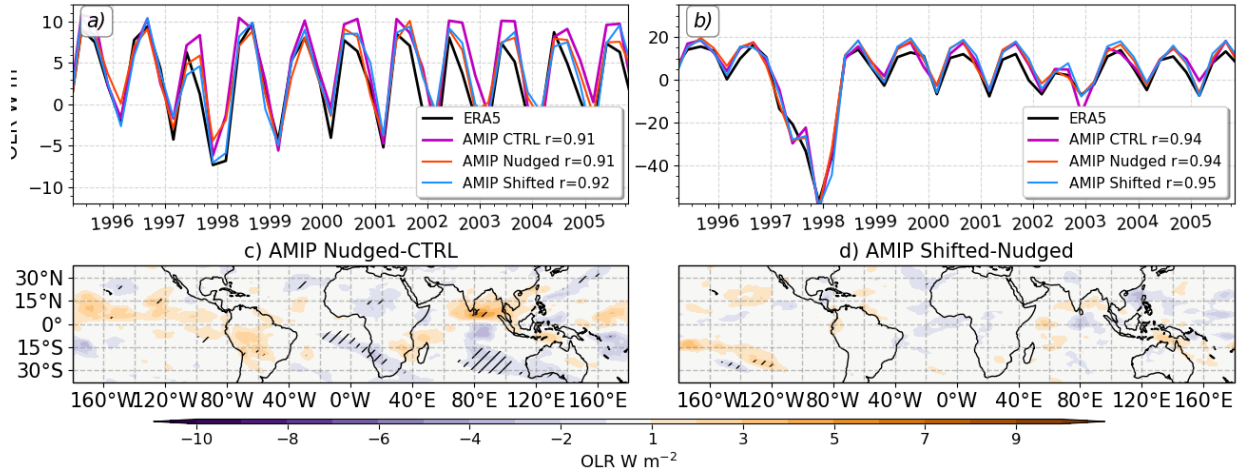


Figure 7.16: (a, b) Time-series of (a) zonal-mean equatorial [5°S - 5°N], and (b) area-averaged EN3.4 OLR in ERA5 and the three amip experiments. For each AMIP experiment the Pearson correlation coefficient between the experiment time-series and ERA5 is shown in the legend. (c) Differences in mean OLR between AMIP Nudged and Control and (d) between AMIP Shifted and Nudged. Significant (95% confidence level) differences according to a Mann-Whitney U test in (c, d) are highlighted with hatching.

SSTs (AMIP Shifted) result in different responses.

The analysis of the tropical out-going longwave radiation (OLR) shows that nudging does not significantly modify the simulated OLR (Fig. 7.16). The time-series of equatorially averaged OLR (Fig. 7.16a) is indistinguishable between the three types of atmosphere-only experiments and similar results are found for OLR averaged in the EN3.4 region (Fig. 7.16b). The correlation coefficients of the time-series also indicate no difference between the experiments. Similarly, the horizontal distribution of the mean OLR also shows no robust

differences between the Control, Nudged and Shifted experiments (Fig. 7.16c-d) so there is no effect of nudging for the mean state or variability of OLR in AMIP experiments.

These results suggest that the QBO winds are secondary to the effect of the SSTs for the precipitation response in these atmosphere-only experiments. The AMIP Shifted experiment has a better representation of the stratospheric variability in temperature and vertical wind shear; however, the precipitation response associated with the QBO variability is entirely different to the AMIP Nudged experiments, with the difference between these two experiments being the underlying SSTs. Results also suggest that the stratospheric winds, nudged or not, have little effect over the resulting OLR. These results suggest that improving the representation of the QBO is not enough to replicate the observed QBO response or to change the simulated characteristics of convective activity because the SST forcing dominates.

This section shows that relaxing the zonal wind in the stratosphere in atmosphere-only experiments does not modify the mean state of the tropospheric tropical circulation or the characteristics of convection. In other words, in these experiments the surface response of precipitation is largely associated with the underlying SSTs and not the QBO winds. However, whether there is any feedback mechanism between the QBO and SSTs cannot be answered by this atmosphere-only configuration, which leads to the next section which analyses the coupled nudged experiments.

7.4.2 Coupled experiments

This section presents the results of the coupled ocean-atmosphere experiments with (Nudged) and without (Control) nudging the tropical stratosphere. Note that all the individual experiments in this section are the same length (35 yr) and that the Coupled Nudged ensemble-mean refers to the mean results of the six ensemble members with nudging and the Control ensemble-mean to the mean of the two ensemble members.

First, differences in SSTs are analysed, as the previous section showed that the SST forcing dominates over the nudging in atmosphere-only experiments. The annual mean QBO W-E difference in tropical SSTs in HadSST the coupled ensemble members (Fig. 7.17) show that the control experiments follow closely the response of HadSST and GC3

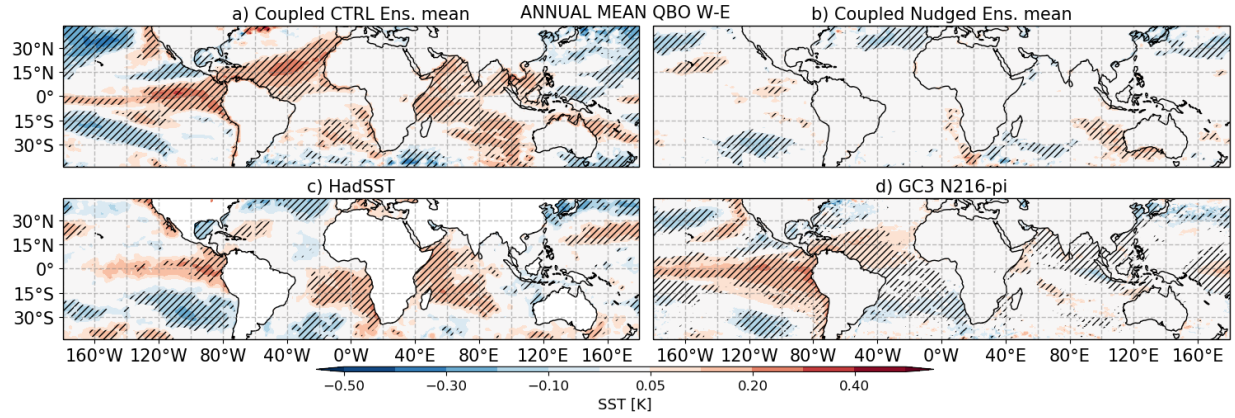


Figure 7.17: Annual mean SST [K] QBO W-E differences in (a) Coupled Control and (b) Coupled Nudged ensemble mean, and the (c) HadSST dataset and (d) GC3 N216-pi datasets. Hatching denotes significance to the 95% confidence level according to a bootstrapping with replacement test.

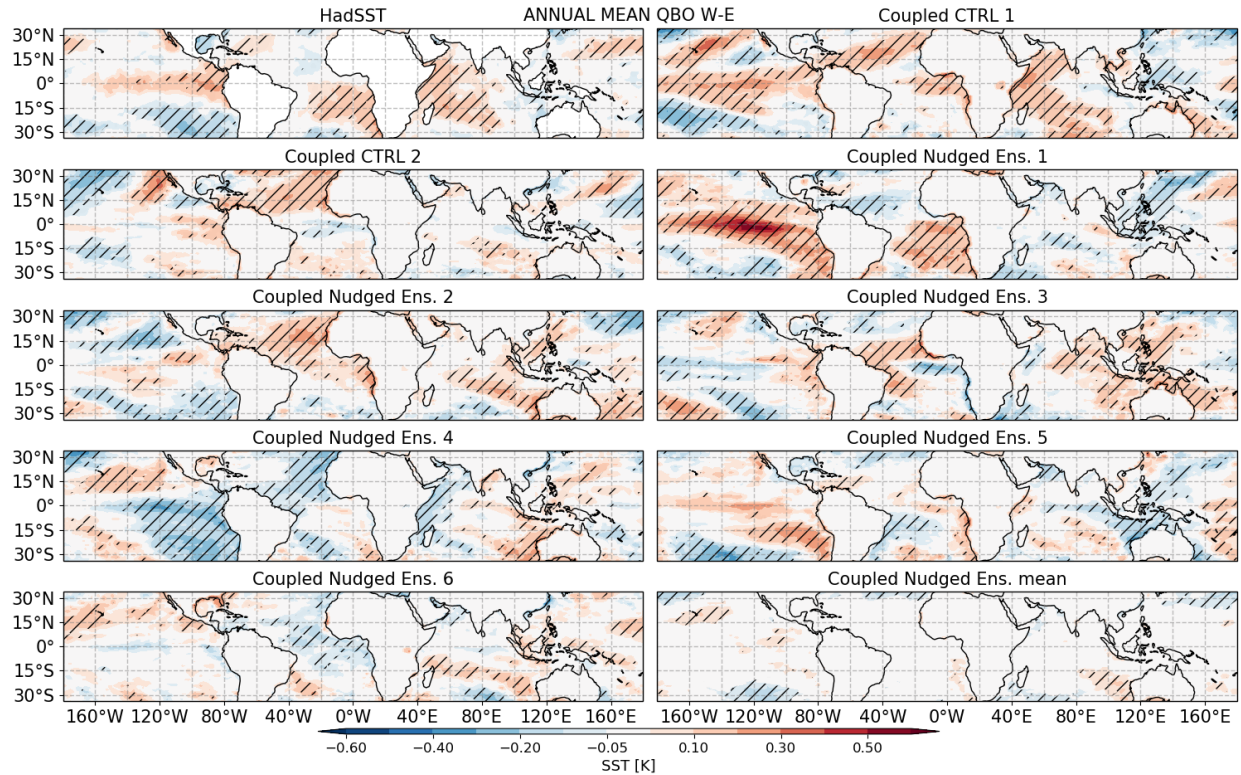


Figure 7.18: Annual-mean SST differences between QBO phases in the HadSST, Coupled Control and Coupled Nudged simulations.

N216-pi. These QBO W-E responses are characterized by a warmer East Pacific, and equatorial Atlantic and Indian Oceans.

The nudged ensemble-mean, however, shows a very weak or null response (Fig. 7.17b)

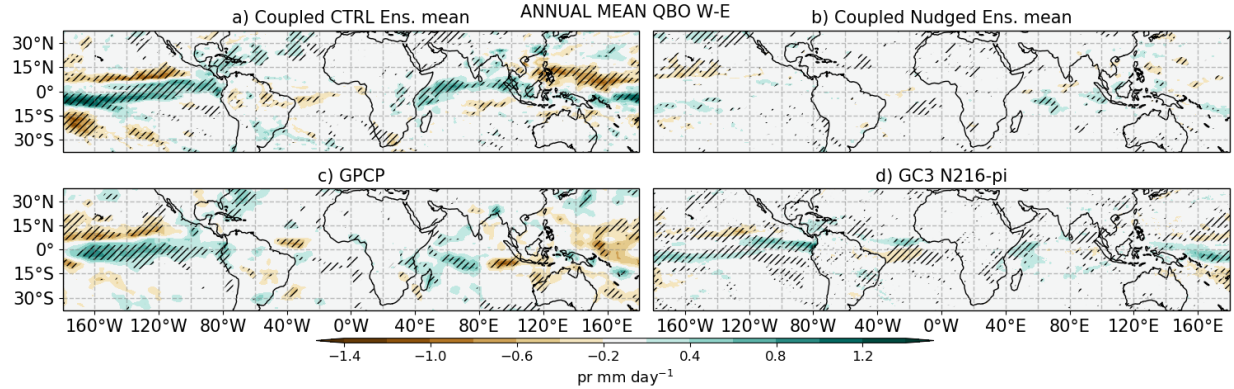


Figure 7.19: As in Fig. 7.17 but for precipitation [mm day^{-1}] using (c) GPCP as the observational dataset.

compared to the control experiments. The ensemble-mean weak response is a result of very different responses from each ensemble member (Fig. 7.18) which cancel each other out to a large extent indicative that the responses in each ensemble member is the result of other features of internal variability and not the nudged QBO. In seasonal-mean differences the SST response also appears to be stronger in the tropics in the free-running Coupled Control experiments than in the nudged experiments. [These results suggest that SST differences diagnosed in two types of control simulations are missing when the nudging is implemented.](#)

The precipitation response is also weaker when the nudging is applied to the couple setup. The annual mean difference between QBO phases (Fig. 7.19) in the control experiments show two significant QBO W-E differences: a significant El Niño-like response over the Central and Eastern Pacific Ocean, and a wetter western Indian Ocean. These two precipitation responses are also observed in GPCP and GC3 N216-pi. The ensemble-mean of the nudged experiments, however, show no robust or region-wide significant differences (Fig. 7.19b).

The weaker response in the ensemble-mean of the nudged experiments is also due to opposite responses found in each ensemble member which cancel out. In specific seasons, robust QBO W-E responses in convective precipitation are observed in the Control experiments, ERA5 and GC3 N216-pi, for example, a northward shift of the Atlantic ITCZ in MAM (Fig. 7.20) and a wetter Caribbean Sea in JJA. These results confirm that the control experiments exhibit QBO-related precipitation impacts similar to those found in the

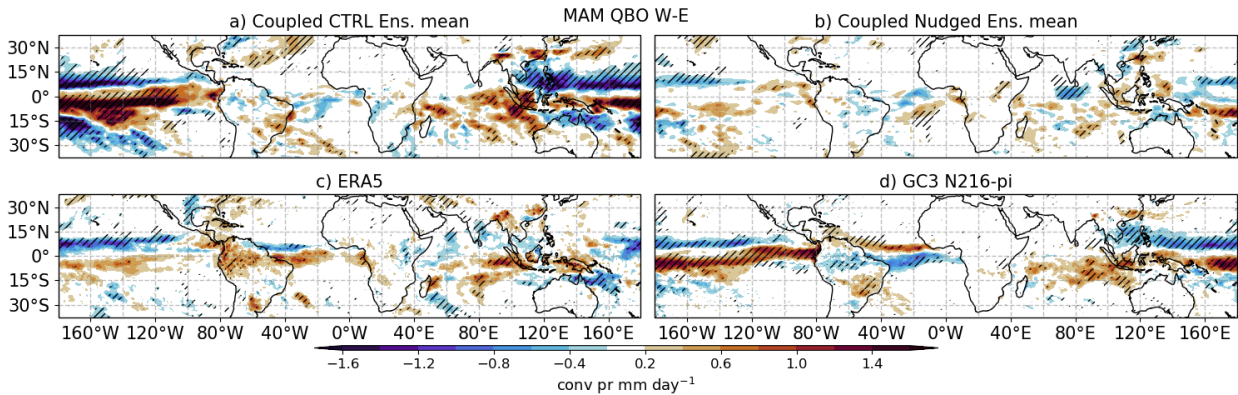


Figure 7.20: As in Figure 7.19, but for the MAM season and convective precipitation.

CMIP6 experiments and in some instances also similar to the observed impacts. However, these precipitation anomalies disappear in the nudged experiments.

Robust relationships between the QBO phase and IOD) and ENSO indices are observed in the CMIP6 experiments. Figure 7.21 shows the mean values of ENSO and IOD indices for nudged and control experiments. Coupled control experiments (Figs. 7.21a, e) show a significant difference for both IOD and ENSO indices identical to the CMIP6 results, i.e., both indices tend to be positive under QBOW and negative under QBOE. For the IOD index, these differences are observed from Jul-to-Jan and for ENSO the differences are found almost year-round but are stronger during boreal fall and winter. However, the nudged ensemble-mean shows no relationships between these indices and the QBO phase.

The long CMIP6 picontrol simulations were analysed by computing QBO W-E differences of the indices for 35-yr long randomly selected periods iteratively 10000 times. The selection of 35-yr periods is to match the length of the observed period, to investigate how frequently would a QBO W-E difference value be found if the picontrol simulations were of the same length as observations. This approach leads to a probability density function (PDF) of QBO W-E differences that aims to sample the role of internal variability within the long piControl integration on the QBO impacts and to evaluate how these coupled experiments fit within those distributions with and without nudging.

Figure 7.21d, for instance, shows that the QBO W-E differences in the SON IOD index are predominantly positive in the GC3 N96-pi distribution, and the control experiment differences are all positive as well. However, the Coupled Nudged ensemble members are

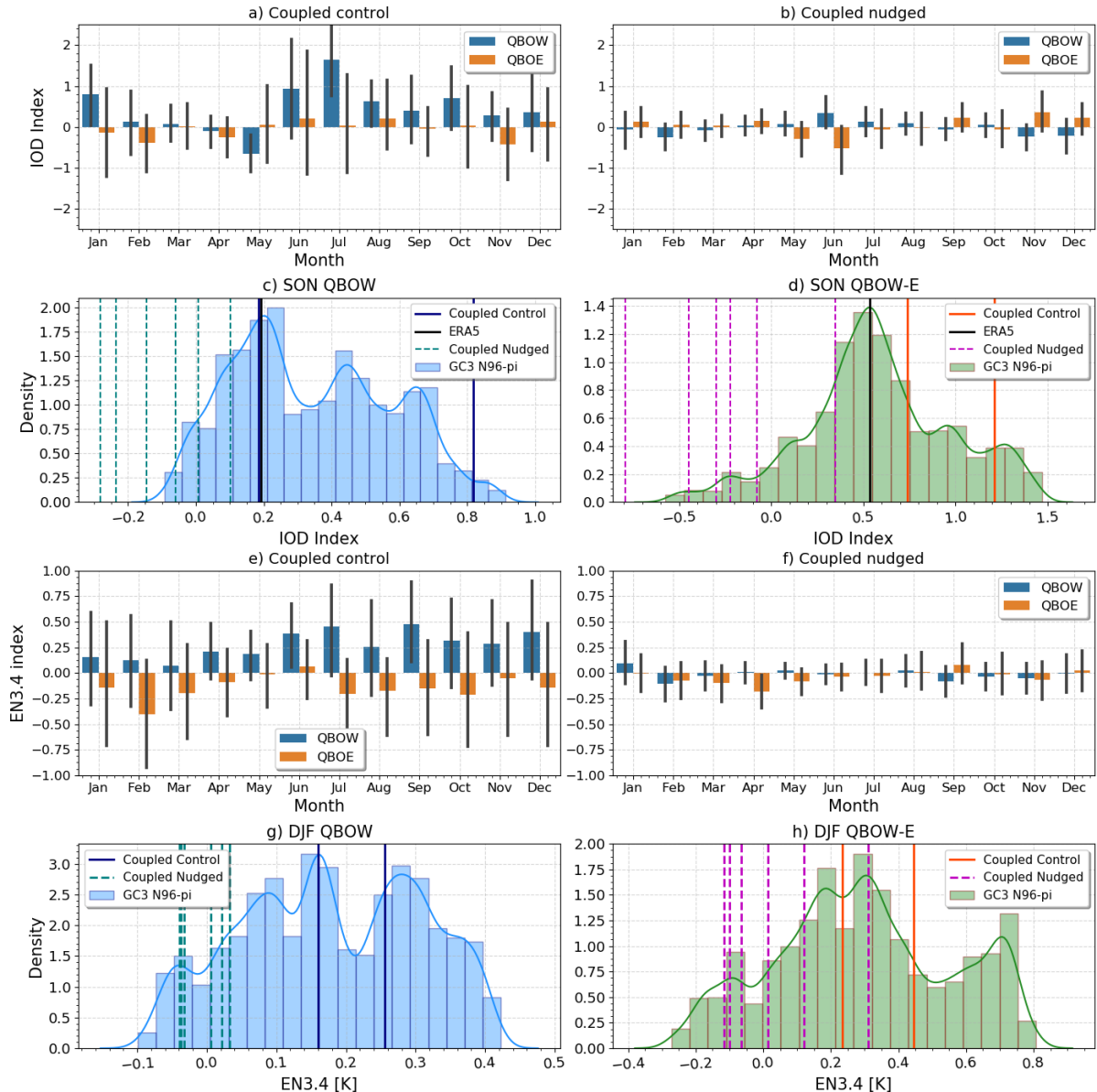


Figure 7.21: (a, b) Monthly-mean convective precipitation IOD index [mm day^{-1}] in coupled (a) control and (b) nudged ensemble-means separated by QBO phase. (c, d) Probability density functions (PDFs) of the IOD convective precipitation index for (c) the mean SON during QBOW months and (d) the SON difference between QBO W-E. The PDF is obtained from the 500 yrs of the GC3 N96-pi by bootstrapping 10,000 times into 35-yr periods and obtaining the averages and differences in each subsample. (e-f) as in (a, b) but for monthly-mean EN3.4 index [K] in the ensemble mean (e) Coupled control and (f) Coupled Nudged simulations separated by QBO phase. (g-h) as in (c-d) but for the EN3.4 index in DJF.

mostly negative and two of them fall outside the 99% low end of the PDF. The EN3.4 index is also more frequently positive under QBOW (Fig. 7.21g) than under QBOE in the CMIP6 and control experiments, but this relationship is missing in the nudged experiments

and the ENSO-QBO relationship is less clear in this PDF.

This section shows that in the coupled configuration experiments there are notable QBO-related impacts that are removed when nudging is applied to the model. In the control experiments, impacts over the ITCZs, ENSO and the IOD, to name a few, are robust and similar to results from observations and CMIP6 integrations of the model. However, in the nudged experiments, little-to-no robust responses were observed, as each ensemble member exhibited a different response, leading to a cancellation of the differences in the ensemble-mean.

7.5 Summary and discussion

Observational evidence suggests that the stratospheric QBO can modulate tropical deep convection and influence tropical surface climate (Collimore et al., 2003; Liess and Geller, 2012; Gray et al., 2018). However, the short observational record available and the strong influence of ENSO limits the robustness of any analysis seeking to evaluate the tropical route of QBO teleconnections using observations. The first part of this chapter investigates the tropical route of QBO teleconnections in the 500-year long pre-industrial control experiments of the MOHC focusing on the medium-resolution simulation from HadGEM3 GC3.1 N216.

Results in the CMIP6 simulations support observational evidence (Collimore et al., 2003; Liess and Geller, 2012; Gray et al., 2018) that there is a QBO impact over tropical precipitation, mainly over the tropical oceans in the East Pacific and Atlantic ITCZs and in the Indian Ocean. The phase of the QBO was found to be statistically linked to the strength of the Pacific ITCZ and the position of the Atlantic ITCZ, whereas wetter conditions were simulated in the Caribbean Sea and western Indian Ocean during QBOW compared to QBOE. Several impacts are also diagnosed in Southern Hemisphere monsoons but little effect is seen for Northern Hemisphere monsoons. More robust and largest differences are seen over the ocean than over land, which points to the relevance of SST feedbacks for any QBO impact but also means that the impact of the QBO over the convective profile over land is weak in the model.

Observed relationships between the frequency of ENSO events and the phase of the QBO are also found in the simulations. El Niño events are more frequently found in QBOW conditions and La Niña events are more frequently found in QBOE conditions. This finding suggests that the observed QBO-ENSO relationship is not due to observational uncertainty but may be causally linked. A precipitation index of the IOD, that measures the zonal gradient of precipitation in the Indian Ocean, was also significantly different depending on the QBO phase in boreal fall. Positive IOD events were more frequently found in QBOW and negative IOD events in QBOE.

The hypothesis that the QBO may influence the mean-state of the Walker circulation suggested by previous observational studies to explain zonally asymmetric tropical responses to the QBO (e.g. Collimore et al., 2003; Liess and Geller, 2012) is confirmed as the Walker circulation varies by up to 10% between QBO phases, even when the effect of ENSO events is taken into account. Specifically, the Walker circulation is found to be weaker during QBOW than during QBOE. In DJF, this anomaly of the overturning circulation in the Pacific is likely linked to the anomalously strong East Pacific ITCZ, and in SON, the changes to the overturning are likely linked to the ascending and descending motions in the Indian Ocean that generate the IOD response.

These results are amongst the first pieces of evidence of QBO-tropical convection signals in a GCM. However, the methodology used does not allow to conclusively separate the cause-effect of the diagnosed relationships. For example, the ENSO-QBO relationships could be explained by anomalous tropical wave activity associated with ENSO modifying the downward propagation of the QBO (Schirber, 2015), but previous evidence found no such impact in the HadGEM3 GC3.1 configuration (Serva et al., 2020).

Alternatively, a top-down influence of the QBO in the tropics could explain these results. Several hypotheses have been put forth to explain a causal link between the QBO and tropical convection (Hitchman et al., 2021; Haynes et al., 2021). Arguably, the leading hypothesis suggests that UTLS temperature variability modifies the upper-level static stability to the extent of affecting the height and strength of convection.

Results from the first part of the chapter appear to contradict this hypothesis as zonally asymmetric responses appear in all seasons and impacts are largest over land than over the

ocean. The UTLS static stability mechanism should produce zonally symmetric effects or at least be relevant in all deep convective regions and there is no reason why land monsoon regions should be less affected by the UTLS static stability.

Rather, our results support the hypothesis that the links between the QBO and the Walker circulation best explain the characteristics of the responses (Hitchman et al., 2021). One could reasonably assume that a robust local effect over the Maritime continent, for instance the UTLS static stability hypothesis, would then influence the strength of deep convection in the ascending branch of the Walker circulation and thereafter propagate to the rest of the tropical atmosphere. However, there is no way of identifying the causal pathways of this stratospheric-tropospheric coupling without targeted model experiments.

For that reason, atmosphere-only and coupled ocean-atmosphere experiments were conducted with the model stratosphere relaxed towards ERA5 in the QBO region. These experiments notably improve the QBO amplitude in the lower stratosphere and simulate a stronger impact of the QBO on the UTLS static stability. These experiments were analysed under the hypothesis that stronger surface impacts would be observed in the nudged experiments relative to the control experiments.

The SST and precipitation responses appear to be muted in the nudged experiments, whereas the control experiments, which are very similar to the CMIP6 configuration, reproduce all the impacts diagnosed in the first part of the chapter. Individual ensemble members with nudging show significant responses but the ensemble-mean response is null for all seasons. Furthermore, the diagnosed relationships of the QBO with ENSO and the IOD in the CMIP6 models are also found in the control experiments but disappear in the nudged experiments.

The results from the nudging experiments can be interpreted in various ways. First, since the experiments in which the influence from the troposphere to the stratosphere was removed by nudging the stratosphere in the model show no surface response, one could reasonably conclude that there is no downward tropical route of the QBO. Similar questions have arisen regarding the MJO-QBO relationships with some studies suggesting that there is no causal link, and the observed relationship is a result of statistical effects (Wang et al., 2019).

A second plausible explanation is that the UTLS static stability mechanism is not the causal pathway through which the QBO influences the tropical troposphere. Several lines of evidence in this chapter seems to contradict the predictions of the UTLS static stability mechanism as no zonally symmetric impacts are observed within the model and there is little impact over land regions. Another mechanism, one that has been muted by the nudging may be at play.

However, given the results of this chapter, even if there is no downward stratospheric-tropospheric teleconnection, one would still have to explain why some robust sensitivity to the QBO phase appears in the model for several convective features. For example, why is the ENSO index more frequently positive under QBOW, given that the ENSO has little-to-no effect over the descent rates and amplitude of the QBO (Serva et al., 2020) in this model. Further work is needed to investigate what mechanisms explain the robust relationships found in various model configurations, some of which remarkably match observations, in this chapter. Suggestions for future research directions are given in the next chapter.

8

Conclusions

This chapter summarises the main findings and conclusions of this thesis, discusses the limitations of this research and potential future work.

8.1 Summary and contributions

Biases in the dynamics of the American monsoon: Assessment of GCM biases in CMIP cohorts is seldom done with an emphasis on biases relevant for the monsoons in the Americas. For this reason, less is known about the relationship between large and regional-scale biases for the AMS region compared to other monsoons. The first results chapter aims to provide a detailed account of the biases relevant for American monsoons in the CMIP6 MOHC simulations of UKESM1 and HadGEM3. A key bias found is the overestimation of precipitation in the boreal summer ITCZ in the East Pacific Ocean. Similarly, the position of the austral summer Atlantic ITCZ is biased southward in the coupled experiments, leading to biases in the dynamics of the South American monsoon. This bias is reduced in the atmosphere-only experiments suggesting a key role played by equatorial Atlantic SST biases for the representation of precipitation over land and in the ITCZ region. The dynamics and seasonality of the North American monsoon and MSD regions are relatively better represented than for the South American monsoon. The Earth System processes represented by UKESM1 do not considerably improve the representation

of the monsoon compared to HadGEM3. However, increasing the horizontal resolution and forcing the model with observed SSTs improves several biases in the large-scale dynamics and monsoon rainfall. This chapter finds that the MOHC models can simulate a bimodal signal in the seasonal cycle of precipitation, known as the Mid-summer drought, as well as relationships between the stratospheric QBO and ENSO teleconnections in the tropics. **This chapter provides one of the scarce assessments of the AMS in a CMIP model, published very early in the CMIP6 phase, and evidenced both shortcomings (the dry Amazon biases) and strengths (the MSD) of the MOHC models.**

A portable method to diagnose monsoon timings: Existing methods used to separate the timings of the seasonal cycle in a monsoon are usually tailored to a dataset, which complicates comparisons of multiple datasets or simulations in which the seasonal cycle or climatological precipitation is non-stationary. A wavelet transform (WT) method was developed using the Haar wavelet aiming to diagnose onset and retreat as sharp or abrupt changes to the signal of precipitation. The results obtained using the WT method are comparable to other methodologies and the portability of the method is illustrated using observational datasets, reanalysis and climate model output. Results show that the WT method reasonably captures the mean dates of onset and retreat as well as changes in the meteorological conditions associated with the monsoons in India and North America compared to existing methodologies. The method can also separate the timings of a bimodal signal by finding the dates where the drier period begins and ends. The diagnosis of the timings of the MSD simulated by the MOHC simulations using this methodology shows similar results to observations, indicating a good representation of the intricate seasonal cycle of precipitation in the MSD region by these models. **The contribution from this chapter is a portable method to diagnose onset and retreat from various datasets including climate model output and in any monsoon region with a similar performance to more tailored methods.**

A limited role for existing theories to explain the Mid-summer drought: Evidence from ERA5 and GCMs suggest that the SST-cloud-radiative feedback and solar declination hypotheses are not suited to explain the occurrence of a bimodal signal of precipitation in

Central America and southern Mexico. Chapter 6 uses the WT method to separate the timings of the seasonal cycle and investigate closely these two hypotheses in the CMIP6 MOHC simulations and in ERA5. No evidence is found that the East Pacific SST variability drives the precipitation, as expected by the first mechanism, or that the absorbed solar radiation by the surface is the driving mechanism, as suggested in the second hypothesis. Rather, the results suggest that absorbed solar radiation by the surface co-varies with precipitation and cloudiness. The conclusion of this analysis is that the observed interannual variability or the differences in the representation of the MSD in the CMIP6 experiments cannot be explained through the arguments of these two mechanisms, suggesting other factors may be more important for the seasonality of rainfall in the region. This chapter presents one of the most comprehensive analyses of the hypotheses that could explain the occurrence of the Midsummer Drought in southern Mexico and Central America and highlights that the predictions of the leading theories do not reasonably explain the characteristics of the MSD.

The role of moisture transport for precipitation in the MSD region: The horizontal moisture transport by the zonal flow in the Caribbean, i.e., by the Caribbean Low-Level Jet (CLLJ) is found to explain some aspects of the MSD in the CMIP6 MOHC simulations and in reanalysis. The vertically integrated moisture transport and total water content decrease considerably from the period of the first peak period to the drier MSD period, and these diagnostics similarly increase in late summer during the second wet period. The moisture transport and total water content changes are explained to a certain extent by the seasonality in the CLLJ. The CLLJ variability explains to a certain extent the precipitation increases during the transition from the MSD period to the second peak period. However, the magnitude of the precipitation decrease in early summer, from the first peak to drier MSD periods is not as well explained by the CLLJ as it is by the integrated moisture transport. The evidence to support the CLLJ in Chapter 6 is the first observational and modelling work to indicate a mechanical forcing mechanism rather than radiative-thermodynamic mechanisms, which are arguably more supported by the literature.

The moist static energy budget provides useful insight to the MSD problem: The moist static energy (MSE) budget framework is a useful technique to investigate physical processes associated with tropical precipitation. The MSE budget is used in Chapter 6 to investigate how the MSE changes in the MSD region in the simulations and in the reanalysis and how the budget terms could be related to variations in precipitation. A strong relationship is found between the vertical advection term of the budget and precipitation, indicative of the relationship between vertical velocity and precipitation in the tropics. The horizontal advection of MSE also varies notably between the wetter and drier periods, however, there was little evidence to indicate a direct link between the magnitude of the horizontal advection term and precipitation. Both models and reanalysis suggest a limited role for surface fluxes in the variability of precipitation, although considerable biases in the surface energy budget of the models are apparent from this analysis. In short, the MSE budget framework may be used in future work to explain the seasonal cycle of precipitation and its variability. [The MSE analysis is the first instance where this budget framework was applied for the region, and the main contribution is the clear indication that this budget can be further used to investigate the variability of precipitation on the MSD time-scales.](#)

The tropical route of the QBO teleconnections in a GCM: An investigation of the tropical route of QBO teleconnections in the MOHC models was done in the last chapter of this thesis. In the long pre-industrial control experiments of CMIP6, several responses that had previously been reported in observational works were confirmed, for example, the impacts to the East Pacific ITCZ. The main findings of this analysis were impacts to the strength of the Atlantic and Pacific ITCZs, as well as wetter conditions in the Caribbean Sea and Indian Oceans during QBOW compared to QBOE. Most of these impacts were found to be seasonally varying and the season of strongest influence varied from model to model. A previously unknown relationship between the QBO phase and the zonal distribution of precipitation in the Indian Ocean was diagnosed in the GCM. This relationship is characterized by an IOD-like response, i.e., wetter conditions in the western Indian Ocean and drier conditions in the eastern Indian Ocean during QBOW and the opposite during QBOE. Similarly, El Niño events are more frequent during QBOW and

La Niña events are more frequent during QBOE in observations and in these simulations. Finally, changes to the strength of the Walker circulation were also diagnosed to be robust; this response is characterised by a weaker overturning during QBOW than during QBOE. The results in this chapter suggest a possible effect of the QBO on the ITCZs, the IOD, ENSO and the Walker circulation. This chapter constitutes one of the few analyses of QBO-tropical convection relationships in a GCM, finding and reconciling observational evidence that was thought to be due to observational uncertainty in very long integrations.

QBO tropical teleconnections in a model with a nudged stratosphere: GCM experiments in which the zonal wind in the equatorial stratosphere was relaxed towards a reanalysis were performed and analysed in atmosphere-only and coupled ocean-atmosphere configurations. The atmosphere-only experiments show a limited sensitivity of the tropical circulation and convective activity to the phase of the imposed or simulated QBO. Several relationships between the QBO and convective phenomena such as the ITCZs were found in the Coupled Control experiments but these relationships disappear in the relaxation experiments. The mean state of the Walker circulation is driven closer to observations by the relaxation technique, alleviating biases in the upper-level branch of the circulation. Yet, the variability in the Walker circulation associated with the QBO of the nudged experiments is weaker and of a different sign than in the control experiments. In short, the relaxation experiments show a stronger temperature variance in the UTLS in response to the imposed QBO shear, yet the tropical teleconnections are not stronger than in the control experiments. These results mean that the relaxation has removed relevant processes through which the QBO interacts with tropical convection. The nudging experiments contribute to the stratospheric-tropospheric community first by pointing to the limitations of nudging, and, secondly, by providing evidence the leading hypothesis for a QBO tropical route of teleconnections (the static stability hypothesis).

8.2 Limitations and future work

The investigations presented in this thesis leave several open questions that require future work. The main limitations of each part of the research in this thesis and a discussion on how future research could address these limitations is provided below.

The general problem with GCM biases: GCM biases have been described and discussed throughout this thesis as reasons for uncertainty in the simulated teleconnections and impacts for the AMS. From monsoon dynamics to the stratosphere, biases in the representation of the mean-state and variability in a GCM limit our ability to draw conclusions from their output. One example is the QBO impacts to the tropical troposphere, in which the poor simulation of tropical convective features, such as the MJO, and biases in the QBO, in CMIP models leaves little room for these models to be used for the purposes of untangling stratospheric-tropospheric interactions. Future steps may use GCMs that are of higher resolution (10-km scale) or alternatively investigate these questions using cloud-resolving models which may improve several dynamical factors that have made difficult to draw strong conclusions from Chapter 7 in this thesis.

Analysis of observational and model trends in monsoon timings: Chapter 5 shows that the WT method can be used in any observational or model data and for any monsoon so that the advantage of the method is portability. In contrast, one limitation of the method is that the WT cannot be computed in a real-time or forecasting scenario, so the method is only useful for *post hoc* processing. This limitation is due to the way the WT is computed, which requires the availability of data several months past the date of monsoon onset or retreat to compute the WT. Nevertheless, due to the advantages of the method, one further application of the method would be to diagnose observed and simulated trends in the onset and retreat dates in the global monsoon. Several regional studies exist that characterise trends in the seasonality of precipitation but due to the nature of the WT method, this diagnosis could be done across the CMIP6 cohort of models, the existing reanalysis datasets and all the gridded precipitation datasets available. This research could provide a more

comprehensive analysis of if and how the seasonality of the global monsoon is changing and whether these changes are also seen in CMIP6 models.

The diagnosis of cloud-radiative effects and other quantities from observations:

Chapter 6 uses ERA5 data to diagnose several quantities such as cloud-radiative effects (CREs) and surface fluxes that are known to be biased in reanalyses compared to satellite products or other observational datasets. Throughout the chapter, ERA5 data is used to compare with the CMIP6 models, yet the reanalysis does not assimilate and rather simulates some of the diagnostics used in the chapter. In this way, ERA5 can only be used as a best-model and not as real-world observations of the MSD. Further work could use other observational products to validate the results found in the chapter. In particular, a characterisation of the seasonality of CRE in observational datasets could provide insight to how CRE vary temporally in the rainy season and a comparison of simulated surface fluxes with observations could better assess how biased is the surface energy balance in the models in the East Pacific ITCZ.

A full moist-static energy budget: Accurate computation of the MSE budget is difficult in reanalysis and models because there is a need for high temporal resolution data in order for the budget to close. This limitation is typically addressed by computing the budget terms online within a model. An experiment using the MOHC models that computes the MSE with a high frequency would better show how the budget terms vary at each grid-point with the evolution of the rainy season. Similarly, the full ERA5 data was not used to compute the budget. A daily-mean and a coarser horizontal resolution than available were used to compute all the budget terms due to time limitations, which led to the MSE budget calculation not closing exactly. A more detailed calculation could provide a more precise quantification of how the budget variations relate to precipitation. Future steps could also investigate how the shape of the vertical profile of the vertical velocity varies with the stages of the MSD in the East Pacific and overland. The shape of this profile is known to determine the vertical advection of MSE and gives relevant information of the state of the convective

profile, and, therefore, evaluating temporal changes to the shape of the vertical velocity could also point to relevant processes that could affect the MSD.

QBO teleconnections in a single model: Chapter 7 diagnoses the response of the tropical circulation and precipitation to the phase of the QBO in the MOHC CMIP6 simulations. These simulations are all from the same modelling centre and the models are all based on the UM, i.e., these simulations use the same dynamical core and share many of their parametrisation schemes and large-scale circulation biases. The teleconnections diagnosed in that chapter could also be analysed in different models of CMIP6 and differences in the properties of the simulated QBO and surface response amongst the models could point to processes that link convection and the QBO in this cohort of models. Similarly, experiments using the same model but varying the type of convective or gravity-wave schemes could also highlight which processes are most important to represent connections in the UTLS region, while also pointing to routes for model improvement.

Nudging the MOHC UM: The relaxation experiments described in Chapter ?? suggest that the nudging protocol reduced the connection between the tropical stratosphere and troposphere. Several reasons could explain these results but only future work can definitively provide an answer. Firstly, several types of nudging are possible with a GCM, for example, the nudging can be done through a relaxation of the zonal-mean field and not at all grid points. This type of relaxation would allow waves simulated in the troposphere to propagate to the stratosphere whereas the nudging implemented in this thesis would constrain the wave propagation from the troposphere. Therefore, relaxation experiments in a model that (1) has a good representation of the QBO and (2) has the capability of performing a zonal-mean nudging could be better suited to diagnose the directions of causality of the relationships between the QBO and tropical climate found in this chapter.

Bibliography

- Adams, D. K. and Comrie, A. C. (1997), 'The north American monsoon', *Bulletin of the American Meteorological Society* **78**(10), 2197–2214.
- Adams, D. K., Gutman, S. I., Holub, K. L. and Pereira, D. S. (2013), 'GNSS observations of deep convective time scales in the Amazon', *Geophysical Research Letters* **40**(11), 2818–2823.
- Addison, P. S. (2017), *The illustrated wavelet transform handbook: introductory theory and applications in science, engineering, medicine and finance*, CRC press.
- Adler, R. F., Huffman, G. J., Chang, A., Ferraro, R., Xie, P.-P., Janowiak, J., Rudolf, B., Schneider, U., Curtis, S., Bolvin, D., Gruber, A., Susskind, J., Arkin, P. and Nelkin, E. (2003), 'The version-2 global precipitation climatology project (GPCP) monthly precipitation analysis (1979–present)', *Journal of hydrometeorology* **4**(6), 1147–1167.
- Allan, R. P. (2011), 'Combining satellite data and models to estimate cloud radiative effect at the surface and in the atmosphere', *Meteorological Applications* **18**(3), 324–333.
- Allen, T. L. and Mapes, B. E. (2017), 'The late spring Caribbean rain-belt: climatology and dynamics', *International Journal of Climatology* **37**(15), 4981–4993.
- Amador, J. A. (2008), 'The intra-Americas sea low-level jet: Overview and future research', *Annals of the New York Academy of Sciences* **1146**(1), 153–188.
- Anderson, T. G., Anchukaitis, K. J., Pons, D. and Taylor, M. (2019), 'Multiscale trends and precipitation extremes in the Central American Midsummer Drought', *Environmental Research Letters* **14**(12), 124016.
- Andreoli, R. V., Ferreira de Souza, R. A., Kayano, M. T. and Candido, L. A. (2012), 'Seasonal anomalous rainfall in the central and eastern amazon and associated anomalous oceanic and atmospheric patterns', *International Journal of Climatology* **32**(8), 1193–1205.
- Andrews, D. G., Holton, J. R. and Leovy, C. B. (1987), *Middle atmosphere dynamics*, Vol. 40, Academic press.
- Andrews, M. B., Knight, J. R., Scaife, A. A., Lu, Y., Wu, T., Gray, L. J. and Schenzinger, V. (2019b), 'Observed and simulated teleconnections between the stratospheric quasi-biennial oscillation and northern hemisphere winter atmospheric circulation', *Journal of Geophysical Research: Atmospheres* **124**(3), 1219–1232.
- Andrews, M., Ridley, J., Wood, R., Andrews, T., Blockley, E., Booth, B., Burke, E., Dittus, A., Florek, P., Gray, L., Haddad, S., Hardiman, S., Hermanson, L., Hodson, D., Hogan, E., Jones, G., Knight, J., Kuhlbrodt, T., Misios, S. and Sutton, R. (2020), 'Historical simulations with

- HadGEM3-GC3.1 for CMIP6', *Journal of Advances in Modeling Earth Systems* .
- Andrews, T., Andrews, M. B., Bodas-Salcedo, A., Jones, G. S., Kuhlbrodt, T., Manners, J., Menary, M. B., Ridley, J., Ringer, M. A., Sellar, A. A., Senior, C. A. and Tang, Y. (2019a), 'Forcings, feedbacks, and climate sensitivity in HadGEM3-GC3. 1 and UKESM1', *Journal of Advances in Modeling Earth Systems* **11**(12), 4377–4394.
- Angeles, M. E., González, J. E., Ramírez-Beltrán, N. D., Tepley, C. A. and Comarazamy, D. E. (2010), 'Origins of the Caribbean rainfall bimodal behavior', *Journal of Geophysical Research: Atmospheres* **115**(D11).
- Annamalai, H. (2020), 'ENSO precipitation anomalies along the equatorial Pacific: Moist static energy framework diagnostics', *Journal of Climate* **33**(21), 9103–9127.
- Anstey, J. A. and Shepherd, T. G. (2014), 'High-latitude influence of the quasi-biennial oscillation', *Quarterly Journal of the Royal Meteorological Society* **140**(678), 1–21.
- Anstey, J. A., Simpson, I. R., Richter, J. H., Naoe, H., Taguchi, M., Serva, F., Gray, L. J., Butchart, N., Hamilton, K., Osprey, S. et al. (2021), 'Teleconnections of the Quasi-Biennial Oscillation in a multi-model ensemble of QBO-resolving models', *Quarterly Journal of the Royal Meteorological Society* .
- Arias, P. A., Fu, R. and Mo, K. C. (2012), 'Decadal Variation of Rainfall Seasonality in the North American Monsoon Region and Its Potential Causes', *Journal of Climate* **25**(12), 4258–4274.
- Arritt, R. W., Goering, D. C. and Anderson, C. J. (2000), 'The North American monsoon system in the Hadley Centre coupled ocean-atmosphere GCM', *Geophysical Research Letters* **27**(4), 565–568.
- Ashok, K. and Yamagata, T. (2009), 'The El Niño with a difference', *Nature* **461**(7263), 481–484.
- Back, L. and Bretherton, C. (2006), 'Geographic variability in the export of moist static energy and vertical motion profiles in the tropical Pacific', *Geophysical research letters* **33**(17).
- Baldwin, M., Gray, L., Dunkerton, T., Hamilton, K., Haynes, P., Randel, W., Holton, J., Alexander, M., Hirota, I., Horinouchi, T. et al. (2001), 'The quasi-biennial oscillation', *Reviews of Geophysics* **39**(2), 179–229.
- Barlow, M., Nigam, S. and Berbery, E. H. (1998), 'Evolution of the North American monsoon system', *Journal of Climate* **11**(9), 2238–2257.
- Bayr, T., Domeisen, D. I. and Wengel, C. (2019), 'The effect of the equatorial Pacific cold SST bias on simulated ENSO teleconnections to the North Pacific and California', *Climate Dynamics* **53**(7), 3771–3789.
- Bayr, T., Dommelen, D., Martin, T. and Power, S. B. (2014), 'The eastward shift of the Walker Circulation in response to global warming and its relationship to ENSO variability', *Climate dynamics* **43**(9-10), 2747–2763.
- Bechtold, P., Semane, N., Lopez, P., Chaboureau, J.-P., Beljaars, A. and Bormann, N. (2014), 'Representing equilibrium and nonequilibrium convection in large-scale models', *Journal of Atmospheric Sciences* **71**(2), 734–753.

- Becker, A., Finger, P., Meyer-Christoffer, A., Rudolf, B. and Ziese, M. (2011), 'GPCC full data reanalysis version 6.0 at 1.0: monthly land-surface precipitation from rain-gauges built on GTS-based and historic data', *Global Precipitation Climatology Centre (GPCC): Berlin, Germany*.
- Bellucci, A., Gualdi, S. and Navarra, A. (2010), 'The double-ITCZ syndrome in coupled general circulation models: The role of large-scale vertical circulation regimes', *Journal of Climate* **23**(5), 1127–1145.
- Biasutti, M., Voigt, A., Boos, W. R., Braconnot, P., Hargreaves, J. C., Harrison, S. P., Kang, S. M., Mapes, B. E., Scheff, J., Schumacher, C. et al. (2018), 'Global energetics and local physics as drivers of past, present and future monsoons', *Nature Geoscience* **11**(6), 392–400.
- Bischoff, T. and Schneider, T. (2016), 'The Equatorial Energy Balance, ITCZ Position, and Double-ITCZ Bifurcations', *Journal of Climate* **29**(8), 2997–3013.
- Bjerknes, J. (1969), 'Atmospheric teleconnections from the equatorial Pacific', *Mon. Wea. Rev* **97**(3), 163–172.
- Blanford, H. F. (1886), 'Rainfall of india', *Monsoon Monograph – India Meteorological Department* **3**(658).
- Bombardi, R. J., Moron, V. and Goodnight, J. S. (2020), 'Detection, variability, and predictability of monsoon onset and withdrawal dates: A review', *International Journal of Climatology* **40**(2), 641–667.
- Bony, S., Dufresne, J.-L., Le Treut, H., Morcrette, J.-J. and Senior, C. (2004), 'On dynamic and thermodynamic components of cloud changes', *Climate Dynamics* **22**(2-3), 71–86.
- Boos, W. and Pascale, S. (2021), 'Mechanical forcing of the north american monsoon by orography', *599*, 611–615.
- Boos, W. R. (2015), 'A review of recent progress on Tibet's role in the South Asian monsoon', *CLIVAR Exch* **19**(66), 23–27.
- Boos, W. R. and Korty, R. L. (2016), 'Regional energy budget control of the intertropical convergence zone and application to mid-Holocene rainfall', *Nature Geoscience* **9**(12), 892–897.
- Bordoni, S. and Schneider, T. (2008), 'Monsoons as eddy-mediated regime transitions of the tropical overturning circulation', *Nature Geoscience* **1**(8), 515–519.
- Brooks, I. M. (2003), 'Finding boundary layer top: Application of a wavelet covariance transform to lidar backscatter profiles', *Journal of Atmospheric and Oceanic Technology* **20**(8), 1092–1105.
- Bushell, A. C., Anstey, J. A., Butchart, N., Kawatani, Y., Osprey, S. M., Richter, J. H., Serva, F., Braesicke, P., Cagnazzo, C., Chen, C.-C., Chun, H.-Y., Garcia, R. R., Gray, L. J., Hamilton, K., Kerzenmacher, T., Kim, Y.-H., Lott, F., McLandress, C., Naoe, H., Scinocca, J., Smith, A. K., Stockdale, T. N., Versick, S., Watanabe, S., Yoshida, K. and Yukimoto, S. (2020), 'Evaluation of the Quasi-Biennial Oscillation in global climate models for the SPARC QBO-initiative', *Quarterly Journal of the Royal Meteorological Society* pp. 1–31.
- URL:** <https://rmets.onlinelibrary.wiley.com/doi/abs/10.1002/qj.3765>

- Bussmann, A., Elagib, N. A., Fayyad, M. and Ribbe, L. (2016), 'Sowing date determinants for Sahelian rainfed agriculture in the context of agricultural policies and water management', *Land Use Policy* **52**, 316 – 328.
- Byrne, M. P. and Schneider, T. (2016), 'Narrowing of the ITCZ in a warming climate: Physical mechanisms', *Geophysical Research Letters* **43**(21), 11–350.
- Byrne, M. P. and Zanna, L. (2020), 'Radiative effects of clouds and water vapor on an axisymmetric monsoon', *Journal of Climate* **33**(20), 8789–8811.
- C3S (2017), 'ERA5: Fifth generation of ECMWF atmospheric reanalyses of the global climate.', *Copernicus Climate Change Service Climate Data Store (CDS)*. date of access: 18 March 2019, <https://climate.copernicus.eu/climate-reanalysis>.
- Cai, W., McPhaden, M., Grimm, A., Rodrigues, R., Taschetto, A., Garreaud, R., Dewitte, B., Poveda, G., Ham, Y.-G., Santoso, A., Ng, B., Anderson, W., Wang, G., Geng, T., Jo, H., Marengo, J., Alves, L., Osman, M., Li, S. and Vera, C. (2020), 'Climate impacts of the El Niño–Southern Oscillation on South America', *Nature Reviews Earth & Environment* **1**(4), 215–231.
- Cai, W., Wu, L., Lengaigne, M., Li, T., McGregor, S., Kug, J.-S., Yu, J.-Y., Stuecker, M. F., Santoso, A., Li, X., Ham, Y.-G., Chikamoto, Y., Ng, B., McPhaden, M. J., Du, Y., Dommenech, D., Jia, F., Kajtar, J. B., Keenlyside, N., Lin, X., Luo, J.-J., Martín-Rey, M., Ruprich-Robert, Y., Wang, G., Xie, S.-P., Yang, Y., Kang, S. M., Choi, J.-Y., Gan, B., Kim, G.-I., Kim, C.-E., Kim, S., Kim, J.-H. and Chang, P. (2019), 'Pantropical climate interactions', *Science* **363**(6430), eaav4236.
- Camargo, S. J. and Sobel, A. H. (2010), 'Revisiting the influence of the quasi-biennial oscillation on tropical cyclone activity', *Journal of Climate* **23**(21), 5810–5825.
- Campetella, C. M. and Vera, C. S. (2002), 'The influence of the andes mountains on the south american low-level flow', *Geophysical Research Letters* **29**(17), 7–1.
- Capotondi, A., Wittenberg, A. T., Newman, M., Di Lorenzo, E., Yu, J.-Y., Braconnot, P., Cole, J., Dewitte, B., Giese, B., Guilyardi, E. et al. (2015), 'Understanding enso diversity', *Bulletin of the American Meteorological Society* **96**(6), 921–938.
- Carvalho, L. M., Jones, C. and Liebmann, B. (2004), 'The South Atlantic convergence zone: Intensity, form, persistence, and relationships with intraseasonal to interannual activity and extreme rainfall', *Journal of Climate* **17**, 88–108.
- Carvalho, L. M. V., Jones, C., Posadas, A. N. D., Quiroz, R., Bookhagen, B. and Liebmann, B. (2012), 'Precipitation characteristics of the South American Monsoon System derived from multiple datasets', *Journal of Climate* **25**(13), 4600–4620.
- Cavazos, T., Luna-Niño, R., Cerezo-Mota, R., Fuentes-Franco, R., Méndez, M., Pineda Martinez, L. F. and Valenzuela, E. (2020), 'Climatic trends and regional climate models intercomparison over the CORDEX-CAM (Central America, Caribbean, and Mexico) domain', *International Journal of Climatology* **40**(3), 1396–1420.

- Chan, J. C. (1995), 'Tropical cyclone activity in the western North Pacific in relation to the stratospheric quasi-biennial oscillation', *Monthly Weather Review* **123**(8), 2567–2571.
- Chao, W. C. and Chen, B. (2001), 'The origin of monsoons', *Journal of the Atmospheric Sciences* **58**(22), 3497–3507.
- Chen, J., Wilson, C., Tapley, B., Yang, Z. and Niu, G. (2009), '2005 drought event in the Amazon River basin as measured by GRACE and estimated by climate models', *Journal of Geophysical Research: Solid Earth* **114**(B5).
- Chevuturi, A., Turner, A. G., Woolnough, S. J., Martin, G. M. and MacLachlan, C. (2019), 'Indian summer monsoon onset forecast skill in the UK Met Office initialized coupled seasonal forecasting system (GloSea5-GC2)', *Climate dynamics* **52**(11), 6599–6617.
- Chou, C. and Neelin, J. D. (2004), 'Mechanisms of global warming impacts on regional tropical precipitation', *Journal of Climate* **17**(13), 2688–2701.
- Christensen, H., Berner, J., Coleman, D. R. and Palmer, T. (2017), 'Stochastic parameterization and El Niño–Southern Oscillation', *Journal of Climate* **30**(1), 17–38.
- Christiansen, B., Yang, S. and Madsen, M. S. (2016), 'Do strong warm ENSO events control the phase of the stratospheric QBO?', *Geophysical Research Letters* **43**(19), 10–489.
- Chuvieco, E., Opazo, S., Sione, W., Valle, H. d., Anaya, J., Bella, C. D., Cruz, I., Manzo, L., López, G., Mari, N., González-Alonso, F., Morelli, F., Setzer, A., Csiszar, I., Kanpandegi, J. A., Bastarrika, A. and Libonati, R. (2008), 'Global burned-land estimation in Latin-America using MODIS composite data', *Ecological Applications* **18**(1), 64–79.
- Claud, C. and Terray, P. (2007), 'Revisiting the possible links between the quasi-biennial oscillation and the Indian summer monsoon using ncep r-2 and cmap fields', *Journal of Climate* **20**(5), 773–787.
- Collimore, C. C., Martin, D. W., Hitchman, M. H., Huesmann, A. and Waliser, D. E. (2003), 'On the relationship between the QBO and tropical deep convection', *Journal of Climate* **16**(15), 2552–2568.
- Cook, B. I. and Buckley, B. M. (2009), 'Objective determination of monsoon season onset, withdrawal, and length', *Journal of Geophysical Research: Atmospheres* **114**(D23).
- Cook, B. and Seager, R. (2013), 'The response of the North American Monsoon to increased greenhouse gas forcing', *Journal of Geophysical Research: Atmospheres* **118**(4), 1690–1699.
- Corrales-Suastegui, A., Fuentes-Franco, R. and Pavia, E. G. (2020), 'The mid-summer drought over Mexico and Central America in the 21st century', *International Journal of Climatology* **40**(3), 1703–1715.
- Curtis, S. (2002), 'Interannual variability of the bimodal distribution of summertime rainfall over Central America and tropical storm activity in the far-eastern Pacific', *Climate Research* **22**, 141–146.
- Curtis, S. and Gamble, D. W. (2008), 'Regional variations of the Caribbean mid-summer drought', *Theoretical and Applied Climatology* **94**, 25–34.

- Davis, S. M., Liang, C. K. and Rosenlof, K. H. (2013), 'Interannual variability of tropical tropopause layer clouds', *Geophysical Research Letters* **40**(11), 2862–2866.
- de Sousa, K., Casanoves, F., Sellare, J., Ospina, A., Suchini, J. G., Aguilar, A. and Mercado, L. (2018), 'How climate awareness influences farmers' adaptation decisions in Central America?', *Journal of Rural Studies* **64**, 11–19.
- Derbyshire, S., Maidens, A., Milton, S., Stratton, R. and Willett, M. (2011), 'Adaptive detrainment in a convective parametrization', *Quarterly Journal of the Royal Meteorological Society* **137**(660), 1856–1871.
- Deser, C., Alexander, M. A., Xie, S.-P. and Phillips, A. S. (2010), 'Sea surface temperature variability: Patterns and mechanisms', *Annual review of marine science* **2**, 115–143.
- Dilley, M. (1996), 'Synoptic controls on precipitation in the Valley of Oaxaca, Mexico', *International Journal of Climatology: A Journal of the Royal Meteorological Society* **16**(9), 1019–1031.
- Dimdore-Miles, O., Gray, L. and Osprey, S. (2021), 'Origins of multi-decadal variability in sudden stratospheric warmings', *Weather and Climate Dynamics* **2**(1), 205–231.
- Dinku, T., Ruiz, F., Connor, S. J. and Ceccato, P. (2010), 'Validation and intercomparison of satellite rainfall estimates over Colombia', *Journal of Applied Meteorology and Climatology* **49**(5), 1004–1014.
- Doi, T., Vecchi, G. A., Rosati, A. J. and Delworth, T. L. (2012), 'Biases in the atlantic itcz in seasonal–interannual variations for a coarse-and a high-resolution coupled climate model', *Journal of Climate* **25**(16), 5494–5511.
- Domeisen, D. I., Garfinkel, C. I. and Butler, A. H. (2019), 'The teleconnection of El Niño Southern Oscillation to the stratosphere', *Reviews of Geophysics* **57**(1), 5–47.
- Dominguez, F., Kumar, P. and Vivoni, E. R. (2008), 'Precipitation recycling variability and ecoclimatological stability—A study using NARR data. Part II: North American monsoon region', *Journal of Climate* **21**(20), 5187–5203.
- Dommeneget, D., Bayr, T. and Frauen, C. (2013), 'Analysis of the non-linearity in the pattern and time evolution of El Niño Southern Oscillation', *Climate Dynamics* **40**(11-12), 2825–2847.
- Donohoe, A., Marshall, J., Ferreira, D. and Mcgee, D. (2013), 'The Relationship between ITCZ Location and Cross-Equatorial Atmospheric Heat Transport: From the Seasonal Cycle to the Last Glacial Maximum', *Journal of Climate* **26**(11), 3597–3618.
- Douglas, M. W., Maddox, R. A., Howard, K. and Reyes, S. (1993), 'The mexican monsoon', *Journal of Climate* **6**(8), 1665–1677.
- Durán-Quesada, A. M., Gimeno, L. and Amador, J. (2017), 'Role of moisture transport for Central American precipitation', *Earth System Dynamics* **8**(1), 147–161.
- Ebdon, R. (1960), 'Notes on the wind flow at 50 mb in tropical and sub-tropical regions in January 1957 and January 1958', *Quarterly Journal of the Royal Meteorological Society* **86**(370), 540–542.

- Emanuel, K. (2007), 'Quasi-equilibrium dynamics of the tropical atmosphere', *The Global Circulation of the Atmosphere* **186**, 218.
- Emanuel, K. A. et al. (1994), *Atmospheric convection*, Oxford University Press on Demand.
- Eyring, V., Bony, S., Meehl, G. A., Senior, C. A., Stevens, B., Stouffer, R. J. and Taylor, K. E. (2016), 'Overview of the Coupled Model Intercomparison Project Phase 6 (CMIP6) experimental design and organization', *Geoscientific Model Development (Online)* **9**.
- Fasullo, J. and Webster, P. (2003), 'A hydrological definition of Indian monsoon onset and withdrawal', *Journal of Climate* **16**(19), 3200–3211.
- Faulk, S., Mitchell, J. and Bordoni, S. (2017), 'Effects of rotation rate and seasonal forcing on the ITCZ extent in planetary atmospheres', *Journal of the Atmospheric Sciences* **74**(3), 665–678.
- Fereday, D., Chadwick, R., Knight, J. and Scaife, A. (2020), 'Tropical Rainfall Linked to Stronger Future ENSO-NAO Teleconnection in CMIP5 Models', *Geophysical Research Letters* **47**(22), e2020GL088664.
- Fisher, R. A. (1992), Statistical methods for research workers, in 'Breakthroughs in statistics', Springer, pp. 66–70.
- Forbes, R. M. and Ahlgrimm, M. (2014), 'On the representation of high-latitude boundary layer mixed-phase cloud in the ECMWF global model', *Monthly Weather Review* **142**(9), 3425–3445.
- Franchito, S. H., Rao, V. B., Vasques, A. C., Santo, C. M. and Conforte, J. C. (2009), 'Validation of TRMM precipitation radar monthly rainfall estimates over Brazil', *Journal of Geophysical Research: Atmospheres* **114**(D2).
- Fritsch, J. and Chappell, C. (1980), 'Numerical prediction of convectively driven mesoscale pressure systems. Part I: convective parameterization', *Journal of Atmospheric Sciences* **37**(8), 1722–1733.
- Fu, D., Chang, P., Patricola, C. M., Saravanan, R., Liu, X. and Beck, H. E. (2021), 'Central american mountains inhibit eastern north pacific seasonal tropical cyclone activity', *Nature communications* **12**(1), 1–11.
- Fuentes-Franco, R., Coppola, E., Giorgi, F., Pavia, E. G., Diro, G. T. and Graef, F. (2015), 'Inter-annual variability of precipitation over Southern Mexico and Central America and its relationship to sea surface temperature from a set of future projections from CMIP5 GCMs and RegCM4 CORDEX simulations', *Climate Dynamics* **45**(1-2), 425–440.
- Fujiwara, M., Manney, G. L., Gray, L. J. and Wright, J. S. (2021), SPARC Reanalysis Intercomparison Project (S-RIP) Final Report, Technical report, World Climate Research Programme, SPARC Report No. 10.
www.sparc-climate.org/publications/sparc-reports.
- Funk, C., Peterson, P., Landsfeld, M., Pedreros, D., Verdin, J., Shukla, S., Husak, G., Rowland, J., Harrison, L., Hoell, A. and Michaelsen, J. (2015), 'The climate hazards infrared precipitation with stations—a new environmental record for monitoring extremes', *Scientific data* **2**, 150066.
- Gadgil, S. (2018), 'The monsoon system: Land–sea breeze or the itcz?', *Journal of Earth System*

- Science* **127**(1), 1.
- Gadgil, S. and Rupa Kumar, K. (2006), *The Asian monsoon — agriculture and economy*, Springer Berlin Heidelberg, Berlin, Heidelberg, pp. 651–683.
- Gamble, D. W., Parnell, D. B. and Curtis, S. (2008), ‘Spatial variability of the Caribbean mid-summer drought and relation to north Atlantic high circulation’, *International Journal of Climatology* **28**(3), 343–350.
- Gan, M., Kousky, V. and Ropelewski, C. (2004), ‘The South America monsoon circulation and its relationship to rainfall over west-central Brazil’, *Journal of climate* **17**, 47–66.
- García-Franco, J. L., Osprey, S. and Gray, L. J. (2021), ‘A wavelet transform method to determine monsoon onset and retreat from precipitation time-series’, *International Journal of Climatology* **41**(11), 5295–5317.
- URL:** <https://rmets.onlinelibrary.wiley.com/doi/abs/10.1002/joc.7130>
- García-Franco, J. L., Gray, L. J. and Osprey, S. (2020), ‘The American monsoon system in HadGEM3 and UKESM1’, *Weather and Climate Dynamics* **1**(2), 349–371.
- URL:** <https://wcd.copernicus.org/articles/1/349/2020/>
- García-Martínez, I. M. and Bollasina, M. A. (2020), ‘Sub-monthly evolution of the Caribbean Low-Level Jet and its relationship with regional precipitation and atmospheric circulation’, *Climate Dynamics* pp. 1–18.
- Garcia, S. R. and Kayano, M. T. (2013), ‘Some considerations on onset dates of the rainy season in Western-Central Brazil with antisymmetric outgoing longwave radiation relative to the equator’, *International Journal of Climatology* **33**(1), 188–198.
- Garfinkel, C. I. and Hartmann, D. (2010), ‘Influence of the quasi-biennial oscillation on the North Pacific and El Niño teleconnections’, *Journal of Geophysical Research: Atmospheres* **115**(D20).
- Garfinkel, C. I. and Hartmann, D. L. (2011), ‘The influence of the quasi-biennial oscillation on the troposphere in winter in a hierarchy of models. Part II: Perpetual winter WACCM runs’, *Journal of the Atmospheric Sciences* **68**(9), 2026–2041.
- Geen, R., Bordoni, S., Battisti, D. S. and Hui, K. (2020), ‘Monsoons, ITCZs and the Concept of the Global Monsoon’, *Reviews of Geophysics* p. e2020RG000700.
- Geen, R., Lambert, F. H. and Vallis, G. K. (2019), ‘Processes and Timescales in Onset and Withdrawal of “Aquaplanet Monsoons”’, *Journal of the Atmospheric Sciences* **76**(8), 2357–2373.
- Geil, K. L., Serra, Y. L. and Zeng, X. (2013), ‘Assessment of CMIP5 model simulations of the North American monsoon system’, *Journal of Climate* **26**(22), 8787–8801.
- Giannini, A., Kushnir, Y. and Cane, M. A. (2000), ‘Interannual variability of Caribbean rainfall, ENSO, and the Atlantic Ocean’, *Journal of Climate* **13**, 297–311.
- Gill, A. E. (1980), ‘Some simple solutions for heat-induced tropical circulation’, *Quarterly Journal of the Royal Meteorological Society* **106**(449), 447–462.
- Giorgetta, M. A., Bengtsson, L. and Arpe, K. (1999), ‘An investigation of QBO signals in the east Asian and Indian monsoon in GCM experiments’, *Climate dynamics* **15**(6), 435–450.

- Good, P., Chadwick, R., Holloway, C. E., Kennedy, J., Lowe, J. A., Roehrig, R. and Rushley, S. S. (2021), 'High sensitivity of tropical precipitation to local sea surface temperature', *Nature* **589**(7842), 408–414.
- Gray, L., Brown, M., Knight, J., Andrews, M., Lu, H., O'Reilly, C. and Anstey, J. (2020), 'Forecasting extreme stratospheric polar vortex events', *Nature communications* **11**(1), 1–9.
- Gray, L. J., Anstey, J. A., Kawatani, Y., Lu, H., Osprey, S. and Schenzinger, V. (2018), 'Surface impacts of the Quasi Biennial Oscillation', *Atmospheric Chemistry and Physics* **18**(11), 8227–8247.
- Gray, W. M. (1984), 'Atlantic seasonal hurricane frequency. Part I: El Niño and 30 mb quasi-biennial oscillation influences', *Monthly Weather Review* **112**(9), 1649–1668.
- Gray, W. M., Sheaffer, J. D. and Knaff, J. A. (1992), 'Influence of the stratospheric QBO on ENSO variability', *Journal of the Meteorological Society of Japan. Ser. II* **70**(5), 975–995.
- Grimm, A. M. (2011), 'Interannual climate variability in South America: impacts on seasonal precipitation, extreme events, and possible effects of climate change', *Stochastic Environmental Research and Risk Assessment* **25**(4), 537–554.
- Guo, Y., Ting, M., Wen, Z. and Lee, D. E. (2017), 'Distinct patterns of tropical pacific sst anomaly and their impacts on north american climate', *Journal of Climate* **30**(14), 5221–5241.
- Guo, Z., Zhou, T., Wang, M. and Qian, Y. (2015), 'Impact of cloud radiative heating on East Asian summer monsoon circulation', *Environmental Research Letters* **10**(7), 074014.
- Ha, K.-J., Moon, S., Timmermann, A. and Kim, D. (2020), 'Future Changes of Summer Monsoon Characteristics and Evaporative Demand Over Asia in CMIP6 Simulations', *Geophysical Research Letters* **47**(8), e2020GL087492.
- Halley, E. (1687), 'An historical account of the trade winds, and monsoons, observable in the seas between and near the tropicks, with an attempt to assign the physical cause of the said winds', *Philosophical Transactions of the Royal Society of London* **16**(183), 153–168.
- URL:** <https://royalsocietypublishing.org/doi/abs/10.1098/rstl.1686.0026>
- Hansen, F., Matthes, K. and Wahl, S. (2016), 'Tropospheric QBO–ENSO interactions and differences between the Atlantic and Pacific', *Journal of Climate* **29**(4), 1353–1368.
- Harris, I., Jones, P. D., Osborn, T. J. and Lister, D. H. (2014), 'Updated high-resolution grids of monthly climatic observations—the cru ts3. 10 dataset', *International journal of climatology* **34**(3), 623–642.
- Harrop, B. E. and Hartmann, D. L. (2016), 'The role of cloud radiative heating in determining the location of the itcz in aquaplanet simulations', *Journal of Climate* **29**(8), 2741–2763.
- Hartmann, D. L. (2015), *Global physical climatology*, Vol. 103, Newnes.
- Harvey, C. A., Saborio-Rodríguez, M., Martínez-Rodríguez, M. R., Viguera, B., Chain-Guadarrama, A., Vignola, R. and Alpizar, F. (2018), 'Climate change impacts and adaptation among smallholder farmers in Central America', *Agriculture & Food Security* **7**(1), 57.

- Hastenrath, S. (2006), ‘Circulation and teleconnection mechanisms of northeast brazil droughts’, *Progress in Oceanography* **70**(2-4), 407–415.
- Hastenrath, S. L. (1967), ‘Rainfall distribution and regime in Central America’, *Archiv für Meteorologie, Geophysik und Bioklimatologie, Serie B* **15**(3), 201–241.
- Haynes, P., HITCHCOCK, P., HITCHMAN, M., YODEN, S., HENDON, H., KILADIS, G., KODERA, K. and SIMPSON, I. (2021), ‘The influence of the stratosphere on the tropical troposphere’, *Journal of the Meteorological Society of Japan. Ser. II*.
- Hellin, J., Cox, R. and López-Ridaura, S. (2017), ‘Maize Diversity, Market Access, and Poverty Reduction in the Western Highlands of Guatemala’, *Mountain Research and Development* **37**(2), 188 – 197.
- Hénin, R., Liberato, M. L., Ramos, A. M. and Gouveia, C. M. (2018), ‘Assessing the use of satellite-based estimates and high-resolution precipitation datasets for the study of extreme precipitation events over the Iberian Peninsula’, *Water* **10**(11), 1688.
- Herrera, E., Magaña, V. and Caetano, E. (2015), ‘Air–sea interactions and dynamical processes associated with the midsummer drought’, *International Journal of Climatology* **35**(7), 1569–1578.
- Hersbach, H., Bell, B., Berrisford, P., Hirahara, S., Horányi, A., Muñoz-Sabater, J., Nicolas, J., Peubey, C., Radu, R., Schepers, D., Simmons, A., Soci, C., Abdalla, S., Abellan, X., Balsamo, G., Bechtold, P., Biavati, G., Bidlot, J., Bonavita, M., De Chiara, G., Dahlgren, P., Dee, D., Diamantakis, M., Dragani, R., Flemming, J., Forbes, R., Fuentes, M., Geer, A., Haimberger, L., Healy, S., Hogan, R. J., Hólm, E., Janisková, M., Keeley, S., Laloyaux, P., Lopez, P., Lupu, C., Radnoti, G., de Rosnay, P., Rozum, I., Vamborg, F., Villaume, S. and Thépaut, J.-N. (2020), ‘The ERA5 global reanalysis’, *Quarterly Journal of the Royal Meteorological Society* **146**(730), 1999–2049.
- Higgins, R., Yao, Y. and Wang, X. (1997), ‘Influence of the North American monsoon system on the US summer precipitation regime’, *Journal of Climate* **10**(10), 2600–2622.
- Hill, K., Taschetto, A. and England, M. (2009), ‘South american rainfall impacts associated with inter-el niño variations’, *Geophysical Research Letters* **36**(19).
- Hill, S. A. (2019), ‘Theories for past and future monsoon rainfall changes’, *Current Climate Change Reports* **5**(3), 160–171.
- Hitchman, M. H., Yoden, S., Haynes, P. H., Kumar, V. and Tegtmeier, S. (2021), ‘An observational history of the direct influence of the stratospheric quasi-biennial oscillation on the tropical and subtropical upper troposphere and lower stratosphere’, *Journal of the Meteorological Society of Japan. Ser. II*.
- Ho, C.-H., Kim, H.-S., Jeong, J.-H. and Son, S.-W. (2009), ‘Influence of stratospheric quasi-biennial oscillation on tropical cyclone tracks in the western north pacific’, *Geophysical Research Letters* **36**(6).
- Holton, J. R. and Tan, H.-C. (1980), ‘The influence of the equatorial quasi-biennial oscillation on

- the global circulation at 50 mb', *Journal of the Atmospheric Sciences* **37**(10), 2200–2208.
- Hoskins, B. J. and Karoly, D. J. (1981), 'The steady linear response of a spherical atmosphere to thermal and orographic forcing', *Journal of Atmospheric Sciences* **38**(6), 1179–1196.
- Hoskins, B., Yang, G.-Y. and Fonseca, R. (2020), 'The detailed dynamics of the June–August Hadley Cell', *Quarterly Journal of the Royal Meteorological Society* **146**(727), 557–575.
- Htway, O. and Matsumoto, J. (2011), 'Climatological onset dates of summer monsoon over Myanmar', *International Journal of Climatology* **31**(3), 382–393.
- Huang, B., Hu, Z.-Z., Kinter, J. L., Wu, Z. and Kumar, A. (2012), 'Connection of stratospheric qbo with global atmospheric general circulation and tropical sst. part i: Methodology and composite life cycle', *Climate dynamics* **38**(1-2), 1–23.
- Huffman, G. J., Adler, R. F., Bolvin, D. T. and Nelkin, E. J. (2010), The TRMM multi-satellite precipitation analysis (TMPA), in 'Satellite rainfall applications for surface hydrology', Springer, pp. 3–22.
- Huffman, G. J., Bolvin, D. T., Nelkin, E. J., Wolff, D. B., Adler, R. F., Gu, G., Hong, Y., Bowman, K. P. and Stocker, E. F. (2007), 'The TRMM Multisatellite Precipitation Analysis (TMPA): Quasi-Global, Multiyear, Combined-Sensor Precipitation Estimates at Fine Scales', *Journal of Hydrometeorology* **8**(1), 38–55.
- Inoue, K. and Back, L. E. (2015), 'Gross moist stability assessment during TOGA COARE: Various interpretations of gross moist stability', *Journal of Atmospheric Sciences* **72**(11), 4148–4166.
- Inoue, K., Biasutti, M. and Fridlind, A. M. (2021), 'Evidence that horizontal moisture advection regulates the ubiquitous amplification of rainfall variability over tropical oceans', *Journal of the Atmospheric Sciences* **78**(2), 529–547.
- Insel, N., Poulsen, C. J. and Ehlers, T. A. (2010), 'Influence of the andes mountains on south american moisture transport, convection, and precipitation', *Climate Dynamics* **35**(7), 1477–1492.
- Jain, M., Naeem, S., Orlove, B., Modi, V. and DeFries, R. S. (2015), 'Understanding the causes and consequences of differential decision-making in adaptation research: Adapting to a delayed monsoon onset in Gujarat, India', *Global Environmental Change* **31**, 98 – 109.
- Jakob, C. (2014), 'Going back to basics', *Nature Climate Change* **4**(12), 1042.
- Jaramillo, A., Dominguez, C., Raga, G. and Quintanar, A. I. (2021), 'The combined qbo and enso influence on tropical cyclone activity over the north atlantic ocean', *Atmosphere* **12**(12), 1588.
- Jiménez-Esteve, B. and Domeisen, D. I. (2018), 'The tropospheric pathway of the enso–north atlantic teleconnection', *Journal of Climate* **31**(11), 4563–4584.
- Jiménez-Esteve, B. and Domeisen, D. I. V. (2020), 'Nonlinearity in the tropospheric pathway of ENSO to the North Atlantic', *Weather and Climate Dynamics* **1**(1), 225–245.
- Jimenez, J. C., Marengo, J. A., Alves, L. M., Sulca, J. C., Takahashi, K., Ferrett, S. and Collins, M. (2021), 'The role of enso flavours and tna on recent droughts over amazon forests and the

- northeast brazil region', *International Journal of Climatology* **41**(7), 3761–3780.
- Jobbová, E., Helmke, C. and Bevan, A. (2018), 'Ritual responses to drought: An examination of ritual expressions in Classic Maya written sources', *Human Ecology* **46**(5), 759–781.
- Johns, T. C., Durman, C. F., Banks, H. T., Roberts, M. J., McLaren, A. J., Ridley, J. K., Senior, C. A., Williams, K., Jones, A., Rickard, G. et al. (2006), 'The new Hadley Centre climate model (HadGEM1): Evaluation of coupled simulations', *Journal of climate* **19**(7), 1327–1353.
- Jones, C. (2019), 'Recent changes in the south america low-level jet', *npj Climate and Atmospheric Science* **2**(1), 1–8.
- Jones, C. and Carvalho, L. M. (2013), 'Climate change in the South American monsoon system: present climate and CMIP5 projections', *Journal of Climate* **26**(17), 6660–6678.
- Jones, C. and Carvalho, L. M. (2018), 'The influence of the Atlantic multidecadal oscillation on the eastern Andes low-level jet and precipitation in South America', *npj Climate and Atmospheric Science* **1**(1), 1–7.
- Jorgetti, T., da Silva Dias, P. L. and de Freitas, E. D. (2014), 'The relationship between South Atlantic SST and SACZ intensity and positioning', *Climate dynamics* **42**(11-12), 3077–3086.
- Junquas, C., Li, L., Vera, C. S., Le Treut, H. and Takahashi, K. (2016), 'Influence of south america orography on summertime precipitation in southeastern south america', *Climate Dynamics* **46**(11), 3941–3963.
- Junquas, C., Vera, C., Li, L. and Le Treut, H. (2012), 'Summer precipitation variability over southeastern south america in a global warming scenario', *Climate dynamics* **38**(9), 1867–1883.
- Karnauskas, K. B., Seager, R., Giannini, A. and Busalacchi, A. J. (2013), 'A simple mechanism for the climatological midsummer drought along the Pacific coast of Central America', *Atmosfera* **26**, 261–281.
- Kennedy, J., Rayner, N., Smith, R., Parker, D. and Saunby, M. (2011), 'Reassessing biases and other uncertainties in sea surface temperature observations measured in situ since 1850: 2. biases and homogenization', *Journal of Geophysical Research: Atmospheres* **116**(D14).
- Kim, H., Caron, J. M., Richter, J. H. and Simpson, I. R. (2020), 'The lack of QBO-MJO Connection in CMIP6 Models', *Geophysical Research Letters* **47**(11), e2020GL087295. e2020GL087295 2020GL087295.
- Kitoh, A. and Uchiyama, T. (2006), 'Changes in onset and withdrawal of the East Asian summer rainy season by multi-model global warming experiments', *Journal of the Meteorological Society of Japan. Ser. II* **84**(2), 247–258.
- Kuhlbrodt, T., Jones, C. G., Sellar, A., Storkey, D., Blockley, E., Stringer, M., Hill, R., Graham, T., Ridley, J., Blaker, A., Calvert, D., Copsey, D., Ellis, R., Hewitt, H., Hyder, P., Ineson, S., Mulcahy, J., Siahaan, A. and Walton, J. (2018), 'The low-resolution version of HadGEM3 GC3. 1: Development and evaluation for global climate', *Journal of advances in modeling earth systems* **10**(11), 2865–2888.
- Lawrence, P. J., Feddema, J. J., Bonan, G. B., Meehl, G. A., O'Neill, B. C., Oleson, K. W., Levis,

- S., Lawrence, D. M., Kluzek, E., Lindsay, K. and Thornton, P. E. (2012), 'Simulating the Biogeochemical and Biogeophysical Impacts of Transient Land Cover Change and Wood Harvest in the Community Climate System Model (CCSM4) from 1850 to 2100', *Journal of Climate* **25**(9), 3071–3095.
- Lee, J. C. K. and Klingaman, N. P. (2018), 'The effect of the quasi-biennial oscillation on the Madden–Julian oscillation in the Met Office Unified Model Global Ocean Mixed Layer configuration', *Atmospheric Science Letters* **19**(5), e816.
- Li, D., Shine, K. and Gray, L. (1995), 'The role of ozone-induced diabatic heating anomalies in the quasi-biennial oscillation', *Quarterly Journal of the Royal Meteorological Society* **121**(524), 937–943.
- Li, G. and Xie, S.-P. (2014), 'Tropical biases in CMIP5 multimodel ensemble: The excessive equatorial Pacific cold tongue and double ITCZ problems', *Journal of Climate* **27**(4), 1765–1780.
- Li, T. and Hsu, P.-c. (2018), *Fundamentals of tropical climate dynamics*, Springer.
- Li, W., Fu, R. and Dickinson, R. E. (2006), 'Rainfall and its seasonality over the Amazon in the 21st century as assessed by the coupled models for the IPCC AR4', *Journal of Geophysical Research: Atmospheres* **111**(D2).
- Liebmann, B. and Marengo, J. (2001), 'Interannual variability of the rainy season and rainfall in the Brazilian Amazon Basin', *Journal of Climate* **14**(22), 4308–4318.
- Liebmann, B. and Mechoso, C. R. (2011), *The South American Monsoon System*, World Scientific Series on Asia-Pacific Weather and Climate, chapter 9, pp. 137–157.
- Liess, S. and Geller, M. A. (2012), 'On the relationship between qbo and distribution of tropical deep convection', *Journal of Geophysical Research: Atmospheres* **117**(D3).
- Lorenz, E. N. (1967), *The nature and theory of the general circulation of the atmosphere*, Vol. 218, World Meteorological Organization Geneva.
- Lu, H., Hitchman, M. H., Gray, L. J., Anstey, J. A. and Osprey, S. M. (2020), 'On the role of rossby wave breaking in the quasi-biennial modulation of the stratospheric polar vortex during boreal winter', *Quarterly Journal of the Royal Meteorological Society* **146**(729), 1939–1959.
- Lucas-Picher, P., Christensen, J. H., Saeed, F., Kumar, P., Asharaf, S., Ahrens, B., Wiltshire, A. J., Jacob, D. and Hagemann, S. (2011), 'Can regional climate models represent the Indian] Monsoon?', *Journal of Hydrometeorology* **12**(5), 849–868.
- Ma, D., Sobel, A. H., Kuang, Z., Singh, M. S. and Nie, J. (2019), 'A moist entropy budget view of the South Asian summer monsoon onset', *Geophysical Research Letters* **46**(8), 4476–4484.
- Machado, L., Laurent, H., Dessay, N. and Miranda, I. (2004), 'Seasonal and diurnal variability of convection over the Amazonia: A comparison of different vegetation types and large scale forcing', *Theoretical and Applied Climatology* **78**(1-3), 61–77.
- Magaña, V., Amador, J. A. and Medina, S. (1999), 'The midsummer drought over Mexico and Central America', *Journal of Climate* **12**, 1577–1588.
- Magaña, V. and Caetano, E. (2005), 'Temporal evolution of summer convective activity over the

- Americas warm pools', *Geophysical Research Letters* **32**(2).
- Magaña, V. O., Vázquez, J. L., Pérez, J. L. and Pérez, J. B. (2003), 'Impact of El Niño on precipitation in Mexico', *Geofísica internacional* **42**(3), 313–330.
- Maldonado, T., Alfaro, E., Rutgersson, A. and Amador, J. A. (2017), 'The early rainy season in Central America: the role of the tropical North Atlantic SSTs', *International Journal of Climatology* **37**(9), 3731–3742.
- Malhi, Y., Aragão, L. E., Galbraith, D., Huntingford, C., Fisher, R., Zelazowski, P., Sitch, S., McSweeney, C. and Meir, P. (2009), 'Exploring the likelihood and mechanism of a climate-change-induced dieback of the Amazon rainforest', *Proceedings of the National Academy of Sciences* **106**(49), 20610–20615.
- Mapes, B. E., Liu, P. and Buenning, N. (2005), 'Indian monsoon onset and the Americas midsummer drought: Out-of-equilibrium responses to smooth seasonal forcing', *Journal of Climate* **18**(7), 1109–1115.
- Marengo, J. A., Liebmann, B., Grimm, A. M., Misra, V., Silva Dias, P. L., Cavalcanti, I. F. A., Carvalho, L. M. V., Berbery, E. H., Ambrizzi, T., Vera, C. S., Saulo, A. C., Nogues-Paegle, J., Zipser, E., Seth, A. and Alves, L. M. (2012), 'Recent developments on the South American monsoon system', *International Journal of Climatology* **32**, 1–21.
- Marengo, J. A., Liebmann, B., Kousky, V. E., Filizola, N. P. and Wainer, I. C. (2001), 'Onset and end of the rainy season in the Brazilian Amazon Basin', *Journal of Climate* **14**(5), 833–852.
- Marengo, J., Chou, S., Torres, R., Giarolla, A., Alves, L. and Lyra, A. (2014), 'Climate change in central and South America: recent trends, future projections, and impacts on regional agriculture'.
- Marotzke, J., Jakob, C., Bony, S., Dirmeyer, P., O'Gorman, P., Hawkins, E., Perkins-Kirkpatrick, S., Quéré, C., Nowicki, S., Paulavets, K., Seneviratne, S., Stevens, B. and Tuma, M. (2017), 'Climate research must sharpen its view', *Nature climate change* **7**(2), 89–91.
- Martin, Z., Orbe, C., Wang, S. and Sobel, A. (2021a), 'The MJO–QBO Relationship in a GCM with Stratospheric Nudging', *Journal of Climate* **34**(11), 4603–4624.
- Martin, Z., Son, S.-W., Butler, A., Hendon, H., Kim, H., Sobel, A., Yoden, S. and Zhang, C. (2021b), 'The influence of the quasi-biennial oscillation on the madden–julian oscillation', *Nature Reviews Earth & Environment* pp. 1–13.
- Martin, Z., Vitart, F., Wang, S. and Sobel, A. (2020), 'The Impact of the Stratosphere on the MJO in a Forecast Model', *Journal of Geophysical Research: Atmospheres* **125**(4), e2019JD032106.
- Martin, Z., Wang, S., Nie, J. and Sobel, A. (2019), 'The Impact of the QBO on MJO Convection in Cloud-Resolving Simulations', *Journal of the Atmospheric Sciences* **76**(3), 669–688.
- Martinez, C., Goddard, L., Kushnir, Y. and Ting, M. (2019), 'Seasonal climatology and dynamical mechanisms of rainfall in the caribbean', *Climate dynamics* **53**(1-2), 825–846.
- McKenna, S., Santoso, A., Gupta, A. S., Taschetto, A. S. and Cai, W. (2020), 'Indian Ocean Dipole in CMIP5 and CMIP6: characteristics, biases, and links to ENSO', *Scientific reports*

- 10(1), 1–13.
- McPhaden, M. J., Zebiak, S. E. and Glantz, M. H. (2006), ‘Enso as an integrating concept in earth science’, *science* **314**(5806), 1740–1745.
- Menary, M. B., Kuhlbrodt, T., Ridley, J., Andrews, M. B., Dimdore-Miles, O. B., Deshayes, J., Eade, R., Gray, L., Ineson, S., Mignot, J., Roberts, C. D., Robson, J., Wood, R. A. and Xavier, P. (2018), ‘Preindustrial control simulations with HadGEM3-GC3. 1 for CMIP6’, *Journal of Advances in Modeling Earth Systems* **10**(12), 3049–3075.
- Mestas-Nuñez, A. M., Enfield, D. B. and Zhang, C. (2007), ‘Water vapor fluxes over the Intra-Americas Sea: Seasonal and interannual variability and associations with rainfall’, *Journal of Climate* **20**(9), 1910–1922.
- Misios, S., Gray, L. J., Knudsen, M. F., Karoff, C., Schmidt, H. and Haigh, J. D. (2019), ‘Slowdown of the Walker circulation at solar cycle maximum’, *Proceedings of the National Academy of Sciences* **116**(15), 7186–7191.
- Mission, T. R. M. (2011), ‘TRMM (TMPA/3B43) Rainfall Estimate L3 1 Month 0.25 Degree×0.25 Degree V7’, *Version, Greenbelt, MD, Goddard Earth Sciences Data and Information Services Center (GES DISC)*. Accessed: [12-Jan-2019].
URL: https://disc.gsfc.nasa.gov/datasets/TRMM_3B42_7/summary
- Mo, K. C. and Paegle, J. N. (2001), ‘The pacific–south american modes and their downstream effects’, *International Journal of Climatology: A Journal of the Royal Meteorological Society* **21**(10), 1211–1229.
- Montini, T. L., Jones, C. and Carvalho, L. M. (2019), ‘The south american low-level jet: A new climatology, variability, and changes’, *Journal of Geophysical Research: Atmospheres* **124**(3), 1200–1218.
- Moron, V. and Robertson, A. W. (2014), ‘Interannual variability of Indian summer monsoon rainfall onset date at local scale’, *International journal of climatology* **34**(4), 1050–1061.
- Mosino, A. and García, E. (1966), Evaluación de la sequía intraestival en la República Mexicana, in ‘Proc. Conf. Reg. Latinoamericana Unión Geogr. Int’, Vol. 3, pp. 500–516.
- Mulcahy, J. P., Jones, C., Sellar, A., Johnson, B., Boutle, I. A., Jones, A., Andrews, T., Rumbold, S. T., Molland, J., Bellouin, N., Johnson, C. E., Williams, K. D., Grosvenor, D. P. and McCoy, D. T. (2018), ‘Improved aerosol processes and effective radiative forcing in HadGEM3 and UKESM1’, *Journal of Advances in Modeling Earth Systems* **10**(11), 2786–2805.
- Muñoz, E., Busalacchi, A. J., Nigam, S. and Ruiz-Barradas, A. (2008), ‘Winter and summer structure of the Caribbean low-level jet’, *Journal of Climate* **21**(6), 1260–1276.
- Neelin, J. D. (2007), ‘Moist dynamics of tropical convection zones in monsoons, teleconnections, and global warming’.
- Neelin, J. D., Battisti, D. S., Hirst, A. C., Jin, F.-F., Wakata, Y., Yamagata, T. and Zebiak, S. E. (1998), ‘ENSO theory’, *Journal of Geophysical Research: Oceans* **103**(C7), 14261–14290.
- Neelin, J. D. and Su, H. (2005), ‘Moist teleconnection mechanisms for the tropical South American

- and Atlantic sector', *Journal of Climate* **18**(18), 3928–3950.
- Nesbitt, S. W., Gochis, D. J. and Lang, T. J. (2008), 'The diurnal cycle of clouds and precipitation along the sierra madre occidental observed during name-2004: Implications for warm season precipitation estimation in complex terrain', *Journal of Hydrometeorology* **9**(4), 728–743.
- Nie, J., Boos, W. R. and Kuang, Z. (2010), 'Observational evaluation of a convective quasi-equilibrium view of monsoons', *Journal of Climate* **23**(16), 4416–4428.
- Nie, J. and Sobel, A. H. (2015), 'Responses of tropical deep convection to the QBO: Cloud-resolving simulations', *Journal of the Atmospheric Sciences* **72**(9), 3625–3638.
- Nieto Ferreira, R. and Chao, W. C. (2013), 'Aqua-planet simulations of the formation of the south atlantic convergence zone', *International journal of climatology* **33**(3), 615–628.
- Nieto-Ferreira, R. and Rickenbach, T. M. (2011), 'Regionality of monsoon onset in South America: a three-stage conceptual model', *International Journal of Climatology* **31**(9), 1309–1321.
- Nobre, P., De Almeida, R. A., Malagutti, M. and Giarolla, E. (2012), 'Coupled ocean–atmosphere variations over the south atlantic ocean', *Journal of Climate* **25**(18), 6349–6358.
- O'Neill, B. C., Kriegler, E., Ebi, K. L., Kemp-Benedict, E., Riahi, K., Rothman, D. S., van Ruijven, B. J., van Vuuren, D. P., Birkmann, J., Kok, K. et al. (2017), 'The roads ahead: Narratives for shared socioeconomic pathways describing world futures in the 21st century', *Global environmental change* **42**, 169–180.
- O'Neill, B. C., Tebaldi, C., Vuuren, D. P. v., Eyring, V., Friedlingstein, P., Hurt, G., Knutti, R., Kriegler, E., Lamarque, J.-F., Lowe, J. et al. (2016), 'The scenario model intercomparison project (ScenarioMIP) for CMIP6', *Geoscientific Model Development* **9**(9), 3461–3482.
- Ordoñez, P., Nieto, R., Gimeno, L., Ribera, P., Gallego, D., Ochoa-Moya, C. A. and Quintanar, A. I. (2019), 'Climatological moisture sources for the Western North American Monsoon through a lagrangian approach: their influence on precipitation intensity', *Earth System Dynamics* **10**(1), 59–72.
- Oueslati, B. and Bellon, G. (2013), 'Convective entrainment and large-scale organization of tropical precipitation: Sensitivity of the CNRM-CM5 hierarchy of models', *Journal of climate* **26**(9), 2931–2946.
- Oueslati, B. and Bellon, G. (2015), 'The double ITCZ bias in CMIP5 models: Interaction between SST, large-scale circulation and precipitation', *Climate dynamics* **44**(3-4), 585–607.
- Pahlavan, H. A., Fu, Q., Wallace, J. M. and Kiladis, G. N. (2021), 'Revisiting the quasi-biennial oscillation as seen in era5. part i: Description and momentum budget', *Journal of the Atmospheric Sciences* **78**(3), 673–691.
- Palmer, M. and McNeall, D. (2014), 'Internal variability of earth's energy budget simulated by cmip5 climate models', *Environmental Research Letters* **9**(3), 034016.
- Palmer, T. (2019), 'Stochastic weather and climate models', *Nature Reviews Physics* **1**(7), 463–471.
- Palmer, T. and Stevens, B. (2019), 'The scientific challenge of understanding and estimating climate change', *Proceedings of the National Academy of Sciences* **116**(49), 24390–24395.

- Pascale, S., Carvalho, L. M., Adams, D. K., Castro, C. L. and Cavalcanti, I. F. (2019), 'Current and Future Variations of the Monsoons of the Americas in a Warming Climate', *Current Climate Change Reports* **5**(3), 125–144.
- Perdigón-Morales, J., Romero-Centeno, R., Barrett, B. S. and Ordoñez, P. (2019), 'Intraseasonal variability of summer precipitation in Mexico: MJO influence on the midsummer drought', *Journal of Climate* **32**(8).
- Perdigón-Morales, J., Romero-Centeno, R., Ordóñez, P. and Barrett, B. S. (2018), 'The midsummer drought in Mexico: perspectives on duration and intensity from the CHIRPS precipitation database', *International Journal of Climatology* **38**, 2174–2186.
- Perez, G. M. P., Vidale, P. L., Klingaman, N. P. and Martin, T. C. M. (2021), 'Atmospheric convergence zones stemming from large-scale mixing', *Weather and Climate Dynamics* **2**(2), 475–488.
- URL:** <https://wcd.copernicus.org/articles/2/475/2021/>
- Plumb, R. A. and Bell, R. C. (1982), 'A model of the quasi-biennial oscillation on an equatorial beta-plane', *Quarterly Journal of the Royal Meteorological Society* **108**(456), 335–352.
- Rauscher, S. A., Giorgi, F., Diffenbaugh, N. S. and Seth, A. (2008), 'Extension and intensification of the Meso-American mid-summer drought in the twenty-first century', *Climate Dynamics* **31**, 551–571.
- Reed, R. (1964), 'A tentative model of the 26-month oscillation in tropical latitudes', *Quarterly Journal of the Royal Meteorological Society* **90**(386), 441–466.
- Ribera, P., Peña-Ortiz, C., García-Herrera, R., Gallego, D., Gimeno, L. and Hernández, E. (2004), 'Detection of the secondary meridional circulation associated with the quasi-biennial oscillation', *Journal of Geophysical Research: Atmospheres* **109**(D18).
- Richter, I., Xie, S.-P., Behera, S. K., Doi, T. and Masumoto, Y. (2014), 'Equatorial atlantic variability and its relation to mean state biases in cmip5', *Climate dynamics* **42**(1-2), 171–188.
- Richter, J. H., Anstey, J. A., Butchart, N., Kawatani, Y., Meehl, G. A., Osprey, S. and Simpson, I. R. (2020), 'Progress in simulating the Quasi-Biennial Oscillation in CMIP models', *Journal of Geophysical Research: Atmospheres* **125**(8), e2019JD032362. e2019JD032362 10.1029/2019JD032362.
- Ridley, J., Menary, M., Kuhlbrodt, T., Andrews, M. and Andrews, T. (2018), 'MOHC HadGEM3-GC31-LL model output prepared for CMIP6 CMIP piControl'.
- URL:** <https://doi.org/10.22033/ESGF/CMIP6.6294>
- Ridley, J., Menary, M., Kuhlbrodt, T., Andrews, M. and Andrews, T. (2019a), 'Mohc hadgem3-gc31-ll model output prepared for cmip6 cmip amip'.
- URL:** <https://doi.org/10.22033/ESGF/CMIP6.5853>
- Ridley, J., Menary, M., Kuhlbrodt, T., Andrews, M. and Andrews, T. (2019b), 'MOHC HadGEM3-GC31-LL model output prepared for CMIP6 CMIP historical'.
- URL:** <https://doi.org/10.22033/ESGF/CMIP6.6109>

- Ridley, J., Menary, M., Kuhlbrodt, T., Andrews, M. and Andrews, T. (2019c), 'MOHC HadGEM3-GC31-MM model output prepared for CMIP6 CMIP piControl'.
URL: <https://doi.org/10.22033/ESGF/CMIP6.6297>
- Rodrigues, R. R., Haarsma, R. J., Campos, E. J. and Ambrizzi, T. (2011), 'The impacts of inter-El Niño variability on the tropical Atlantic and northeast Brazil climate', *Journal of Climate* **24**(13), 3402–3422.
- Rodwell, M. J. and Hoskins, B. J. (2001), 'Subtropical anticyclones and summer monsoons', *Journal of Climate* **14**(15), 3192–3211.
- Ropelewski, C. F. and Halpert, M. S. (1986), 'North american precipitation and temperature patterns associated with the el niño/southern oscillation (enso)', *Monthly Weather Review* **114**(12), 2352–2362.
- Ropelewski, C. F. and Halpert, M. S. (1987), 'Global and regional scale precipitation patterns associated with the El Niño/Southern Oscillation', *Monthly weather review* **115**(8), 1606–1626.
- Ryu, J.-H. and Hayhoe, K. (2014), 'Understanding the sources of Caribbean precipitation biases in CMIP3 and CMIP5 simulations', *Climate dynamics* **42**(11-12), 3233–3252.
- Sahana, A. S., Ghosh, S., Ganguly, A. and Murtugudde, R. (2015), 'Shift in Indian summer monsoon onset during 1976/1977', *Environmental Research Letters* **10**(5), 054006.
- Saji, N., Goswami, B. N., Vinayachandran, P. and Yamagata, T. (1999), 'A dipole mode in the tropical Indian Ocean', *Nature* **401**(6751), 360–363.
- Saurral, R. I., Camilloni, I. A. and Ambrizzi, T. (2015), 'Links between topography, moisture fluxes pathways and precipitation over south america', *Climate dynamics* **45**(3), 777–789.
- Schenzinger, V., Osprey, S., Gray, L. and Butchart, N. (2017), 'Defining metrics of the Quasi-Biennial oscillation in global climate models', *Geoscientific Model Development* **10**(6).
- Schirber, S. (2015), 'Influence of ENSO on the QBO: Results from an ensemble of idealized simulations', *Journal of Geophysical Research: Atmospheres* **120**(3), 1109–1122.
- Schneider, T., Bischoff, T. and Haug, G. H. (2014), 'Migrations and dynamics of the Intertropical Convergence Zone', *Nature* **513**(7516), 45.
- Seastrand, S., Serra, Y., Castro, C. and Ritchie, E. (2015), 'The dominant synoptic-scale modes of north american monsoon precipitation', *International Journal of Climatology* **35**(8), 2019–2032.
- Sellar, A. A., Jones, C. G., Mulcahy, J., Tang, Y., Yool, A., Wiltshire, A., O'Connor, F. M., Stringer, M., Hill, R., Palmieri, J., Woodward, S., de Mora, L., Kuhlbrodt, T., Rumbold, S., Kelley, D. I., Ellis, R., Johnson, C. E., Walton, J., Abraham, N. L., Andrews, M. B., Andrews, T., Archibald, A. T., Berthou, S., Burke, E., Blockley, E., Carslaw, K., Dalvi, M., Edwards, J., Folberth, G. A., Gedney, N., Griffiths, P. T., Harper, A. B., Hendry, M. A., Hewitt, A. J., Johnson, B., Jones, A., Jones, C. D., Keeble, J., Liddicoat, S., Morgenstern, O., Parker, R. J., Predoi, V., Robertson, E., Siahaan, A., Smith, R. S., Swaminathan, R., Woodhouse, M. T., Zeng, G. and Zerroukat, M. (2019), 'UKESM1: Description and evaluation of the UK Earth System Model', *Journal of Advances in Modeling Earth Systems* **11**(12), 4513–4558.

- Serva, F., Anstey, J. A., Bushell, A. C., Butchart, N., Cagnazzo, C., Gray, L., Kawatani, Y., Osprey, S. M., Richter, J. H. and Simpson, I. R. (submitted), 'The impact of the QBO near the tropical tropopause layer in QBOi models: present-day simulations', *Quarterly Journal of the Royal Meteorological Society*.
- Serva, F., Cagnazzo, C., Christiansen, B. and Yang, S. (2020), 'The influence of enso events on the stratospheric qbo in a multi-model ensemble', *Climate Dynamics* **54**(3), 2561–2575.
- Shepherd, T. G. (2014), 'Atmospheric circulation as a source of uncertainty in climate change projections', *Nature Geoscience* **7**(10), 703–708.
- Siongco, A. C., Hohenegger, C. and Stevens, B. (2015), 'The atlantic itcz bias in cmip5 models', *Climate Dynamics* **45**(5), 1169–1180.
- Small, R. J. O., De Szoeke, S. P. and Xie, S.-P. (2007), 'The Central American midsummer drought: Regional aspects and large-scale forcing', *Journal of Climate* **20**(19), 4853–4873.
- Smyth, J. E., Hill, S. A. and Ming, Y. (2018), 'Simulated responses of the West African Monsoon and zonal-mean tropical precipitation to early holocene orbital forcing', *Geophysical Research Letters* **45**(21), 12–049.
- Smyth, J. E. and Ming, Y. (2020), 'Characterizing drying in the South American monsoon onset season with the moist static energy budget', *Journal of Climate* **33**(22), 9735–9748.
- Sobel, A. H., Nilsson, J. and Polvani, L. M. (2001), 'The weak temperature gradient approximation and balanced tropical moisture waves', *Journal of the atmospheric sciences* **58**(23), 3650–3665.
- Son, S.-W., Lim, Y., Yoo, C., Hendon, H. H. and Kim, J. (2017), 'Stratospheric control of the Madden–Julian oscillation', *Journal of Climate* **30**(6), 1909–1922.
- Stensrud, D. J., Gall, R. L. and Nordquist, M. K. (1997), 'Surges over the Gulf of California during the Mexican monsoon', *Monthly Weather Review* **125**(4), 417–437.
- Storkey, D., Blaker, A. T., Mathiot, P., Megann, A., Aksenov, Y., Blockley, E. W., Calvert, D., Graham, T., Hewitt, H. T., Hyder, P. et al. (2018), 'UK Global Ocean GO6 and GO7: A traceable hierarchy of model resolutions', *Geoscientific Model Development* **11**(8), 3187–3213.
- Straffon, A., Zavala-Hidalgo, J. and Estrada, F. (2019), 'Preconditioning of the precipitation interannual variability in southern Mexico and Central America by oceanic and atmospheric anomalies', *International Journal of Climatology* .
- Sulca, J., Takahashi, K., Espinoza, J.-C., Vuille, M. and Lavado-Casimiro, W. (2018), 'Impacts of different ENSO flavors and tropical Pacific convection variability (ITCZ, SPCZ) on austral summer rainfall in South America, with a focus on Peru', *International Journal of Climatology* **38**(1), 420–435.
- Sultan, B., Baron, C., Dingkuhn, M., Sarr, B. and Janicot, S. (2005), 'Agricultural impacts of large-scale variability of the west african monsoon', *Agricultural and Forest Meteorology* **128**(1), 93 – 110.
- Taguchi, M. (2010), 'Observed connection of the stratospheric quasi-biennial oscillation with el niño–southern oscillation in radiosonde data', *Journal of Geophysical Research: Atmospheres*

- 115(D18).
- Tang, Y., Rumbold, S., Ellis, R., Kelley, D., Mulcahy, J., Sellar, A., Walton, J. and Jones, C. (2019a), ‘MOHC UKESM1.0-LL model output prepared for CMIP6 CMIP historical’.
- URL:** <https://doi.org/10.22033/ESGF/CMIP6.6113>
- Tang, Y., Rumbold, S., Ellis, R., Kelley, D., Mulcahy, J., Sellar, A., Walton, J. and Jones, C. (2019b), ‘MOHC UKESM1.0-LL model output prepared for CMIP6 CMIP piControl’.
- URL:** <https://doi.org/10.22033/ESGF/CMIP6.6298>
- Taschetto, A. S., Rodrigues, R. R., Meehl, G. A., McGregor, S. and England, M. H. (2016), ‘How sensitive are the pacific–tropical north atlantic teleconnections to the position and intensity of el niño-related warming?’, *Climate Dynamics* **46**(5), 1841–1860.
- Tebaldi, C., Debeire, K., Eyring, V., Fischer, E., Fyfe, J., Friedlingstein, P., Knutti, R., Lowe, J., O’Neill, B., Sanderson, B., van Vuuren, D., Riahi, K., Meinshausen, M., Nicholls, Z., Tokarska, K. B., Hurtt, G., Kriegler, E., Lamarque, J.-F., Meehl, G., Moss, R., Bauer, S. E., Boucher, O., Brovkin, V., Byun, Y.-H., Dix, M., Gualdi, S., Guo, H., John, J. G., Kharin, S., Kim, Y., Koshiro, T., Ma, L., Olivié, D., Panickal, S., Qiao, F., Rong, X., Rosenbloom, N., Schupfner, M., Séférian, R., Sellar, A., Semmler, T., Shi, X., Song, Z., Steger, C., Stouffer, R., Swart, N., Tachiiri, K., Tang, Q., Tatebe, H., Volodin, E., Wyser, K., Xin, X., Yang, S., Yu, Y. and Ziehn, T. (2021), ‘Climate model projections from the scenario model intercomparison project (scenariomip) of cmip6’, *Earth System Dynamics* **12**(1), 253–293.
- URL:** <https://esd.copernicus.org/articles/12/253/2021/>
- Tedeschi, R. G., Grimm, A. M. and Cavalcanti, I. F. (2015), ‘Influence of Central and East ENSO on extreme events of precipitation in South America during austral spring and summer’, *International Journal of Climatology* **35**(8), 2045–2064.
- Tegtmeier, S., Anstey, J., Davis, S., Dragani, R., Harada, Y., Ivanciu, I., Pilch Kedzierski, R., Krüger, K., Legras, B., Long, C., Wang, J. S., Wargan, K. and Wright, J. S. (2020a), ‘Temperature and tropopause characteristics from reanalyses data in the tropical tropopause layer’, *Atmospheric Chemistry and Physics* **20**(2), 753–770.
- Tegtmeier, S., Anstey, J., Davis, S., Ivanciu, I., Jia, Y., McPhee, D. and Pilch Kedzierski, R. (2020b), ‘Zonal Asymmetry of the QBO Temperature Signal in the Tropical Tropopause Region’, *Geophysical Research Letters* **47**(24), e2020GL089533. e2020GL089533 2020GL089533.
- Telford, P., Braesicke, P., Morgenstern, O. and Pyle, J. (2008), ‘Description and assessment of a nudged version of the new dynamics unified model’, *Atmospheric Chemistry and Physics* **8**(6), 1701–1712.
- Trejo, F. J. P., Barbosa, H. A., Peñaloza-Murillo, M. A., Moreno, M. A. and Farías, A. (2016), ‘Intercomparison of improved satellite rainfall estimation with CHIRPS gridded product and rain gauge data over Venezuela’, *Atmósfera* **29**(4), 323–342.
- Trenberth, K. E. (1997), ‘The definition of el nino’, *Bulletin of the American Meteorological Society* **78**(12), 2771–2778.

- Trenberth, K. E., Branstator, G. W., Karoly, D., Kumar, A., Lau, N.-C. and Ropelewski, C. (1998), 'Progress during TOGA in understanding and modeling global teleconnections associated with tropical sea surface temperatures', *Journal of Geophysical Research: Oceans* **103**(C7), 14291–14324.
- Troup, A. (1965), 'The 'southern oscillation'', *Quarterly Journal of the Royal Meteorological Society* **91**(390), 490–506.
- Turner, A. G. and Annamalai, H. (2012), 'Climate change and the South Asian summer monsoon', *Nature Climate Change* **2**(8), 587–595.
- Turrent, C. and Cavazos, T. (2009), 'Role of the land-sea thermal contrast in the interannual modulation of the North American Monsoon', *Geophysical Research Letters* **36**(2).
- Van Der Wiel, K., Matthews, A. J., Stevens, D. P. and Joshi, M. M. (2015), 'A dynamical framework for the origin of the diagonal south pacific and south atlantic convergence zones', *Quarterly Journal of the Royal Meteorological Society* **141**(691), 1997–2010.
- Vera, C., Higgins, W., Amador, J., Ambrizzi, T., Garreaud, R., Gochis, D., Gutzler, D., Lettenmaier, D., Marengo, J., Mechoso, C. R., Nogues-Paegle, J., Dias, P. L. S. and Zhang, C. (2006), 'Toward a unified view of the American monsoon systems', *Journal of Climate* **19**(20), 4977–5000.
- Walker, G. T. (1924), 'Correlations in seasonal variations of weather. I. A further study of world weather', *Mem. Indian Meteorol. Dep.* **24**, 275–332.
- Walters, D., Boutle, I., Brooks, M., Melvin, T., Stratton, R., Vosper, S., Wells, H., Williams, K., Wood, N., Allen, T., Bushell, A., Copsey, D., Earnshaw, P., Edwards, J., Gross, M., Hardiman, S., Harris, C., Heming, J., Klingaman, N., Levine, R., Manners, J., Martin, G., Milton, S., Mittermaier, M., Morcrette, C., Riddick, T., Roberts, M., Sanchez, C., Selwood, P., Stirling, A., Smith, C., Suri, D., Tennant, W., Vidale, P. L., Wilkinson, J., Willett, M., Woolnough, S. and Xavier, P. (2019), 'The Met Office Unified Model global atmosphere 7.0/7.1 and JULES global land 7.0 configurations', *Geoscientific Model Development* **12**(5), 1909–1963.
- Wang, B., Biasutti, M., Byrne, M. P., Castro, C., Chang, C.-P., Cook, K., Fu, R., Grimm, A. M., Ha, K.-J., Hendon, H. et al. (2021), 'Monsoons climate change assessment', *Bulletin of the American Meteorological Society* **102**(1), E1–E19.
- Wang, B. and Ding, Q. (2008), 'Global monsoon: Dominant mode of annual variation in the tropics', *Dynamics of Atmospheres and Oceans* **44**(3-4), 165–183.
- Wang, C. and Picaut, J. (2004), 'Understanding ENSO physics—A review', *Earth's Climate: The Ocean–Atmosphere Interaction, Geophys. Monogr* **147**, 21–48.
- Wang, P. X., Wang, B., Cheng, H., Fasullo, J., Guo, Z., Kiefer, T. and Liu, Z. (2017), 'The global monsoon across time scales: Mechanisms and outstanding issues', *Earth-Science Reviews* **174**, 84–121.
- Wang, S., Tippett, M. K., Sobel, A. H., Martin, Z. and Vitart, F. (2019), 'Impact of the QBO on prediction and predictability of the MJO convection', *J. Geophys. Res. Atmos.*

- Wang, X. and Wang, C. (2014), 'Different impacts of various El Niño events on the Indian Ocean Dipole', *Climate dynamics* **42**(3-4), 991–1005.
- Watanabe, M., Kug, J.-S., Jin, F.-F., Collins, M., Ohba, M. and Wittenberg, A. T. (2012), 'Uncertainty in the enso amplitude change from the past to the future', *Geophysical Research Letters* **39**(20).
- Webb, M. J., Andrews, T., Bodas-Salcedo, A., Bony, S., Bretherton, C. S., Chadwick, R., Chepfer, H., Douville, H., Good, P., Kay, J. E. et al. (2017), 'The cloud feedback model intercomparison project (CFMIP) contribution to CMIP6', *Geoscientific Model Development* **10**(1), 359–384.
- Webster, P. J. (2020), *Dynamics of the Tropical Atmosphere and Oceans*, John Wiley & Sons.
- Webster, P. J. and Yang, S. (1992), 'Monsoon and Enso: Selectively Interactive Systems', *Quarterly Journal of the Royal Meteorological Society* **118**(507), 877–926.
- Whitcher, B., Guttorp, P. and Percival, D. B. (2000), 'Wavelet analysis of covariance with application to atmospheric time series', *Journal of Geophysical Research: Atmospheres* **105**(D11), 14941–14962.
- Wilks, D. S. (2011), *Statistical methods in the atmospheric sciences*, Vol. 100, Academic press.
- Williams, K. D., Copsey, D., Blockley, E. W., Bodas-Salcedo, A., Calvert, D., Comer, R., Davis, P., Graham, T., Hewitt, H. T., Hill, R., Hyder, P., Ineson, S., Johns, T. C., Keen, A. B., Lee, R. W., Megann, A., Milton, S. F., Rae, J. G. L., Roberts, M. J., Scaife, A. A., Schiemann, R., Storkey, D., Thorpe, L., Watterson, I. G., Walters, D. N., West, A., Wood, R. A., Woollings, T. and Xavier, P. K. (2018), 'The Met Office global coupled model 3.0 and 3.1 (GC3. 0 and GC3. 1) configurations', *Journal of Advances in Modeling Earth Systems* **10**(2), 357–380.
- Wing, A. A., Camargo, S. J., Sobel, A. H., Kim, D., Moon, Y., Murakami, H., Reed, K. A., Vecchi, G. A., Wehner, M. F., Zarzycki, C. et al. (2019), 'Moist static energy budget analysis of tropical cyclone intensification in high-resolution climate models', *Journal of Climate* **32**(18), 6071–6095.
- Xie, P. and Arkin, P. A. (1997), 'Global precipitation: A 17-year monthly analysis based on gauge observations, satellite estimates, and numerical model outputs', *Bulletin of the American Meteorological Society* **78**, 2539–2558.
- Xie, P., Arkin, P. A. and Janowiak, J. E. (2007), *CMAP: The CPC Merged Analysis of Precipitation*, Springer Netherlands, Dordrecht, pp. 319–328.
- Yang, B., Zhang, Y., Qian, Y., Song, F., Leung, L. R., Wu, P., Guo, Z., Lu, Y. and Huang, A. (2019), 'Better monsoon precipitation in coupled climate models due to bias compensation', *NPJ Climate and Atmospheric Science* **2**(1), 1–8.
- Yin, L., Fu, R., Shevliakova, E. and Dickinson, R. E. (2013), 'How well can CMIP5 simulate precipitation and its controlling processes over tropical South America?', *Climate Dynamics* **41**(11-12), 3127–3143.
- Yoon, J.-H. and Zeng, N. (2010), 'An Atlantic influence on Amazon rainfall', *Climate dynamics* **34**(2), 249–264.
- Yu, B. and Zwiers, F. W. (2010), 'Changes in equatorial atmospheric zonal circulations in recent

- decades', *Geophysical Research Letters* **37**(5).
- Zanchettin, D., Bothe, O., Müller, W., Bader, J. and Jungclaus, J. H. (2014), 'Different flavors of the atlantic multidecadal variability', *Climate Dynamics* **42**(1), 381–399.
- Zermeño-Díaz, D. M. (2019), 'The spatial pattern of midsummer drought as a possible mechanistic response to lower-tropospheric easterlies over the intra-americas seas', *Journal of Climate* **32**(24), 8687–8700.
- Zhai, J. and Boos, W. (2015), 'Regime transitions of cross-equatorial Hadley circulations with zonally asymmetric thermal forcings', *Journal of the Atmospheric Sciences* **72**(10), 3800–3818.
- Zhao, Z., Holbrook, N. J., Oliver, E. C., Ballesteros, D. and Vargas-Hernandez, J. M. (2020), 'Characteristic atmospheric states during mid-summer droughts over Central America and Mexico', *Climate Dynamics* pp. 1–21.
- Zhao, Z. and Zhang, X. (2021), 'Evaluation of methods to detect and quantify the bimodal precipitation over Central America and Mexico', *International Journal of Climatology* **41**, E897–E911.
- Zhou, J. and Lau, K. (1998), 'Does a monsoon climate exist over south america?', *Journal of climate* **11**(5), 1020–1040.
- Zhou, T., Turner, A. G., Kinter, J. L., Wang, B., Qian, Y., Chen, X., Wu, B., Liu, B., Zou, L. and Bian, H. (2016), 'GMMIP (v1. 0) contribution to CMIP6: global monsoons model inter-comparison project', *Geoscientific Model Development* **9**, 3589–3604.
- Zilli, M. T., Carvalho, L. M. and Lintner, B. R. (2019), 'The poleward shift of south atlantic convergence zone in recent decades', *Climate Dynamics* **52**(5), 2545–2563.
- Zilli, M. T. and Hart, N. C. (2021), 'Rossby wave dynamics over south america explored with automatic tropical-extratropical cloud band identification framework', *Journal of Climate* **34**(20), 8125–8144.
- Zou, L. and Zhou, T. (2015), 'Asian summer monsoon onset in simulations and CMIP5 projections using four Chinese climate models', *Advances in Atmospheric Sciences* **32**(6), 794–806.